Complex spin structures in frustrated ultrathin films

Doctorate Thesis

Sebastian Meyer

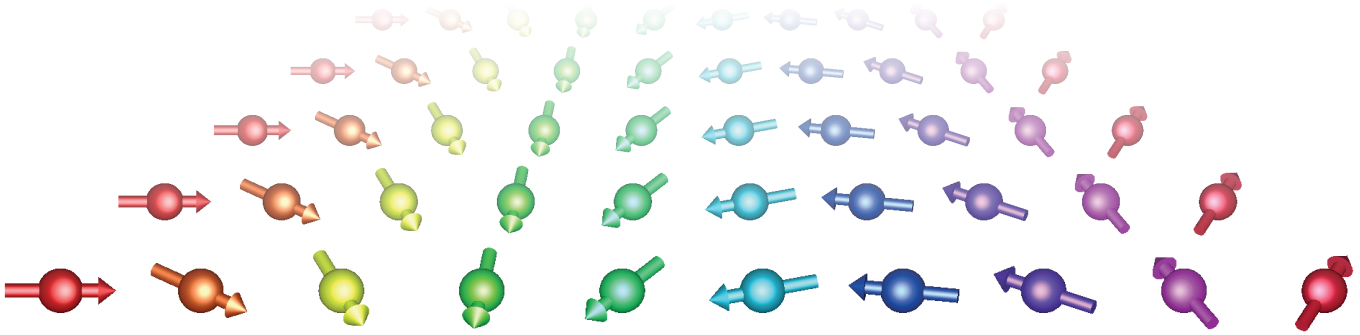

KIEL 2020

Complex spin structures in frustrated ultrathin films

Dissertation
zur Erlangung des Doktorgrades
der Mathematisch-Naturwissenschaftlichen Fakultät
der Christian-Albrechts-Universität zu Kiel

vorgelegt von
Sebastian Meyer

Kiel, Germany - Juli 2020

Erster Gutachter: Prof. Dr. Stefan Heinze
Zweiter Gutachter: Prof. Dr. Richard Berndt
Dritter Gutachter: Prof. Dr. Matthias Bode

Tag der mündlichen Prüfung: 15.10.2020

Inhaltsangabe

In der vorliegenden Arbeit werden komplexe, durch Frustration der magnetischen Wechselwirkungen verursachte Spinstrukturen in ultradünnen Co und Mn Filmen untersucht. Dazu werden Ergebnisse aus Dichtefunktionaltheorie [engl. density functional theory (DFT)] Rechnungen mittels der so genannten "full potential linearized augmented planewave" Methode auf ein atomistisches Spinmodell abgebildet. Daraus werden die Größen der magnetischen Wechselwirkungen bestimmt und daraufhin Spindynamik Simulationen durchgeführt, um magnetische Eigenschaften nicht-kollinearer Strukturen wie Domänenwände [engl. domain walls (DWs)], Skyrmionen oder Antiskyrmionen zu untersuchen. Die dargestellten Ergebnisse werden ebenfalls mit Messungen aus spin-polarisierter Rastertunnelmikroskopie [engl. spin-polarized scanning tunnelling microscopy (SP-STM)] verglichen, die von Kooperationspartnern durchgeführt wurden.

Für die, in magnetischen Multilagensystemen, bereits gut untersuchte Pt/Co/Ir Grenzschicht wurden additive Effekte für die Dzyaloshinskii-Moriya Wechselwirkung [engl. Dzyaloshinskii-Moriya interaction (DMI)] vorhergesagt. Bei der Untersuchung von ultradünnen Co Monolagen und Pt/Co Bilagen auf der Ir(111) Oberfläche wird allerdings gezeigt, dass additive Effekte bei der Erhöhung der DMI keine Rolle spielen und darüber hinaus, dass sich die DMI an den Pt/Co/Ir Grenzflächen deutlich komplexer verhält als bisher angenommen. Im Zuge dessen werden Frustrationseffekte der DMI in den untersuchten Übergangsmetall-Grenzflächen vorhergesagt – Effekte, die in diesem Forschungsbereich bisher nicht berücksichtigt wurden. Die Folge der DMI Frustration ist eine Abhängigkeit des Rotationssinns von der Periode der betrachteten Spinspirale. Berechnungen zur DMI können als Folge der Frustration zu falschen Ergebnissen führen, wenn ungeeignete nicht-kollineare Spinstrukturen zur Analyse herangezogen werden. Die Austauschwechselwirkung im untersuchten Co/Ir(111) kann mithilfe von 4*d* Adlagen von leicht ferromagnetisch (FM) zu stark FM variiert werden. Wird das Ir(111) Substrat weiter mit dem isoelektronischen 4*d* Substrat Rh(111) ausgetauscht, können gezielt Wechselwirkungen justiert werden, die von der Spin-Bahn Kopplung verursacht werden. In dieser Untersuchung zeigt Rh/Co/Ir(111) ein außergewöhnlich hohes Maß an Frustration, was die Stabilisierung von atomar kleinen, nicht-kollinearen Spinstrukturen wie beispielsweise DWs, Skyrmionen oder Antiskyrmionen begünstigt – sogar ohne ein von außen angelegtes Magnetfeld. SP-STM Experimente konnten diese Vorhersage einerseits bestätigen und zusätzlich Skyrmionen und DWs mit nicht-magnetischen Spitzen nachweisen. Ein starker, an der Fermi Energie lokalisierter nicht-kollinearer Magnetowiderstand, wird durch das Mischen eines Majoritäts d_{xz} und eines Minoritäts p_z Zustandes in der Rh/Co Bilage erklärt.

Antiferromagnetische (AFM) Materialien haben sich als vielversprechend im Hinblick auf spintronische Anwendungsmöglichkeiten herausgestellt. Mn ist ein prototypischer AFM und besitzt ein großes Spektrum an magnetischen und strukturellen Eigenschaften. Obwohl mittels SP-STM ein vermeintlich einfacher $c(2 \times 2)$ AFM Grundzustand in einer Mn Doppellage auf der W(001) Oberfläche gefunden wurde, weisen die DFT Rechnungen auf eine tote magnetische Mn Zwischenlage hin, in der das Ausbilden des magnetischen Moments durch Frustrationseffekte völlig unterdrückt wird. Die hervorragende Übereinstimmung zwischen Theorie und Experiment bestätigt diese Annahme. Im ultradünnen Filmsystem Mn/Re(0001) konnten Experimentatoren zum ersten Mal einen reihenweisen Antiferromagneten [engl. row-wise antiferromagnet (RW-AFM)] und einen 3Q Zustand mittels STM nachweisen. Die hier dargestellten Berechnungen heben eine starke Frustration des Austauschs, der DMI, aber auch von Wechselwirkungen höherer Ordnung hervor. Die Effekte sind die Folge einer starken Hybridisierung zwischen der Mn Lage und des Re(0001) Substrates. Eine Kopplung des RW-AFM an das Gitter für Mn_{fcc} kann durch das Zusammenspiel der dipolaren und der pseudo-dipolaren Wechselwirkung erklärt werden. Für eine hcp Stapelung der Mn Lage wird ein neuer Zustand mittels DFT vorgeschlagen: eine Verzerrung des 3Q Zustandes in Richtung des RW-AFM.

Abstract

In this thesis, complex spin structures driven by frustration of magnetic interactions are studied in ultrathin Co and Mn films. Therefore, density functional theory (DFT) calculations using the full potential linearized augmented planewave method are mapped onto an atomistic spin model. On this basis, spindynamics simulations are performed to analyse the properties of non-collinear spin structures such as domain walls (DWs), skyrmions and antiskyrmions. The obtained results are compared to spin-polarized scanning tunnelling microscopy (SP-STM) measurements performed by experimental collaborators.

For the prominent Pt/Co/Ir interface, additive effects have been proposed in magnetic multilayer systems to enhance the Dzyaloshinskii-Moriya interaction (DMI); however, here it is shown that this phenomenon does not occur in atomic Pt/Co bilayers (BLs) on Ir(111). Even though an enhancement of the DMI from Co/Ir(111) to Pt/Co/Ir(111) is observed, the interfacial DMI appears more complex and a frustration of DMI is predicted – an effect which has been neglected so far. It results in a dependence of the rotational sense on the period of spin spirals and demonstrates that DMI calculations can give wrong results when unsuitable non-collinear spin structures are considered. Furthermore, the exchange interaction of Co/Ir(111) is tuned with 4*d* top layers from weakly to strongly ferromagnetic. Replacing Ir(111) by its 4*d* equivalent Rh(111), the spin-orbit coupling dependent interactions can be controlled. Exceptionally large frustration is found for Rh/Co/Ir(111). This stabilizes atomic-scale non-collinear spin structures such as DWs and skyrmions without an external magnetic field. SP-STM measurements confirm this prediction and reveal a large non-collinear magnetoresistance at the Fermi energy. This effect is explained by a spin mixing of a majority d_{xz} and a minority p_z state in the Rh/Co BL and allows for the detection of skyrmions and DWs with non-magnetic tips.

Antiferromagnetic (AFM) materials are promising for spintronic applications and the prototypical AFM Mn holds a wide spectrum of magnetic and structural properties. Although a seemingly simple $c(2 \times 2)$ AFM ground state in a Mn double layer on W(001) has been suggested by SP-STM measurements, the presented DFT calculations highlight a dead magnetic layer in the Mn subsurface driven by strong frustration effects. This is confirmed by excellent agreement of theory and experiment. In Mn/Re(0001), experimental collaborators have discovered the row-wise antiferromagnetic (RW-AFM) and the 3Q state in STM measurements. Calculations point out strong frustration of exchange and DMI, but also of higher order exchange interactions due to hybridization of Mn and Re(0001). The coupling of the RW-AFM state to the lattice in Mn_{fcc} is explained by the interplay of dipolar and pseudo-dipolar interactions, whereas a distortion of the 3Q state in Mn_{hcp} towards the RW-AFM is predicted by DFT.

Contents

List of Publications **9**

List of Acronyms **11**

1 Introduction **1**

I Theoretical Description 9

2 Density Functional Theory **11**
2.1 The electron density $n(\mathbf{r})$ . . . 12
2.2 Theorems of Hohenberg and Kohn . . . 12
2.3 Kohn-Sham equations . . . 13
2.4 Spin-Polarization in Density Functional Theory . . . 15
2.5 Relativistic Density Functional Theory . . . 16
2.6 Spin-orbit coupling in Density Functional Theory . . . 18
2.7 Exchange Correlation Functionals . . . 19
2.8 Self-Consistency in Density Functional Theory Calculations . . . 21
2.9 Total energy . . . 22
2.10 Force theorem . . . 23

3 Solution of Kohn-Sham equations within FLAPW **25**
3.1 Generalized Eigenvalue problem . . . 25
3.2 The Bloch theorem . . . 26
3.3 The planewave basis set . . . 26
3.4 The APW method . . . 27
3.5 The LAPW method . . . 28
3.6 The FLAPW method . . . 30
3.7 Local Orbitals . . . 30
3.7.1 Films in FLAPW . . . 31
3.7.2 Scalar-relativistic approximation in FLAPW . . . 33
3.7.3 Spin spirals and the generalized Bloch theorem . . . 34
3.7.4 First order perturbation theory: spin spirals including SOC . . . 35

4 Models of magnetism **37**
4.1 Stoner model of magnetism . . . 37
4.2 Tersoff-Hamann model . . . 39
4.3 Atomistic spin model . . . 42
4.3.1 Exchange interaction . . . 42

4.3.2 Higher order exchange interaction . . . 44
4.3.3 Dzyaloshinskii-Moriya interaction . . . 45
4.3.4 Magnetocrystalline anisotropy . . . 46
4.3.5 Dipole-dipole interaction . . . 47
4.3.6 Anisotropic symmetric exchange interaction . . . 48
4.3.7 The atomistic spin model . . . 48
4.4 Investigation of non-symmetric magnetic states . . . 49
4.4.1 Atomistic spindynamics . . . 49
4.4.2 Geodesic Nudged Elastic Band Method . . . 50

II Non-collinear spin structures in ferromagnetic Cobalt 53

5 Domain walls and Dzyaloshinskii-Moriya interaction in Co/Ir(111) and Pt/Co/Ir(111) 55
5.1 Computational details . . . 56
5.2 FM ground state properties of Co/Ir(111) . . . 59
5.3 FM ground state properties of Pt/Co/Ir(111) . . . 62
5.4 Experimental observations . . . 66
5.5 Comparing theory and experiments . . . 68
5.6 Additive DMI in Pt/Co/Co/Ir(111) and Pt/Pt/Co/Ir(111) . . . 70
5.7 Conclusion . . . 72

6 Frustration of Dzyaloshinskii-Moriya interaction in Co/Ir interfaces 73
6.1 Computational details . . . 74
6.2 Comparison of atomistic spin model and effective nearest neighbour approximation . . . 75
6.3 Origin of frustration of DMI in Pt/Co/Ir interfaces . . . 78
6.4 Effect of DMI frustration on non-collinear magnetic structures in Co_{hcp}/Ir(111) . . . 82
6.5 DMI frustration in spindynamics . . . 85
6.6 Conclusion . . . 88
6.7 Outlook . . . 89
6.8 Test calculations . . . 90
6.8.1 Dependence of magnetic interactions on substrate thickness . . . 90
6.8.2 Conical spin spiral states . . . 93

7 Tuning exchange frustration in Co films 97
7.1 Computational Details . . . 98
7.2 Electronic structure and magnetic properties . . . 99
7.3 Describing magnetic interactions . . . 104
7.4 Conclusion . . . 111

8 Detection of isolated zero field sub-10 nm skyrmions in ultrathin Co films 115
8.1 Computational Details . . . 116
8.2 Exchange and DMI frustration in Rh/Co/Ir(111) . . . 118
8.3 Magnetic and electronic properties . . . 122
8.4 Prediction of skyrmions and antiskyrmions in Rh_{fcc}/Co/Ir(111) . . . 124
8.5 Experimental observation of atomic-scale domain walls and skyrmions in Rh_{hcp}/Co/Ir(111) . . . 126
8.6 Swapping Rh and Co – a 100% intermixed film system . . . 127
8.7 Zero field skyrmions and the chimera collapse mechanism in Rh_{hcp}/Co/Ir(111) . . . 129
8.8 Non-collinear tunnelling magnetoresistance in Rh_{hcp}/Co/Ir(111) . . . 135
8.9 Conclusion . . . 140
8.10 Test calculations . . . 142
8.10.1 Convergence of spin spiral states and the atomistic spin model beyond nearest neighbours . . . 142
8.10.2 Conical spin spiral states . . . 144
8.10.3 Influence of *xc* potential on DFT results . . . 146
8.10.4 Determining magnetic interactions from domain wall properties 147

III Strongly frustrated antiferromagnetic Manganese 149

9 Magnetic moment quenching through hybridization and frustration - Mn double layer on W(001) 151
9.1 Previous study on Mn/Mn/W(001) . . . 152
9.2 Experimental observation of a $c(2\times2)$ antiferromagnetic ground state . 152
9.3 Computational details . . . 153
9.4 $c(2\times2)$ antiferromagnetic ground state . . . 155
9.5 Detection of a dead magnetic layer . . . 159
9.6 Artificial stabilization of a magnetic moment in the Mn interface layer . 162
9.7 Conclusion . . . 165

10 Competition of higher order exchange interactions: Mn/Re(0001) 167
10.1 Experimental observation of RW-AFM and 3Q states . . . 168
10.2 Computational Details . . . 170
10.3 Competition of higher order exchange interactions from first-principles 172
10.4 Electronic structure in Mn/Re(0001) . . . 175
10.5 Coupling magnetic states to the lattice - anisotropic symmetric exchange 177
10.6 Conversion of Multi-Q states . . . 178
10.7 Conclusion . . . 184

11 Summary 185

Summary **185**

Bibliography **189**

List of Figures **209**

List of Tables **212**

Appendices

Appendix A Layer resolved DMI in Co/Ir(111) and Pt/Co/Ir(111) **215**

Appendix B Skyrmion collapse mechanisms in Rh/Co/Ir(111) **219**

Appendix C Orbital resolved LDOS for Rh_{hcp}/Co/Ir(111) **223**

Appendix D Multi-Q states in DFT **227**

List of Publications

During this PhD, several manuscripts were published which are marked as Roman letters in the text. These are listed below.

I **Domain walls and Dzyaloshinskii-Moriya interaction in epitaxial Co/Ir(111) and Pt/Co/Ir(111)**
Marco Perini, **Sebastian Meyer**, Bertrand Dupé, Stephan von Malottki, André Kubetzka, Kirsten von Bergmann, Roland Wiesendanger, and Stefan Heinze, Physical Review B **97**, 184425 (2018)

II **Isolated zero field sub-10 nm skyrmions in ultrathin Co films**
Sebastian Meyer, Marco Perini, Stephan von Malottki, André Kubetzka, Roland Wiesendanger, Kirsten von Bergmann, and Stefan Heinze, Nature Communications **10**, 3823 (2019)

III **Electrical detection of domain walls and skyrmions in Co films using noncollinear magnetoresistance**
Marco Perini, **Sebastian Meyer**, André Kubetzka, Roland Wiesendanger, Stefan Heinze, and Kirsten von Bergmann, Physical Review Letters **123**, 237205 (2019)

IV **Dead magnetic layers at the interface: Moment quenching through hybridization and frustration**
Sebastian Meyer, Martin Schmitt, Matthias Vogt, Matthias Bode and Stefan Heinze, Physical Review Research **2**, 012075(R) (2020)

V **Discovery of Magnetic Single- and Triple-q States in Mn/Re(0001)**
Jonas Spethmann, **Sebastian Meyer**, Kirsten von Bergmann, Roland Wiesendanger, Stefan Heinze and André Kubetzka, Physical Review Letters **124**, 227203 (2020)

Additional publications which are not part of this thesis:

- **Dzyaloshinskii-Moriya interaction at an antiferromagnetic interface: First-principles study of Fe/Ir bilayers on Rh(001)**
  Sebastian Meyer, Bertrand Dupé, Paolo Ferriani, and Stefan Heinze, Physical Review B **96**, 094408 (2017)
- **Competition of Dzyaloshinskii-Moriya and Higher-Order Exchange Interactions in Rh/Fe Atomic Bilayers on Ir(111)**
  Niklas Romming, Henning Pralow, André Kubetzka, Markus Hoffmann, Stephan von Malottki, **Sebastian Meyer**, Bertrand Dupé, Roland Wiesendanger, Kirsten von Bergmann, and Stefan Heinze, Physical Review Letters **20**, 207201 (2018)
- **First-principles prediction of sub-10-nm skyrmions in Pd/Fe bilayers on Rh(111)**
  Soumyajyoti Haldar, Stephan von Malottki, **Sebastian Meyer**, Pavel F. Bessarab, and Stefan Heinze, Physical Review B **98**, 060413(R) (2018)

List of Acronyms

2D	two-dimensional
3D	three-dimensional
App.	Appendix
AFM	antiferromagnetic, antiferromagnet, antiferromagnetically
APW	augmented planewave
ASE	anisotropic symmetric exchange
bcc	body centred cubic
BL	bilayer
BO	Born-Oppenheimer
BZ	Brillouin zone
CCW	counterclockwise
CW	clockwise
DFT	density functional theory
DL	double layer
DMI	Dzyaloshinskii-Moriya interaction
DML	dead magnetic layer
DW	domain wall
fcc	face centred cubic
Fig.	Figure
FLAPW	full potential linearized augmented planewave
FM	ferromagnetic, ferromagnet, ferromagnetically
GGA	generalized gradient approximation
GNEB	geodesic nudged elastic band
hcp	hexagonal close packed
HOI	higher order exchange interaction
IR	interstitial region
LAFM	layered antiferromagnetic, layered antiferromagnet, layered antiferromagnetically
LAPW	linearized augmented planewave
LDA	local density approximation
LDOS	local density of states
LSDA	local spin density approximation

MAE	magnetocrystalline anisotropy energy
MEP	minimum energy path
ML	monolayer
MR	magnetoresistance
MT	muffin tin
NCMR	non-collinear magnetoresistance
Pub.	Publication
Ref.	Reference
RKKY	Ruderman-Kittel-Kasuya-Yoshida
RW-AFM	row-wise antiferromagnetic, row-wise antiferromagnet, row-wise antiferromagnetically
SOC	spin-orbit coupling
SP	saddle point
SP-STM	spin-polarized scanning tunnelling microscopy, spin-polarized scanning tunnelling microscope
STM	scanning tunnelling microscopy, scanning tunnelling microscope
Tab.	Table
TAMR	tunnelling anisotropic magnetoresistance
TL	trilayer
TMR	tunnelling magnetoresistance
TM	transition metal
TOM	topological orbital moment
UML	unsupported monolayer
xc	exchange correlation

Chapter 1

Introduction

Non-collinear spin structures such as chiral domain walls (DWs), skyrmions or antiskyrmions hold great promise for future spintronic applications, e.g. in racetrack memory devices, for neuromorphic computing or for magnetic random access memory devices [1–9]. Chiral DWs attracted a lot attention due to their fast current induced motion mediated by spin-orbit torques and spin Hall effect [10–17] and appear to be suited in the field of spintronics – employed in magnetic memory and logic devices [1, 13, 18–22].

Promising properties for spintronic applications are also predicted for magnetic skyrmions – particle like, topologically protected whirling objects. They require less space and can be moved at lower electric current densities than DWs which would lead to denser and faster storage devices [3, 4, 23]. Since their theoretical prediction around 30 years ago [24, 25], skyrmions moved into the focus again after their first experimental observations in different classes of materials [26–31]. To be potentially useful in spintronic devices, the requirements on skyrmions are challenging [2, 3, 7, 8, 32, 33]. In order to compete with state-of-the-art applications it is envisioned that skyrmions should be smaller than 10 nm and stable at room temperature without applying an external magnetic field. Furthermore, an all-electrical readout is favourable [34].

In recent years, this triggered a quest for finding the right material composition which could host skyrmions with the demanded properties. Some of the above mentioned objectives could be achieved in magnetic multilayer systems [35–37], nanostructures [38, 39] or synthetic antiferromagnets [40] where examples are presented in Fig. 1.1.

Despite the large effort, all of these structures do not appear in the desired size or need a magnetic field to be stabilized in remanence. These occurring restrictions can be narrowed down to one key issue: The targeted control of magnetic interactions. While sputtered multilayer systems can be seen as potentially suitable for applications, such imperfectly prepared films are hard to model from first-principles. In particular, intermixing, structural imperfections and the number of involved elements can be seen as major challenges for state-of-the art first-principles methods.

Therefore, the search for the right material composition is still ongoing and is one motivation for the theoretical study in this thesis. Compared to the experimental and applicable approach to find the right material, we aim for a deeper understanding of complex spin structures and their underlying interaction mechanisms.

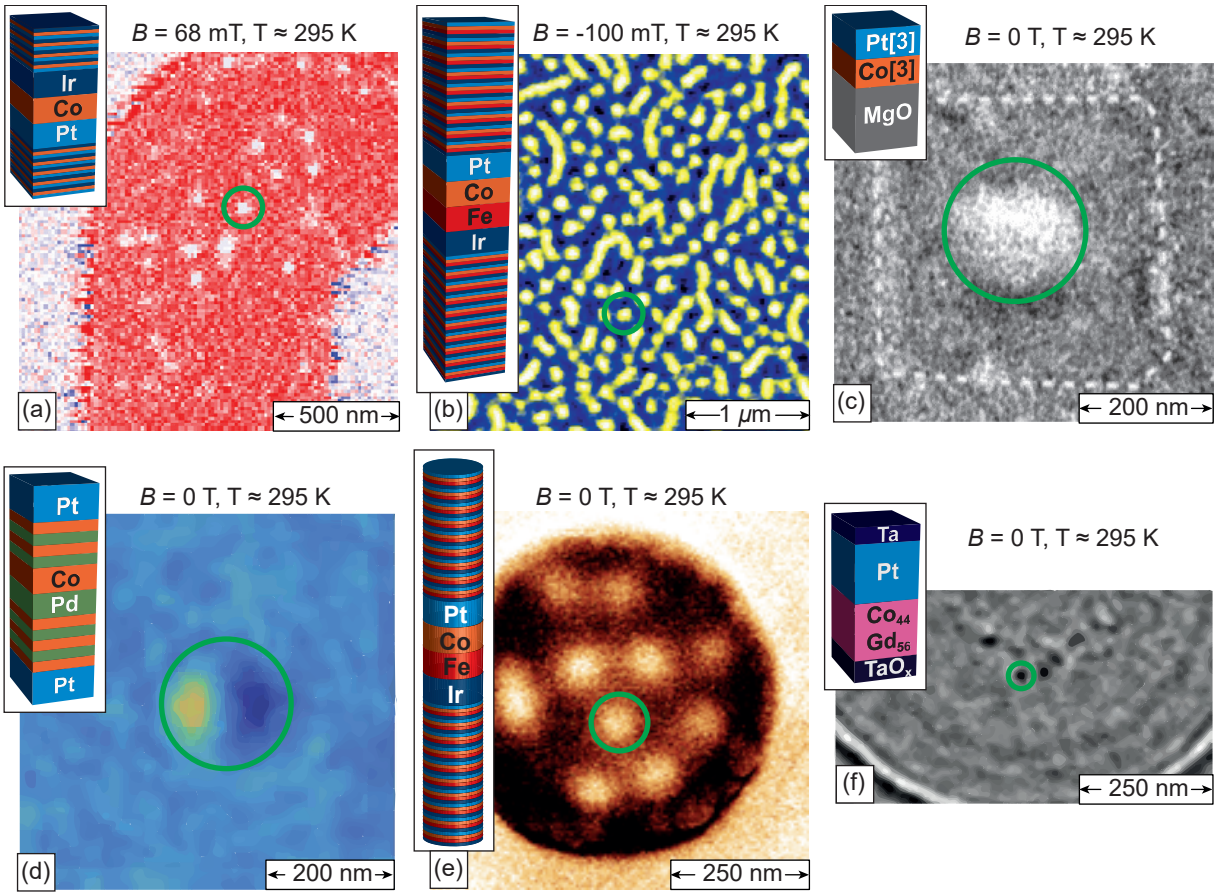

Figure 1.1 | Experimentally observed room temperature stable skyrmions in magnetic structures. (a) Out-of-plane magnetization m_z map measured with scanning transmission X-ray microscopy of a $[Ir/Co/Pt]_{10}$ multilayer stack at room temperature and with an external magnetic field of $B = 68\,mT$. Adapted from [35]. (b) Magnetic force microscopy image of a $[Pt/Co/Fe/Ir]_{20}$ multilayer stack at room temperature with an external magnetic field of $B = -100\,mT$. Adapted from [36]. (c) Photoemission electron microscopy and X-ray magnetic circular dichroism image of an ultrathin Pt[3]/Co[3]/MgO sample at room temperature and no magnetic field. Three monolayers are grown for Pt and Co, respectively. Adapted from [38]. (d) Lorentz transmission electron microscopy image of Co/Pd multilayer stack at room temperature and no magnetic field. Adapted from [37]. (e) Magnetic force microscopy image of a $[Pt/Co/Fe/Ir]_{20}$ multilayer sub-μm dots at room temperature and no magnetic field. Adapted from [39]. (f) X-ray holography image of $Pt/Co_{44}Gd_{56}/TaO_x$ at room temperature and no magnetic field. Adapted from [40]. All reprints are made with permission. Note that in the absence of magnetic field, the images are taken in the remanent state. The images in the insets represent the magnetic systems whereas in (a,b,d,e), the layers in the middle are presented larger for clarification of the material. The green circles in each panel exemplary encircle the magnetic skyrmions. Note the different scale bar for each image.

As a result, we try to provide a strategy to find material compositions that could exhibit topological spin structures with the desired properties. To do so, we study the magnetism in ultrathin magnetic films. Ultrathin films are best suited comparing theory with experimental spin-polarized scanning tunnelling microscopy (SP-STM) measurements due to their film quality and the resulting well defined interfaces. The agreement between theory and experiment can give the required insight to understand the physics behind complex magnetic structures.

In the course of that, the interfacial Dzyaloshinskii-Moriya interaction (DMI) has been discovered in $3d/5d$ interfaces based on the comparison between experiment and theory in a Mn monolayer (ML) on W(110) [42]. The complex antiferromagnetic (AFM) helical spin spiral ground state [Fig. 1.2 (a)] has been successively explained by the interplay of AFM nearest neighbour exchange and DMI. On the W(001) surface, a Mn ML exhibits a ferromagnetic (FM) spin spiral state which also has been explained based on the interplay of exchange and DMI [Ref. 43 and Fig. 1.2 (b)].

The discovery of the nano-skyrmion lattice in Fe/Ir(111) [29] has further opened a new class for magnetic skyrmions: transition metal (TM) interfaces. Additionally, the observations of a conical AFM cycloidal spin spiral in Mn/Mn/W(110) and canted and straight up-up-down-down states in Rh_{hcp}/Fe/Ir(111) [44] and Fe/Rh(111) [45], respectively have confirmed the existence of higher order exchange interactions (HOIs) in ultrathin magnetic films [Figs. 1.2 (c-f)]. These examples have demonstrated, how deep knowledge about complex magnetic structures can be gained comparing experiments and theory in ultrathin films.

Triggered by the phenomena presented above, this thesis presents a density functional theory (DFT) study on complex collinear and non-collinear magnetic structures in ultrathin films driven by strong frustration of magnetic interactions such as exchange, DMI and higher order spin interactions. We focus on two magnetic materials, the prototypical FM Co and the prototypical AFM Mn. As shown above, Co is widely used in applicable magnetic systems which could stabilize room temperature skyrmions (cf. Fig. 1.1) whereas Mn holds various different magnetic and structural properties depending on the prevalent conditions. Calculating the total energies of non-collinear spin structures including spin-orbit coupling (SOC) within the full potential linearized augmented planewave (FLAPW) method, the results are mapped onto an atomistic spin model. Subsequent spindynamics simulations and geodesic nudged elastic band calculations are performed to analyse the magnetic properties of non-collinear spin structures such as DWs, skyrmions and antiskyrmions. The calculations throughout this PhD thesis are compared to SP-STM measurements from experimental collaborators similarly as it has been introduced above (cf. Fig. 1.2). Consequently, we demonstrate how the synergy of experiment and theory is used to understand complex magnetic structures and provides a strategy to design materials compositions which can exhibit such spin structures.

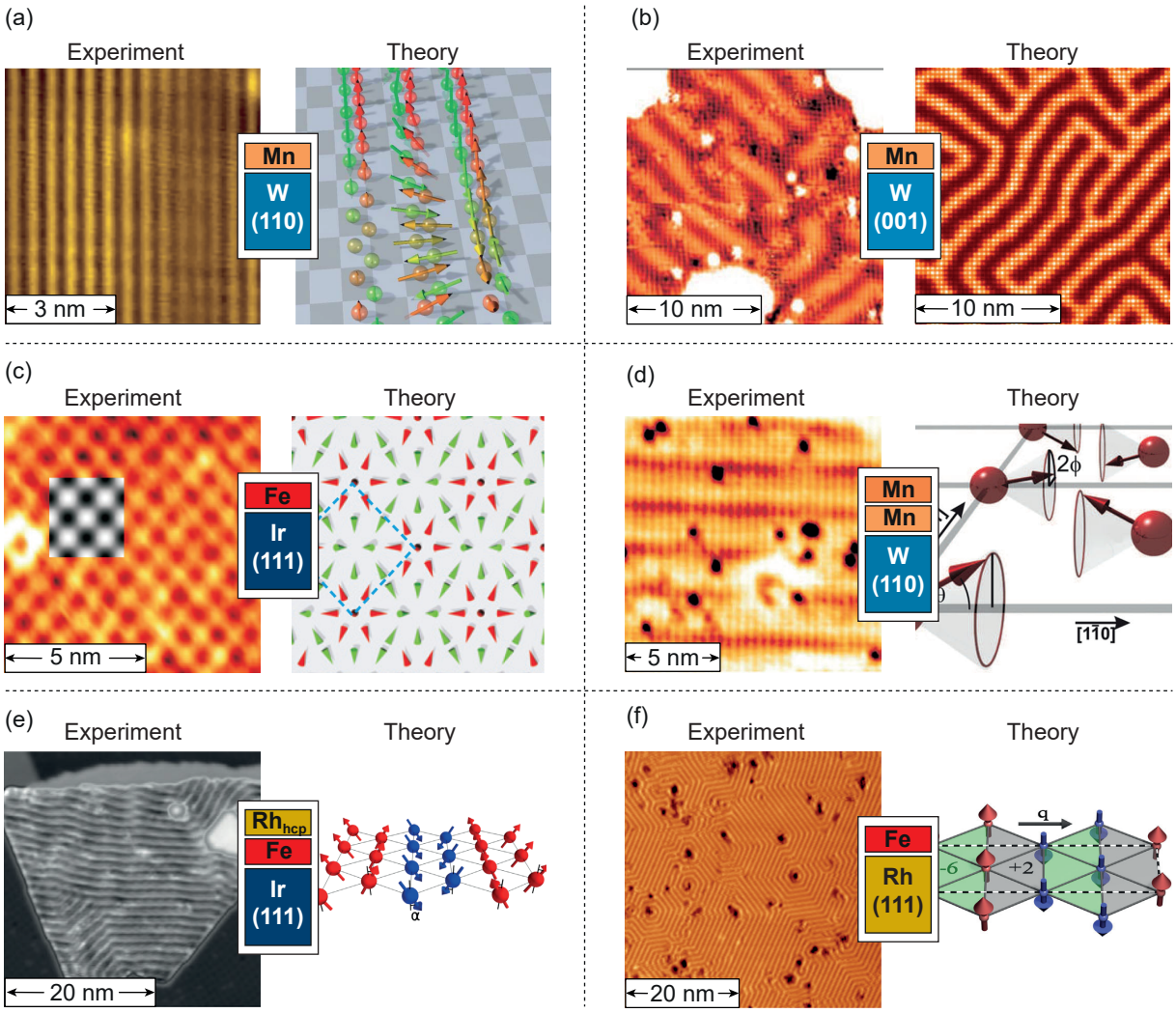

Figure 1.2 | Comparison between experimentally observed complex magnetic structures with their theoretical explanations in different ultrathin film systems. (a) Experimental spin-polarized scanning tunnelling microscopy (SP-STM) image on Mn/W(110) (left) and theoretically obtained cycloidal antiferromagnetic (AFM) spin spiral induced by Dzyaloshinskii-Moriya interaction (DMI) (right). Adapted from [42]. (b) Experimental SP-STM image of Mn/W(001) (left) and STM simulation of the theoretically obtained spin spiral state induced by DMI (right). Adapted from [43]. (c) Experimental SP-STM image on Fe/Ir(111) (left) and theoretically obtained nano-skyrmion lattice (scanning tunnelling microscopy (STM) simulation as inset) induced by higher order exchange interactions (HOIs) and DMI. Adapted from [29]. (d) Experimental SP-STM image on Mn/Mn/W(110) (left) and theoretically obtained AFM conical spin spiral state found induced by HOIs and DMI (right). Adapted from [46]. (e) Experimental SP-STM image on Rh_{hcp}/Fe/Ir(111) (left) and theoretically obtained canted up-up-down-down state induced by HOIs and DMI (right). Adapted from [44]. (f) Experimental SP-STM image on Fe/Rh(111) (left) and theoretically obtained up-up-down-down state induced by HOIs (right). Adapted from [45]. All reprints are made with permission. Note the different scale bars for each image which are up to three orders of magnitude smaller than in Fig. 1.1.

In the first part of the thesis, the theoretical model is introduced. The DFT calculations are carried out with the FLEUR code [47] in which the FLAPW method is implemented. Therefore, Ch. 2 provides the theoretical background for DFT whereas Ch. 3 is dedicated to the FLAPW method for solving the Kohn-Sham equations. To interpret the calculations, we apply different spin models, which are reviewed in Ch. 4.

The starting point of the Co study is the prominent Pt/Co/Ir interface (cf. Fig. 1.1) for which additive DMI effects are predicted [35, 36]. We therefore study the DMI in Co/Ir(111) and Pt/Co/Ir(111) ultrathin films and show that a DMI enhancement from Co/Ir(111) to Pt/Co/Ir(111) is not dedicated to additive effects from both Pt/Co and Co/Ir interfaces (Ch. 5). In fact, the DMI is strongly dependent on the stacking of the Pt/Co bilayer (BL) and for certain stackings, even a reduction of DMI is observed. Increasing the Co thickness to Pt/Co/Co/Ir(111), we can address an enhancement of DMI to additive effects, but our study demonstrates how sensitive the DMI reacts on stackings and interface composition. Our findings are supported by SP-STM measurements on chiral, Néel type DWs performed in the group of Prof. Wiesendanger (University of Hamburg) in these films which are in good agreement with our DFT results (Pub. I).

The DMI at these TM interfaces can be even more complex. In Ch. 6, we therefore explain the occurrence of DMI frustration – an effect which has been neglected in the field. A detailed analysis of the film Co_{hcp}/Ir(111) gives rise to the conclusion that the hybridization between Co and the Ir(111) surface layer is crucial and leads to a sign change of the DMI, i.e. a dependence of the preferred rotational sense on the spin spiral period. When frustrated DMI occurs, the determination of this interaction can lead to wrong results when unsuitable non-collinear supercell calculations are taken into account as commonly found in the literature.

We further systematically study how one can tune the magnetic interactions in Co/Ir(111) (Ch. 7). Adding different 4*d* top layers from Tc, Ru over Rh to Pd allow to vary the effective nearest neighbour exchange in the film from weakly to strongly FM. With replacing the Ir(111) substrate by the 4*d* isoelectronic Rh(111) substrate gives rise to similar exchange interaction, but the SOC dependent terms – DMI and magnetocrystalline anisotropy energy (MAE) are reduced significantly. The study provides a strategy for controlling the magnetic interactions in Co films and proposes certain material compositions which have desirable properties to host non-collinear spin structures.

In that view, Rh/Co/Ir(111) shows the most promising properties which we analyse in Ch. 8. The interplay of large exchange frustration with large out-of-plane MAE and moderate DMI gives rise to a stabilization of atomically sized DWs and skyrmions for a wide range of an applied magnetic field – even at $B_z = 0\,\mathrm{T}$. The magnetic properties of the film enlarge the energy barrier preventing the skyrmions from vanishing into the FM ground state. STM and SP-STM measurements at the University of Hamburg

could confirm the occurrence of such skyrmions in the virgin state without applying a magnetic field (Pub. II). Furthermore, measurements can resolve the structures with non-magnetic tips. The underlying effect, the non-collinear magnetoresistance is about 20 % at the Fermi energy and allows for all-electrical readout of skyrmions and DWs. Based on our DFT calculations in combination with a simplified tight-binding model, we can show that the effect stems from spin mixing between a majority d_{xz} and a minority p_z state in the Rh/Co BL (Pub. III).

From the FM element Co, we pass over to the AFM material Mn. Since three ultrathin films of Mn/W(001) [43], Mn/W(110) [42, 48] and Mn/Mn/W(110) [46] (cf. Fig. 1.2 (b,a,d), respectively) show complex magnetic structures, we study the complementary film of Mn/Mn/W(001) (Ch. 9). Previous DFT calculations have predicted a FM ground state; however, STM experiments from the University Würzburg reveal a collinear $c(2 \times 2)$ AFM state of the Mn surface layer. In agreement with our DFT calculations, this coincides when the Mn interface layer, Mn(I) appears to be magnetically dead. We show that the magnetic moment in Mn(I) is quenched due to strong hybridization with the W(001) surface as well as the frustration stemming from the symmetrically checkerboard AFM state at the surface. The unique orbital composition of both Mn surface and interface atoms allow for imaging the subsurface atoms with STM (Pub. IV).

About 20 years ago, a Mn ML on Cu(111) was predicted to exhibit a three-dimensional 3Q state based on DFT. The 3Q state is a superposition of three row-wise antiferromagnetic (RW-AFM) (single-Q) states [49] and shows a tetrahedron angle of $\sim 109°$ between neighbouring spins. Both 3Q and row-wise antiferromagnet (RW-AFM) have been studied theoretically in the past [49, 50], but could never be observed experimentally. In recent experiments, SP-STM measurements performed in the group of Prof. Wiesendanger (University of Hamburg) could resolve the RW-AFM and the 3Q state in fcc and hcp stacking of a Mn ML on Re(0001). Our DFT calculations show that in contradiction to Mn/Cu(111), where the hybridization with the substrate has a minor impact on the electronic structure and the magnetic ground state of the Mn top layer, the hybridization between Mn and the Re(0001) substrate is crucial. It results in very small energy differences and frustration of magnetic interactions, not only of exchange, but also of HOIs. Consequently, the occurring SOC effects are decisive for Mn/Re(0001) forming the magnetic ground state. This is shown in Ch. 10. An observed coupling of the RW-AFM to the lattice in Mn_{fcc}/Re(0001) is explained by including the dipolar and pseudo-dipolar interaction.

Based on experiments, the 3Q state has been concluded to be the ground state in Mn_{hcp}/Re(0001) (cf. Ref. 51 and Pub. V). Our DFT calculations suggest a distorted 3Q state might be even more favourable and can explain the unexpected coupling to the atomic lattice. The perfect tetrahedron angles are canted by about $\sim 20°$ towards the RW-AFM state. So far, previous interactions fail to explain such a ground state and

shows the importance to further study this complex magnetic system. As the HOIs appear as strongly frustrated, higher order terms that are negligible in other film systems may be important to exhibit a canted 3Q state.

The results presented throughout this PhD thesis demonstrate how deep understanding on complex magnetic structures can be gained based on the synergy of DFT calculations and experiments. This is summarized in Ch. 11 where we provide a conclusive overview on the complete work.

Part I

Theoretical Description

Chapter 2

Density Functional Theory

When studying quantum mechanical systems, the many-body Schrödinger equation (2.1) needs to be solved. It is written as

$$\left[\sum_{i}^{N}\left(\frac{-\hbar^2}{2m}\nabla_i^2 + V(\mathbf{r}_i)\right) + \sum_{i<j} U(\mathbf{r}_i,\mathbf{r}_j)\right]\psi(\mathbf{r}_1,\ldots,\mathbf{r}_N) = E\psi(\mathbf{r}_1,\ldots,\mathbf{r}_N) \tag{2.1}$$

While i denotes all particles, V represents a potential and U is the interaction between all particles. However, describing solids, equation (2.1) cannot be solved, neither analytically, nor numerically due to the amount of particles. This is the reason why the investigation of complex many-particle systems like solids relies on approximations.

The velocity of electrons is much faster than the velocity of the nuclei because of their large differences in mass

$$m_I >> m_i \tag{2.2}$$

Here, m_I is the mass of the nuclei and m_i the mass of the electrons. Therefore, the electronic motion can be decoupled from the nuclei motion. The electrons will obtain their equilibrium much faster than the nuclei which is used in the so-called Born-Oppenheimer (BO) approximation [52]. The nuclei will be fixed and Eq. (2.1) will take the form of an electronic Schrödinger equation in dependence of the electronic positions $\mathbf{r}$

$$\left[\sum_{i}^{n}\frac{-\hbar^2}{2m}\nabla_i^2 - \sum_{i}^{n}\sum_{I}^{M}\frac{Z_I e^2}{|\mathbf{r}_i-\mathbf{R}_I|} + \frac{1}{2}\sum_{i\neq j}\frac{e^2}{|\mathbf{r}_i-\mathbf{r}_j|}\right]\psi(\mathbf{r}_1,\ldots,\mathbf{r}_n) = E\psi(\mathbf{r}_1,\ldots,\mathbf{r}_n) \tag{2.3}$$

The first term describes the kinetic energy of the electrons, the second term represents the interaction between the nuclei and the electrons while the third one takes into account the interaction between the electrons. Despite this simplification, the antisymmetry and multi-dimensionality of the N electron wave function $\psi(\mathbf{r}_1,\ldots,\mathbf{r}_n)$ will increase the computational effort exponentially with the number of electrons when solving Eq. (2.3).

The density functional theory (DFT) will use a different approach calculating the ground state properties of many-particle systems like solids. Instead of the wave function, we solve the Schrödinger equation by using the electron density. This approach, which is known as density functional theory, will briefly discussed in the following sections.

In Sec. 2.1 the electron density will be introduced. Sec. 2.2 will set the basis for DFT by the theorems of Hohenberg and Kohn who showed that the electron density is a sufficient quantity to describe the ground state properties of many-particle systems. Sec. 2.3 introduces the Kohn-Sham equations which have the form of a single particle Schrödinger equation in order to replace the many-particle equation. Sec. 2.4 sets the frame for spin-polarized systems and expands the theorems of Hohenberg and Kohn as well as the Kohn-Sham equations. Relativistic effects and spin-orbit coupling (SOC) are introduced in Secs. 2.5 and 2.6. Formally, DFT is correct, but in practice, approximations have to be used for correlational and exchange effects. Therefore, Sec. 2.7 shows how to deal with the exchange correlation (*xc*) potential. Sec. 2.8 presents the self-consistency cycle, which is used to solve the Kohn-Sham equations in practice. In the self-consistency cycle, the total energy can be calculated which will be discussed in Sec. 2.9. In the concluding Sec. 2.10, the force theorem is introduced in order to calculate small perturbations of states.

For further and more detailed information about DFT, references [53–59] are recommended.

2.1 The electron density $n(\mathbf{r})$

The keynote of the BO approximation (2.3) is the importance of electrons describing many-particle systems. The electronic wave function $\psi(\mathbf{r}_1, \mathbf{r}_2, \ldots, \mathbf{r}_N)$ contains every information about the electronic systems. Here, N denotes the total number of electrons. The electron density on the other hand is defined as

$$n(\mathbf{r}) = N \int \ldots \int |\psi(\mathbf{r}_1, \mathbf{r}_2, \ldots, \mathbf{r}_N)|^2 \mathrm{d}\mathbf{r}_2 \ldots \mathbf{r}_N \tag{2.4}$$

It represents a single particle quantity. For the description of ground state properties of solids it is not necessary to keep every information which is stored in the wave function. Measurable quantities of a physical system can further be derived by the expectation values of the quantum-mechanical operators.

The central objective of DFT is the reduction of the complexity in the system from the electronic wave function down to the electron density. The electron density contains several information of the investigated system, i.e. the total number of electrons

$$N = \int n(\mathbf{r}) \mathrm{d}\mathbf{r} \tag{2.5}$$

or information about the nuclear number

$$\left.\frac{\partial \langle n(\mathbf{r}) \rangle}{\partial r}\right|_{r=r_j} = -2Z_I \langle n(\mathbf{r}_I) \rangle \tag{2.6}$$

2.2 Theorems of Hohenberg and Kohn

As stated previously, the electron density still contains enough information to describe the ground state properties of many particle systems. Hohenberg and Kohn proofed

that the non-degenerate ground state wave function is an explicit functional of the ground state electron density [60]. This is known as **1. Theorem of Hohenberg and Kohn**

$$\psi_0(\mathbf{r}_1,\ldots,\mathbf{r}_N) = \psi[n_0(\mathbf{r})] \tag{2.7}$$

Therefore, given an external potential V_{ext}, all ground state properties can be calculated from this electron density.

In the **2. Theorem of Hohenberg and Kohn**, the true ground state electron density $n_0(\mathbf{r})$ minimizes the energy functional $E[n(\mathbf{r})]$

$$E[n(\mathbf{r})] \geq E[n_0(\mathbf{r})] = E_0 \tag{2.8}$$

In order to obtain the ground state electron density, the energy functional is minimized via variational principle with the restriction of a constant number of electrons:

$$\frac{\delta}{\delta n(\mathbf{r})}\left\{E[n(\mathbf{r})] - \mu\int n(\mathbf{r})\mathrm{d}\mathbf{r}\right\} = 0 \tag{2.9}$$

Here, μ is the chemical potential being a Lagrange parameter. The energy functional $E[n(\mathbf{r})]$ can be separated into three different terms consisting of the kinetic energy T, the Coulomb interaction U and an external potential V_{ext}, so that

$$E[n(\mathbf{r})] = T[n(\mathbf{r})] + U[n(\mathbf{r})] + V_{\text{ext}}[n(\mathbf{r})] \tag{2.10}$$

Considering the case when all terms of Eq. (2.10) are known, the minimization with respect to $n(\mathbf{r})$ [Eq. (2.9)], can be done leading to the ground state energy E_0, Eq. (2.8) and therefore all observables of the ground state can be determined.

However, in practice this is not possible because the functionals $T[n(\mathbf{r})]$ and $V_{\text{ext}}[n(\mathbf{r})]$ contain correlation effects which cannot be calculated analytically. As a consequence, $E[n(\mathbf{r})]$ is unknown which is why a different approach for its solution is required.

2.3 Kohn-Sham equations

Taking $E[n(\mathbf{r})]$ of Eq. (2.10), Kohn and Sham suggested to split it into four sub-functionals [61]

$$E[n(\mathbf{r})] = T_{\text{S}}[n(\mathbf{r})] + E_{\text{H}}[n(\mathbf{r})] + E_{\text{ext}}[n(\mathbf{r})] + E_{xc}[n(\mathbf{r})] \tag{2.11}$$

Here, $T_{\text{S}}[n(\mathbf{r})]$ denotes the kinetic energy of non-interacting electrons, $E_{\text{H}}[n(\mathbf{r})]$ the Hartree energy, $E_{\text{ext}}[n(\mathbf{r})]$ an external energy and $E_{xc}[n(\mathbf{r})]$ the so-called exchange correlation energy.

The electron density itself can be expressed as a sum over occupied orbitals of single-particle wave functions. This is done i.e. for non-interacting electrons

$$n(\mathbf{r}) = 2 \sum_{i \in \mathrm{occ}} |\psi_i(\mathbf{r})|^2 \tag{2.12}$$

The factor 2 arises due to degeneracy of spins. The four terms of Eq. (2.11) can be rewritten as:

$$T_\mathrm{S}[n(\mathbf{r})] = -2 \sum_i^n \int \psi_i^*(\mathbf{r}) \frac{\hbar^2}{2m} \nabla^2 \psi_i(\mathbf{r}) \, \mathrm{d}\mathbf{r} \tag{2.13a}$$

$$E_\mathrm{H}[n(\mathbf{r})] = \frac{1}{2} \iint \frac{n(\mathbf{r}) n(\mathbf{r}')}{|\mathbf{r} - \mathbf{r}'|} \, \mathrm{d}\mathbf{r}\mathrm{d}\mathbf{r}' \tag{2.13b}$$

$$E_\mathrm{ext}[n(\mathbf{r})] = \int V_\mathrm{ext}(\mathbf{r}) n(\mathbf{r}) \, \mathrm{d}\mathbf{r} \tag{2.13c}$$

$$E_{xc}[n(\mathbf{r})] = \text{unknown} \tag{2.13d}$$

The first three terms, Eqs. (2.13a) - (2.13c), can be derived explicitly whereas the term $E_{xc}[n(\mathbf{r})]$ is unknown. The latter contains all kinds of correlations, one part from the kinetic term Eq. (2.13a) and another part from the electron-electron interaction. Furthermore, the quantum-mechanical exchange is contained in E_{xc}.

Minimizing the energy functional (2.11) with respect to the wave functions ψ_i, ψ_i^* and regarding the condition of a normalized wave function leads to

$$\int |\psi_i(\mathbf{r})|^2 \, \mathrm{d}\mathbf{r} = 1. \tag{2.14}$$

This condition is satisfied with the Lagrange parameter ϵ_i where due to variation of Eq. (2.11), the so called Kohn-Sham equations can be derived

$$\left\{ -\frac{\hbar^2}{2m} \nabla^2 + V_\mathrm{eff}(\mathbf{r}) \right\} \psi_i(\mathbf{r}) = \epsilon_i \psi_i(\mathbf{r}) \tag{2.15}$$

The effective potential V_eff is then defined as

$$V_\mathrm{eff}(\mathbf{r}) = V_\mathrm{ext}(\mathbf{r}) + V_\mathrm{H}(\mathbf{r}) + V_{xc}(\mathbf{r}) \tag{2.15a}$$

It includes the external potential V_ext, the Hartree potential

$$V_\mathrm{H}(\mathbf{r}) = \int \frac{n(\mathbf{r}')}{|\mathbf{r} - \mathbf{r}'|} \, \mathrm{d}\mathbf{r} \tag{2.15b}$$

and the *xc* potential

$$V_{xc}(\mathbf{r}) = \frac{\delta E_{xc}|n(\mathbf{r})|}{\delta n(\mathbf{r})} \tag{2.15c}$$

The *xc* energy E_{xc} is a priori unknown [Eq. (2.13d)] and therefore, the *xc* potential V_{xc} relies on approximations. This is the reason why formally, DFT is exact, but in practice due to V_{xc}, assumptions have to be considered.

The Kohn-Sham equations (2.15) represent single-particle Schrödinger equations. The main advantage of DFT consequently is the reduction of a complex many-body system [Eq. (2.1)] to effective single-particle Schrödinger equations [Eq. (2.15)]. However, since both Hartree potential and *xc* potential are dependent on the electron density itself, the solution of the Kohn-Sham equations is not straightforward. Therefore, self-consistent procedures are required which are discussed later on.

2.4 Spin-Polarization in Density Functional Theory

In this thesis, we investigate complex magnetic structures, whereas the previous description of DFT holds true for non-magnetic systems. However, starting from spin dependent electron densities $n^{\uparrow}(\mathbf{r})$, $n^{\downarrow}(\mathbf{r})$, we can rewrite the electron density as

$$n(\mathbf{r}) = n^{\uparrow}(\mathbf{r}) + n^{\downarrow}(\mathbf{r}) \tag{2.16a}$$

We can further define the magnetization density as

$$\mathbf{m}(\mathbf{r}) = n^{\uparrow}(\mathbf{r}) - n^{\downarrow}(\mathbf{r}) \tag{2.16b}$$

The two theorems after Hohenberg and Kohn, Eqs. (2.7) and (2.8) can be extended for the spin-polarized case [62, 63] so that

$$E[n(\mathbf{r})] \quad \rightarrow \quad E[n(\mathbf{r}), \mathbf{m}(\mathbf{r})] \geq E[n_0(\mathbf{r}), \mathbf{m}_0(\mathbf{r})] \tag{2.17}$$

Now, the Kohn-Sham orbitals ψ_i [Eq. (2.15)] have to be represented as Pauli spinors

$$\psi_i(\mathbf{r}) = \begin{pmatrix} \psi_i^{\uparrow}(\mathbf{r}) \\ \psi_i^{\downarrow}(\mathbf{r}) \end{pmatrix} \tag{2.18}$$

Consequently for both electron and magnetization density are written as

$$n(\mathbf{r}) = \sum_i^N |\psi_i(\mathbf{r})|^2 \tag{2.19a}$$

$$\mathbf{m}(\mathbf{r}) = \sum_i^N \psi_i^*(\mathbf{r}) \sigma \psi_i(\mathbf{r}) \tag{2.19b}$$

with σ being the Pauli spin matrices.

Merging Eqs. (2.19a), (2.19b) with Eq. (2.15), the Kohn-Sham equations look like a Pauli-Schrödigner equation

$$\left\{-\frac{\hbar^2}{2m}\nabla^2 + V_{\text{eff}}(\mathbf{r}) + \sigma \cdot \mathbf{B}_{\text{eff}}(\mathbf{r})\right\}\psi_i(\mathbf{r}) = \epsilon_i \psi_i(\mathbf{r}) \tag{2.20}$$

It contains V_{eff} from Eq. (2.15a) and an effective magnetic field $\mathbf{B}_{\text{eff}}$

$$\mathbf{B}_{\text{eff}}(\mathbf{r}) = \mathbf{B}_{\text{ext}}(\mathbf{r}) + \mathbf{B}_{xc}(\mathbf{r}) \tag{2.20a}$$

Here, $\mathbf{B}_{\text{ext}}$ denotes an external magnetic field and $\mathbf{B}_{xc}$ the xc field

$$\mathbf{B}_{xc}(\mathbf{r}) = \frac{\delta E_{xc}[n(\mathbf{r}), \mathbf{m}(\mathbf{r})]}{\delta \mathbf{m}(\mathbf{r})} \tag{2.20b}$$

Describing non-collinear magnetism within DFT, it is necessary to use another description for the electron density and magnetization density. The density matrix is defined as

$$\underline{n}(\mathbf{r}) = \frac{1}{2}n(\mathbf{r})\mathbb{1}_2 + \underline{\sigma} \cdot \mathbf{m}(\mathbf{r}) = \frac{1}{2}\begin{pmatrix} n(\mathbf{r}) + m_z(\mathbf{r}) & m_x(\mathbf{r}) - i m_y(\mathbf{r}) \\ m_x(\mathbf{r}) + i m_y(\mathbf{r}) & n(\mathbf{r}) - m_z(\mathbf{r}) \end{pmatrix} \tag{2.21}$$

It allows for calculations of non-collinear magnetic structures because in the off-diagonal, the elements contain the magnetization direction of x, y. When these vanish, the collinear magnetic case reappears. Here, $\mathbb{1}_2$ is a 2×2 identity matrix. Corresponding to the density matrix, it is possible to define a potential matrix, consisting of the scalar potential $V(\mathbf{r})$ and the magnetic field $\mathbf{B}(\mathbf{r})$:

$$\underline{V}(\mathbf{r}) = V(\mathbf{r})\mathbb{1}_2 + \mu_{\text{B}}\underline{\sigma} \cdot \mathbf{B}(\mathbf{r}) \tag{2.22}$$

Taking these descriptions into account, we can write the Kohn-Sham equations for spin-polarization as

$$\left[\left(-\frac{\hbar^2}{2m}\nabla^2 + \sum_\alpha \int \frac{n_{\alpha\alpha}(\mathbf{r})}{|\mathbf{r} - \mathbf{r}'|}\,\mathrm{d}\mathbf{r}'\right)\mathbb{1}_2 + \underline{V}(\mathbf{r}) + \frac{\delta E_{xc}}{\delta \underline{n}(\mathbf{r})}\right]\begin{pmatrix} \psi_i^{\uparrow}(\mathbf{r}) \\ \psi_i^{\downarrow}(\mathbf{r}) \end{pmatrix} = \epsilon_i \begin{pmatrix} \psi_i^{\uparrow}(\mathbf{r}) \\ \psi_i^{\downarrow}(\mathbf{r}) \end{pmatrix} \tag{2.23}$$

In case of collinear magnetism, the Hamiltonian of this equation can be diagonalized and two decoupled equations can be solved for each spin direction. Such a decoupling is impossible for non-collinear magnetic structures which is why the computational effort increases compared to the collinear case.

2.5 Relativistic Density Functional Theory

When describing magnetic structures within DFT, the spin-polarization of the Hamiltonian, Eq. (2.20) is not the only extension which has to be included. The kinetic energy in the vicinity of the nuclei becomes large. Therefore, relativistic effects have to be included in the description, especially around the core region [64].

Including these effects, The Kohn-Sham equations (2.15) appear as one-particle Dirac equations

$$\left[c\underline{\alpha}\cdot\hat{\mathbf{p}}+\left(\underline{\beta}-\mathbb{1}\right)mc^2+V_{\text{eff}}(\mathbf{r})\right]\psi_i=\epsilon_i\psi_i \tag{2.24}$$

where $\underline{\alpha},\underline{\beta}$ represent Dirac matrices

$$\underline{\alpha}=\begin{pmatrix}0 & \underline{\sigma}\\ \underline{\sigma} & 0\end{pmatrix} \tag{2.24a}$$

and

$$\underline{\beta}=\begin{pmatrix}\mathbb{1}_2 & 0\\ 0 & -\mathbb{1}_2\end{pmatrix} \tag{2.24b}$$

Furthermore, $\underline{\sigma}$ is the vector of the Pauli spin matrices, $\sigma_x,\sigma_y,\sigma_z$, $\hat{\mathbf{p}}$ denotes the momentum operator and ψ the relativistic, four-component Dirac spinor and can be expressed via

$$\psi_i=\begin{pmatrix}\varphi_i(\mathbf{r})\\ \chi_i(\mathbf{r})\end{pmatrix} \tag{2.24c}$$

Here, the spinor is represented by the large and small components $\varphi_i(\mathbf{r})$, $\chi_i(\mathbf{r})$, where the index i includes Bloch vector $\mathbf{k}$, the band index and the quantum spin number σ.

The charge and magnetization densities can be expressed now as

$$n(\mathbf{r})=\sum_{i=1}^{N}\left(\varphi_i^\dagger(\mathbf{r})\varphi_i(\mathbf{r})+\chi_i^\dagger(\mathbf{r})\chi_i(\mathbf{r})\right) \tag{2.25a}$$

and

$$\mathbf{m}(\mathbf{r})=\sum_{i=1}^{N}\left(\varphi_i^\dagger(\mathbf{r})\underline{\sigma}\varphi_i(\mathbf{r})+\chi_i^\dagger(\mathbf{r})\underline{\sigma}\chi_i(\mathbf{r})\right) \tag{2.25b}$$

Solving Eq. (2.24) is computationally very demanding. However, expanding this equation with respect to $1/c^2$, the effort decreases and Eq. (2.24) reduces to relativistically corrected Kohn-Sham equations. A sophisticated way to such a correction is called scalar-relativistic approximation [65].

Considering the limit of slow valence electrons, in case of $v^2/c^2 << 1$, the above mentioned expansion in v^2/c^2 of the Dirac equation can be transformed [66] and thus, result in the Kohn-Sham equations with relativistic corrections. The Hamiltonian is called the Pauli operator, which has the form

$$\mathcal{H}_{\text{Pauli}}=\mathcal{H}_{\text{non-rel}}+\mathcal{H}_{\text{rel}}+\mathcal{H}_{\text{SOC}}=\mathcal{H}_{\text{SCA}}+\mathcal{H}_{\text{SOC}} \tag{2.26}$$

The non-relativistic $\mathcal{H}_{\text{non-rel}}$ contribution represent the kinetic and the electrostatic potential energy, respectively

$$\mathcal{H}_{\text{non-rel}}=\frac{\hat{\mathbf{p}}^2}{2m}-e\cdot v \tag{2.26a}$$

The scalar-relativistic approximated Hamiltonian $\mathcal{H}_{\mathrm{SCA}}$ consists of the non-relativistic and the scalar-relativistic Hamiltonian $\mathcal{H}_{\mathrm{rel}}$. The latter is independent of the spin and contains a correction term due to relativistic mass enhancement as well as a smearing of the electrostatic interaction between electrons and nuclei

$$\mathcal{H}_{\mathrm{rel}} = -\frac{\hat{\mathbf{p}}^4}{8m^3c^2} + \frac{e\hbar^2}{8m^2c^2}\nabla\cdot\mathbf{E} \tag{2.26b}$$

The smearing of the second term appears due to rapid quantum oscillations. Therefore, the electrons respond to the electrical field $\mathbf{E}$. It is also called Darwin term. Due to the rapid vibration movements of the electrons which are on the order of the Compton wavelength $\lambda_{\mathrm{C}} = \hbar/mc$, the expectation value of $\mathbf{r}$ does not have a sharp eigenfunction.

The last part $\mathcal{H}_{\mathrm{SOC}}$ of the Hamiltonian in Eq. (2.26) describes the SOC contribution. It couples the spin of electrons to the magnetic field which they experience due to the movement around the nuclei. This orbital movement couples directly to the crystal lattice due to the electric potential of the ions[1]. The form of the Hamiltonian is

$$\mathcal{H}_{\mathrm{SOC}} = \frac{e\hbar^2}{4m^2c^2}\underline{\sigma}\cdot(\mathbf{E}\times\hat{\mathbf{p}}) \tag{2.26c}$$

2.6 Spin-orbit coupling in Density Functional Theory

The Hamiltonian of SOC, Eq. (2.26c), occurs in particular in the vicinity of the nuclei. There, the kinetic energy of the electrons and the gradient of the potential is the largest. As an approximation, we can express the potential as a spherical one, like

$$v(\mathbf{r}) \approx v(|\mathbf{r}|) \tag{2.27}$$

The electric field is defined as

$$\mathbf{E}(\mathbf{r}) = -\nabla v(\mathbf{r}) = -\frac{\mathbf{r}}{r}\frac{\mathrm{d}v}{\mathrm{d}r} \tag{2.28}$$

Replacing Eq. (2.28) in Eq. (2.26c), the Hamiltonian gets the form

$$\begin{aligned}\mathcal{H}_{\mathrm{SOC}} &= -\frac{e\hbar^2}{4m^2c^2r}\frac{\mathrm{d}v}{\mathrm{d}r}\underline{\sigma}\cdot(\mathbf{r}\times\hat{\mathbf{p}}) \\ &= \xi(r)\hat{\mathbf{L}}\cdot\hat{\mathbf{S}}\end{aligned} \tag{2.29}$$

$\hat{\mathbf{L}}$, $\hat{\mathbf{S}}$ are the operator of the angular momentum and the spin operator, respectively. The quantity $\xi(r)$ represents the strength of the SOC and is dependent on the material. It

[1] This is the reason why in case of magnetocrystalline anisotropy energy, the spin prefers a certain direction in the lattice.

contains the first part of the equation

$$\xi(r) = -\frac{e\hbar^2}{4m^2c^2r}\frac{\mathrm{d}v}{\mathrm{d}r} \tag{2.29a}$$

In this thesis, we investigate magnetic structures in transition metals (TMs). The magnetism is mediated by their d electrons, which is why we assume the SOC stemming from the d electrons. Eq. (2.29a) can be approximated by the radial mean value over all d orbitals $\xi(r) = \xi$. Taking into account the potential

$$v(r) = -\frac{Ze}{r} \tag{2.30a}$$

and the non-relativistic radial function

$$R_{\text{non-rel}}(r) \propto r^l \tag{2.30b}$$

where l is the angular momentum quantum number, the SOC constant ξ can be written as

$$\xi_{nl} \propto \langle nl|\frac{1}{r}\frac{Z}{r^2}|nl\rangle\frac{Z^4}{a_\mathrm{B}^3 n^3 l^2} \tag{2.30}$$

where n is the first quantum number and a_B the Bohr radius. From Eq. (2.30) it can be seen, that the strength of the SOC is dependent on the fourth order of the atomic number Z. In Ref. 67 it has been shown that for $3d$ TMs, ξ_{nl} is around $\sim 50\,\mathrm{meV}$.

2.7 Exchange Correlation Functionals

Previously, we introduced how the Kohn-Sham equations can look when spin-polarization or relativistic effects are taken into account. In every case, the effective potential V_eff ($\mathbf{B}_\mathrm{eff}$) occurs which is also dependent on the xc potential V_{xc} ($\mathbf{B}_{xc}$). As mentioned above, the xc potential contains all correlation and exchange effects which take place when many particles interact with each other. However, since an exact description of V_{xc} ($\mathbf{B}_{xc}$) is missing, the xc potential needs to be approximated. A more detailed description of the problem can be found in Refs. 54, 57, 59, 68, 69. The most common approximations are named local density approximation (LDA) and generalized gradient approximation (GGA) and will be briefly described. Both ones are used throughout the thesis.

Local density approximation The first form of the xc energy was proposed by Hohenberg and Kohn [60]. The xc energy density $\varepsilon_{xc}^\mathrm{uni}[n(\mathbf{r})]$ can be linked to the uniform electron gas with the density $n(\mathbf{r})$. To find an analytical expression of the exchange energy density ε_x, the Hartree-Fock approximation can be used so that [70]

$$\varepsilon_x^\mathrm{uni}[n(\mathbf{r})] = -\frac{3}{4}\left(\frac{3n(\mathbf{r})}{\pi}\right)^{1/3} \tag{2.31a}$$

The exchange energy then can be written as

$$E_x^{\mathrm{LDA}}[n(\mathbf{r})] = \int n(\mathbf{r})\varepsilon_x^{\mathrm{uni}}(n(\mathbf{r}))\,\mathrm{d}\mathbf{r} \tag{2.31b}$$

However, a correspondent functional for the correlation energy density ε_c; however, is unknown. Therefore, approximations based on Monte-Carlo simulations are taken into account. As a general trend, the correlation energy appeared to be underestimated, while the exchange energy, Eq. (2.31b) is overestimated. When combining both, a good approximation for the *xc* energy can be found

$$E_{xc}^{\mathrm{LDA}}[n(\mathbf{r})] = \int n(\mathbf{r})\varepsilon_{xc}^{\mathrm{uni}}(n(\mathbf{r}))\,\mathrm{d}\mathbf{r} \tag{2.31}$$

In the case of spin-polarization, the LDA can be extended to the local spin density approximation (LSDA), where now the spin dependent electron density and magnetization density are taken into account

$$E_{xc}^{\mathrm{LSDA}}[n(\mathbf{r}),|\mathbf{m}(\mathbf{r})|] = \int n(\mathbf{r})\varepsilon_{xc}^{\mathrm{uni}}(n(\mathbf{r}),|\mathbf{m}(\mathbf{r})|)\,\mathrm{d}\mathbf{r} \tag{2.32}$$

Note that ε_{xc} is not a functional, but a function, dependent on $n(\mathbf{r})$, $|\mathbf{m}(\mathbf{r})|$. Due to the local approximation in $\varepsilon_{xc}^{\mathrm{uni}}$, the *xc* energy is only dependent on the magnitude of the magnetization and not on its direction. As a consequence, $\mathbf{m}(\mathbf{r})$ and $\mathbf{B}_{xc}(\mathbf{r})$ always show the same direction.

Despite of the simplicity, the approximation works fine in particular describing molecular properties such as equilibrium structures, harmonic frequencies, charge moments or – an important aspect for this thesis – properties of itinerant magnetic structures [71]. On the other hand, structural properties of films, such as the lattice constant of different materials are typically underestimated due to an overestimation of the binding energies [72]. This is the reason why structural relaxations in this thesis are performed within the GGA *xc* potential.

Generalized gradient approximation Due to some limitations of the LDA described above, the GGA was developed. There, the *xc* energy does not depend on the electron density $n(\mathbf{r})$, but also on the gradient of the density, $\nabla n(\mathbf{r})$. Therefore, Eq. (2.31) is modified accordingly

$$E_{xc}^{\mathrm{GGa}}[n(\mathbf{r})] = \int n(\mathbf{r})\varepsilon_{xc}^{\mathrm{uni}}(n(\mathbf{r}))\,F_{xc}(n(\mathbf{r},\nabla n(\mathbf{r})))\,\mathrm{d}\mathbf{r} \tag{2.33}$$

Here, $F_{xc}(n(\mathbf{r},\nabla n(\mathbf{r})))$ is an analytic function, denoted as enhancement function. Perdew, Burke and Ernzerhof provided a form, which is often used in DFT calculations – throughout this thesis it will be referred to as PBE [73]. This *xc* potential could improve the calculated binding energies of the LDA, but did not provide large improvements describing itinerant magnetic systems [71].

The extension of GGA to spin-polarized systems is not straightforward as for the LDA because the gradient of the electron density has to be calculated at each point as well as three spacial coordinates of the magnetization density. A description of GGA applied to spin polarized cases can therefore be found e.g. in Ref. 49.

2.8 Self-Consistency in Density Functional Theory Calculations

As presented in Sec. 2.3, both Hartree and *xc* potential depend on the electron density. In order to solve the Kohn-Sham equations (2.15), an iterative approach is required – it is the self-consistency cycle which is schematically presented in Fig. 2.1.

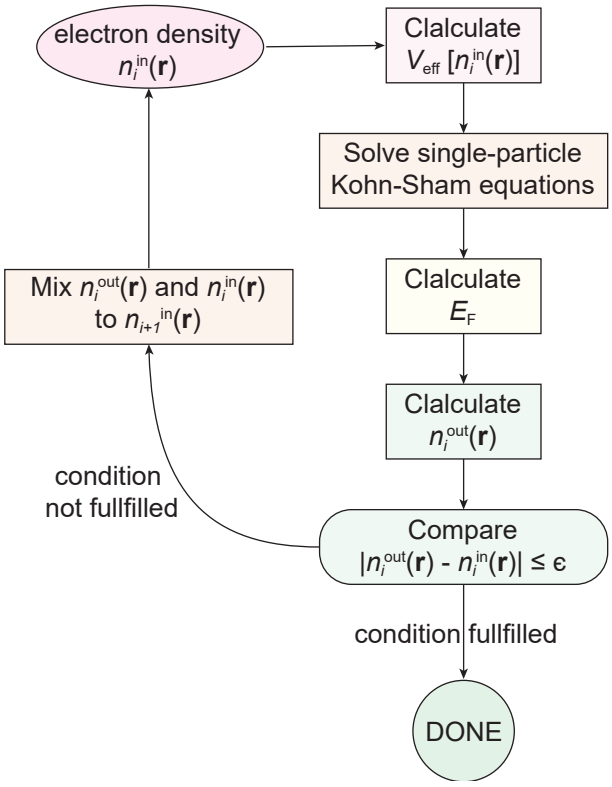

Figure 2.1 | Schematic flow-chart of the self-consistency cycle in DFT. The cycle is started with an electron density $n_i^{\text{in}}(\mathbf{r})$ from which the effective potential V_{eff} is calculated. Inserting this potential into the Kohn-Sham equations (2.15), the effective single-particle Schrödinger equation is solved and the Fermi energy E_{F} is determined. Summing up all occupied states, a new electron density $n_i^{\text{out}}(\mathbf{r})$ is calculated. If $n_i^{\text{in}}(\mathbf{r})$ and $n_i^{\text{out}}(\mathbf{r})$ are in agreement within a certain condition ϵ, the electron density is called converged and the self-consistency cycle is completed. In case of an unfulfilled condition, both densities are mixed with a certain scheme and determine the electron density $n_{i+1}^{\text{in}}(\mathbf{r})$ of the next iteration of the cycle.

Every iteration of the self-consistency cycle requires an electron density $n_i^{\text{in}}(\mathbf{r})$. Without provision, a starting density is constructed based on the electron density of single non-interacting atoms. Calculating the Hartree and *xc* potential with this electron density $V_{\text{H}}[n_i^{\text{in}}(\mathbf{r})]$ and $V_{xc}[n_i^{\text{in}}(\mathbf{r})]$, the effective potential $V_{\text{eff}}[n_i^{\text{in}}(\mathbf{r})]$ is constructed.

Inserting $V_{\text{eff}}[n_i^{\text{in}}(\mathbf{r})]$ into the Kohn-Sham equations, the effective single-particle Schrödinger equation is solved by diagonalizing the Hamiltonian for every single k point in the irreducible wedge of the Brillouin zone. In case of periodic crystals, this is done by applying the Bloch theorem. From the resulting eigenvalues and eigenstates, the Fermi energy E_{F} is determined with the occupation of the bands which are assigned to the energy E_ν of the band ν.

A new electron density $n_i^{\text{out}}(\mathbf{r})$ can be calculated by the sum over all occupied

states/Kohn-Sham orbitals $\psi_{k,\nu}$ of each k point and band

$$n_i^{\text{out}}(\mathbf{r}) = \sum_{k,\nu}^{\text{occ}} |\psi_{k,\nu}(\mathbf{r})|^2 \tag{2.34}$$

When the difference of both electron densities $n_i^{\text{in}}(\mathbf{r})$ and $n_i^{\text{out}}(\mathbf{r})$ is smaller than a certain condition ϵ, it is known as converged and the electron density reflects the ground state electron density n_0. From the theorems of Hohenberg and Kohn, the determined energy E_0 will then be the ground state energy. Note that due to the approximations for the *xc* potential, the true ground state electron density is unknown. However, a good approximation of *xc* will lead to a good ground state electron density from which all other ground state properties can be calculated.

If the condition ϵ is not fulfilled, the iterative cycle needs to be run through again. Simply using $n_i^{\text{out}}(\mathbf{r})$ as new electron density $n_{i+1}^{\text{in}}(\mathbf{r})$ leads to a divergence of the electron density. Therefore, a mixing of both $n_i^{\text{in}}(\mathbf{r})$ and $n_i^{\text{out}}(\mathbf{r})$ with a small contribution of the latter has shown to be suitable as $n_{i+1}^{\text{in}}(\mathbf{r})$.

The simplest mixing method is called straight mixing, where

$$n_{i+1}^{\text{in}}(\mathbf{r}) = (1-\alpha) n_i^{\text{in}}(\mathbf{r}) + \alpha n_i^{\text{out}}(\mathbf{r}) \tag{2.35}$$

In order to achieve convergence, the mixing parameter α should be chosen sufficiently small. Besides the straight mixing, other schemes have been suggested which show faster convergence of the self-consistency cycle [74–77].

2.9 Total energy

The total energy of a system is one of the key quantities in DFT from which a lot of interpretations start. When describing solids and calculate ground state energies, i.e. lattice constants of crystals, the Coulomb interaction becomes an additional contribution compared to Eq. (2.11)

$$E[n(\mathbf{r})] = T_{\text{S}}[n(\mathbf{r})] + E_{\text{H}}[n(\mathbf{r})] + E_{\text{ext}}[n(\mathbf{r})] + E_{xc}[n(\mathbf{r})] + E_{II} \tag{2.36}$$

where

$$E_{II} = e^2 \sum_{\substack{I,I'=1 \\ I \neq I'}}^{M} \frac{Z^I Z^{I'}}{|\mathbf{R}^I - \mathbf{R}^{I'}|} \tag{2.36a}$$

Here, I sums over all atoms of the crystal at position $\mathbf{R}^I$.

While the kinetic energy, $T_{\text{S}}[n(\mathbf{r})]$, Eq. (2.13a), with its Nabla operator ∇^2 can not be calculated explicitly, it will be rewritten to depend on the single particle eigenvalues

ϵ_i. Therefore, Eq. (2.20) can be expressed as

$$-\frac{\hbar^2}{2m}\nabla^2\psi_i(\mathbf{r})(\mathbf{r}) = \epsilon_i\psi_i(\mathbf{r}) - V_{\text{eff}}(\mathbf{r}) - \sigma\cdot\mathbf{B}_{\text{eff}}(\mathbf{r})\psi_i(\mathbf{r}) \tag{2.37a}$$

Multiplying this equation from left with $\int \mathrm{d}^3 r\psi_i^*(\mathbf{r},\sigma)$ and summing over all occupied states results in the kinetic energy

$$T_{\text{S}}[n(\mathbf{r})] = \sum_{i=1}^{N}\epsilon_i - \int n(\mathbf{r})V_{\text{eff}}(\mathbf{r})\mathrm{d}^3 r - \int \mathbf{m}(\mathbf{r})\cdot\mathbf{B}_{\text{eff}}\mathrm{d}^3 r \tag{2.37}$$

Neglecting an external magnetic field and assuming that the external potential V_{ext} is given by the nuclei, the total energy will be written [68]

$$\begin{aligned} E[n(\mathbf{r}),\mathbf{m}(\mathbf{r})] = &\sum_{i=1}^{N}\epsilon_i - \int n(\mathbf{r})V_{\text{eff}}(\mathbf{r})\mathrm{d}^3 r - \int \mathbf{m}(\mathbf{r})\cdot\mathbf{B}_{xc}\mathrm{d}^3 r \\ &-4\pi e^2\sum_{I=1}^{M}\int\frac{n(\mathbf{r})Z^I}{|\mathbf{r}-\mathbf{R}^I|}\mathrm{d}^3 r + 4\pi e^2\frac{1}{2}\int\frac{n(\mathbf{r})n'(\mathbf{r})}{|\mathbf{r}-\mathbf{r}'|}\mathrm{d}^3 r\mathrm{d}^3 r' \\ &+\int n(\mathbf{r})\varepsilon_{xc}(n(\mathbf{r}),|\mathbf{m}(\mathbf{r})|)\mathrm{d}^3 r + 4\pi e^2\sum_{\substack{I,I'=1\\ I\neq I'}}^{M}\frac{Z^I Z^{I'}}{|\mathbf{R}^I-\mathbf{R}^{I'}|} \end{aligned} \tag{2.38a}$$

Introducing the *xc* functionals Eqs. (2.15c) and (2.20b), this can be represented as

$$\begin{aligned} E[n(\mathbf{r}),\mathbf{m}(\mathbf{r})] = &\sum_{i=1}^{N}\epsilon_i - \int n(\mathbf{r})V_{xc}(\mathbf{r})\mathrm{d}^3 r - \int \mathbf{m}(\mathbf{r})\cdot\mathbf{B}_{xc}\mathrm{d}^3 r \\ &+4\pi e^2\frac{1}{2}\int\frac{n(\mathbf{r})n'(\mathbf{r})}{|\mathbf{r}-\mathbf{r}'|}\mathrm{d}^3 r\mathrm{d}^3 r' \\ &+\int n(\mathbf{r})\varepsilon_{xc}(n(\mathbf{r}),|\mathbf{m}(\mathbf{r})|)\mathrm{d}^3 r + 4\pi e^2\sum_{\substack{I,I'=1\\ I\neq I'}}^{M}\frac{Z^I Z^{I'}}{|\mathbf{R}^I-\mathbf{R}^{I'}|} \end{aligned} \tag{2.38}$$

Due to the iterative approach introduced in the previous Sec. 2.8, the total energy is only an approximation. A significant problem arises due to the Hartree and Coulomb contributions from the nuclei which are diverging. However, it could be shown that such singularities can be cancelled [78].

2.10 Force theorem

When calculating small differences in total energy between an initial state and a slightly perturbed state, a self-consistent calculation of the latter is not always required. The force theorem [79–81] shows that the energy differences due to small

perturbation of the densities $n(\mathbf{r})$, $\mathbf{m}(\mathbf{r})$ can be calculated as a sum of the eigenvalues of the two states. In a linear approximation, the total energy only shows slight differences after a small perturbation and the interaction drops out of the change of total energy. Such a perturbation can be e.g. a small canting between two magnetic states or – what is mainly applied in this thesis – the energy contribution of the SOC. For the latter, the second variation is applied to use the basis functions of the scalar-relativistic Hamiltonian $\mathcal{H}_{\mathrm{SCA}}$ [Eq. (2.26)] in order to represent the energy eigenvalues of the relativistic Hamiltonian.

The total energy of a system is represented by the sum of all single particle eigenvalues ϵ_i and the energy corrections E' which contain the remaining energy contributions. Therefore, the unperturbed energy of the initial state can be expressed as

$$E_0 = \sum_i^N \epsilon_{i,0} + E_0' \tag{2.39a}$$

and for the perturbed state

$$E_1 = \sum_i^N \epsilon_{i,1} + E_1' \tag{2.39b}$$

In first order perturbation, the second terms cancel each other and the single particle eigenvalues remain. As stated before it means, that the interactions drop out. If the perturbation is small enough, it is sufficient to compare the sum over the single particle eigenvalues to get the change in total energy.

Since we apply the force theorem for the magnetocrystalline anisotropy energy, the SOC is the perturbation, the Hamiltonian is $\mathcal{H}_{\mathrm{SOC}}$ and the energy contribution due to the SOC is

$$\Delta E_{\mathrm{SOC}} = \sum_i^N \epsilon_{i,1} - \sum_i^N \epsilon_{i,0} \tag{2.40}$$

Chapter 3

Solution of Kohn-Sham equations within FLAPW

In the previous chapter, we introduced the concept of density functional theory (DFT), where the focus in this chapter is the solution of the Kohn-Sham equations. Therefore, a suitable basis set needs to be found. Since the calculations in this thesis are performed with the program FLEUR [47] in which the full potential linearized augmented planewave (FLAPW) method is implemented [82, 83], we introduce this basis set step by step in the following. For more detailed information, see e.g. Refs. 68, 69, 84.

3.1 Generalized Eigenvalue problem

The Kohn-Sham equations (2.15) are a non-linear eigenvalue problem. We can introduce the Dirac formalism as

$$\left\{-\frac{\hbar^2}{2m}\nabla^2 + V_{\text{eff}}(\mathbf{r})\right\}\psi_i(\mathbf{r}) = \epsilon_i\psi_i(\mathbf{r}) \quad \xrightarrow{\text{Dirac}} \quad \mathcal{H}\,|\psi_i(\mathbf{r})\rangle = \epsilon_i\,|\psi_i(\mathbf{r})\rangle \tag{3.1}$$

The Kohn-Sham orbitals ψ_i can be expressed as linear combination of basis functions $\phi_i(\mathbf{r})$ and the expansion coefficients $c_{i,\alpha}$

$$\psi_i(\mathbf{r}) = \sum_\alpha c_{i,\alpha}\,|\phi_\alpha(\mathbf{r})\rangle \tag{3.2a}$$

This expression can be inserted in Eq. (3.1) and consequently, the eigenvalue problem is written as

$$\sum_\alpha c_{i,\alpha}\,\langle\phi'_\alpha(\mathbf{r})|\,\mathcal{H}\,|\phi_\alpha(\mathbf{r})\rangle = \epsilon_i\,\langle\phi'_\alpha(\mathbf{r})|\phi_\alpha(\mathbf{r})\rangle \tag{3.2b}$$

The former term can be interpreted as a Hamilton matrix $\underline{\mathcal{H}}$, whereas the second term represents the overlap matrix $\underline{S}$ which is hermitian and positive definite. Eq. (3.2b) can be rewritten as

$$\left\{\underline{\mathcal{H}} - \epsilon_i\underline{S}_i\right\}\mathbf{c}_i = 0 \tag{3.2}$$

Here, $\mathbf{c}_i$ denotes the vector of expansion coefficients. The Kohn-Sham equations can consequently be expressed as a generalized eigenvalue problem and can be solved by diagonalizing the matrix $\left\{\underline{\mathcal{H}} - \epsilon_i\underline{S}_i\right\}$. This can be done e.g. with the help of Cholesky decomposition [85].

3.2 The Bloch theorem

In this work, the magnetism appears in crystalline structures which can be seen as semi-infinite. Therefore, the Bloch theorem can be applied which allows for a calculation of electronic structure in systems with large number of particles [86]. Using the condition of a periodic lattice, the potential of this lattice is periodic as well and can be written as

$$V(\mathbf{r}) = V(\mathbf{r} + \mathbf{R}) \tag{3.3}$$

The wave function of an electron is then given by

$$\psi_{\mathbf{k}}(\mathbf{r}) = \mathrm{e}^{i\mathbf{k}\cdot\mathbf{r}} u_{\mathbf{k}}(\mathbf{r}) \tag{3.4a}$$

$$u_{\mathbf{k}}(\mathbf{r}) = u_{\mathbf{k}}(\mathbf{r} + \mathbf{R}) \tag{3.4b}$$

denotes the Bloch function describing the periodicity of the crystal lattice.
The vector $\mathbf{R}$ in real space is defined as

$$\mathbf{R} = m_1\mathbf{a}_1 + m_2\mathbf{a}_2 + m_3\mathbf{a}_3 \tag{3.4c}$$

Here, $m_i \in \mathbb{Z}$ and $\mathbf{a}_i$ represent the basis vectors of the unit cell. The Bloch function is also periodic in reciprocal space, when $\mathbf{G}$ denotes the reciprocal lattice vector

$$u_{\mathbf{k}(\mathbf{r})} = u_{\mathbf{k}+\mathbf{G}}(\mathbf{r}) \tag{3.4d}$$

The wave function of two particles within a distance $\mathbf{R}$ between each other deviate by a phase factor

$$\psi_{\mathbf{k}}(\mathbf{r} + \mathbf{R}) = \mathrm{e}^{i\mathbf{k}\cdot\mathbf{R}} u_{\mathbf{k}}(\mathbf{r}) \tag{3.4}$$

The probability density remains unchanged

$$|\psi_{\mathbf{k}}(\mathbf{r} + \mathbf{R})|^2 = |\mathrm{e}^{i\mathbf{k}\cdot\mathbf{R}} u_{\mathbf{k}}(\mathbf{r})|^2 = |\psi_{\mathbf{k}}(\mathbf{r})|^2 \tag{3.4e}$$

Consequently, the first Brillouin zone contains all information about the electronic structure. Therefore, the Bloch theorem is decisive for calculating the electronic structure of crystals.

3.3 The planewave basis set

The eigenvalue problem can be inserted into a planewave basis set. Assuming a large distance between two atoms, the potential between those atoms can be approximated as constant. Planewaves represent the solution of the Schrödinger equation for a

constant, external potential. The expansion of the electronic wave function, Eq. (3.2a) can be done within the planewave basis set, where the Bloch theorem is applied

$$\phi(\mathbf{r}) = \sum_{|\mathbf{k}+\mathbf{G}|\leq k_{\max}} c_i e^{i(\mathbf{k}+\mathbf{G})} \tag{3.5}$$

Here, $\mathbf{k}$ is the Bloch vector and $\mathbf{G}$ is the reciprocal lattice vector. Basically, every complex problem can be represented by a superposition of planewaves; however, the calculational effort increases with the amount of considered planewaves. The cutoff parameter $k_{\max}$ indicates, how many planewaves for the basis set are considered. A large $k_{\max}$ leads to an increasing computational effort while due to the variational principle, the calculated energy is decreasing. A lower $k_{\max}$ on the other hand increases the computational error. Therefore, in DFT it is crucial to choose $k_{\max}$ so that a reasonable balance between computational effort and error exists. A system is known as converged with respect to the cutoff energy, when no further information in real space are obtained by increasing $k_{\max}$.

However, in the vicinity of the nuclei, the electronic wave function is oscillating strongly due to the crystal potential. In order to capture this behaviour, large $k_{\max}$ are necessary which increase the computational effort over a reasonable amount. The convergence in the self-consistency cycle described in Sec. 2.8 therefore is very slow and might be impossible.

3.4 The APW method

Planewaves can serve as a reasonable basis set since for a constant external potential they are the fundamental solution of the Schrödinger equation. In the vicinity of the nuclei; however, they appear as inapplicable. Therefore, the basis set is extended and divided in two regions. One region – interstitial region (IR) – between the nuclei, the potential can still be approximated as constant and described with the planewave basis set. In the region around the nuclei, a different basis set is applied where the potential is approximated as radial symmetric

$$V(r) = \begin{cases} V_0 & \text{interstitial region (IR)} \\ V_0(r) & \text{muffin-tin (MT) sphere} \end{cases} \tag{3.6}$$

The muffin tin (MT) spheres for which the radii R^{MT} are chosen to not overlap are placed around the atomic nuclei. This is schematically shown in Fig. 3.1.

The radial Schrödinger equation for a spherical potential is solved by radial functions u_l multiplied by spherical harmonics $Y_{l,m}$. Therefore, the planewave basis set, Eq. (3.5),

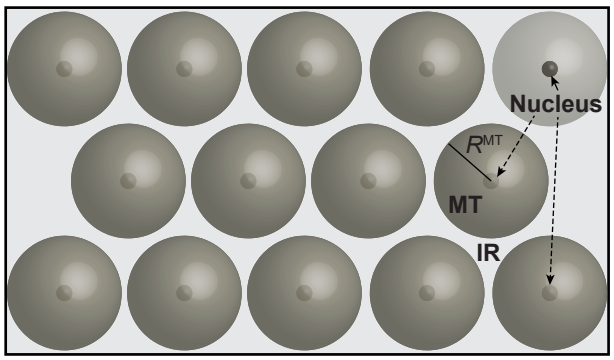

Figure 3.1 | Schematic representation of the augmented planewave (APW) method. The space is divided into two parts, interstitial interstitial region (IR) where the potential between the atoms is approximated as constant and the muffin tin (MT) spheres with their radius R^{MT} surrounding the nuclei. Inside the MT spheres, the potential is approximated as radial symmetric.

is extended to

$$\phi_{\mathbf{G}}(\mathbf{k},\mathbf{r}) = \begin{cases} \frac{1}{\sqrt{\Omega}} e^{i(\mathbf{k}+\mathbf{G})\cdot\mathbf{r}} & \text{IR} \\ \sum_{l,m} A_{l,m} u_l(r) Y_{l,m}(\hat{\mathbf{r}}) & \text{MT sphere} \end{cases} \tag{3.7}$$

Here, Ω denotes the volume of the unit cell and $\hat{\mathbf{r}}$ is the radial symmetric unit vector inside the MT with respect to the centre. The coefficients $A_{l,m}$ (l, m are the angular momentum quantum numbers and magnetic quantum number, respectively) are chosen so that the basis functions at the transition from the IR to the MT are continuous.

The solutions u_l of the radial Schrödinger equation including the energy parameter E_l and the spherical potential $V(r)$ are

$$\left\{ -\frac{\hbar^2}{2m}\frac{\partial^2}{\partial r^2} + \frac{\hbar^2}{2m}\frac{l(l+1)}{r^2} + V(r) - E_l \right\} r u_l(r) = 0 \tag{3.8}$$

Despite the fact that the APWs form a complete set of basis functions for the whole space, several disadvantages occurred. On the one hand, the energy parameters E_l as well as the quantum numbers l, m are fixed. A correct description of the system is only given when the energy parameters are equal to the band energies. Therefore, the variational freedom is missing. Since the u_l are dependent on the band energies, a simple diagonalization of the Hamiltonian is not possible which leads to a non-linear problem. Additionally, for infinitesimal small u_l the asymptotic problem arises, since the basis functions at the transition from IR to MT are not continuous and the basis functions decouple.

3.5 The LAPW method

Due to the problems of the APW method, the basis set was linearised [87, 88]. A Taylor expansion of $u_l(\epsilon, r)$ around E_l leads to

$$u_l(\epsilon, r) = u_l(E_l, r) + \dot{u}_l(E_l, r)(\epsilon - E_l) + O\left[(\epsilon - E_l)^2\right] \tag{3.9}$$

Here, the energy derivative of the radial solution is defined as

$$\dot{u}_l(\epsilon, r) = \frac{\partial u_l(\epsilon, r)}{\partial \epsilon} \tag{3.9a}$$

The quadratic error of the energy difference $O\left[(\epsilon - E_l)^2\right]$ arises due to the construction of the APW/linearized augmented planewave (LAPW) basis functions which are constructed from linear combinations of u_l and $\dot{u}_l$. Calculating the band energies within the variational principle will decrease the error to $O\left[(\epsilon - E_l)^4\right]$. This error can be seen as small enough so that $\dot{u}_l$ is sufficient to cover the large required energy range.

The basis set of the LAPW method is written as

$$\phi_{\mathbf{G}}(\mathbf{k}, \mathbf{r}) = \begin{cases} \frac{1}{\sqrt{\Omega}} e^{i(\mathbf{k}+\mathbf{G})\cdot\mathbf{r}} & \text{IR} \\ \sum_{l,m} \left\{A_{l,m} u_l(r) + B_{l,m} \dot{u}_l(r)\right\} Y_{l,m}(\hat{\mathbf{r}}) & \text{MT sphere} \end{cases} \tag{3.10}$$

Compared to Eq. (3.7), the term $B_{l,m}\dot{u}_l(r)Y_{l,m}$ arises. The required continuation between the basis sets of the IR and MT spheres is fulfilled not only for u_l, but also for its derivative $\dot{u}_l$. A schematic example is shown in Fig. 3.2.

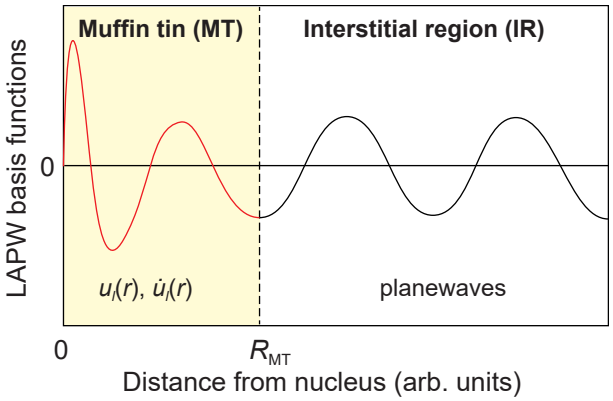

Figure 3.2 | Sketch of an linearized augmented planewave (LAPW) basis function depending on the distance to an atomic core. Inside the muffin tin (MT) spheres, the solution of the radial Schrödinger equation u_l and its derivative $\dot{u}_l$ is used. Both functions are continuous at the MT boundary.

The asymptotic problem of the APW method consequently is solved. The determination of $\dot{u}_l$ can be obtained from

$$\left\{-\frac{\hbar^2}{2m}\frac{\partial^2}{\partial r^2} + \frac{\hbar^2}{2m}\frac{l(l+1)}{r^2} + V(r) - E_l\right\} r\dot{u}_l(r) = r u_l(r) \tag{3.11}$$

In comparison to the APW method, the Hamilton matrix is independent of the energy and the energies can be determined with a single diagonalization. Furthermore, it is now possible to extend the potentials with non-spherical parts inside MTs. This idea is used in the FLAPW method.

One decisive disadvantage occurs in the LAPW method: due to the increased variational freedom, the computational effort increases.

3.6 The FLAPW method

When open structures such as surfaces or interfaces need to be described, both APW and LAPW method fail to provide accurate results because of the shape approximations applied to the potential. Those approximations [82, 83] will be replaced in the FLAPW method, where the potentials of the IR and the MTs get a periodic character correspondent to the lattice and a non-spherical term, respectively. The potential now reads as

$$V(\mathbf{r}) = \begin{cases} \sum\limits_{\mathbf{G}} V_{\mathrm{IR}} \mathrm{e}^{i\mathbf{G}\mathbf{r}} & \text{IR} \\ \sum\limits_{l,m} V_{\mathrm{MT}}^{l,m}(r) Y_{l,m}(\mathbf{r}) & \text{MT sphere} \end{cases} \tag{3.12}$$

The charge density $\rho(\mathbf{r})$ can be written in the same way

$$\rho(\mathbf{r}) = \begin{cases} \sum\limits_{\mathbf{G}} \rho_{\mathrm{IR}} \mathrm{e}^{i\mathbf{G}\mathbf{r}} & \text{IR} \\ \sum\limits_{l,m} \rho_{\mathrm{MT}}^{l,m}(r) Y_{l,m}(\mathbf{r}) & \text{MT sphere} \end{cases} \tag{3.13}$$

Note that the charge density in related to the electron density via $\rho(\mathbf{r}) = -en(\mathbf{r})$, whereas in the FLEUR code, $e = 1$ [47].

3.7 Local Orbitals

States close to the nuclei do not contribute to the chemical bonds since they act like states in a free atom. Such states are called core states. On the other hand, states which are responsible for the chemical bonding present at the atomic boundary are called valence states. In the FLAPW method, core states are found within the MTs whereas valence states are leaking out of the MT spheres.

When two states having the same quantum number l, but different main quantum numbers n and are treated as valence states, the physical description of the system fails. Those semi-core states can reach out of the MT spheres, but are far away from the valence energy parameters. The occurrence of those states cause convergence problems in the self-consistency cycle.

To overcome this problem, it is possible to ensure the treatment of semi-core states as valence electrons by extending the (F)LAPW basis set by local orbitals [69]. A local orbital is introduced for one quantum number l (one function for every magnetic quantum number m) and is confined inside the MT (Fig. 3.3).

Local orbitals are constructed as

$$\phi_{l,m}^{\mathrm{LO}}(\mathbf{r}) = \left[A_{l,m}^{\mathrm{LO}} u_l(r, E_l) + B_{l,m}^{\mathrm{LO}} \dot{u}_l(r, E_l) + C_{l,m}^{\mathrm{LO}} u_l^{\mathrm{LO}}(r, E_l^{\mathrm{LO}}) \right] Y_{l,m} \tag{3.14}$$

Here, $u_l(r, E_l)$, $\dot{u}_l(r, E_l)$ are the solutions of the radial Schrödinger equation and its

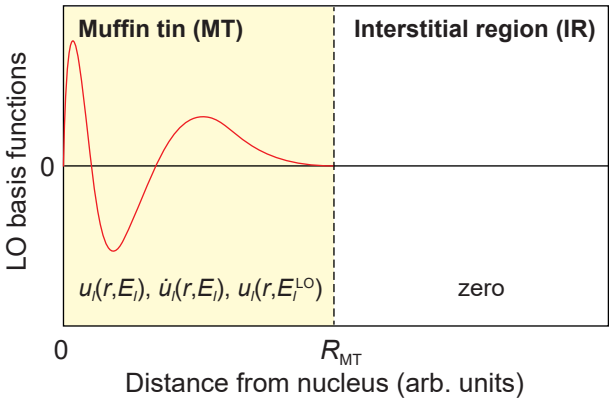

Figure 3.3 | Sketch of an local orbital basis function depending on the distance to an atomic core. Semi-core states are treated as valence electrons and compared to the linearized augmented planewave (LAPW) basis set, an additional term, $u_l(r, E_l^{\mathrm{LO}})$ occurs. Both value and slope are zero at the muffin tin (MT) boundary.

derivative from the APW/LAPW basis set[1]. Compared to the known LAPW basis, another radial function $u_l^{\mathrm{LO}}(r, E_l^{\mathrm{LO}})$ occurs. It can be constructed by a solution to the spherical potential at a certain energy parameter close to the semi-core state, $u_l^{\mathrm{LO}}(r, E_l^{\mathrm{LO}}) = u_l(r, E_l^{\mathrm{LO}})$. The three coefficients $A_{l,m}^{\mathrm{LO}}$, $B_{l,m}^{\mathrm{LO}}$, $C_{l,m}^{\mathrm{LO}}$ are determined to ensure a zero value and slope at the MT boundary (Fig. 3.14) and are used as normalization of the local orbitals over the MT sphere.

Despite the small increase of the set of basis functions due to local orbitals and the increased computational effort, the treatment of semi-core states within local orbitals is a proper way to circumvent long self-consistency cycles when DFT calculations are hard to converge. In this thesis, especially with the 5*d* element W, local orbitals have been used.

3.7.1 Films in FLAPW

Describing ultrathin film systems, the crucial geometrical parts occur at the interfaces and surfaces. At surfaces, the translational symmetry is broken. Instead of a three-dimensional (3D) symmetry, only a two-dimensional (2D) symmetry is left which is parallel to the surface. While we divided the space in the APW and LAPW method into two regions, IR and MT, the FLAPW method introduces a third space describing a vacuum region (Fig. 3.4) [89].

In the previous descriptions of the basis sets, the IR is infinite in every direction of the 3D coordinate system. While the basis set for the MT spheres is unchanged comparing bulk and film, the IR for film systems is restricted in z direction and stretches from $-D/2$ to $D/2$. Without periodicity in z direction, the unit cell increases to $\pm\infty$. Since the symmetry is only broken along z, the planewave basis set for the IR has to be modified

$$\phi_{\mathbf{G}_\parallel, G_\perp}(\mathbf{k}_\parallel, \mathbf{r}) = \frac{1}{\sqrt{\Omega}} \mathrm{e}^{i(\mathbf{k}_\parallel + \mathbf{G}_\parallel)\mathbf{r}_\parallel} \, \mathrm{e}^{iG_\perp z} \tag{3.15}$$

Here, $\mathbf{G}_\parallel, \mathbf{k}_\parallel$ denote the 2D wave- and Bloch vectors parallel to the film, whereas $\mathbf{r}_\parallel$ represents the parallel component of $\mathbf{r}$. To describe the IR in z direction, the wave

[1] Note that for clarification, here $u_l(r, E_l)$ whereas before, $u_l(r)$.

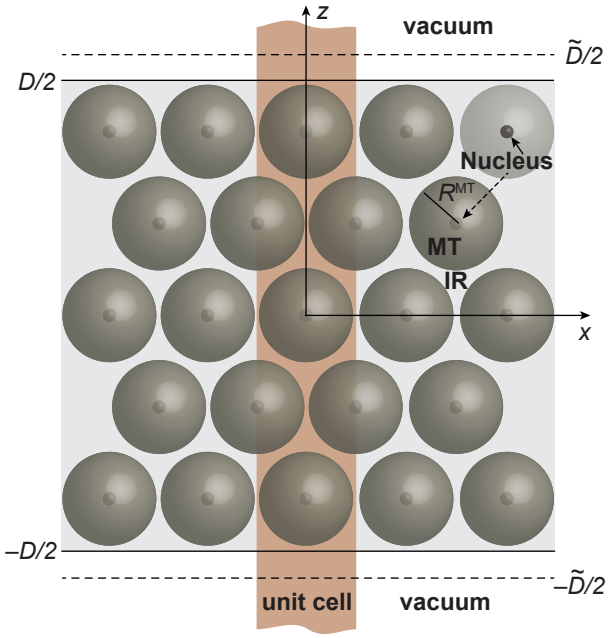

Figure 3.4 | Schematic representation of the unit cell in a film calculation using the full potential linearized augmented planewave (FLAPW) method. The space is divided into three parts, interstitial IR where the potential between the atoms is approximated as constant and the muffin tin (MT) spheres with their radius R^{MT} surrounding the cores. Inside the MT spheres, the potential is approximated as radial symmetric.

vector perpendicular to the film, $G_\perp$ is introduced which is defined as

$$G_\perp = \frac{2\pi n}{\tilde{D}} \tag{3.15a}$$

In order to gain more variational freedom, $G_\perp$ is not defined in terms of D, but $\tilde{D}$ (Fig. 3.4), whereas $\tilde{D} > D$. This ensures that the nodal points do not come together at the region between IR and vacuum.

For the vacuum basis set, a mixed approach consisting of MT spheres and IR is adapted. Parallel to the film plane, planewaves are considered, while perpendicular to the film, a z dependent function $u_{\mathbf{G}_\parallel}(\mathbf{k}_\parallel, z)$ is used. Similar to Eq. (3.8), $u_{\mathbf{G}_\parallel}(\mathbf{k}_\parallel, z)$ solves the one-dimensional Schrödinger equation

$$\left\{-\frac{\hbar^2}{2m}\frac{\partial^2}{\partial z^2} + \frac{\hbar^2}{2m}\left(\mathbf{G}_\parallel + \mathbf{k}_\parallel\right)^2 + V_0(z) - E_{\mathrm{vac}}\right\} u_{\mathbf{G}_\parallel}(\mathbf{k}_\parallel, z) = 0 \tag{3.16a}$$

Here, E_{vac} and $V_0(z)$ denote the vacuum energy parameters and the planar averaged part of the vacuum potential. Corresponding to the basis set of the MTs, the derivative, $\dot{u}_{\mathbf{G}_\parallel}(\mathbf{k}_\parallel, z)$ is needed to ensure the continuation at the vacuum boundary. It can be derived from

$$\left\{-\frac{\hbar^2}{2m}\frac{\partial^2}{\partial z^2} + \frac{\hbar^2}{2m}\left(\mathbf{G}_\parallel + \mathbf{k}_\parallel\right)^2 + V_0(z) - E_{\mathrm{vac}}\right\} \dot{u}_{\mathbf{G}_\parallel}(\mathbf{k}_\parallel, z) = u_{\mathbf{G}_\parallel}(\mathbf{k}_\parallel, z) \tag{3.16b}$$

The resulting basis function for the vacuum region then reads as

$$\phi_{\mathbf{G}_\parallel, G_\perp}(\mathbf{k}_\parallel, \mathbf{r}) = \left\{A_{\mathbf{G}_\parallel, G_\perp}(\mathbf{k}_\parallel) u_{\mathbf{G}_\parallel}(\mathbf{k}_\parallel, z) + B_{\mathbf{G}_\parallel, G_\perp}(\mathbf{k}_\parallel) \dot{u}_{\mathbf{G}_\parallel}(\mathbf{k}_\parallel, z)\right\} \mathrm{e}^{i(\mathbf{k}_\parallel + \mathbf{G}_\parallel)\mathbf{r}_\parallel} \tag{3.16}$$

Equivalent to the MTs, the coefficients A, B guarantee that both function and its derivative are steady and differentiable at the vacuum boundary. The number of basis functions in the vacuum is lower than for the IR. In order to increase this number, the energy parameter E_{vac} is replaced by a series of parameters E^i_{vac} covering any energy region. The variational freedom can be increased by choosing

$$E^i_{\text{vac}} = E^{G_\perp}_{\text{vac}} = E_{\text{vac}} - \frac{\hbar^2}{2m} G_\perp^2 \tag{3.16c}$$

The basis functions $u_{\mathbf{G}_\parallel, G_\perp}(\mathbf{k}_\parallel, z)$ now depend on $G_\perp$ [90].

The whole set of basis functions in the FLAPW method for film calculations can be summarized as

$$\phi_{\mathbf{G}_\parallel, G_\perp}(\mathbf{k}_\parallel, \mathbf{r}) = \begin{cases} \frac{1}{\sqrt{\Omega}} e^{i(\mathbf{k}_\parallel + \mathbf{G}_\parallel)\mathbf{r}_\parallel} \quad e^{iG_\perp z} & \text{IR} \\ \sum\limits_{l,m} \left\{ A_{l,m} u_l(r) + B_{l,m} \dot{u}_l(r) \right\} Y_{l,m}(\hat{\mathbf{r}}) & \text{MT sphere} \\ \{ A_{\mathbf{G}_\parallel, G_\perp}(\mathbf{k}_\parallel) u_{\mathbf{G}_\parallel}(\mathbf{k}_\parallel, z) + \\ \quad B_{\mathbf{G}_\parallel, G_\perp}(\mathbf{k}_\parallel) \dot{u}_{\mathbf{G}_\parallel}(\mathbf{k}_\parallel, z) \} e^{i(\mathbf{k}_\parallel + \mathbf{G}_\parallel)\mathbf{r}_\parallel} & \text{vacuum region} \end{cases} \tag{3.17}$$

3.7.2 Scalar-relativistic approximation in FLAPW

As shown in Sec. 2.5, the relativistic effects in DFT can be treated approximately. The scalar-relativistic approximated Hamiltonian, $\mathcal{H}_{\text{SCA}} = \mathcal{H}_{\text{non-rel}} + \mathcal{H}_{\text{rel}}$ [Eq. (2.26)] typically is larger than the Hamiltonian of the spin-orbit coupling (SOC), $\mathcal{H}_{\text{SOC}}$ [Eq. (2.26c)]

$$\mathcal{H}_{\text{SCA}} >> \mathcal{H}_{\text{SOC}} \tag{3.18}$$

Therefore, the scalar-relativistic approximation [65] drops the SOC contribution of the Pauli operator [Eq. (2.26)]. The SOC Hamiltonian is the only part that couples both spin ↑ and spin ↓ contributions and thus, the scalar-relativistic approximation allows for a decoupling of the two spin components in the Pauli equation.

Introducing the approximation into the FLAPW method exploits the fact that relativistic effects in particular become important in the vicinity of the nuclei. Consequently, electrons which are inside the MTs are treated relativistically, whereas IR and the vacuum region remain non-relativistic. The solution of the radial Schrödinger equation $u_l(r)$ and its derivative $\dot{u}_l(r)$ need to be replaced by the equivalent solutions of the relativistic radial Schrödinger equation $g_l(r), \dot{g}_l(r)$ and $h_l(r), \dot{h}_l(r)$. Since spin ↑ and spin ↓ contributions are decoupled, the problem can be solved independently for each spin direction within the scalar-relativistic approximation. The Pauli-spinors are obsolete. The complete basis set in FLAPW in

scalar-relativistic approximation reads as

$$\phi_{\mathbf{G}_\parallel,G_\perp}(\mathbf{k}_\parallel,\mathbf{r}) = \begin{cases} \frac{1}{\sqrt{\Omega}} e^{i(\mathbf{k}_\parallel+\mathbf{G}_\parallel)\mathbf{r}_\parallel} \quad e^{iG_\perp z} & \text{IR} \\ \sum\limits_{l,m}\left\{A_{l,m}\begin{pmatrix} g_l(r) \\ h_l(r)\end{pmatrix} + B_{l,m}\begin{pmatrix} \dot{g}_l(r) \\ \dot{h}_l(r)\end{pmatrix}\right\} Y_{l,m}(\hat{\mathbf{r}}) & \text{MT sphere} \\ \{A_{\mathbf{G}_\parallel,G_\perp}(\mathbf{k}_\parallel)u_{\mathbf{G}_\parallel}(\mathbf{k}_\parallel,z)+ \\ \quad B_{\mathbf{G}_\parallel,G_\perp}(\mathbf{k}_\parallel)\dot{u}_{\mathbf{G}_\parallel}(\mathbf{k}_\parallel,z)\}e^{i(\mathbf{k}_\parallel+\mathbf{G}_\parallel)\mathbf{r}_\parallel} & \text{vacuum region} \end{cases} \tag{3.19}$$

3.7.3 Spin spirals and the generalized Bloch theorem

In order to find and explain the magnetic ground state of complex spin structures, it is not sufficient to analyse collinear magnetic structures. Calculating non-collinear spin structures such as domain walls or skyrmions within DFT requires the application of large unit cells since the translational symmetry of the magnetic structure is broken and the Bloch theorem can not be used any more. To circumvent this problem, we compare homogeneous spin spiral states applying the generalized Bloch theorem which can be interpreted within the Heisenberg model as we will present later.

Spin spirals can be characterised by their reciprocal spin spiral vector $\mathbf{q}$ which determines the propagation direction of the spiral as well as the angle φ_i between two adjacent spins. Taking into account the position $\mathbf{R}_i$ of the ith atom in real space, the angle between two spins is given by

$$\varphi_i = \mathbf{q}\cdot\mathbf{R}_i \tag{3.20a}$$

and the direction of the magnetic moment by

$$\mathbf{M}_i = M\begin{pmatrix} \cos\varphi_i \sin\theta \\ \sin\varphi_i \sin\theta \\ \cos\theta \end{pmatrix} \tag{3.20}$$

Here, θ denotes the opening angle for conical spin spirals. As an overview for different φ_i, θ, different spin spiral states are presented in Fig. 3.5.

Without SOC, the spin lattice is decoupled from the lattice and the rotation axis (red line in Fig. 3.5) is not relevant. The energy between the spin spiral states in Fig. 3.5 then only depend on the vector $\mathbf{q}$ or in other words, the angle φ_i between adjacent spins. As a consequence, structures of (a) and (c) are energetically degenerate which also takes effect for (b) and (d).

In a homogeneous spin spiral without SOC, every atom of the spin structure is equivalent because the absolute value of the magnetic moment is constant. That means that an atom at position $\mathbf{R}_i$ has the exact same surrounding as the atom at $\mathbf{R}_{i+1}$. Therefore, taking the scalar-relativistic approximated Hamiltonian, $\mathcal{H}_{\mathrm{SCA}}$ in

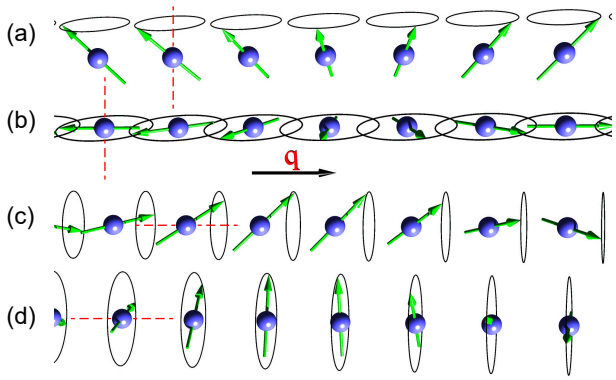

Figure 3.5 | Schematic representation of spin spiral states with different opening angle θ. (a) Conical spin spiral propagating along $\mathbf{q}$ with $\theta = \pi/4$. The purple spheres show the position of the atom and the green arrow the direction of its magnetic moment. The rotation axis (red dashed line) is perpendicular to $\mathbf{q}$. (b) Flat spin spiral with $\theta = \pi/2$. (c) Cycloidal spin spiral with $\theta = \pi/4$ and the rotation axis along $\mathbf{q}$. (d) Flat cycloidal spin spiral with $\theta = \pi/2$. The figure is taken from [68].

Eq. (2.26b) into account, only the *xc* field changes from atom to atom. A translation of the lattice can be described by a rotation in spin space where the scalar-relativistic Hamiltonian satisfies the condition

$$\mathcal{H}_{\mathrm{SCA}}(\mathbf{r}+\mathbf{R}_i) = U(\mathbf{q}\cdot\mathbf{R}_i)\mathcal{H}_{\mathrm{SCA}}(\mathbf{r})U^{\dagger}(\mathbf{q}\cdot\mathbf{R}_i) \tag{3.21}$$

The translational symmetry of the lattice is still valid. The rotation matrix of spin 1/2 can be chosen to point along z and thus the off-diagonal elements vanish. Note that this only can be done in the absence of SOC

$$U(\mathbf{q}\cdot\mathbf{R}_i) = \begin{pmatrix} e^{-i\varphi/2} & 0 \\ 0 & e^{i\varphi/2} \end{pmatrix} \tag{3.21a}$$

According to the Bloch theorem, the generalized Bloch theorem can be formulated where the eigenstates can be chosen so that

$$U(-\mathbf{q}\cdot\mathbf{R}_i)\psi(\mathbf{k},\mathbf{r}+\mathbf{R}_i) = e^{i\mathbf{k}\cdot\mathbf{R}_i}\psi(\mathbf{k},\mathbf{r}) \tag{3.22a}$$

Another representation of the generalized Bloch theorem is

$$\psi(\mathbf{k},\mathbf{r}) = \begin{pmatrix} e^{-i\mathbf{q}\cdot\mathbf{r}/2}u^{\uparrow}(\mathbf{k},\mathbf{r}) \\ e^{+i\mathbf{q}\cdot\mathbf{r}/2}u^{\downarrow}(\mathbf{k},\mathbf{r}) \end{pmatrix} \tag{3.22b}$$

Compared to the Bloch theorem, an additional phase factor occurs which is connected to the rotation around the z axis. The functions $u^{\uparrow}(\mathbf{k},\mathbf{r}), u^{\downarrow}(\mathbf{k},\mathbf{r})$ show translational periodicity, i.e. $u^{\uparrow}(\mathbf{k},\mathbf{r}) = u^{\uparrow}(\mathbf{k},\mathbf{r}+\mathbf{R}_i)$. This periodicity is a key aspect implementing spin spirals into FLAPW since it relies on planewaves and Fourier transforms.

3.7.4 First order perturbation theory: spin spirals including SOC

The generalized Bloch theorem is only valid when SOC is neglected. One possibility of calculating spin spirals with SOC is to fall back on large supercell structures which

depend on the spiral vector **q** and consequently the periodicity of the spin structure. Assuming that the SOC Hamiltonian, $\mathcal{H}_{\mathrm{SOC}}$ [Eq. (2.29)] holds just a small contribution compared to the scalar-relativistic Hamiltonian $\mathcal{H}_{\mathrm{SCA}}$,

$$\mathcal{H} = \mathcal{H}_{\mathrm{SCA}} + \mathcal{H}_{\mathrm{SOC}} \approx \mathcal{H}_{\mathrm{SCA}} \tag{3.23}$$

it is possible to apply first order perturbation to the unperturbed self-consistently calculated spin spiral states $|\psi_{k,\nu}\rangle$. Here, k, ν are the reciprocal Bloch vector and ν the band index. The energy shift $\delta\epsilon_{k\nu}$ of these states due to the SOC Hamiltonian can be written as

$$\delta\epsilon_{k\nu} = \langle\psi_{k,\nu}|\mathcal{H}_{\mathrm{SOC}}|\psi_{k,\nu}\rangle \tag{3.24}$$

whereas the energy correction represents the sum over all occupied states

$$\Delta E_{\mathrm{SOC}} = \sum_{k,\nu}^{\mathrm{occ}} \delta\epsilon_{k\nu} \tag{3.25}$$

For more information, see Ref. 91.

Chapter 4

Models of magnetism

The previously discussed method of density functional theory (DFT) calculations serves to find the ground state electron density as well as the subsequent properties of the calculated structures. Within total energy calculations, we can determine the energy of different magnetic states and therefore the possible ground state which has the lowest energy. However, using DFT calculations only gives rise to the (potential) magnetic ground state, whereas the reason for its formation often requires further understanding. In order to interpret the results of DFT calculations, we apply several models which are widely used for magnetic structures. In the following, the important models for this thesis are briefly presented.

4.1 Stoner model of magnetism

The occurrence of ferromagnetism in itinerant systems can be understood in terms of the Stoner model [92–94]. In spin DFT, the magnetization density $\mathbf{m}(\mathbf{r})$ is a small parameter compared to the electron density $n(\mathbf{r})$. The exchange correlation (xc) potential in local spin density approximation can be developed with respect to m/n and can be further approximated as

$$V_{xc}^{\pm}(\mathbf{r}) = V_{xc}^{0}(\mathbf{r}) \mp \mathbf{m}(\mathbf{r})\tilde{V}(n(\mathbf{r})) \tag{4.1}$$

The xc potential V_{xc}^{0} illustrates the non-magnetic case while higher orders in $\mathbf{m}(\mathbf{r})$ are neglected. The majority spins (+) are attracted and minority spins (−) are repelled compared to the non-magnetic case because the mean value of $\tilde{V} > 0$. In the Stoner model, this change in the potential is captured by the approximation

$$V_{xc}^{\pm}(\mathbf{r}) = V_{xc}^{0}(\mathbf{r}) \mp \frac{1}{2} IM \tag{4.2}$$

Here, M represents the local magnetic moment per atom, which is given as an integral of the magnetization density over the unit cell, in the case of the full potential linearized augmented planewave (FLAPW) method, the whole muffin tin (MT)

$$M = \int_{\mathrm{MT}} \mathbf{m}(\mathbf{r}) \mathrm{d}\mathbf{r} \tag{4.2a}$$

The exchange integral I is called Stoner parameter and replaces the term $\tilde{V}$. Compared to the non-magnetic case, a constant shift of the potential by $\mp\frac{1}{2}IM$ does not change

the wave function $\psi_i^{\pm}(\mathbf{r})$. The energy eigenvalues $\epsilon_i^{\pm}$ on the other hand will be increased or reduced by the potential

$$\psi_{k,\nu}^{\pm}(\mathbf{r}) = \psi_0(\mathbf{r}) \tag{4.3a}$$

The indices k, ν represent the wave vector and the band index, respectively.

$$\epsilon_{k,\nu}^{\pm} = \epsilon_{k,\nu,0} \mp \frac{1}{2} IM \tag{4.3b}$$

The shift in Eq. (4.3b) leads to a constant shift of the spin-resolved bandstructure. Compared to the non-magnetic local density of states (LDOS) $n^0(E)$, the same shift appears for $n^{\pm}(E)$ which is also called exchange splitting

$$n^{\pm}(E) = \sum_{\nu} \int_{\mathrm{BZ}} \delta\left(E - \epsilon_{k,\nu}^{\pm}\right) \mathrm{d}^3k = n^0(E \pm \frac{1}{2} IM) \tag{4.4}$$

Here, the integral is applied over the whole Brillouin zone (BZ). Integrating Eq. (4.4) for all occupied states, the number of electrons N and the magnetic moment M per unit cell is given by

$$N = \int_{\mathrm{occ}} \left[n^0(E + \frac{1}{2} IM) + n^0(E - \frac{1}{2} IM) \right] \mathrm{d}E \tag{4.5a}$$

$$M = \int_{\mathrm{occ}} \left[n^0(E + \frac{1}{2} IM) - n^0(E - \frac{1}{2} IM) \right] \mathrm{d}E \tag{4.5b}$$

In order to determine the Fermi energy, Eq. (4.5a) can be applied assuming charge neutrality. When $n^0(E)$, N is known and the Fermi energy is defined as $E_{\mathrm{F}} = E_{\mathrm{F}}(M)$. The solution of the magnetic moment M gets a non-linear equation which has to be solved self-consistently

$$M = F(M) = \int_{E<E_{\mathrm{F}}} \left[n^0(E + \frac{1}{2} IM) - n^0(E - \frac{1}{2} IM) \right] \mathrm{d}E \tag{4.6}$$

The function $F(M)$ satisfies the following conditions when $n^0(E) > 0$ is taken into account

$$\begin{aligned} F(M) &= -F(-M) \qquad & F(0) &= 0 \\ F(\pm\infty) &= \pm M_\infty \qquad & F'(M) &> 0 \end{aligned} \tag{4.7}$$

Here, M_∞ is the saturation magnetization for the case of full spin-polarization, meaning that all majority spin states are occupied and all minority states are

unoccupied. According to Hund's rule, the magnetic moment gets largest. Taking Eq. (4.6), its derivative

$$\begin{aligned} F'(M) = \frac{1}{2}\left[n^0(E+\frac{1}{2}IM) + n^0(E-\frac{1}{2}IM)\right] \\ + \left[n^0(E+\frac{1}{2}IM) - n^0(E-\frac{1}{2}IM)\right]\frac{\mathrm{d}E_\mathrm{F}}{\mathrm{d}M} \quad \overset{M=0}{\Longrightarrow} \quad F'(0) = In^0(E_\mathrm{F}) \end{aligned} \tag{4.8}$$

From that, the Stoner criterion for a formation of a ferromagnetic state is given by

$$In^0(E_\mathrm{F}) > 1 \tag{4.9}$$

For a large exchange Integral I and a large non-magnetic LDOS at the Fermi energy, $n^0(E_\mathrm{F})$, the ferromagnetic phase is more stable than the paramagnetic one.

For d bands in transition metals (TMs), the LDOS is approximately proportional to the inverse of the bandwidth. Consequently, a reduced band width strengthens the magnetic ground state. In the single-atom limit, the bandwidth is zero and thus, for atoms, the Stoner criterion is fulfilled. In bulk materials, this holds true for Fe, Co and Ni. On the other hand, reducing the bandwidth due to a reduced coordination number, e.g. at a surface, even non-magnetic bulk elements can exhibit a magnetic moment. This especially can be seen for elements with large spin susceptibility such as Rh.

4.2 Tersoff-Hamann model

Throughout this thesis, different comparisons will be drawn between our theoretical description and experimental observations made either at the University of Hamburg or Würzburg. All presented measurements are carried out with scanning tunnelling microscopes (STMs) [95, 96] and in order to compare the results with theory, a theoretical model for the STM is needed. A STM consists of a probe tip attached to a piezoelectric element which can contract or expand in three-dimensional (3D), x, y, z due to an applied voltage. This allows for a movement of the tip. The tip is moved along the measured surface without touching it and hence, the flowing current I is weak and can only be explained by the quantum mechanical effect of the tunnelling mechanism through the vacuum [97].

An electron with a kinetic energy E_kin can tunnel through a barrier with a higher potential $V_\mathrm{vac} > E_\mathrm{kin}$, where the barrier is formed by the vacuum. The wave function $\psi(z)$ of the electrons decays exponentially as

$$\psi(z) \propto \mathrm{e}^{-\kappa z} \tag{4.10}$$

The decay constant κ depends on the electron mass m and the energy of the electronic

state E that takes part in the tunnelling process

$$\kappa = \sqrt{\frac{2m}{\hbar^2}|E|} \tag{4.10a}$$

Following the tunnelling Hamiltonian formalism of Bardeen [97], the tunnelling current I between the STM tip (denoted as T) and the sample (denoted as S) in the non-spin-polarized case is given by

$$I(V_{\text{bias}}, \mathbf{R}_{\text{T}}) = \frac{2\pi e}{\hbar} \sum_{\mu,\nu} \left[f\left(E_\mu^{\text{S}} - E_{\text{F}}^{\text{S}}\right) - f\left(E_\nu^{\text{T}} - E_{\text{F}}^{\text{T}}\right) \right] |M_{\mu,\nu}|^2 \delta\left(E_\mu^{\text{T}} - E_\nu^{\text{S}} - eV_{\text{bias}}\right) \tag{4.11}$$

The tunnel current is a function of the sample bias voltage V_{bias} and the position $\mathbf{R}_{\text{T}}$ of the tip. The function $f(E - E_{\text{F}})$ is the Fermi-Dirac function

$$f(E - E_{\text{F}}) = \frac{1}{1 + \mathrm{e}^{(E-E_{\text{F}})/k_{\text{B}}T}} \tag{4.11a}$$

Furthermore, E_{F}^{T}, E_{F}^{S} are the Fermi energies of the tip and sample, respectively, $M_{\mu,\nu}$ is the tunnelling matrix element between two states Ψ_μ^{S}, Ψ_ν^{T} of the sample and the tip. The eigenstates Ψ_μ, Ψ_ν are non-orthogonal and belong to different Hamiltonians. $E_{\mu/\nu}^{\text{T/S}}$ denote the energies of the states $\Psi_{\mu/\nu}^{\text{T/S}}$ in absence of the tunnelling. The δ function conserves the energy during the elastic tunnelling process.

Assuming a low bias voltage $V_{\text{bias}} \to 0$, low temperature, spherical tip shape with an approximated s wave function as well as a constant LDOS of the tip, Tersoff and Hamann [156] reduced the problem to

$$I(V_{\text{bias}}, \mathbf{R}_{\text{T}}) \propto eV_{\text{bias}} n^{\text{S}}(\mathbf{R}_{\text{T}}, E_{\text{F}}) \tag{4.12a}$$

Here, the LDOS of the sample at the Fermi energy which is defined as

$$n^{\text{S}}(\mathbf{R}_{\text{T}}, E_{\text{F}}) = \sum_\mu |\Psi_\mu(\mathbf{R}_{\text{T}})|^2 \delta(E_\mu^{\text{S}} - E_{\text{F}}) \tag{4.12b}$$

The differential conductance is then derived as

$$\frac{\mathrm{d}I}{\mathrm{d}V_{\text{bias}}} \propto en^{\text{S}}(\mathbf{R}_{\text{T}}, E_{\text{F}}) \tag{4.12c}$$

The consequence of the Tersoff-Hamann model is that STM images obtained in the constant current mode correspond to the sample LDOS at the position of the tip $\mathbf{R}_{\text{T}}$, i.e. in the vacuum and at the Fermi energy [Eq. (4.12a)]. The differential conductivity [Eq. (4.12c)] which can be measured by scanning tunnelling spectroscopy and is related to the LDOS of the sample.

Due to the approximation of s states in the STM tip, the description is not accurate enough when the tips consist of TMs showing electronic structure which is governed by d electrons at the Fermi energy. This is the case e.g. for W tips. To overcome this problem, an extension of the Tersoff-Hamann model for arbitrary tip orbitals was proposed [98–100].

In the spin-polarized case, the wave functions Ψ needs to be expressed as spinors [101–103]. Approximating the magnetic tip to be in collinear order, the spinor can be represented with respect to the magnetization axis $\mathbf{e}_M^{\hat{\mathrm{T}}}$.

$$\Psi_{\nu\uparrow}^{\mathrm{T}}(\mathbf{r}) = \psi_{\nu\uparrow}^{\mathrm{T}}(\mathbf{r})\begin{pmatrix}1\\0\end{pmatrix} \qquad \Psi_{\nu\downarrow}^{\mathrm{T}}(\mathbf{r}) = \psi_{\nu\downarrow}^{\mathrm{T}}(\mathbf{r})\begin{pmatrix}0\\1\end{pmatrix} \tag{4.13a}$$

The spin mixing due to non-collinearity can be taken into account by the spinor of the sample

$$\Psi_{\mu}^{\mathrm{S}} = \begin{pmatrix}\psi_{\mu\uparrow}^{\mathrm{S}}\\ \psi_{\mu\downarrow}^{\mathrm{S}}\end{pmatrix} \tag{4.13b}$$

For magnetic structures, the spin-polarized tunnelling current is decomposed into two parts, one non-magnetic and one magnetic part

$$I(V_{\mathrm{bias}}, \mathbf{R}_{\mathrm{T}}, \theta, \phi) \propto (n_{\mathrm{T}}\tilde{n}_{\mathrm{S}}(\mathbf{R}_{\mathrm{T}}, V_{\mathrm{bias}}) + \mathbf{m}_{\mathrm{T}}\tilde{\mathbf{m}}_{\mathrm{S}}(\mathbf{R}_{\mathrm{T}}, V_{\mathrm{bias}})) \tag{4.14a}$$

Here, $\tilde{n}_{\mathrm{S}}(\mathbf{R}_{\mathrm{T}}, V_{\mathrm{bias}}) = \tilde{n}_{\mathrm{S}}^{\uparrow}(\mathbf{R}_{\mathrm{T}}, V_{\mathrm{bias}}) + \tilde{n}_{\mathrm{S}}^{\downarrow}(\mathbf{R}_{\mathrm{T}}, V_{\mathrm{bias}})$ is the energy-integrated LDOS of the sample. $\tilde{\mathbf{m}}_{\mathrm{S}}(\mathbf{R}_{\mathrm{T}}, V_{\mathrm{bias}})$ is the correspondent vector the integrated spin-polarized LDOS. These are defined as

$$\tilde{n}_{\mathrm{S}}^{\sigma}(\mathbf{R}_{\mathrm{T}}, V_{\mathrm{bias}}) = \int g_{V,T}(E) n_{\mathrm{S}}^{\sigma}(\mathbf{R}_{\mathrm{T}}, E)\mathrm{d}E \tag{4.14b}$$

$$\tilde{\mathbf{m}}_{\mathrm{S}}(\mathbf{R}_{\mathrm{T}}, V_{\mathrm{bias}}) = \int g_{V,T}(E) \sum_{\mu} \delta(E_{\mu} - E)\Psi_{\mu}^{\dagger}(\mathbf{R}_{\mathrm{T}})\sigma\Psi_{\mu}(\mathbf{R}_{\mathrm{T}})\mathrm{d}E \tag{4.14c}$$

Here, σ is the Pauli spin matrix and the function $g_{V,T}(E)$ is introduced with f being the Fermi distribution function. It ensures a smearing of the integral limits due to elevated temperatures. The magnetization vector of the tip is $\mathbf{m}_{\mathrm{T}} = m_{\mathrm{T}}(\cos\phi\sin\theta, \sin\phi\sin\theta, \cos\theta)$. The differential conductivity can be written as

$$\frac{\mathrm{d}I}{\mathrm{d}V_{\mathrm{bias}}} \propto n_{\mathrm{T}} n_{\mathrm{S}}\left(\mathbf{R}_{\mathrm{T}}, E_{\mathrm{F}} + eV_{\mathrm{bias}}\right) + \mathbf{m}_{\mathrm{T}}\mathbf{m}_{\mathrm{S}}\left(\mathbf{R}_{\mathrm{T}}, E_{\mathrm{F}} + V_{\mathrm{bias}}\right) \tag{4.14d}$$

Therefore, $\mathrm{d}I/\mathrm{d}U$ spectra are directly proportional to the LDOS of the sample at $E_{\mathrm{F}} + eV_{\mathrm{bias}}$.

4.3 Atomistic spin model

In order to describe the magnetic properties in the investigated ultrathin films, we make use of model Hamiltonians which contains several magnetic interactions. Those interactions are known to contribute to the magnetic ground states in solids. Therefore, the results of the obtained DFT calculations are interpreted within the model Hamiltonians which in our case is the extended classical Heisenberg model. We map total energy DFT calculations to an atomistic spin model [104]. This approximation can only be done because the itinerant magnetism is described by d electrons which are strongly localized at a lattice site i. Further, the magnetic moments in the systems are large and do not vary much in magnitude when changing the direction of neighbouring magnetic moments. The magnetic moment (on the order of $2-3\,\mu_B$ and in the following also denoted as spin) of an atom at lattice site i is then treated as a classical vector with the assumption that all spins have the same magnitude.

$$\mathbf{M}_i = M^2 \qquad \text{for all } i \tag{4.15}$$

We show in various test calculations that this approximation is reasonably well fulfilled (see Secs. Test calculations in the end of the respective chapter). Depending on the complexity of the studied system, we use different extensions of the classical Heisenberg model. These will be briefly discussed in the following.

4.3.1 Exchange interaction

The largest energy contribution typically stems from the Heisenberg exchange interaction which occurs regardless of spin-orbit coupling (SOC). Starting from the Hubbard model [105], there are two contributions to the Hamiltonian which describe the hopping of electrons t between adjacent lattice sites and the Coulomb interaction due to on-site repulsion of the electrons U. Within a perturbed approach in second order $U >> t$ for spin $\pm\frac{1}{2}$ particles [106], the exchange interaction can be derived as

$$\mathcal{H}_{\text{Exc}} = -\sum_{i,j} J_{ij}\left(\mathbf{m}_i \cdot \mathbf{m}_j\right) \tag{4.16}$$

Here, J_{ij} denotes the Heisenberg exchange integral between two spins $\mathbf{m}_i, \mathbf{m}_j$, where $\mathbf{m}_{i,j} = \mathbf{M}_{i,j}/M_{i,j}$. $J_{ij} > 0$ denotes a ferromagnetic (FM) and $J_{ij} < 0$ antiferromagnetic (AFM) alignment between the two spins, which is illustrated in Fig. 4.1 (a). In itinerant systems, the exchange integral follows the characteristics of the Ruderman-Kittel-Kasuya-Yoshida (RKKY) interaction [107–109]. It describes the coupling of localized magnetic moments within indirect exchange through the conducting electrons.

In complex magnetic structures, the exchange can be frustrated due to RKKY and the exchange beyond nearest neighbours J_1 needs to be taken into account, $J_2, J_3, J_4, \ldots$.

Considering $J_1 > 0$ (FM) and an AFM next nearest neighbour interaction $J_2 < 0$ with a comparable strength as J_1, a collinear alignment cannot satisfy this condition [third sketch in Fig. 4.1 (a)]. Spin spirals are the general solution of the classical Heisenberg model on a periodic lattice and hence, a spin spiral state can form due to exchange frustration [sketch on the right in Fig. 4.1 (a)]. Here, the threshold for FM (AFM) alignment is a canting angle below (above) 90° between two spins. Note that due to the scalar product in Eq. (4.16), the rotation direction of the spin spiral is unclear since without SOC, left and right rotating states are energetically degenerate.

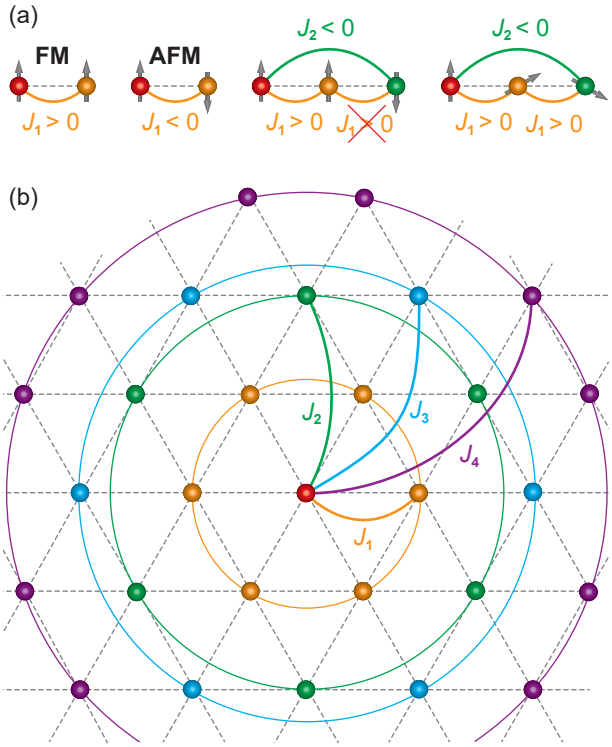

Figure 4.1 | Illustration of the exchange interaction. (a) One-dimensional chain illustrating the exchange interaction between nearest neighbours $J_1 > 0$ for ferromagnetic (FM) and $J_1 < 0$ for antiferromagnetic (AFM) configurations $J_1 < 0$. The effect of frustration is illustrated when the second neighbour is taken into account. Considering a FM alignment between adjacent spins $J_1 > 0$ and AFM alignment for next nearest neighbouring spins $J_2 < 0$ with comparable strength, one condition can not be satisfied (denoted as red cross). As a solution, a spiral can form due to exchange frustration, where the threshold for FM (AFM) alignment is a canting angle below (above) 90° between two spins. (b) Illustration of isotropic exchange interaction on a two-dimensional hexagonal lattice. Spins with the same distance from the centred atom are interacting with the same exchange constant.

The exchange is isotropic, i.e. $J_{ij} \to J_i$. Considering a hexagonal lattice, every neighbour within the same distance from the centring atom is treated with the same exchange integral [Fig. 4.1 (b)]. This is illustrated as coloured rings through the respective neighbours of the lattice.

Since the magnetism is investigated on a periodic lattice, the Heisenberg Hamiltonian can be represented as sum of its discrete Fourier components

$$\mathcal{H}_{\mathrm{Exc}} = -NM^2 J(\mathbf{q}) \tag{4.17}$$

Here, N are the number of lattice sites at $\mathbf{R}_i$ the exchange integral is given as Fourier

component

$$J(\mathbf{q}) = \sum_{\delta} J_{\delta} \mathrm{e}^{-i\mathbf{q}\mathbf{R}_{\delta}} \tag{4.17a}$$

The distance is $\mathbf{R}_{\delta} = \mathbf{R}_j - \mathbf{R}_i$. The vector $\mathbf{q}$ represents the spin spiral vector in reciprocal space as introduced in Sec. (3.7.3). The general solutions of the Heisenberg model for exchange on a periodic Bravais lattice are those spin spirals, given by

$$\mathbf{M}_i = 2\Big(\mathbf{R}_{\mathbf{Q}} \cos(\mathbf{Q}\cdot\mathbf{R}_i) - \mathbf{I}_{\mathbf{Q}} \sin(\mathbf{Q}\cdot\mathbf{R}_i)\Big) \tag{4.18}$$

In the absence of SOC, the solutions are helical or cycloidal spin structures and thus the real and imaginary part of the spin $\mathbf{R}_{\mathbf{Q}}, \mathbf{I}_{\mathbf{Q}}$ can be seen as vectors spanning the xy plane [68]. This is the case for flat spin spirals with an opening angle of $\theta = 90°$. That is why, in the thesis we determine the energy dispersions $E(\mathbf{q})$ for flat cycloidal spin spirals without SOC and map the Heisenberg model on the DFT results to determine the exchange constants J_{ij}.

4.3.2 Higher order exchange interaction

In some itinerant magnetic systems, the pair-wise exchange interaction of the Heisenberg model fails to capture the correct magnetic ground state. The reason is found in the strongly localized spin model. In the Heisenberg model, neglecting SOC, spin spiral states (also denoted as single-Q state) and superpositions of different spin spiral states (also denoted as multi-Q states) are energetically degenerate. An example is given in Fig. 4.2 (a) for the up-up-down-down (uudd or ↑↑↓↓). Consequently, an energy difference between those states found e.g. from DFT calculations cannot be explained by the Heisenberg exchange. Going beyond the second order perturbation theory of the Hubbard model, so-called higher order exchange interactions (HOIs) occur. Applying the fourth order perturbation to the Hubbard model for spin 1/2 particles for $\frac{t}{U} << 1$ terms occur which typically are one order of magnitude in strength smaller than the exchange.

Biquadratic interaction The biquadratic exchange interaction describes the hopping between two lattice sites as $i \to j \to i \to j \to i$ [Fig. 4.2 (b)]. The Hamiltonian of the biquadratic term is given by

$$\mathcal{H}_{\mathrm{Biq}} = -\sum_{i,j} \mathbf{B}_{ij} \Big(\mathbf{m}_i \cdot \mathbf{m}_j\Big)^2 \tag{4.19}$$

Corresponding to the exchange parameter J_{ij}, the biquadratic exchange parameter B_{ij} determines the strength of the isotropic coupling.

Four-spin four-site interaction The second term from fourth order perturbation describes the hopping of electrons between four lattice sites $i \to j \to k \to l \to i$. In the sketch [light red rhombs in Fig. 4.2 (b)], two different possible paths are shown for

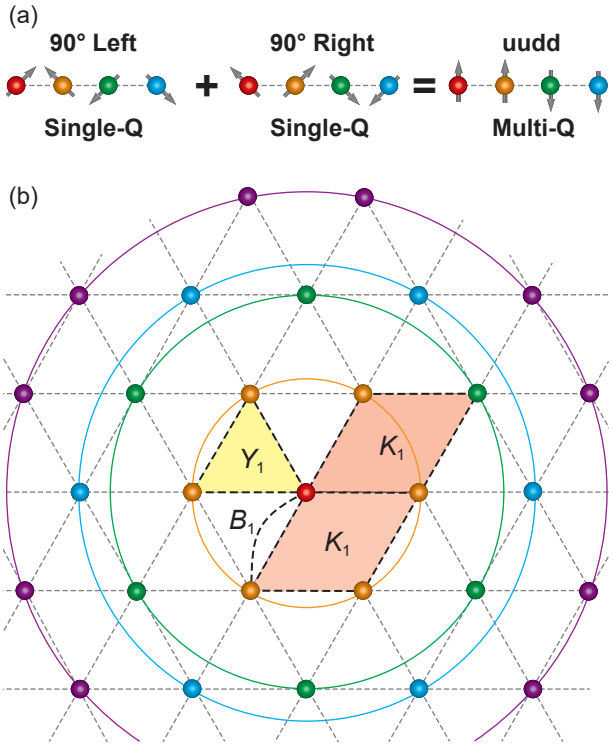

Figure 4.2 | Illustration of higher order exchange interactions (HOIs). (a) Construction of an up-up-down-down (uudd, Multi-Q) state due to superpositions of one left and one right rotating spin spiral (Single-Q) state. An energy difference between single-Q and multi-Q states can only be explained due to the presence of HOIs. (b) Minimal hopping paths (dashed black lines) for the biquadratic interaction B_1, three-site four-spin term Y_1 and four-site four-spin term K_1 of the HOIs. The coloured areas for the paths emphasize the path where for Y_1 six areas and for K_1 twelve possibilities occur. For the latter two possible paths are shown.

this hopping. Each rhomb therefore has six possibilities with respect to the reference atoms. With the four-spin four-site exchange parameter K_{ijkl}, the Hamiltonian is given by

$$\mathcal{H}_{\text{4-site}} = -\sum_{i,j,k,l} K_{ijkl}\Big[(\mathbf{m}_i\cdot\mathbf{m}_j)(\mathbf{m}_k\cdot\mathbf{m}_l)+(\mathbf{m}_i\cdot\mathbf{m}_l)(\mathbf{m}_j\cdot\mathbf{m}_k)-(\mathbf{m}_i\cdot\mathbf{m}_k)(\mathbf{m}_j\cdot\mathbf{m}_l)\Big] \quad (4.20)$$

Four-spin three-site interaction Recently, it has been proposed to take systems with a higher spin $S \geq 1$ into account in the model [45, 110]. Considering the fourth order perturbation theory of a multi-band Hubbard model as presented previously, an additional term, the four-spin three-site interaction occurs. Consistent with its four-site equivalent, it describes the hopping between three lattice sites $i \to j \to k \to i$. In the case of the hexagonal lattice, the shape of the path is an equilateral triangle [Fig. 4.2 (b)]. Its Hamiltonian including Y_{ijk} evaluating the strength of the three-site four-spin interaction is given by

$$\mathcal{H}_{\text{3-site}} = -\sum_{i,j,k} Y_{ijk}\Big[(\mathbf{m}_i\cdot\mathbf{m}_j)(\mathbf{m}_j\cdot\mathbf{m}_k)+(\mathbf{m}_k\cdot\mathbf{m}_j)(\mathbf{m}_j\cdot\mathbf{m}_i)\Big] \quad (4.21)$$

4.3.3 Dzyaloshinskii-Moriya interaction

The previously described interactions do not take SOC into account. The SOC couples the spin structure to the underlying lattice. When both SOC and lack of inversion symmetry occurs in a magnetic film – which is the case for our investigated systems

due the presence of interfaces and surfaces – the antisymmetric exchange interaction, known as Dzyaloshinskii-Moriya interaction (DMI) arises [111, 112]. The interaction of two spins mediated by the conduction electrons of the TM gives rise to the DMI. Dependent on their spin direction, the conduction electrons are scattered in the presence of SOC. According to Dzyaloshinskii [111] this mechanism is represented by the cross product between the two spins and modulated by the vector **D** so that

$$\mathcal{H}_{\mathrm{DMI}} = -\sum_{i,j} \mathbf{D}_{ij} \cdot (\mathbf{m}_i \times \mathbf{m}_j) \tag{4.22}$$

Here, the Dzyaloshinskii-Moriya vector $\mathbf{D}_{ij}$ represents the strength and the direction of the DMI which depends on the symmetry of the present system [113]. The DMI strongly depends on hybridization of a magnetic element with two adjacent non-magnetic atoms with a large SOC as shown in Fig. 4.3. The cross product in Eq. (4.22) implies that canted structures are preferred by the DMI which have a certain chirality depending on the sign of the vector $\mathbf{D}_{ij}$. Note that e.g. left and right rotating spin spiral states are energetically degenerate within the Heisenberg exchange. Including SOC, this degeneracy is lifted by the DMI.

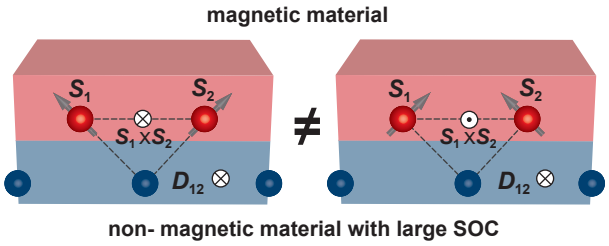

Figure 4.3 | Illustration of Dzyaloshinskii-Moriya interaction (DMI). In the Levy-Fert model [114], a magnetic thin film interacts with a non-magnetic substrate with large spin-orbit coupling (SOC) where due to the lack of inversion symmetry, the DMI can form preferring a canting between two spins within a certain rotation direction.

For thin magnetic films which interact with heavy metal substrates (Fig. 4.3), the direction of $\mathbf{D}_{ij}$ can be approximated by the rule of Levy and Fert [114] as

$$\mathbf{D}_{ij} = D \frac{\sum_k \mathbf{R}_{ki} \times \mathbf{R}_{kj}}{|\sum_k \mathbf{R}_{ki} \times \mathbf{R}_{kj}|} \tag{4.23}$$

Here, i, j denote the position of the magnetic atoms and k the position of the non-magnetic element and $\mathbf{R}_{ki}$ the vector between the non-magnetic atom and spin i.

4.3.4 Magnetocrystalline anisotropy

Up to now, the presented interactions couple the spins to each other. However, in the presence of SOC, the spins also couple to the underlying lattice. Magnetic materials typically show anisotropic behaviour so that a certain direction of the spin quantization axis is preferred. The responsible interaction which favours the direction of spins to be either perpendicular to the film plane (out-of-plane) or

parallel to the film plane (in-plane) is the magnetocrystalline anisotropy energy (MAE).

It is defined as

$$\mathcal{H}_{\text{Ani}} = \sum_i \mathbf{m}_i \cdot \mathbf{K}_i \cdot \mathbf{m}_i \tag{4.24}$$

Here, $\mathbf{K}_i$ is the tensor of anisotropy denoting the strength of the anisotropy as well as the direction of minimal energy. Considering perfect ultrathin films, all components can be approximated as zero due to the surfaces where one term is left

$$K_i^{zz} = K\delta^{zz} \tag{4.24a}$$

This can be denoted as uniaxial anisotropy where the energy contribution, the MAE is

$$E_{\text{MAE}} = -\mathbf{m}_i^2 K_{\text{Ani}} \cos^2\theta \tag{4.24b}$$

Here, θ is the angle between the magnetization direction and the normal vector of the film plane.

The uniaxial anisotropy constant K_{Ani} (in the following denoted as K) holds two contributions stemming from the dipolar interaction and from SOC. In ultrathin films, the dipolar contribution to the shape anisotropy, typically can be neglected since the SOC contribution is larger. The shape anisotropy stems from the demagnetizing energy which is associated with the shape of the sample [115]. The shape anisotropy prefers an in-plane direction and is defined as

$$E_{\text{shape}} = -\frac{1}{2}\mu_0 M^2 \cos^2\theta \tag{4.25}$$

In our investigations, the determined value of K does not consider the shape.

4.3.5 Dipole-dipole interaction

Compared to the interactions described above which are based on quantum-mechanical effects, the classical magneto-static interaction has a very small energy contribution. Typically, the dipole-dipole interaction can be neglected in ultrathin film systems. However, as we will show in Ch. 10, due to the presence of large frustration of the above mentioned interactions, such small energies can be decisive. While the exchange interaction is localized (Sec. 4.3.1), the dipolar interaction is long-ranged and decays with $\propto 1/R^3$.

Describing the interaction between two magnetic moments $\mu_i = \mu\mathbf{m}_i$, the dipole-dipole

interaction is defined as

$$\mathcal{H}_{\text{dip}} = -\frac{\mu^2}{4\pi\mu_0} \sum_{ij}^{N} \frac{3(\mathbf{R}_{ij}\cdot\mathbf{m}_i)(\mathbf{R}_{ij}\cdot\mathbf{m}_j) - (\mathbf{m}_i\cdot\mathbf{m}_j)R_{ij}^2}{R_{ij}^5} \tag{4.26}$$

Here, $\mathbf{R}_{ij}$ is the vector connecting the spins $\mathbf{m}_i, \mathbf{m}_j$. The summation is performed over all pair interactions of the magnetic moments.

4.3.6 Anisotropic symmetric exchange interaction

Similar to the dipolar interaction, another anisotropy term is typically neglected in ultrathin films. The anisotropic symmetric exchange (ASE) can be seen as a relativistic generalization of the RKKY interaction [116, 117]. When relativistic effects are acting on a similar energy scale as the spin-polarization, a two-site interaction will appear which couples two spin orientations to a certain direction in real space. The ASE has a dipolar form, but originates from SOC. Therefore, it is also referred to as pseudo-dipolar interaction. The Hamiltonian is defined with $\mathbf{R}_{ij}$ being the vector pointing from $\mathbf{m}_i$ to $\mathbf{m}_j$ and J_{ij}^{ASE} giving the strength of the ASE

$$\mathcal{H}_{\text{ASE}} = -\sum_{i,j} J_{ij}^{\text{ASE}}(\mathbf{m}_i\cdot\mathbf{R}_{ij})(\mathbf{m}_j\cdot\mathbf{R}_{ij}) \tag{4.27}$$

The energy due to the ASE typically is one order of magnitude smaller than the MAE.

4.3.7 The atomistic spin model

The magnetic interactions introduced previously can contribute to the spin model in order to describe the magnetism of a system. In strongly FM systems, it appeared to be sufficient using the Hamiltonian consisting of exchange, DMI and MAE within considering the interactions to act between nearest neighbours. We denote this as nearest neighbour approximation. There, the resulting interaction parameters are called J_{eff}, D_{eff} and K and the model is written as

$$\mathcal{H}_{\text{eff}} = -\sum_{\substack{i,j \\ \text{NN}}} J_{\text{eff}}(\mathbf{m}_i\cdot\mathbf{m}_j) - \sum_{\substack{i,j \\ \text{NN}}} \mathbf{D}_{\text{eff}}(\mathbf{m}_i\times\mathbf{m}_j) - \sum_i K(m_i^z)^2 \tag{4.28a}$$

For more complex magnetic systems, it is necessary to take frustration effects of exchange and DMI into account which is captured by the atomistic spin model beyond nearest neighbours. With the interaction parameters $J_{ij}, \mathbf{D}_{ij}$ and K, the atomistic spin Hamiltonian is given by

$$\mathcal{H}_{\text{atomistic}} = -\sum_{i,j} J_{ij}(\mathbf{m}_i\cdot\mathbf{m}_j) - \sum_{i,j} \mathbf{D}_{ij}(\mathbf{m}_i\times\mathbf{m}_j) - \sum_i K(m_i^z)^2 \tag{4.28b}$$

Considering the occurrence of multi-Q states to have different energies than their single-Q corresponding states, the model Hamiltonian needs to be extended with HOIs

$$\begin{aligned}\mathcal{H}_{\text{atomistic + HOI}} = &-\sum_{i,j} J_{ij}(\mathbf{m}_i \cdot \mathbf{m}_j) - \sum_{i,j} \mathbf{D}_{ij}(\mathbf{m}_i \times \mathbf{m}_j) - \sum_i K(m_i^z)^2 \\ &- \sum_{\substack{i,j \\ \text{NN}}} \mathbf{B}_{ij}\left(\mathbf{m}_i \cdot \mathbf{m}_j\right)^2 \\ &- \sum_{\substack{i,j,k,l \\ \text{NN}}} K_{ijkl}\Big[(\mathbf{m}_i \cdot \mathbf{m}_j)(\mathbf{m}_k \cdot \mathbf{m}_l) + (\mathbf{m}_i \cdot \mathbf{m}_l)(\mathbf{m}_j \cdot \mathbf{m}_k) - (\mathbf{m}_i \cdot \mathbf{m}_k)(\mathbf{m}_j \cdot \mathbf{m}_l)\Big] \\ &- \sum_{\substack{i,j,k \\ \text{NN}}} Y_{ijk}\Big[(\mathbf{m}_i \cdot \mathbf{m}_j)(\mathbf{m}_j \cdot \mathbf{m}_k) + (\mathbf{m}_k \cdot \mathbf{m}_j)(\mathbf{m}_j \cdot \mathbf{m}_i)\Big] \\ &- \frac{\mu^2}{4\pi\mu_0} \sum_{ij}^{N} \frac{3(\mathbf{R}_{ij} \cdot \mathbf{m}_i)(\mathbf{R}_{ij} \cdot \mathbf{m}_j) - (\mathbf{m}_i \cdot \mathbf{m}_j)R_{ij}^2}{R_{ij}^5} \\ &- \sum_{i,j} J_{ij}^{\text{ASE}}(\mathbf{m}_i \cdot \mathbf{R}_{ij})(\mathbf{m}_j \cdot \mathbf{R}_{ij})\end{aligned} \tag{4.28c}$$

Here, the HOIs are considered to act along the path of minimal energy, for B_1, K_1, Y_1, respectively, i.e. within the nearest neighbour approximation (cf. Fig. 4.2).

4.4 Investigation of non-symmetric magnetic states

Due to the introduced Hamiltonian of the spin model, it is possible to interpret the magnetism beyond the results of the DFT calculations. The determined interaction parameters[1] can be used for further simulations. In this thesis, we applied atomistic spindynamics simulations calculating the energy costs of domain walls, skyrmions or antiskyrmions. With the geodesic nudged elastic band (GNEB) method, the energy barrier of such states can be estimated preventing a transition into a different state. The two methods will be discussed in the following on a basic level. More detailed information can be found e.g. in Ref. 104.

4.4.1 Atomistic spindynamics

The energy differences between two different magnetic states is found by solving the Landau-Lifshitz equation of spindynamics

$$\hbar \frac{\mathrm{d}\mathbf{m}_i}{\mathrm{d}t} = \frac{\partial \mathcal{H}}{\partial \mathbf{m}_i} \times \mathbf{m}_i - \alpha \left(\frac{\partial \mathcal{H}}{\partial \mathbf{m}_i} \times \mathbf{m}_i \right) \times \mathbf{m}_i \tag{4.29}$$

Here, $\mathbf{m}_i$ is a single spin with a normalization to one, α the damping constant and $\mathcal{H}$ the

[1] E.g. strengths of Heisenberg exchange, DMI, MAE, …

model Hamiltonian introduced previously (Sec. 4.3). The first term on the right side is dedicated to the precession stemming from the interaction of a magnetic moment with an effective magnetic torque field $\mathbf{B}_{\text{eff}} = {}^{\partial\mathcal{H}}/_{\partial\mathbf{m}_i}$. Here, $\mathbf{B}_{\text{eff}}$ occurs due to the magnetic interaction of the model Hamiltonian $\mathcal{H}$ and has the physical meaning of an equivalent external magnetic field. A magnetic moment with an arbitrary direction therefore will precess around the effective field [Fig. 4.4].

The second term on the right side is the so-called damping term and is proportional to $\mathcal{H}$. A precessing magnetic moment will minimize its energy by aligning within the direction of an external magnetic field (or here, the effective field) – the damping term captures this phenomenon. It can further been drawn back to relativistic effects of the spin-orbit coupling [118]. The Landau-Lifshitz equation needs to be applied for N interacting spins and represents a non-linear problem which is solved numerically.

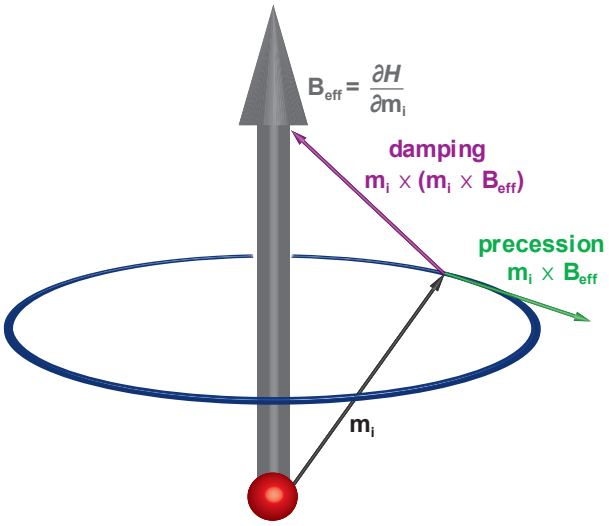

Figure 4.4 | Illustration of a spin interacting with an effective magnetic field. Due to an effective magnetic field $\mathbf{B}_{\text{eff}}$, the spin $\mathbf{m}_i$ performs a precession around the field (blue circle). Due to relativistic effects, the spin will align in the same direction as the effective field (damping).

4.4.2 Geodesic Nudged Elastic Band Method

Further insight into the magnetic properties of the complex spin structures can be gained performing GNEB calculations [119]. When a metastable state in a local minimum occurs, the spontaneous collapse into another minimum (global or local) is prevented by an energy barrier between the two states. The GNEB presents a tool for finding the lowest energy barrier between two states on an arbitrary energy landscape (Fig. 4.5).

Considering the state A to be a metastable state and B as another local or global minimum, a geodesic path in between the two states is generated. The path consists of a chain with discrete representations of the spin system, called images. At each image, an effective field is calculated where the components along a local tangent to the path is replaced by an artificial spring force F. This force between two images ensures a uniform distribution of images along the geodesic path.

The perpendicular component of the effective field $-\nabla E_{\perp}$ is locally minimized for every image and the geodesic path is brought step-by-step into the MEP which is given by

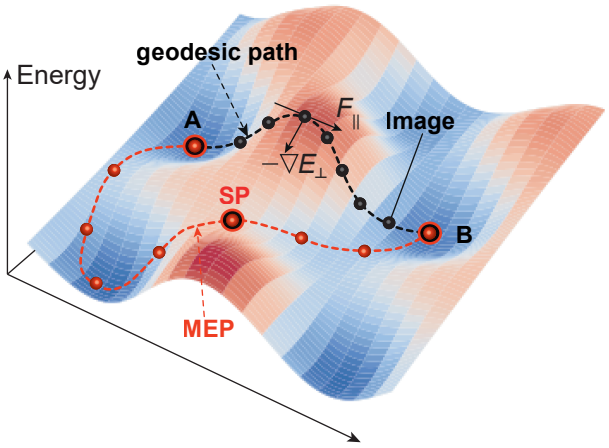

Figure 4.5 | Illustration of the geodesic nudged elastic band (GNEB) method. A geodesic path with discrete images from a metastable state A (local minimum) is generated to another minimum state B. Applying the GNEB method, the path is successively brought into the minimum energy path (MEP) by minimizing the energy gradient $-\nabla E_{\perp}$ for each image. The image with the largest energy between state A and B defines the saddle point (SP), where the artificial spring force $F_{\parallel}$ ensures a uniform distribution of images along the path.

the relaxed positions of the images. Taking the maximum value of the MEP, the SP energy is found. Since an image does not necessarily holds the exact position of the SP, the climbing image technique [120, 121] is applied to accurately describe the position of the SP and consequently an accurate value for the energy barrier.

Part II

Non-collinear spin structures in ferromagnetic Cobalt

Chapter 5

Domain walls and Dzyaloshinskii-Moriya interaction in Co/Ir(111) and Pt/Co/Ir(111)

Non-collinear spin structures such as domain walls (DWs) and skyrmions attract attention due to their promising properties for the field of spintronics [1, 3, 4, 13, 19]. The right choice of material is one of the key challenges in order to stabilize such spin structures. In the recent past, room temperature stable skyrmions have been observed in sputtered multilayer systems, where Co was used as magnetic material [35, 36, 39, 40]. Co is known as as strong ferromagnet (FM), i.e. the FM exchange interaction is dominant.

Due to hybridization with different elements, the exchange as well as other magnetic interactions can be tuned so that they compete with each other on the same energy scale. In this view, the Dzyaloshinskii-Moriya interaction (DMI) preferring non-collinear spin structures over collinear ones can help to stabilize DWs or skyrmions. It has been proposed that non-collinear spin structures with either a Co/Ir or a Co/Pt interfaces prefer opposite sense of rotations [122–124], i.e. have opposite signs of the DMI. When Co is sandwiched between Ir and Pt, this could lead to an enhancement of the total DMI, denoted as additive DMI as it has been proposed for magnetic multilayer systems [35, 125]. Controlling the DMI in such a simple form can open new approaches forming non-collinear spin structures. Even in systems with dominant FM exchange interaction, a specific increase of the DMI will affect the ground state. However, since the mechanism of additive DMI has not always been observed like in Co/Ir/Ni multilayers [126], this mechanism requires a deeper understanding.

In this chapter, we apply density functional theory (DFT) calculations to study the DMI in Pt/Co/Ir interfaces investigating the two ultrathin film systems Co/Ir(111) and Pt/Co/Ir(111). Although we find an increasing DMI from Co/Ir(111) to Pt/Co/Ir(111), simple additive effects from both interfaces can be excluded. In fact, with a Co monolayer (ML) sandwiched between Pt and Ir(111), the whole DMI contribution stems either from the Pt/Co or the Co/Ir interface and is strongly dependent on the stacking of Co and Pt. In specific stackings of Co and Pt, even a reduction of the DMI is observed from Co/Ir(111) to Pt/Co/Ir(111). To verify our results from DFT, we compare the calculations on Néel type DWs to spin-polarized

scanning tunnelling microscopy experiments performed at the University of Hamburg. Measurements are in good agreement with the presented calculations. We published our findings in Pub. I. While additive DMI does not occur in Co ML films, we show that with a second Co layer, i.e. in Pt/Co/Co/Ir(111), an increase of the total DMI can be explained by simply summing the two significant contributions from the Pt/Co and Co/Ir interfaces. Our results emphasize the importance of interface composition on complex interactions such as the DMI.

This chapter is structured as follows: In Sec. 5.1 – 5.3, the films of Co/Ir(111) and Pt/Co/Ir(111) are studied within DFT. Considering every stacking possibility of Co and Pt, i.e. $\mathrm{Co}_{\mathrm{fcc}}$, $\mathrm{Co}_{\mathrm{hcp}}$ as well as $\mathrm{Pt}_{\mathrm{fcc}}$ and $\mathrm{Pt}_{\mathrm{hcp}}$, we discuss the magnetic ground state properties within the effective nearest neighbour approximation. In Sec. 5.4, some experimental observations are presented and compared to the theoretical results. We complete the study by decomposing the role of additive DMI in Pt/Co/Ir interfaces (Sec. 5.6).

5.1 Computational details

For this study, we used the FLEUR code [47] with film geometry. We choose the equilibrium lattice parameter of bulk Ir $a_{\text{Ir-bulk}} = 7.22\,\text{a.u.}$, which was relaxed within the local density approximation (LDA) [127]. For the Co ML as well as the Pt/Co bilayer (BL), all possible stackings, i.e. $\mathrm{Co}_{\mathrm{fcc}}$, $\mathrm{Co}_{\mathrm{hcp}}$ as well as $\mathrm{Pt}_{\mathrm{fcc}}$ and $\mathrm{Pt}_{\mathrm{hcp}}$ are assumed[1]. For the following calculations, the muffin tin (MT) radii were set to $R^{\mathrm{MT}}_{\mathrm{Ir,\,Pt}} = 2.31\,\text{a.u.}$, $R^{\mathrm{MT}}_{\mathrm{Co}} = 2.26\,\text{a.u.}$ for Ir, Pt and Co, respectively. The energy cutoff was set to $k_{\max} = 4.0\,\text{a.u.}^{-1}$.

Structural relaxation The structural relaxations were performed in the FM state using a symmetric film with five layers of Ir(111) and a Co ML, Pt/Co BL, Pt/Co/Co trilayer (TL) or Pt/Pt/Co TL on both sides of the film. Fig. 5.1 (a) exemplary shows the setup for the relaxation of Co/Ir(111).

The forces between the uppermost layers were minimized in [111] direction up to a threshold of $10^{-5}\,\text{htr/a.u.}$ while three Ir layers in the middle are kept fixed at the bulk equilibrium lattice parameter (denoted as $d_{\text{Ir-bulk}}$ in Fig. 5.1). The resulting interlayer distances (denoted as $d_{12}, d_{23}, \ldots$) are presented in Tab. 5.1. For the structural relaxation, we applied 110 k points for Co/Ir(111), 240 k points for Pt/Co/Ir(111), Pt/Co/Co/Ir(111) and Pt/Pt/Co/Ir(111) in the irreducible wedge of the hexagonal two-dimensional (2D) Brillouin zone (BZ) as well as the generalized gradient approximation exchange correlation (xc) functional [73].

Spin spiral calculations Applying the interlayer distances of the structural relaxation, we self-consistently performed spin spiral calculations without spin-orbit coupling (SOC) using an asymmetric film with nine layers of Ir(111), [Fig. 5.1 (b) for Co/Ir(111)]. The vector $\mathbf{q}$ is chosen along the high symmetry directions $\overline{\Gamma}$-$\overline{M}$ and $\overline{\Gamma}$-$\overline{K}$

[1] Without specification of fcc/hcp, i.e. Pt/Co/Ir(111), we denote all stackings.

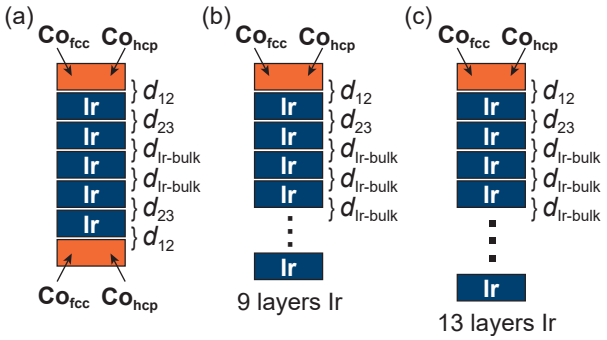

Figure 5.1 | Schematic structural setup for the DFT calculations for the exemplary system of Co/Ir(111). (a) Symmetric film setup for structural relaxations. The substrate is represented by five layers of Ir(111), where on both sides Co in fcc or hcp stacking is added. The Ir layers in the middle are kept fixed on the equilibrium lattice parameter $d_{\text{Ir-bulk}}$ while layers denoted with d_{12}, d_{23} are relaxed in the [111] direction. (b) Asymmetric film setup for spin spiral calculations using a substrate with nine layers of Ir. (c) Asymmetric film setup for calculations of magnetocrystalline anisotropy energy.

Table 5.1 | Relaxed interlayer distances d_{ij} (a.u.) for Co/Ir(111) and Pt/Co/Ir(111). The indices denote the respective layer in the film. The surface layer is denoted with 1, the subsurface layer with 2, etc. Note that for Co/Ir(111) the third and the fourth layers are kept fixed and $d_{34} = d_{45} = d_{\text{Ir-bulk}}$ (for Pt/Co/Ir(111) $d_{45} = d_{\text{Ir-bulk}}$).

System	d_{12}	d_{23}	d_{34}	d_{45}	$d_{\text{Ir-bulk}}$
Co_{fcc}/Ir(111)	4.01	4.37	–	–	4.17
Co_{hcp}/Ir(111)	3.91	4.25	–	–	4.17
Pt_{fcc}/Co_{fcc}/Ir(111)	4.09	3.97	4.35	–	4.17
Pt_{fcc}/Co_{hcp}/Ir(111)	4.11	3.98	4.35	–	4.17
Pt_{hcp}/Co_{fcc}/Ir(111)	4.09	3.97	4.37	–	4.17
Pt_{hcp}/Co_{hcp}/Ir(111)	4.09	3.97	4.35	–	4.17
$Pt_{fcc}/Pt_{fcc}/Co_{fcc}$/Ir(111)	4.75	4.05	3.99	4.35	4.17
$Pt_{fcc}/Co_{fcc}/Co_{fcc}$/Ir(111)	4.10	3.65	4.05	4.35	4.17

of the hexagonal 2D BZ. The energy contribution due to SOC, ΔE_{SOC}, is calculated in first-order perturbation theory for every previously calculated $\mathbf{q}$ point [91, 128, 129]. We restrict ourselves on the effective nearest neighbour approximation around the FM state ($\overline{\Gamma}$ point, $\mathbf{q} \to 0$) for evaluating the Heisenberg exchange interaction J and DMI constant D, labelled as J_{eff} and D_{eff} since the systems are strongly FM. For spin spiral calculations, we used the LDA [127] of the *xc* functional and 1936 k points in the full 2D BZ.

Magnetocrystalline anisotropy energy For the magnetocrystalline anisotropy energy (MAE), we first self-consistently converged an asymmetric film with 13 layers of Ir(111) for Co/Ir(111) and Pt_{fcc}/Co_{fcc}/Ir(111) (nine layers of Ir(111) for other Pt/Co/Ir(111) stackings) in the FM state in scalar-relativistic approximation. The calculational settings are the same as for the spin spiral calculations described above. The values of the MAE, K, are determined by applying the force theorem [80, 81],

where we applied the spin quantization axis with SOC perpendicular the film plane $E_\perp$ and parallel to the film plane $E_\parallel$. The resulting energy difference is determined as $K = E_\perp - E_\parallel$.

To see the effect of unphysical SOC contributions, different thicknesses of the Ir(111) substrate are considered and test calculations have been performed in which the SOC contribution is switched on for one MT after another. With this method it is possible to determine the SOC contribution of an element in the system (Fig. 5.2). For Co_{hcp}/Ir(111) with five Ir layers in an asymmetric film, the SOC contribution of each layer is very large and no convergence in MAE can be seen (dashed line with open squares in Fig. 5.2) . The fluctuation of these contributions decreases with a system of nine Ir layers (dashed lines with open diamonds). For Co/Ir(111) and Pt_{fcc}/Co_{fcc}/Ir(111)[2], we used calculations with 13 layers of Ir, since in the middle of the substrate, the SOC contributions of the Ir are almost constant and for evaluating K, we average the value of five different points as described in the graph. For other stacking possibilities of the Pt/Co BLs, we used a substrate with nine layers of Ir, since the differences between test calculations are smaller than 10 %.

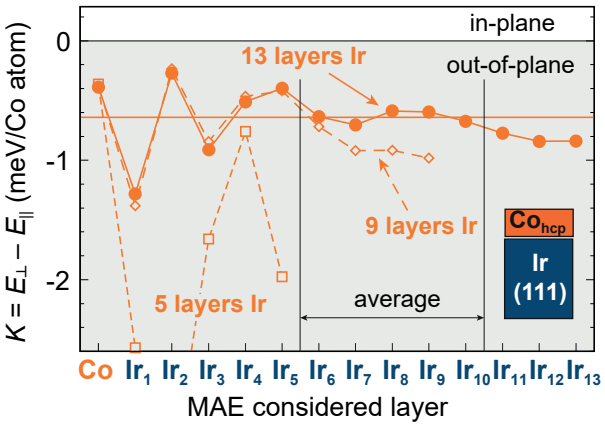

Figure 5.2 | Determination of magnetocrystalline anisotropy energy (MAE) in Co_{hcp}/Ir(111) from DFT calculations. The spin-orbit coupling (SOC) contribution is switched on in one muffin-tin after another to see the contribution to the MAE of every atom in the system. Three substrate thicknesses are considered: five, nine and 13 layers of Ir(111). For Co_{hcp}/Ir(111), the MAE is determined as an average value from calculations where the SOC contributions are in a constant region of the calculation with a 13 layered substrate.

Domain wall properties In order to compare the theoretical results with the experimental observation, we use the calculated values J_{eff}, D_{eff} and K and determine the DW energy $\Delta E_{\text{DW-FM}}$ between a DW and the FM state via

$$\Delta E_{\text{DW-FM}} = \frac{4}{a}\sqrt{2|J_{\text{eff}}K|} - \frac{2}{a}\pi\sqrt{3}|D_{\text{eff}}| \tag{5.1a}$$

The DW width w is defined as

$$w = 2a\sqrt{\frac{3J_{\text{eff}}}{2|K|}} \tag{5.1b}$$

Here a represents the in-plane Ir(111) lattice constant.

[2]Note that these films are compared to the experimental measurements.

5.2 FM ground state properties of Co/Ir(111)

In order to describe the magnetic ground state properties of Co/Ir(111), we present the energy dispersions $E(\mathbf{q})$ of flat, cycloidal spin spiral states for Co/Ir(111) in Figs. 5.3 for $\mathrm{Co_{fcc}}$ and $\mathrm{Co_{hcp}}$, respectively. In the big panels (small insets), the energy dispersions for $\mathbf{q}$ vectors in $\overline{\Gamma}$-$\overline{K}$ ($\overline{\Gamma}$-$\overline{M}$) direction of the 2D hexagonal BZ are shown, where points denote the DFT calculated results and solid lines are the fits to the respective interactions. Neglecting SOC for $\mathrm{Co_{fcc}}$/Ir(111) [grey points in Fig. 5.3 (a,b)] the FMic state at the $\overline{\Gamma}$ point is the lowest in energy. The DFT calculations can be well described by the effective nearest-neighbour approximation of the Heisenberg exchange interaction $J_{\mathrm{eff}} = 17.6\,\mathrm{meV}$ – recognizable by the small deviations between the grey line and points. All obtained values for the magnetic interactions are given in Tab. 5.2.

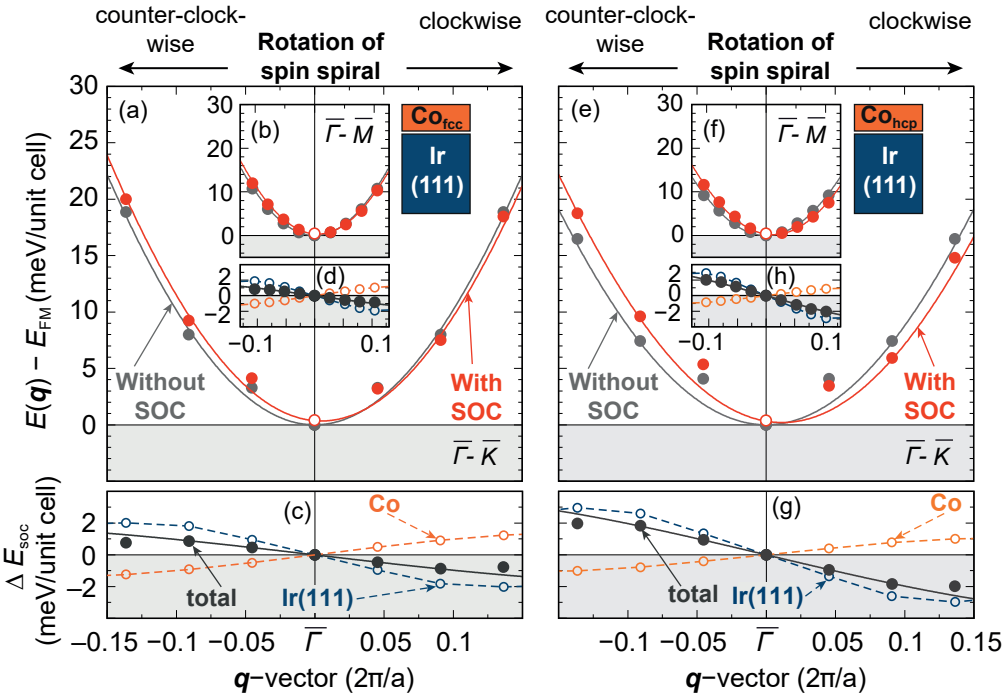

Figure 5.3 | Energy dispersions $E(\mathbf{q})$ of flat cycloidal spin spirals for Co/Ir(111) at $\mathbf{q} \to 0$. (a) Energy dispersion for $\mathrm{Co_{fcc}}$/Ir(111) for clockwise (CW) and counterclockwise (CCW) rotating spin spiral states along the high symmetry path $\overline{\Gamma}$-$\overline{K}$ of the two-dimensional Brillouin zone at $\mathbf{q} \to 0$. The points (grey without spin-orbit coupling (SOC), red with SOC) show calculated energies from DFT with respect to the ferromagnetic (FM) state, whereas lines represent the mapping to the effective nearest neighbour approximation of the atomistic spin model. The grey line is the fit to the exchange interaction applying J_{eff} and the fit of the red line includes exchange, Dzyaloshinskii-Moriya interaction (DMI) (D_{eff}) and magnetocrystalline anisotropy energy. (b) Energy dispersion as in (a) along $\overline{\Gamma}$-$\overline{M}$. (c) Energy contribution due to SOC. The black points show calculated values and the black line is the fit to the DMI. Open circles and dashed lines represent the SOC contribution of the respective element. (d) Energy contribution due to SOC as in (c) along $\overline{\Gamma}$-$\overline{M}$. (e,f,g,h) Energy dispersion for $\mathrm{Co_{hcp}}$/Ir(111).

The total contribution due to SOC [Fig. 5.3 (c,d)] results from a competition of the Co (red circles and dashed lines) and Ir(111) contributions (blue circles and dashed lines). Hence, the DMI slightly prefers CW rotating spin spiral states with $D_{\text{eff}} = +0.54\,\text{meV}$ (cf. Tab. 5.2). Taking the strong out-of-plane MAE into account ($K = -0.73\,\text{meV}$, cf. Tab. 5.2), the magnetic ground state is the FM [red points and curves in Fig. 5.3 (a,b)].

The energy dispersion of Co_{hcp}/Ir(111) is shown in Fig. 5.3 (e-h). Since a change in the stacking affects the third layer from the top, we do not expect a drastic change in the magnetism. The energy differences without SOC [grey points and lines in Fig. 5.3 (e,f)] are slightly reduced compared to Co_{fcc}/Ir(111) and consequently, $J_{\text{eff}} = 15.2\,\text{meV}$ is smaller. However, due to the hcp stacking, the DMI is twice larger than in the fcc stacking. In Fig. 5.3 (g,h), the Ir(111) exhibits a larger contribution to the total SOC whereas the Co contribution is reduced in comparison with Co_{fcc}. With the out-of-plane MAE, $K = -0.64\,\text{meV}$ Co_{hcp}/Ir(111) still shows a FM ground state [red points and lines in Fig. 5.3 (e,f)].

The FM ground state with a perpendicular magnetization direction is slightly preferred over non-collinear states. Due to the small energy differences, we expect FM films in which Néel type DWs can occur. Using the calculated magnetic interactions (Tab. 5.2) and Eqs. (5.1a) and (5.1b), we can estimate the energy cost of a DW as well as the width. The ratio of $J_{\text{eff}}/D_{\text{eff}}$ in Co_{hcp} is smaller compared to Co_{fcc}/Ir(111) and hence, $\Delta E_{\text{DW-FM}}$ is smaller by more than a factor (21 meV/Co vs. 53 meV/Co, Tab. 5.2). Since the DMI does not affect the width of a DW [cf. Eq. (5.1b)] it is the same for both Co stackings (3.2 nm) because in the hcp case, both exchange and MAE are reduced.

Table 5.2 | Obtained values for magnetic interactions in Co/Ir(111) mapping the effective nearest neighbour approximation of the spin model to the DFT results. J_{eff} (meV), D_{eff} (meV), K (meV) are the effective nearest neighbour exchange interaction, Dzyaloshinskii-Moriya interaction and the magnetocrystalline anisotropy energy, respectively. $\Delta E_{\text{DW-FM}}$ (meV/nm) and w (nm) are the calculated domain wall (DW) energy [Eq. (5.1a)] and the DW width [Eq. (5.1b)]. $D_{\text{eff}} > 0$ prefers clockwise rotating spin spiral states and $K < 0$ an out-of-plane easy magnetization axis. The fits were performed at $\mathbf{q} < |0.25\,2\pi/a|$.

System	J_{eff}	D_{eff}	K	$\Delta E_{\text{DW-FM}}$	w
Co_{fcc}/Ir(111)	+17.6	+0.54	−0.73	+53.3	3.2
Co_{hcp}/Ir(111)	+15.2	+1.10	−0.64	+21.0	3.2

Local density of states We gain further insight into the physics by calculating the local density of states (LDOS) which is presented in Fig. 5.4 for the two topmost layers of the films. The shaded LDOS show a reference where the hybridization between Co and Ir is negligible. In the case of Co [Fig. 5.4 (a,c)] it is an unsupported monolayer (UML) with the in-plane lattice constant of Ir(111) and for Ir [Fig. 5.4 (b,d)], a layer out of the middle of the Ir(111) substrate is chosen. Therefore, the differences between the shaded areas and the lines appear due to the hybridization between Co and the Ir surface layer.

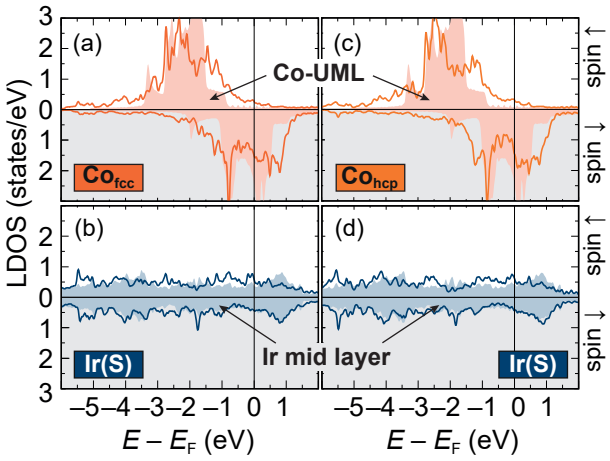

Figure 5.4 | Calculated local density of states (LDOS) for Co/Ir(111) in the ferromagnetic state. (a,b) LDOS of Co_{fcc}/Ir(111) for Co and the Ir(111) surface layer. (c,d) LDOS of Co_{hcp}/Ir(111). The shaded areas represent reference LDOS of a Co unsupported monolayer using the in-plane lattice constant of Ir(111) in (a,c). For Ir, a layer in the middle of the calculated Ir(111) substrate is taken in (b,d).

Comparing the Co UML with the Co layer of the film systems [Fig. 5.4 (a,c)], the exchange splitting of Co decreases from about 1.5 eV to approx. 1 eV due to the presence of the Ir(111) substrate. In Co, almost all significant peaks are reduced in height and broadened from the hybridization with Ir. As a consequence, the magnetic moment of Co in the film system loses about 5 % with respect to the magnetic moment of the Co UML (cf. Tab. 5.3).

The shape of the Ir surface LDOS develops a noticeable exchange splitting mediated by the hybridization with Co which is absent in the middle of the substrate [Fig. 5.4 (b,d)]. Co and Ir are isoelectronic elements and thus, the hybridization between both is very strong. This can be seen by hybridization peaks in both LDOS, (e.g. the peaks in the majority spin channels in Co and Ir at the Fermi energy).

We compare the magnetic moment (Tab. 5.3) with the interlayer distances d from the structural relaxation (cf. Tab. 5.1). For Co_{hcp} the surface layer has a larger relaxation compared to fcc stacking of Co. Because of the stronger hybridization between Co_{hcp} and Ir, the moment of Co slightly decreases and the moment of Ir slightly increases (Tab. 5.3). Furthermore, the stronger hybridization results in smaller exchange interaction and larger DMI for the hcp stacking of Co (cf. Fig. 5.3). It weakens the FM order on a small scale and thus, the DW energy is smaller.

Table 5.3 | Calculated magnetic moments (μ_B) in Co/Ir(111) in the ferromagnetic state. Shown is the Co layer, the Ir surface layer Ir(S) and the subsurface layer Ir(S-1). The bulk Ir moment ($\mu_{\text{Ir-bulk}}$) is taken from the seventh layer in the calculated system. As a reference, the moment of an unsupported monolayer (UML) of Co with the in-plane lattice constant of Ir(111) is shown.

System	μ_{Co}	$\mu_{Ir(S)}$	$\mu_{Ir(S-1)}$	$\mu_{Ir\text{-bulk}}$	$\mu_{Co\text{-UML}}$
Co_{fcc}/Ir(111)	+1.90	+0.21	−0.05	+0.00	+2.04
Co_{hcp}/Ir(111)	+1.89	+0.25	−0.01	−0.00	+2.04

5.3 FM ground state properties of Pt/Co/Ir(111)

We add a ML of Pt on top of Co/Ir(111). Since Pt has one additional valence electron than Co or Ir, Pt/Co/Ir(111) could show stronger FM order than Co/Ir(111), mediated by hybridization. In Fig. 5.5 the energy dispersions of Pt/Co/Ir(111) are presented. For three different stackings of the Pt/Co BLs on Ir(111) the behaviour of $E(\mathbf{q})$ without SOC (grey points and curves) looks very similar which is emphasized by only a small variation of J_{eff} ranging from 18.0 – 19.6 meV (cf. magnetic interactions in Tab. 5.4).

In general, the exchange is slightly increased compared to Co/Ir(111), with exception of $\text{Pt}_{\text{hcp}}/\text{Co}_{\text{fcc}}/\text{Ir}(111)$ [Fig. 5.5 (h,i)]. There, we observe a significant reduction of the energy differences in $E(\mathbf{q})$ and consequently $J_{\text{eff}} \sim 16\,\text{meV}$ is close to that of $\text{Co}_{\text{hcp}}/\text{Ir}(111)$. With an hcp stacking of the top layer and fcc structure below, i.e. $\text{Co}_{\text{hcp}}/\text{Ir}(111)$ and $\text{Pt}_{\text{hcp}}/\text{Co}_{\text{fcc}}/\text{Ir}(111)$, the exchange interaction is smaller than in their differently stacked counterparts.

The energy contributions due to SOC for Pt/Co/Ir(111) are shown in the small panels (c,d,g,h, …) of Fig. 5.5 and are strongly dependent on the stacking of both Co and Pt. While observing the largest contributions in $\text{Pt}_{\text{fcc}}/\text{Co}_{\text{fcc}}/\text{Ir}(111)$, in $\text{Pt}_{\text{hcp}}/\text{Co}_{\text{hcp}}/\text{Ir}(111)$ they are suppressed and for $\text{Pt}_{\text{fcc}}/\text{Co}_{\text{hcp}}$ as well as $\text{Pt}_{\text{hcp}}/\text{Co}_{\text{fcc}}$, ΔE_{SOC} reaches moderate magnitudes. For all stackings [except for $\text{Pt}_{\text{hcp}}/\text{Co}_{\text{hcp}}/\text{Ir}(111)$] the DMI prefers CW rotation of spin spiral states as in Co/Ir(111). Evaluating the strength of DMI, we see an increase from $\text{Co}_{\text{fcc}}/\text{Ir}(111)$ to $\text{Pt}_{\text{fcc}}/\text{Co}_{\text{fcc}}/\text{Ir}(111)$ from +0.5 meV to +1.1 meV and for $\text{Pt}_{\text{hcp}}/\text{Co}_{\text{fcc}}/\text{Ir}(111)$ to +0.8 meV (Tab. 5.4). In the case of $\text{Co}_{\text{hcp}}/\text{Ir}(111)$, D_{eff} is decreasing to +0.8 meV with a Pt_{fcc} top layer and furthermore and it is quenched for $\text{Pt}_{\text{hcp}}/\text{Co}_{\text{hcp}}/\text{Ir}(111)$. From these results, we conclude that on the one hand the DMI in both Co/Ir(111) and Pt/Co/Ir(111) is strongly dependent on the stacking of Co and Pt and on the other hand, we do not always observe an increase of DMI from Co/Ir(111) to Pt/Co/Ir(111) ultrathin films. This emphasizes the complexity of the DMI in transition metal interfaces.

In Co/Ir(111), the SOC contribution of the Co layer was significant [cf. Fig. 5.3 (c,d,g,h)] where due to the presence of a Pt top layer, the SOC contribution of Co vanishes [Fig. 5.5 (c,d,g,h,k,l,o,p)]. In $\text{Pt}_{\text{fcc}}/\text{Co}_{\text{fcc}}$, the major contribution to the DMI is stemming from the Pt site, where the Ir substrate contributes unnoticeably [Fig. 5.5 (c,d)]. Changing the stacking of the top layer to $\text{Pt}_{\text{hcp}}/\text{Co}_{\text{fcc}}$, this impact of contributions in Pt and Ir turn around [Fig. 5.5 (k,l)]. There, Ir has the major contribution preferring CW rotation of spin spirals, competing with the small Pt SOC favouring CCW rotation. This competition is similar for $\text{Pt}_{\text{fcc}}/\text{Co}_{\text{hcp}}/\text{Ir}(111)$ [Fig. 5.5 (g,h)] and shows that – in contradiction to the additive effects which have been claimed for Pt/Co/Ir interfaces in multilayer systems [35, 36] – for Co MLs sandwiched between Pt and Ir, the DMI does not show additive behaviour.

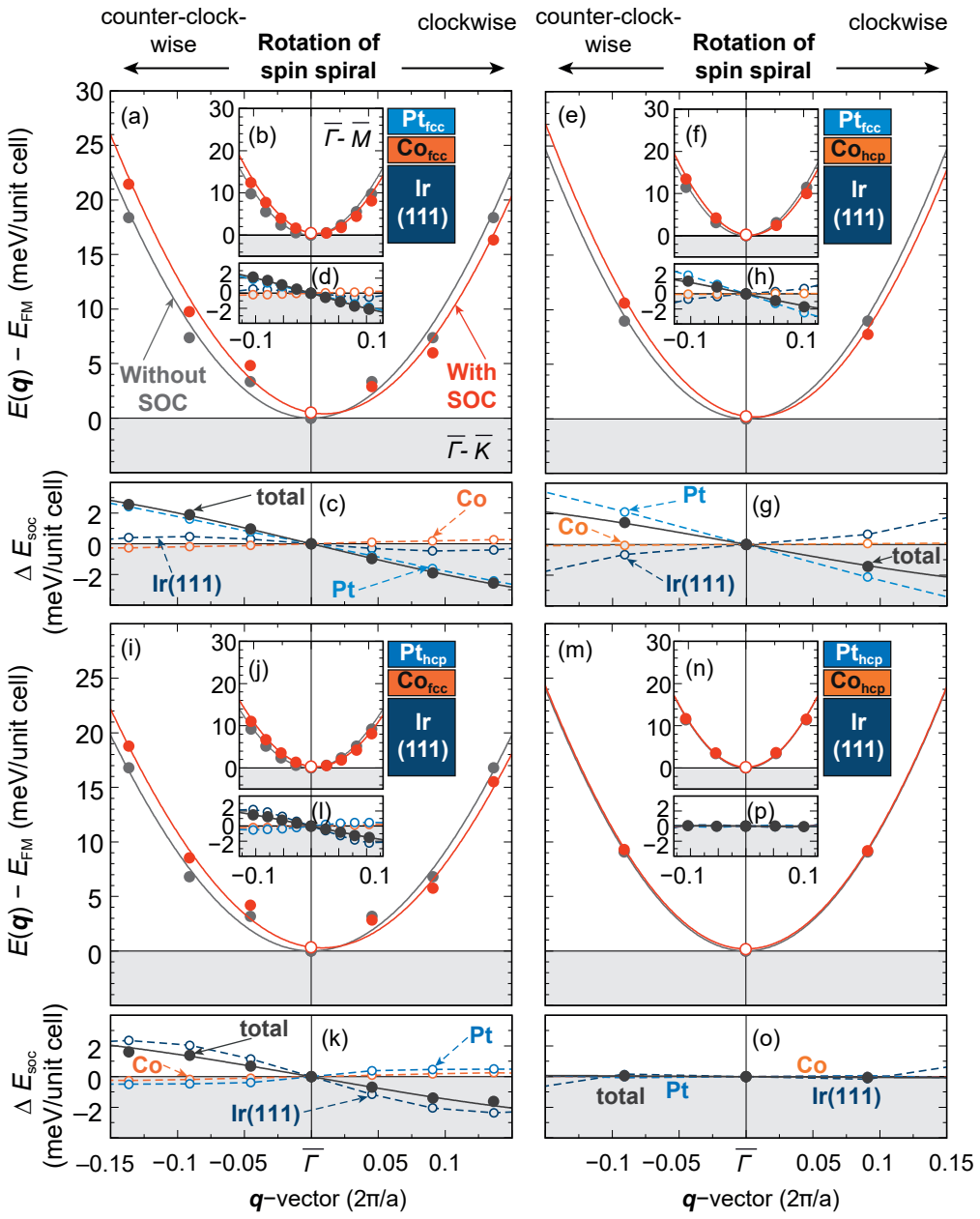

Figure 5.5 | Energy dispersions $E(\mathbf{q})$ of flat cycloidal spin spirals for Pt/Co/Ir(111) at $\mathbf{q} \to 0$. (a) Energy dispersion for $Pt_{fcc}/Co_{fcc}/Ir(111)$ for clockwise (CW) and counterclockwise (CCW) rotating spin spiral states along the high symmetry path $\overline{\Gamma}$-$\overline{K}$ of the two-dimensional Brillouin zone at $\mathbf{q} \to 0$. The points (grey without spin-orbit coupling (SOC), red with SOC) show DFT calculated energies with respect to the ferromagnetic (FM) state, whereas lines represent the mapping to the effective nearest neighbour approximation of the atomistic spin model. The grey line is the fit to the exchange interaction applying J_{eff} and the fit of the red line includes exchange, Dzyaloshinskii-Moriya interaction (DMI) (D_{eff}) and magnetocrystalline anisotropy energy. (b) Energy dispersion as in (a) along $\overline{\Gamma}$-$\overline{M}$. (c) Energy contribution due to SOC. The black points show calculated values and the black line is the fit to the DMI. Open circles and dashed lines represent the SOC contribution of the respective element. (d) Energy contribution due to SOC as in (c) along $\overline{\Gamma}$-$\overline{M}$. (e-h) Energy dispersion for $Pt_{fcc}/Co_{hcp}/Ir(111)$. (i-l) Energy dispersion for $Pt_{hcp}/Co_{fcc}/Ir(111)$. (m-p) Energy dispersion for $Pt_{hcp}/Co_{hcp}/Ir(111)$.

Similar to the DMI, the MAE is strongly dependent on the stacking order of the Pt and Co layers. With an fcc stacked Pt top layer, the DFT calculations predict an out-of-plane anisotropy (Fig. 5.6 and Tab. 5.4). Shifting Co from hcp [$K = -0.45\,\mathrm{meV/Co}$ for $\mathrm{Pt_{fcc}/Co_{hcp}/Ir(111)}$] to fcc [$K = -1.00\,\mathrm{meV/Co}$ for $\mathrm{Pt_{fcc}/Co_{fcc}/Ir(111)}$], the MAE increases by over a factor of two (cf. Tab. 5.4). When Pt has an hcp stacking, the easy axis is changing from out-of-plane to in-plane. Here as well, the MAE in for $\mathrm{Co_{hcp}}$ ($+0.38\,\mathrm{meV/Co}$) is almost twice as large as for the $\mathrm{Co_{fcc}}$ case ($+0.69\,\mathrm{meV/Co}$).

Table 5.4 | Obtained values for magnetic interactions in Pt/Co/Ir(111) mapping the effective nearest neighbour approximation of the spin model to the DFT results. J_{eff} (meV), D_{eff} (meV), K (meV) are the effective nearest-neighbour exchange interaction, Dzyaloshinskii-Moriya interaction and the magnetocrystalline anisotropy energy, respectively. $\Delta E_{\mathrm{DW\text{-}FM}}$ (meV/nm) and w (nm) are the calculated domain wall (DW) energy [Eq. (5.1a)] and the DW width [Eq. (5.1b)]. $D_{\mathrm{eff}} > 0$ prefers clockwise rotating spin spiral states and $K < 0$ an out-of-plane easy magnetization axis. The fits were performed at $\mathbf{q} < |0.25\,2\pi/a|$.

System	J_{eff}	D_{eff}	K	$\Delta E_{\mathrm{DW\text{-}FM}}$	w
$\mathrm{Pt_{fcc}/Co_{fcc}/Ir(111)}$	+18.0	+1.12	−1.00	+43.8	2.8
$\mathrm{Pt_{fcc}/Co_{hcp}/Ir(111)}$	+19.6	+0.84	−0.45	+28.4	4.4
$\mathrm{Pt_{hcp}/Co_{fcc}/Ir(111)}$	+15.7	+0.81	+0.69	+36.3	3.2
$\mathrm{Pt_{hcp}/Co_{hcp}/Ir(111)}$	+19.1	+0.03	+0.38	+55.2	4.7

Due to the procedure of calculating the MAE (cf. computational details in Sec. 5.1), we can investigate the contributions of the different layers to the MAE in more detail (Fig. 5.6). The calculations for $\mathrm{Pt_{fcc}/Co_{fcc}/Ir(111)}$ were performed with 13 layers of Ir substrate as for Co/Ir(111), where for other Pt/Co stackings, a nine layered Ir(111) substrate was used.

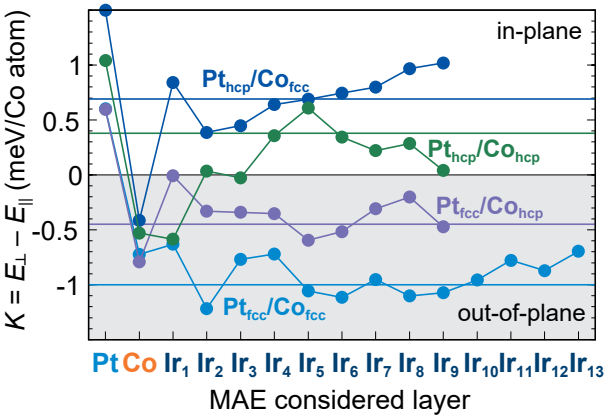

Figure 5.6 | Determination of the magnetocrystalline anisotropy energy (MAE) for Pt/Co/Ir(111). The spin-orbit coupling (SOC) contribution is switched on in one muffin-tin after another to see the contribution to the MAE of every atom in the system. 13 layers of Ir(111) were used to calculate the system of $\mathrm{Pt_{fcc}/Co_{fcc}/Ir(111)}$, while for other stackings, nine layers have been chosen. The MAE is determined as an average value from calculations where the SOC contributions are in a constant region of the calculation.

In all films, the Pt prefers an in-plane magnetization, where in hcp stacking, this contribution is the largest. Summing the SOC in Pt and Co leads to an out-of-plane anisotropy for all stacking variations. Crucial for the preferable direction of MAE are

the SOC contributions from the Ir surface (denoted as Ir_1) and subsurface layer (Ir_2), whereas layers deeper in the substrate do not show large variations and determine the strength of K (Fig. 5.6).

The interplay of exchange, DMI and MAE in Pt/Co/Ir(111) films will exhibit a FM ground state, where DWs are expected. The DW energies and widths are presented in Tab. 5.4 and are comparable with the ones of Co/Ir(111) (cf. Tab 5.2). DWs show higher energy than the FM state, but the energies are in the range of those in Co/Ir(111). The estimated DW widths, $w \sim 3-5\,\mathrm{nm}$, is also comparable to those of Co/Ir(111).

Local density of states We analyse the LDOS for Pt/Co/Ir(111) for the topmost three layers in detail (Fig. 5.7). In (a,d,g,j), the shaded areas show the LDOS of a Pt UML with the lattice constant of Ir(111). The Co and Ir surface layer, Ir(S), are taken from Co_{fcc}/Ir(111) and Co_{hcp}/Ir(111) (cf. Fig. 5.4) to resolve the changes from the presence of Pt. For Pt/Co/Ir(111), a strong hybridization between the three elements is observed since the deviations between lines and areas are significant.

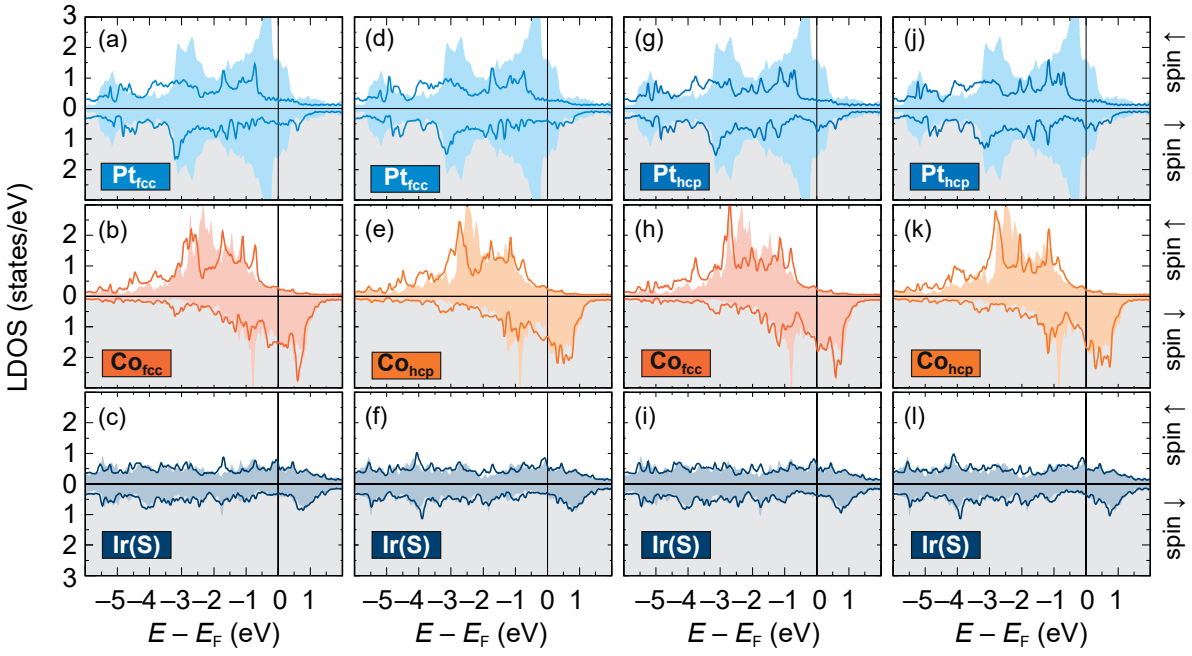

Figure 5.7 | Calculated local density of states (LDOS) for Pt/Co/Ir(111) in the ferromagnetic state. (a,b,c) LDOS of Pt_{fcc}/Co_{fcc}/Ir(111) for Pt, Co and the Ir(111) surface layer, respectively. (d,e,f) LDOS of Pt_{fcc}/Co_{hcp}/Ir(111). (g,h,i) LDOS of Pt_{hcp}/Co_{fcc}/Ir(111). (j,k,l) LDOS of Pt_{hcp}/Co_{hcp}/Ir(111). The shaded areas in (a,d,g,j) show the comparison of an Pt unsupported monolayer using the in-plane lattice constant of Ir(111), while for (b,c,e,f,h,i,k,l) the contributions of the Co and Ir(S) areas are taken from the film systems of Co/Ir(111) (Fig. 5.4).

The Pt UML has large peaks at −0.5 eV, around −3 eV and −5 eV. These peaks hybridize with both Co and Ir(S), while their energy and height is shifted and lowered due to the different stackings. The first peak below E_F shifts to −0.75 eV and is especially visible in the majority spin channel of the Pt top layer hybridizing with the

Co layer underneath. A peak in spin ↑ is occurring which is not large without Pt in the shaded Co area [Fig. 5.7 (b,e,h,k)]; however, it is also present in Ir(S) and supports the hybridization between the three elements. In the spin ↓ states, the significant peaks in both Co/Ir(111) systems at $\sim -0.8\,\mathrm{eV}$ in the Co layers are shifted to lower energies and are reduced in height. This further shows the strong hybridization of Pt, Co and Ir. Beside the deviations for Pt/Co/Ir(111) and Co/Ir(111), we see the most significant differences within Pt/Co/Ir(111) between fcc and hcp stacking in the Pt layer in the spin ↓ states at the Fermi energy. With $\mathrm{Pt_{fcc}}$ [Fig. 5.7 (a,b,d,e)], a small local minimum is present while for $\mathrm{Pt_{hcp}}$ [Fig. 5.7 (g,h,j,k)], a clear maximum is visible in Pt and Co.

We compare the LDOS to the calculated magnetic moments of the topmost four layers presented in Tab. 5.5. Due to the induced exchange splitting in Pt [cf. Fig. 5.7 (a,d,g,j)], an induced magnetic moment ($\mu_{\mathrm{Pt}} \sim +0.25\,\mu_{\mathrm{B}}$) in Pt occurs. In $\mathrm{Pt_{hcp}}$, the peak in the spin ↓ channel at E_{F} is extended into unoccupied states in Fig. 5.7 (g,j) which leads to a slight increase of the magnetic moment for $\mathrm{Pt_{hcp}}$ compared to $\mathrm{Pt_{fcc}}$ (0.28 μ_{B} vs. 0.24 μ_{B}, Tab. 5.5). The magnetic moment in the Co layers are comparably stable $1.9 \pm 4\,\%\,\mu_{\mathrm{B}}$ and similar to those in Co/Ir(111). Since the magnetic interactions, i.e. especially the exchange interaction for Co/Ir(111) and Pt/Co/Ir(111) is differing on a small scale, such a result is expected. The difference in the Ir surface layer can vary over 50 % [0.14 μ_{B} for $\mathrm{Pt_{fcc}/Co_{fcc}}$/Ir(111) and 0.25 μ_{B} for $\mathrm{Pt_{hcp}/Co_{hcp}}$/Ir(111)]. We notice that with $\mathrm{Co_{hcp}}$, the moment of the Ir(S) is slightly increased over that one with $\mathrm{Co_{fcc}}$ stacking, which is in accordance with the bare Co/Ir(111) films (cf. Tab. 5.3).

Table 5.5 | Calculated magnetic moments (μ_{B}) for Pt/Co/Ir(111). Shown is the Pt, Co, Ir surface layer Ir(S) and the subsurface layer Ir(S-1). The bulk Ir moment is taken from the seventh layer in the calculated system.

System	μ_{Pt}	μ_{Co}	$\mu_{\mathrm{Ir(S)}}$	$\mu_{\mathrm{Ir(S-1)}}$	$\mu_{\mathrm{Ir\text{-}bulk}}$
$\mathrm{Pt_{fcc}/Co_{fcc}}$/Ir(111)	+0.24	+1.84	+0.14	−0.05	+0.00
$\mathrm{Pt_{fcc}/Co_{hcp}}$/Ir(111)	+0.24	+1.90	+0.21	−0.01	−0.00
$\mathrm{Pt_{hcp}/Co_{fcc}}$/Ir(111)	+0.28	+1.90	+0.19	−0.04	+0.00
$\mathrm{Pt_{hcp}/Co_{hcp}}$/Ir(111)	+0.27	+1.95	+0.25	−0.00	−0.00

5.4 Experimental observations

While in theory we can assume every stacking possibility in the DFT calculations, experiments could reveal fcc stacking order of both Co and Pt (cf. Pub. I and Ref. [130]). The experiments on the studied systems have been performed by Marco Perini at the University of Hamburg under the supervision of André Kubetzka and Kirsten von Bergmann in the lab of Prof. Roland Wiesendanger[3].

[3]Institute of Applied Physics and and Interdisciplinary Nanoscience Center Hamburg, University of Hamburg, Jungiusstrasse 11, 20355 Hamburg, Germany

Fig. 5.8 (a) shows a sample of Co grown on the Ir(111) surface, where the topography is colourized with a measured spin-polarized differential conductance (dI/dU).

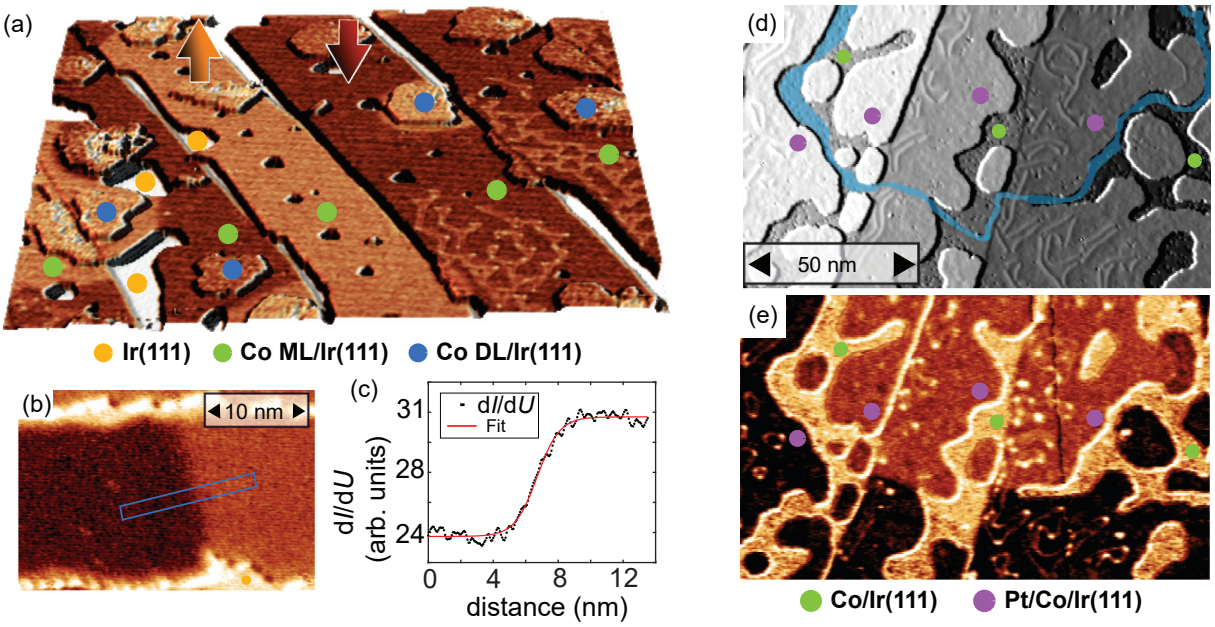

Figure 5.8 | Spin-polarized scanning tunnelling microscopy measurements of Co/Ir(111) and Pt/Co/Ir(111). (a) Perspective view of the topography of about 1.2 atomic layers of Co on Ir(111) ($200 \times 180\,\mathrm{nm}^2$) colourized with the simultaneously measured spin-resolved dI/dU signal. $U = -580\,\mathrm{mV}$, $I = 500\,\mathrm{pA}$, $T = 8\,\mathrm{K}$. The arrows indicate the out-of-plane contrast of two oppositely magnetized ferromagnetic domains. (b) Closeup of a single domain wall (DW) on Co/Ir(111). $U = -450\,\mathrm{mV}$, $I = 500\,\mathrm{pA}$, $T = 8\,\mathrm{K}$. (c) Measured dI/dU signal over a DW on Co/Ir(111) with a fit of Eq. (5.2). $U = -450\,\mathrm{mV}$, $I = 1\,\mathrm{nA}$, $T = 8\,\mathrm{K}$. (d) Constant-current topography maps of Pt/Co/Ir(111) after post-annealing. The differentiated topography signal is superimposed to the maps to enhance the visibility of the topographic details. $U = -550\,\mathrm{mV}$, $I = 1\,\mathrm{nA}$, $T = 8\,\mathrm{K}$. (e) Corresponding dI/dU map measured with out-of-plane magnetic sensitivity. The blue lines trace the position of the DWs, which avoid Pt/Co when possible. The thickness of the lines accounts for the uncertainty of the exact position of the DW. The figure has been adapted from Pub. I.

Due to the growth of Co [regions with green dots in Fig. 5.8 (a)] from the Ir(111) step edge, it is assumed to be fcc stacked. The tip's magnetization direction is mostly out-of-plane and the sample exhibits bright and dark contrast referring to magnetization directions pointing perpendicular to the film plane (denoted as bright and dark arrows pointing up- and downwards).

In constrictions between two oppositely magnetized regions, the DWs minimize their length, where one DW is shown in Fig. 5.8 (b). Taking the dI/dU spectroscopy of the DW gives rise to the spectrum presented in Fig. 5.8 (c) which can be fitted to the function

$$y = y_0 + y_{\mathrm{sp}} \tanh\left(\frac{x - x_0}{w/2}\right) \tag{5.2}$$

in order to extract the DW width w. Here, y_0 (y_{sp}) is the spin-averaged contribution

to the dI/dU signal and x_0 the centre of the DW. In Co/Ir(111), the average value of eight DWs is $w = 2.7 \pm 0.3\,\mathrm{nm}$.

Additional measurements were performed adding a Pt capping layer on top of Co/Ir(111). Pseudomorphic Pt layers show an irregular shape and in order to obtain more extended films, the sample was post-annealed at a temperature of $T \approx 500\,^\circ\mathrm{C}$ [Fig. 5.8 (d,e)]. The spin-resolved dI/dU contrast gives rise to a spin-polarization of the Pt due to hybridization with the Co layer. The Pt/Co BL also exhibits an out-of-plane FM ground state. The blue lines in Fig. 5.8 (d) mark the path of the DW, where in contrast to Co/Ir(111), they do not appear in constrictions, but try to elongate in order to keep the path on the bare Co layer. The DWs seem to avoid the Pt/Co BL. When occurring in the Pt/Co BL, the DWs have a tendency to sit in very small constrictions. The analysis of DWs in Pt/Co/Ir(111) was done on areas which are at minimum twice as large as the width w, where values of 2.7 nm and 3.6 nm were obtained. For detailed information about the experimental procedures, see Ref. 130 or Pub. I.

5.5 Comparing theory and experiments

As presented previously in the experiments, only fcc stacking in both Co and Pt layers has been observed. In our DFT calculations, we find that the $\mathrm{Co_{fcc}}$ stacking costs about 62 meV/Co-atom compared to the $\mathrm{Co_{hcp}}$ stacking, so $\mathrm{Co_{hcp}}$ seems to be favoured. However, Co is growing from Ir(111) step edges which is preferable in fcc stacking. This growing mechanism of Pt can be seen different, especially when including the heating of post-annealing. The presented calculations reveal an energy gain of the fcc stacking of Pt on top of $\mathrm{Co_{fcc}}$ of about 22 meV/Co-atom compared to the hcp Pt. Here, a good agreement between experiment and theory is observed.

The previously presented results on DWs are summarized in Fig. 5.9, where in (a), the DW energies $\Delta E_{\text{DW-FM}}$ are shown depending on the DMI. The points are the values according to Tab. 5.2 and 5.4, while the lines follow Eq. (5.1a). The error bars indicate an error of the MAE by $K \pm 0.1\,\mathrm{meV}$. Negative values of $\Delta E_{\text{DW-FM}}$ would lead to a spin spiral ground state in the energy dispersions $E(\mathbf{q})$ with SOC and vice versa (cf. Figs. 5.3 and 5.5).

$\mathrm{Co_{hcp}}$/Ir(111) and $\mathrm{Pt_{fcc}/Co_{hcp}}$/Ir(111) exhibit the smallest DW energy, while the DW energies for the experimentally measured systems [solid lines and filled circles, $\mathrm{Co_{fcc}}$/Ir(111) and $\mathrm{Pt_{fcc}/Co_{fcc}}$/Ir(111)] are the most unfavourable, together with $\mathrm{Pt_{hcp}/Co_{hcp}}$. The latter has a vanishing DMI which increases the DW energy [cf. Eq. (5.1a)]. However, due to the error bars, energies in a range of about 10 meV/nm can be treated as energetically degenerate. Small errors in the DMI will have the same effect shifting the points down or up the lines. This is the reason why from our calculations, we cannot unambiguously reveal the DWs avoiding the Pt sites in the experiments sitting preferably on the Co.

Fig. 5.9 (b) shows the calculated DW widths for all films. Here, the lines represent the experimentally measured values and the shaded area is the estimated error for Co_{fcc}/Ir(111) from experiment. All DW widths are between 2.5 and 5 nm. Due to the small MAE of Pt/Co_{hcp}/Ir(111) (cf. Tab. 5.4), their DW width is larger (over 1 nm) compared to the other systems. Comparing the experimental values with theory, we find a good agreement for both Co_{fcc}/Ir(111) and Pt_{fcc}/Co_{fcc}/Ir(111), even though the applied effective nearest neighbour approximation of the atomistic spin model is simple and only three magnetic parameters are taken into account.

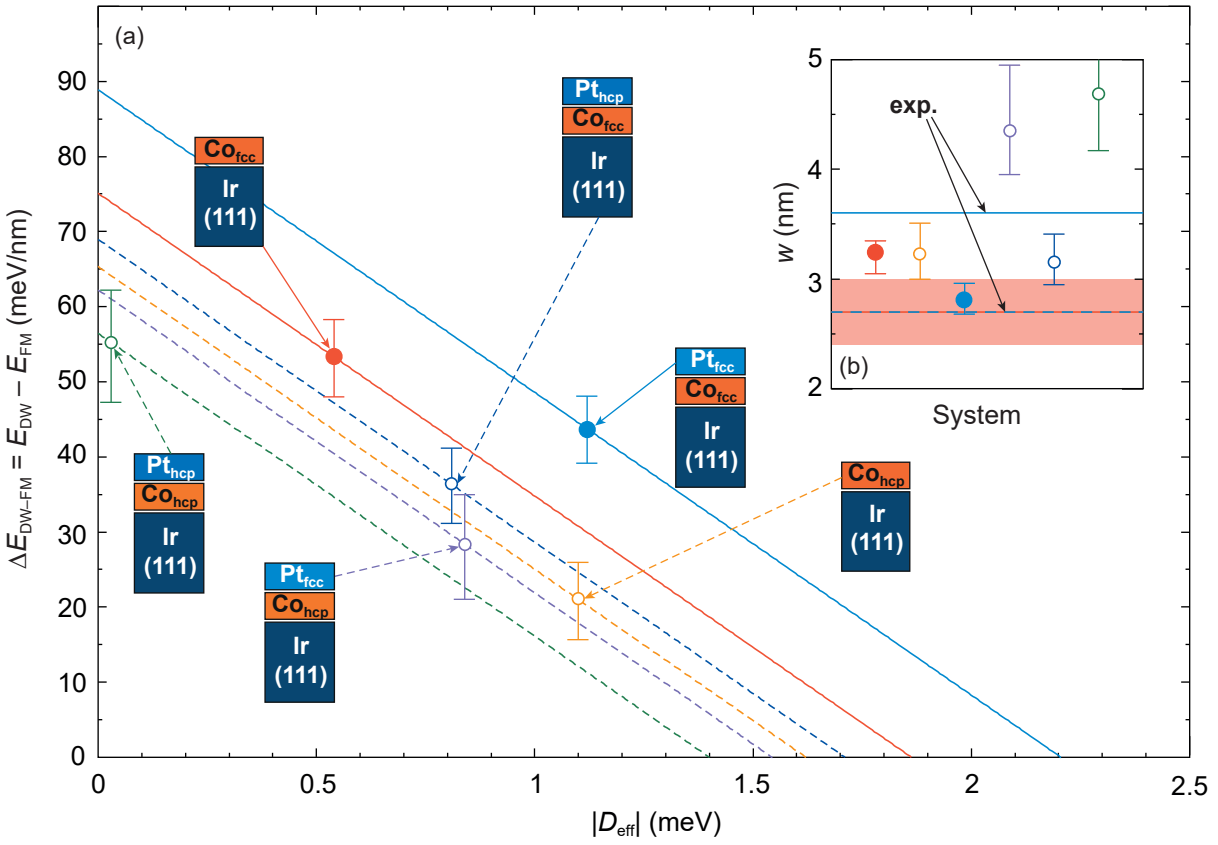

Figure 5.9 | Calculated domain wall (DW) properties for Co/Ir111 and Pt/Co/Ir(111). (a) DW energy $\Delta E_{DW\text{-}FM}$ (meV/nm) dependent on the strength of Dzyaloshinskii-Moriya interaction. The lines follow Eq. (5.1a) and the points are the calculated DW energies with J_{eff}, D_{eff} and K taken from Tab. 5.2 and 5.4. The solid lines and filled circles present the two systems which can be experimentally realized. (b) DW width w (nm) for the systems presented in (a) calculated from Eq. (5.1b). The lines indicate the experimentally observed values for Co_{fcc} and Pt_{fcc}/Co_{fcc} while the shaded area is the estimated error from experiments. All error bars indicate an estimated error of the magnetocrystalline anisotropy energy of about ±0.1 meV.

5.6 Additive DMI in Pt/Co/Co/Ir(111) and Pt/Pt/Co/Ir(111)

As it has been shown previously (Secs. 5.2 and 5.3), a simple additive DMI in the Pt/Co/Ir interfaces could not be observed when a Co ML is sandwiched between a Pt ML and an Ir substrate – contrary to what has been suggested in Ref. 35. The main contributions originate either from the Pt or the Ir interface, depending on the stacking order of the Pt/Co BL. We further want to gain insight in this mechanism and calculated energy dispersions for two additional film systems where we increase either the thickness of Pt or the Co layer. For completeness, we also determine the exchange, MAE as well as DW properties.

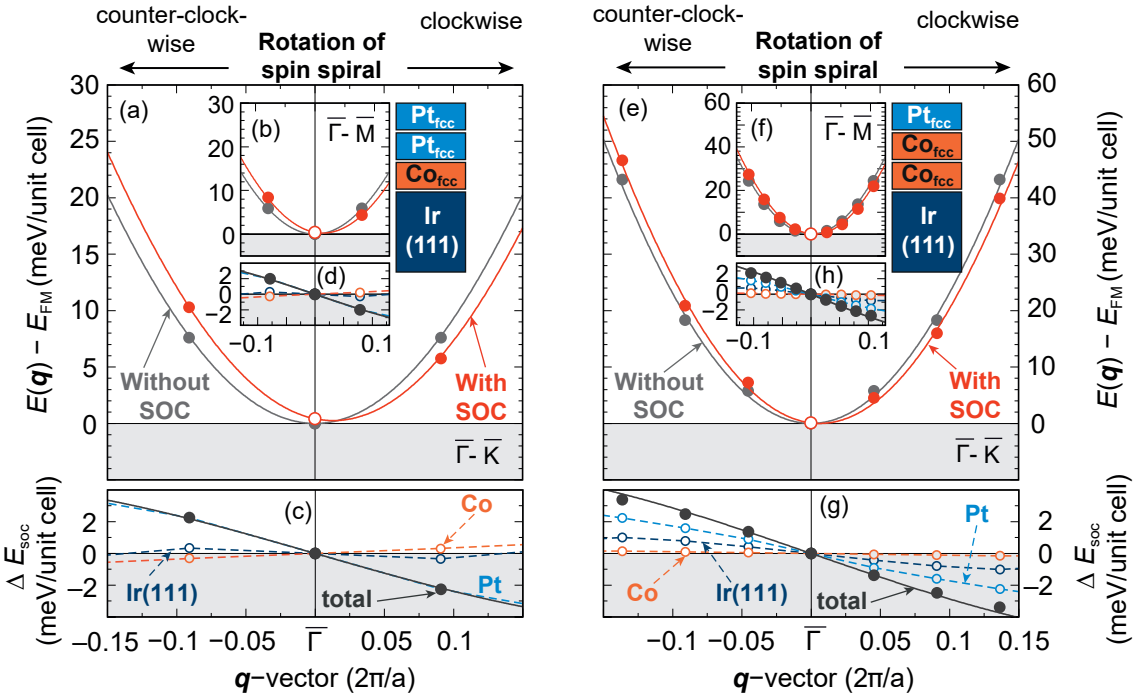

Figure 5.10 | Energy dispersions $E(\mathbf{q})$ of flat cycloidal spin spirals for $Pt_{fcc}/Pt_{fcc}/Co/Ir(111)$ and $Pt_{fcc}/Co_{fcc}/Co_{fcc}/Ir(111)$ at $\mathbf{q} \to 0$. (a) Energy dispersion for $Pt_{fcc}/Pt_{fcc}/Co_{fcc}/Ir(111)$ for clockwise (CW) and counterclockwise (CCW) rotating spin spiral states along the high symmetry path $\overline{\Gamma}$-$\overline{K}$ of the two-dimensional Brillouin zone around $\mathbf{q} \to 0$. The points (grey without spin-orbit coupling (SOC), red with SOC) show the DFT calculated energies with respect to the ferromagnetic (FM) state, whereas lines represent the mapping to the effective nearest neighbour approximation of the atomistic spin model. The grey line is the fit to the exchange interaction applying J_{eff} and the fit of the red line includes exchange, Dzyaloshinskii-Moriya interaction (DMI) (D_{eff}) and magnetocrystalline anisotropy energy. (b) Energy dispersion as in (a) along $\overline{\Gamma}$-$\overline{M}$. (c) Energy contribution due to SOC. The black points show calculated values and the black line is the fit to the DMI. Open circles and dashed lines represent the SOC contribution of the respective element. (d) Energy contribution due to SOC as in (c) along $\overline{\Gamma}$-$\overline{M}$. (e,f,g,h) Energy dispersion for $Pt_{fcc}/Co_{fcc}/Co_{fcc}/Ir(111)$. Note that the energy scale for $Pt_{fcc}/Co_{fcc}/Co_{fcc}/Ir(111)$ is doubled due to the second magnetic layer. The figure has been adapted from Pub. I.

Fig. 5.10 shows the energy dispersions of Pt/Pt/Co/Ir(111) and Pt/Co/Co/Ir(111). For simplification, here we restrict ourselves on only fcc stacked layers of Co and Pt. That is why these systems should be compared to the energy dispersions of Co_{fcc}/Ir(111) (cf. Fig. 5.3) and Pt_{fcc}/Co_{fcc}/Ir(111) (Fig. 5.5).

A second Pt layer will reduce the exchange interaction by about 2 meV (Tab. 5.6) which is also visible from the grey points and curves in Fig. 5.10 (a,b). On the other hand, the energy contribution due to SOC is increasing with the Pt thickness. The DMI raises from $D_{\text{eff}} = +1.12\,\text{meV}$ to $D_{\text{eff}} = +1.33\,\text{meV}$ where the Pt is providing the whole contribution, i.e. in this films, there is no additive behaviour of DMI. The same has been observed Pt/Co/Ir(111) [cf. Fig. 5.5 (c,d)]. The MAE slightly decreases from –1.0 meV in the Pt ML case to –0.8 meV in the Pt double layer (DL) case while the preferred easy axis remains out-of-plane. Taking into account the increased DMI as well as decreased exchange and MAE, the DW energy [Eq. (5.1a)] is reduced almost by a factor of two with a second Pt layer (Tab. 5.6). The width of a DW on the contrary, almost remains constant.

Inserting a second layer of Co in Pt/Co/Ir(111), the energy dispersion is shown on the right side of Fig. 5.10. Note that the energy difference per unit cell is doubled. The resulting values of exchange, DMI and MAE presented in Tab. 5.6 and are given per Co atom so the values are normalized to be comparable with the Co ML films. The exchange is increasing by about 2 meV compared to Pt_{fcc}/Co_{fcc}/Ir(111) and is driven by the presence of a second FM Co layer. The total DMI in the system will be increased [ΔE_{SOC} in Fig. 5.10 (f,g)] and furthermore, the Ir has a significant contribution which is a half as large as that one of the Pt layer. In Pt/Co/Co/Ir(111), the DMI shows additive behaviour from both interfaces. This can be seen as the main difference for the DMI from systems with a ML of Co compared to Pt/Co/Co/Ir(111). In the first case, no additive effect of DMI is seen due to a vanishing contribution of Ir[4].

Table 5.6 | Obtained values for magnetic interactions in $Pt_{fcc}/Pt_{fcc}/Co_{fcc}$/Ir(111) and $Pt_{fcc}/Co_{fcc}/Co_{fcc}$/Ir(111) mapping the effective nearest neighbour approximation of the spin model to the DFT results. J_{eff} (meV), D_{eff} (meV), K (meV) are the effective nearest-neighbour exchange interaction, Dzyaloshinskii-Moriya interaction and the magnetocrystalline anisotropy energy, respectively. $\Delta E_{\text{DW-FM}}$ (meV/nm) and w (nm) are the calculated domain wall (DW) energy [Eq. (5.1a)] and the DW width [Eq. (5.1b)]. $D_{\text{eff}} > 0$ prefers clockwise rotating spin spiral states and $K < 0$ an out-of-plane easy magnetization axis. The fits were performed at $\mathbf{q} < |0.25\,2\pi/a|$.

System	J_{eff}	D_{eff}	K	$\Delta E_{\text{DW-FM}}$	w
$Pt_{fcc}/Pt_{fcc}/Co_{fcc}$/Ir(111)	+16.1	+1.33	−0.83	+23.0	2.9
$Pt_{fcc}/Co_{fcc}/Co_{fcc}$/Ir(111)	+20.0	+0.80	−0.09	−4.1	9.9

Normalizing the DMI, it will be smaller compared to Pt/Co/Ir(111) and the MAE will almost be quenched. The latter is the reason, why – contrarily to the other

[4]Note the stackings in these films are completely fcc.

investigated films – the DW energy is lower than the FM state (Tab. 5.6). Here, a spin spiral ground state is expected; however, the energy difference is very small, which is why spin spirals and the FM state can be considered as energetically degenerate within our DFT accuracy.

5.7 Conclusion

In this chapter, we investigated the DMI for the prominent Pt/Co/Ir interfaces where additive DMI has been predicted in multilayer films [35, 36]. Within the effective nearest neighbour approximation, we analyse the DFT results in ultrathin Co/Ir(111) and Pt/Co/Ir(111) films.

The DMI strongly depends on the stacking of both elements (Pt, Co) and can range from 0.5 meV in Co_{fcc}/Ir(111) up to 1.1 meV in Co_{hcp}/Ir(111) or Pt_{fcc}/Co_{fcc}/Ir(111). For an hcp stacking of Pt and Co, the DMI even vanishes. This shows the complexity of the SOC dependent interaction such as the DMI. The DFT calculations reveal that the effect of additive DMI does not hold true for Pt/Co/Ir films, when Co is present as ML, but can occur in films with a Co DL.

We find a FM ground state for all possible films assuming fcc and hcp stackings of both Co and Pt. Typically, the exchange interaction is slightly increased when adding Pt on top of Co/Ir(111). As for the DMI, the stacking order has a strong impact on the uniaxial anisotropy. Films with Co_{hcp} show smaller MAE than films with Co_{fcc}. The preferred magnetization direction of Co/Ir(111) and Pt_{fcc}/Co/Ir(111) films is out-of-plane while with Pt_{hcp}, the MAE changes to in-plane.

Due to interplay between the magnetic interactions, the formation of DWs in FM states in each investigated film is reasonable, where the DW width can vary between 2.8 nm and 4.7 nm. Experiments from the University of Hamburg have performed measurements on Néel type DWs for Co_{fcc}/Ir(111) and Pt_{fcc}/Co_{fcc}/Ir(111) which show very good agreement with our calculations.

Chapter 6

Frustration of Dzyaloshinskii-Moriya interaction in Co/Ir interfaces

In the previous chapter, we restricted ourselves on applying the effective nearest neighbour approximation for both exchange and Dzyaloshinskii-Moriya interaction (DMI) to describe the magnetic ground state properties of Co/Ir(111) and Pt/Co/Ir(111). Since the films appeared to behave as prototypical ferromagnets (FMs), such a description is valid and results can be compared with experiments (Pub. I). However, it has been shown that frustration of exchange interaction, i.e. competing exchange interactions of different neighbours, can change the formation process of skyrmion lattices [41, 131–133]. In particular, for the ultra-thin film system Pd/Fe/Ir(111) the effect of exchange frustration can have a large impact on the stability of skyrmions [134].

Equivalent to frustration of exchange, the other magnetic interactions, more specifically the DMI can be frustrated (see also the 4*d*/Co/Ir(111) and 4*d*/Co/Rh(111) in the following Ch. 7). However, the DMI acting beyond nearest neighbours has received very little attention so far. Some studies even determine the strength of the DMI from self-consistent density functional theory (DFT) calculations including spin-orbit coupling (SOC) on spin spiral states with an angle of 90° [36, 123]. Such calculations for only one specific spin spiral state a priori do give insight into the DMI beyond nearest neighbours.

In this chapter, we shed light into the mechanism of DMI frustration in Co/Ir interfaces based on the ultra-thin films of Co/Ir(111) and Pt/Co/Ir(111). DFT calculations reveal that in most of the films, DMI prefers clockwise (CW) rotation of FM spin spiral states for $\mathbf{q} \to 0$ (cf. Ch. 5), but change the rotational sense to counterclockwise (CCW) for larger $\mathbf{q}$ vectors. In these films, obtaining the DMI from the derivation of 90° spin spiral states would not only end up in a different strength of the DMI, D_{eff}, but also in the wrong rotational sense which is favoured by the DMI.

This change of sign in the DMI is explained by the SOC contribution of the Ir(111) substrate, where the Ir interface layer at Co has the largest effect. Its consequences on non-collinear spin structures can be seen as two-fold: A description with D_{eff} in the presence of DMI frustration can lead to wrong ground state properties such as the size and shape of e.g. skyrmions. On the other hand, when a certain D_{eff} leads to the same ground state properties of the non-collinear spin structures, its subsequent impact on the stability is small due to the typically small energy contribution of the DMI to the

total energy[1].

This chapter is structured as follows: First, we compare the atomistic spin model with the effective nearest neighbour approximation for both exchange and DMI investigating complete energy dispersions of flat spin spirals (Sec. 6.2). We resolve the DMI contributions for all films and go into details for the exemplary film system of Co_{hcp}/Ir(111) (Sec. 6.3) . For this film, we apply spindynamics simulations in Sec. 6.4 to see the impact of frustration of DMI and exchange on non-collinear spin structures such as domain walls (DWs) and skyrmions. In the last part, we will clarify the role of DMI frustration on magnetic skyrmions with testing different magnetic interaction parameter sets (6.5).

6.1 Computational details

In this study, we look into the details of DMI which we determine based on the calculations of the previous chapter (Ch. 5). Therefore, the computational details for all DFT calculations can be seen in Sec. 5.1. We want to compare the description of the effective nearest neighbour approximation and the atomistic spin model for exchange and more detailed for the DMI in order to understand the mechanism and the consequences of its frustration.

Determination of magnetic interaction parameters For both J_{eff} and D_{eff}, only the region around the FM state ($\overline{\Gamma}$ point), i.e. $\mathbf{q} \to 0$ has been investigated (cf. Ch. 5). For J_{eff}, the fitting for J_1 is used and for D_{eff}, it is the linear approximation as stated in Sec. 5.1. Determining the exchange interaction and DMI beyond nearest neighbours, J_{ij}, D_{ij}, we take care that the DFT calculations for all $\mathbf{q}$ are represented well by the fits with the least amount of neighbours. Including more neighbours into our fits therefore will not significantly improve the description. With this procedure, a different amount of neighbours is used for every respective film system.

Energy integrated DMI We get a detailed insight into the DMI by investigating the energy-resolved contributions to the DMI, for both positive and negative shifts, which are defined according to Eq. (3.24)

$$\delta\epsilon_{k\nu} = \langle\psi_{k,\nu}|\mathcal{H}_{\text{SOC}}|\psi_{k,\nu}\rangle \tag{6.1a}$$

The integration over the two-dimensional (2D) Brillouin zone (BZ) gives rise to

$$e_{\text{DMI}}(E,q) = \sum_{\nu}\int \delta\epsilon_{k\nu}\delta(E - E_{k\nu})\mathrm{d}k \tag{6.1b}$$

It is smoothed by a Gaussian function with a full width of half maximum of 0.1 eV

$$g(x) = \frac{1}{\sqrt{2\pi\sigma^2}}\mathrm{e}^{-\frac{(\delta\epsilon-\delta\epsilon_{k\nu})^2}{2\sigma^2}} \tag{6.1c}$$

[1]Note that this is different to [134], where due to the presence of exchange frustration the impact on the stability of skyrmions has been shown to be large even when the magnetization profiles of spin structures match with the effective nearest neighbour approximation.

The result is then plotted over the binding energy. When integrating Eq. (6.1b), the effective energy integrated DMI energy is defined as

$$E_{\mathrm{DM}}(E,q) = \int_{-\infty} E e_{\mathrm{DMI}}(E',q)\mathrm{d}E' \tag{6.1d}$$

Here, it is important to mention that the choice of the full width of half maximum in the Gaussian has an enormous impact on the quantitative description of E_{DM}. The value of 0.1 eV is chosen because it gives the best ratio between accuracy and qualitative description.

Spindynamics simulations For the exemplary film of $\mathrm{Co_{hcp}}$/Ir(111), we perform atomistic spindynamics simulations in order to obtain the energies for DWs and skyrmions. We chose a 70×70 lattice and apply four different magnetic interaction parameter sets out of $\Big[J_{\mathrm{eff}} + D_{\mathrm{eff}} + K;\quad J_{ij} + D_{\mathrm{eff}} + K;\quad J_{\mathrm{eff}} + D_{ij} + K;\quad J_{ij} + D_{ij} + K\Big]$. Consequently, we can address every change in the simulations to the respective description. We chose a time step of 0.1 fs with 1,000,000 steps and a damping constant of $\alpha = 0.5$.

To compare the consequences of DMI frustration on the stability of non-collinear spin structures, we choose seven arbitrary sets of magnetic interaction parameters, where we vary the degree of DMI frustration. Starting from effective nearest neighbour exchange, CW preferring DMI and an out-of-plane magnetocrystalline anisotropy energy (MAE), $J_{\mathrm{eff}} = 10.0\,\mathrm{meV}$, $D_{\mathrm{eff}} = -1.3\,\mathrm{meV}$, $K = -1.0\,\mathrm{meV}$, the impact of adjusting the DMI is tested and explained by the example of a skyrmion structure. More detailed information about the respective set will be given in Sec. 6.5. For the simulations, we apply a lattice of 70×70 spins and converge the structures within 500,000 time steps of 0.1 fs with a damping constant of $\alpha = 1$.

Geodesic nudged elastic band method calculations With the relaxed skyrmions of the spindynamics simulations, we determine the minimum energy path (MEP) for their annihilation [119]. Therefore, we apply the geodesic nudged elastic band (GNEB) method where we start from the local energy minimum of the skyrmion state and generate the path into the global energy minimum, i.e. the FM state. The path is converged into the MEP consisting of 20 images where we applied the climbing image technique [120, 121] in order to determine the height of the saddle point (SP) and thus the energy barrier.

6.2 Comparison of atomistic spin model and effective nearest neighbour approximation

We first want to see the impact of frustration on the full energy dispersion of spin spirals. In Fig. 6.1, these are presented along the full high symmetry path $\overline{M}$-$\overline{\Gamma}$-$\overline{K}$-$\overline{M}$ of the 2D BZ. While the points display the DFT calculations, we apply two different spin models. Solid lines show curves using the atomistic spin model, i.e. contain exchange

and DMI frustration, respectively. Dashed lines correspond to the effective nearest neighbour approximation around $\mathbf{q} \to 0$, where a deviation between both curves can be seen as degree of frustration of the magnetic interactions.

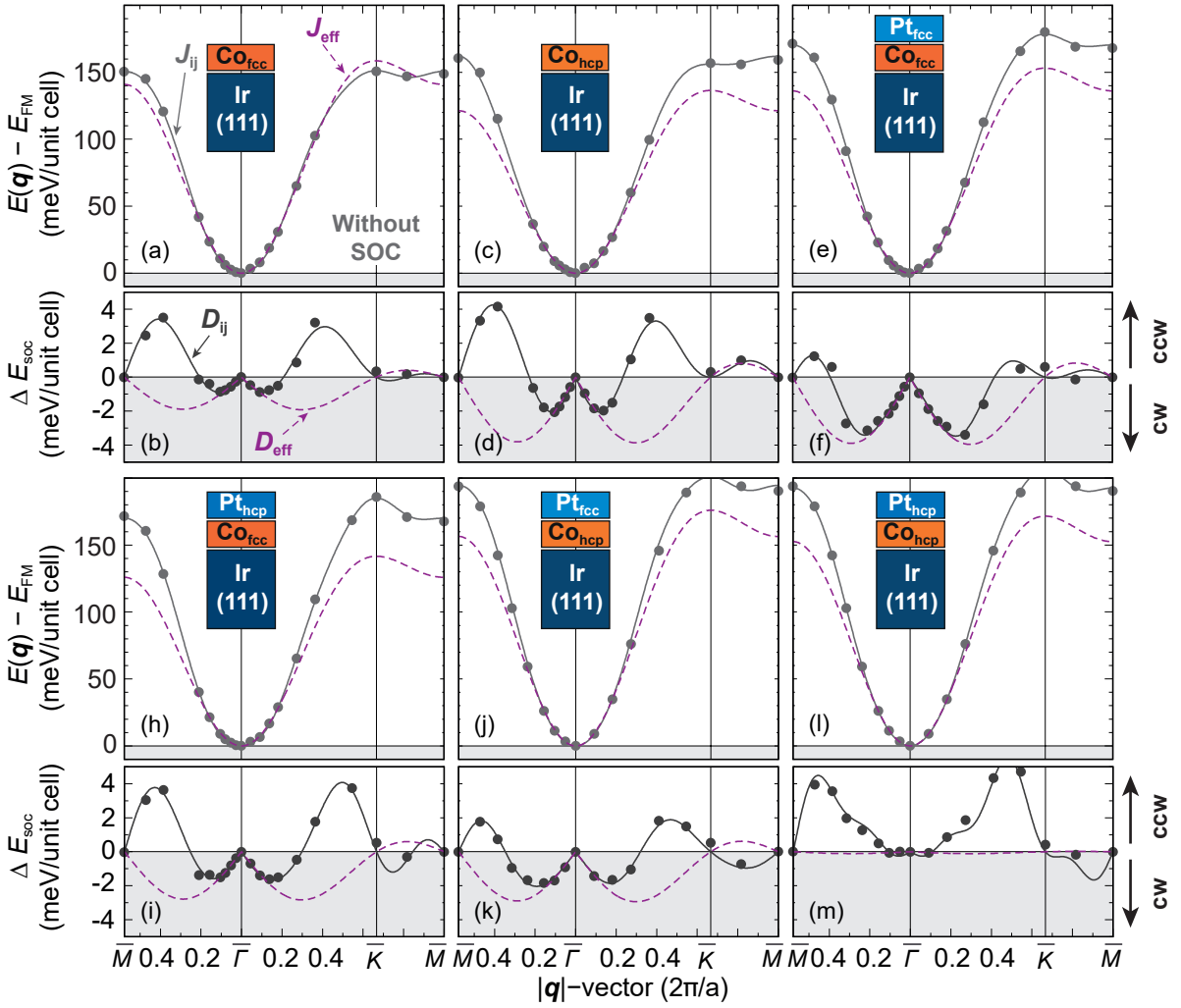

Figure 6.1 | Full energy dispersions $E(\mathbf{q})$ of flat cycloidal spin spirals for Co/Ir(111) and Pt/Co/Ir(111) comparing the atomistic spin model with the effective nearest neighbour approximation. (a) Energy dispersion without spin-orbit coupling (SOC) for Co_{fcc}/Ir(111) along the high symmetry path $\overline{\Gamma}$-$\overline{M}$ and $\overline{\Gamma}$-$\overline{K}$ of the two-dimensional Brillouin zone. Points show calculated energies from DFT with respect to the ferromagnetic (FM) state, whereas solid lines represent the fits to the atomistic spin model J_{ij} for the Heisenberg exchange. The dashed purple curves correspond to the respective fits to the effective nearest neighbour approximation J_{eff} (b) Energy contribution due to SOC for Co_{fcc}/Ir(111). Positive (negative) values correspond to counterclockwise (clockwise) rotation. The lines show the respective fits to the Dzyaloshinskii-Moriya interaction. (c,d) Co_{hcp}/Ir(111). (e-m) Pt/Co/Ir(111) for all assumed stacking possibilities of Pt and Co.

In the upper panels (without SOC) both descriptions match very well up to half the way in $\overline{\Gamma}$-$\overline{K}$ and $\overline{\Gamma}$-$\overline{M}$ directions [Fig. 6.1 (a,c,e,h,j,l)]. As presented in Ch. 5, the effective nearest neighbour approximation works well around the FM ground state. For larger **q** vectors solid and dashed lines are deviating more or less, depending on the film. In case of Co_{fcc}/Ir(111) [Fig. 6.1 (a)], the exchange frustration is small, while for Pt_{hcp}/Co_{fcc}/Ir(111) [Fig. 6.1 (h)], it is the largest among these films. All magnetic interaction parameters for the atomistic spin model can be seen in Tab. 6.1 and can be compared to Tab. 5.2 and 5.4. Both Co/Ir(111) and Pt/Co/Ir(111) exhibit a moderate frustration of exchange when set in relation to highly frustrated film systems such as Fe/Ir(111) [29], Pd/Fe/Ir(111) [134], Rh/Fe/Ir(111) [44] or Fe/Rh(111) [45].

Table 6.1 | Obtained values for magnetic interactions for Co/Ir(111) and Pt/Co/Ir(111) mapping the atomistic spin model to the results of DFT calculations. All values of the i-th neighbour exchange J_i and Dzyaloshinskii-Moriya interaction constants D_i are given in meV. $J > 0$ ($J < 0$) represents ferromagnetic (antiferromagnetic) order and $D > 0$ ($D < 0$) clockwise (counterclockwise) rotation.

Parameter	Co_{fcc}	Co_{hcp}	Pt_{fcc}/Co_{fcc}	Pt_{fcc}/Co_{hcp}	Pt_{hcp}/Co_{fcc}	Pt_{hcp}/Co_{hcp}
J_1	+17.372	+19.283	+20.874	+23.663	+21.257	+23.823
J_2	+2.176	+0.977	+1.071	+1.357	+0.673	+0.609
J_3	−0.729	−1.940	−1.126	−1.197	−1.129	−1.304
J_4	+0.081	–	+0.043	−0.260	+0.213	+0.020
J_5	−0.874	–	−0.731	−0.567	−1.097	−0.769
J_6	–	–	–	−0.121	–	−0.079
J_7	–	–	–	+0.194	–	0.183
D_1	−0.678	−0.694	+0.404	−0.099	−0.566	−1.065
D_2	+0.271	+0.267	+0.392	+0.522	+0.479	+0.581
D_3	+0.434	+0.673	+0.378	+0.189	0.656	+0.451
D_4	–	+0.059	−0.120	−0.013	−0.212	−0.263
D_5	–	–	−0.075	−0.139	+0.162	−0.063
D_6	–	–	–	+0.043	–	−0.050
D_7	–	–	–	–	–	+0.178

For the contributions due to SOC (smaller panels in Fig. 6.1), we see large deviations between the atomistic spin model and the effective nearest neighbour approximation[2]. Around the FM ground state, both descriptions match well. However, the DFT calculations reveal a change of rotational preference from CW to CCW in spin spirals for larger angles between nearest neighbours, i.e. larger **q** [Fig. 6.1 (b,d,f,i,k,m)]. This behaviour is only captured by the atomistic spin model (solid lines).

In four films, both Co/Ir(111) films and Pt_{hcp}/Co_{fcc} as well as Pt_{fcc}/Co_{hcp} [Fig. 6.1 (b,d,i,k)] 90° spin spirals states prefer CCW rotation, whereas the films show CW DMI

[2]Note that the energy scale of exchange and DMI is differing by far.

in their DWs (cf. Pub. I and Sec. 5.4). Here, the determination of DMI applying super cell calculations on 90° spin spirals (1/2 $\overline{\Gamma}$-$\overline{M}$ directions) as in Ref. 123 would not only give rise to a wrong magnitude, but even to the wrong sign.

With Pt_{fcc}/Co_{fcc} and Pt_{hcp}/Co_{hcp} [Fig. 6.1 (f,m)] the behaviour of ΔE_{SOC} appears different to the others. A strong DMI is calculated for the former, where we observe a change of sign at the BZ boundary, i.e. for antiferromagnetic (AFM) states. For the latter, the DMI is vanishing for $\mathbf{q} \to 0$[3], but its contribution is strongly increasing with $\mathbf{q}$.

In particular, for Co/Ir(111) and Pt_{hcp}/Co/Ir(111) $D_1 < 0$ (CCW rotation) having a comparably large magnitude as seen in Tab. 6.1, whereas $D_{eff} > 0$ (cf. Tab. 5.2 and 5.4). In order to match the non-trivial behaviour of the DMI, we need to include more neighbours for mapping the DMI. For $i > 1$, the DMI is competing with similar magnitude. This effect we address to frustration of DMI. In the following, we unravel the origin of this frustration.

6.3 Origin of frustration of DMI in Pt/Co/Ir interfaces

In order to understand why the DMI is frustrated in such a way, we take a detailed look into the element resolved energy contribution to the SOC (Fig. 6.2). The black, filled points correspond to the total contributions where the solid lines are the fits to the DMI as in Fig. 6.1. The coloured circles show the contribution of the respective element, where for Ir(111), it is the sum of all nine Ir layers.

For all investigated systems, the change of rotational sense of spin spirals states from CW to CCW is conducted by the Ir substrate contribution. In both Co/Ir(111) films [Fig. 6.2 (a,b)], the Ir(111) contributions qualitatively match the total SOC, where around the $\overline{\Gamma}$ point, Co reduces the strength of ΔE_{SOC}.

Adding a Pt_{fcc} layer on top of both films [Fig. 6.2 (c,d)] this Co contribution vanishes. The Ir substrate prefers CCW rotation of spin spiral states, whereas the Pt top layer counteracts with a large contribution. The DMI in these films is not vanishing due to a small phase shift of the Ir(111) and the Pt contributions. In Pt_{fcc}/Co_{fcc}/Ir(111), a slight CW preference in Ir(111) can be noticed for $\mathbf{q} \to 0$.

When the stacking of Pt is changed to hcp, [Fig. 6.2 (e,f)], the SOC contributions differ from the ones with Pt_{fcc}[4]. The favoured direction of spin rotation stemming from the Pt top layer is reversed and reduced in strength. The Co contribution counteracts with a slightly smaller value which would lead to an insignificant DMI considering only these two elements. In Pt_{hcp}/Co_{fcc}/Ir(111) and Pt_{hcp}/Co_{hcp}/Ir(111), the total ΔE_{SOC} is almost completely represented by the Ir(111) substrate.

[3] Note, that the first points of ΔE_{SOC} have vanishing contributions in the limit of the linear fitting region of the DMI. That's the reason for D_{eff} being almost zero.

[4] Note that in agreement with chapter 5, for Pt/Co/Ir(111) films we do not see any simple additive DMI contributions from Ir(111) and Pt, but a competition of the two contributions.

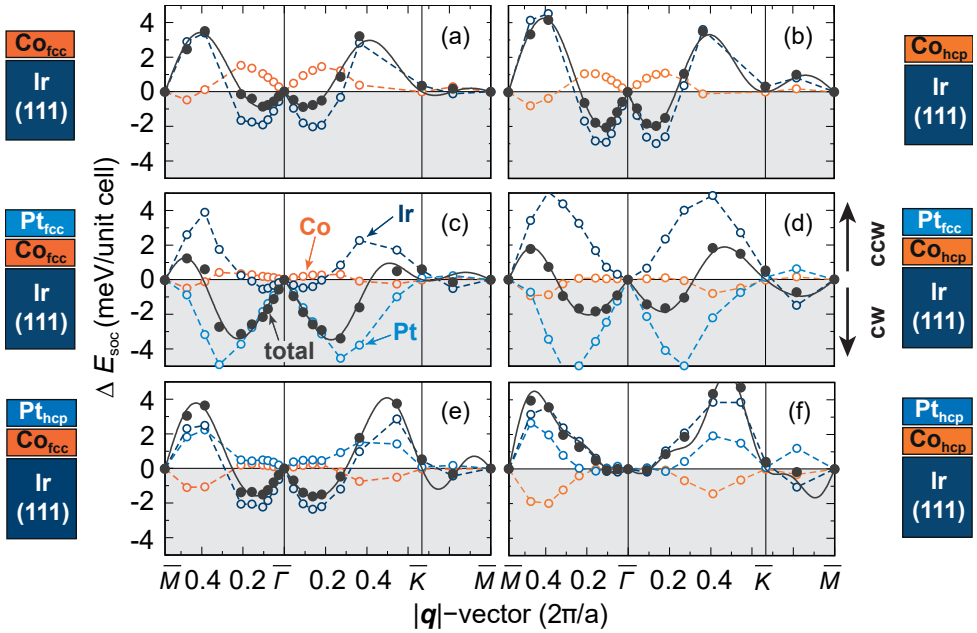

Figure 6.2 | Element resolved energy contribution due to spin-orbit coupling (SOC) to the energy dispersion of cycloidal spin spirals for Co/Ir(111) and Pt/Co/Ir(111). (a) Contribution due to SOC for Co_{fcc}/Ir(111) where positive positive values denote counterclockwise (CCW) rotation and negative values clockwise (CW) rotation. The black points show calculated values from DFT calculations and the black line is the fit to the atomistic spin model of the Dzyaloshinskii-Moriya interaction. Coloured points/lines represent the SOC contribution of the respective element. Note that the Ir(111) contribution (dark blue) of ΔE_{SOC} is the sum of all Ir layers. The coloured lines serve as guide to the eye. (b-f) Contribution due to SOC for Co_{hcp}/Ir(111) and Pt/Co/Ir(111), respectively.

From Fig. 6.2 it is obvious that Ir(111) is responsible for the exhibited DMI frustration, so a decomposition of its contribution is a reasonable consequence. Hence, we will analyse the film of Co_{hcp}/Ir(111) in more detail because there the effect can be distinctly seen. In Fig. 6.3, the contributions to ΔE_{SOC} of all layers in the film are presented [see App. A for Co_{fcc}/Ir(111) and Pt/Co/Ir(111)].

In (a), the total, Co and the Ir(111) contributions are presented as in Fig. 6.2. The Ir(111) substrate is decomposed into the single Ir layers from (b) to (j), where in the background the Ir(111) contribution is shown as reference.

ΔE_{SOC} is reduced in magnitude from layer to layer as expected (cf. Levy-Fert model [114]) and has a negligible contribution from the third layer beneath the surface [Ir(S-3) in Fig. 6.3 (e)]. The Ir surface layer has by far the largest contribution which almost reaches the strength of Ir(111) and we notice the distinct behaviour of the curve with its change of sign [Fig. 6.3 (b)]. This is not observed in the subsurface layer Ir(S-1) [Fig. 6.3 (c)], but reappears for Ir(S-2) [Fig. 6.3 (d)]. Conclusively, the sign change of the DMI, i.e. the DMI frustration is stemming from the Ir(111) substrate and to be more precise from the Ir surface layer at the Co interface. Note that without substrate, a Co/Ir bilayer does not show this effect. At least two Ir layers are needed to induce

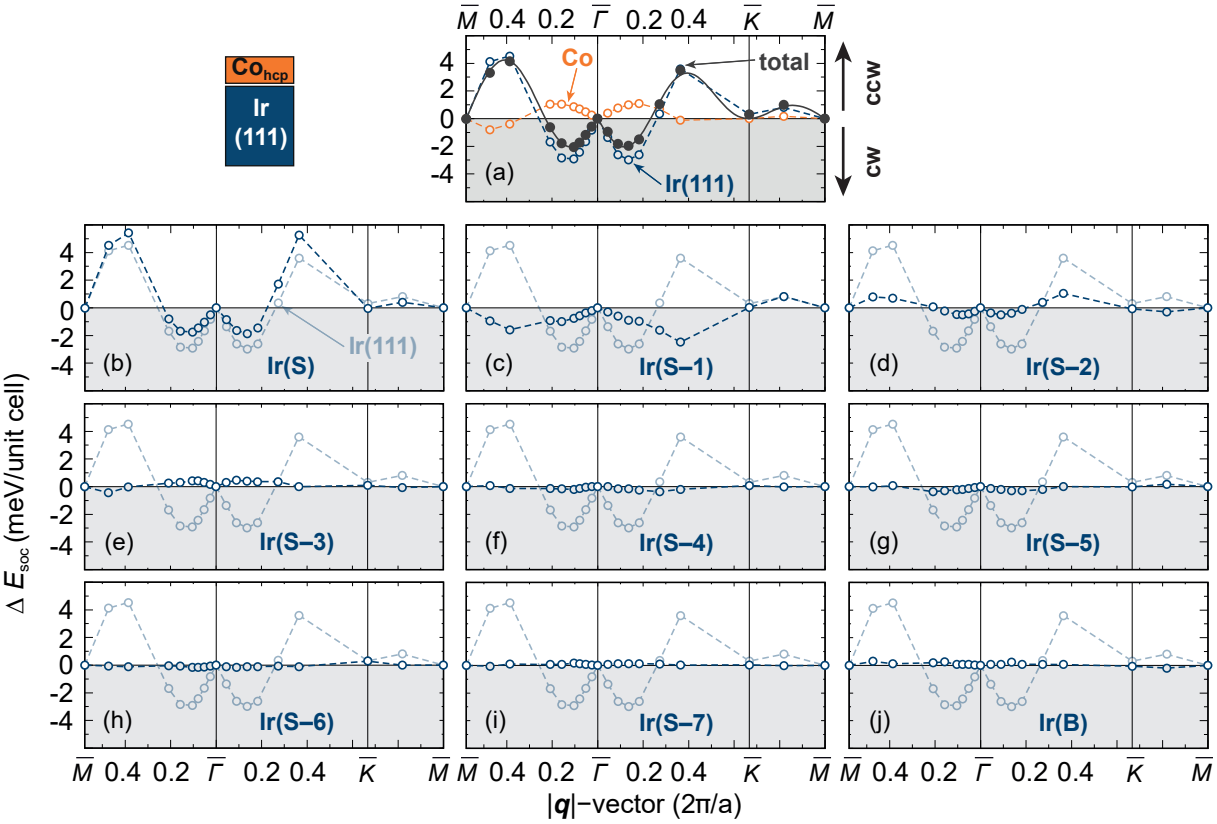

Figure 6.3 | Layer resolved energy contribution due to spin-orbit coupling (SOC) to the energy dispersion of cycloidal spin spirals for Co_{hcp}/Ir(111). (a) Element resolved energy contribution due to SOC as shown in Fig. 6.2. (b-j) Contribution due to SOC of each layer from the Ir(111) substrate presented in (a), where (b) is the contribution of the Ir(111) surface layer Ir(S), (c-i) are the correspondent Ir layers below Ir(S) and in (j) Ir(B) denotes the Ir bottom layer. In the background, the complete contribution of the Ir(111) substrate is shown.

it. In order to unambiguously clarify the origin of DMI frustration in these Co/Ir interfaces, a detailed description of the Ir(S) layer is needed.

We choose three spin spiral vectors **q** to analyse the change of electronic structure at the transition from CW to CCW preferring DMI. In Fig. 6.4 (a), the total SOC is presented, where the investigated states are highlighted in green, orange and red. For each state, we compare the local density of states (LDOS) of Co (b-d) and Ir(S) layer (e-g) in three columns. Fig. 6.4 (h-j) shows the energy resolved DMI contribution for positive and negative shifts $\delta\epsilon_{\mathrm{DMI}}$ with their sum and in (k-m), the effective integrated DMI energy is shown [cf. Eqs. (6.1)].

In collinear states, spin ↑ and spin ↓ states cannot hybridize, but in non-collinear structures such as spin spirals a certain mixing of the spin channels due to canting can be observed. This is the reason why the LDOS in both Co and Ir slightly change for the present spin spiral states.

Bands within the energy range of [−4 eV; −3 eV] exhibit large SOC contributions [Fig. 6.4 (h-j)]. The positions of these peaks match the ones of Ir(S) [Fig. 6.4 (e-g)]. In

the Co [Fig. 6.4 (b-d)], within this energy, some states occur, which are formed by hybridization with the Ir substrate. This can be seen from the comparison to the LDOS of a Co unsupported monolayer [cf. Fig. 5.4]. However, positive and negative SOC shifts are almost cancelling, so these bands are not contributing to the DMI as can be recognized in the effective integrated DMI [Fig. 6.4 (k-l)].

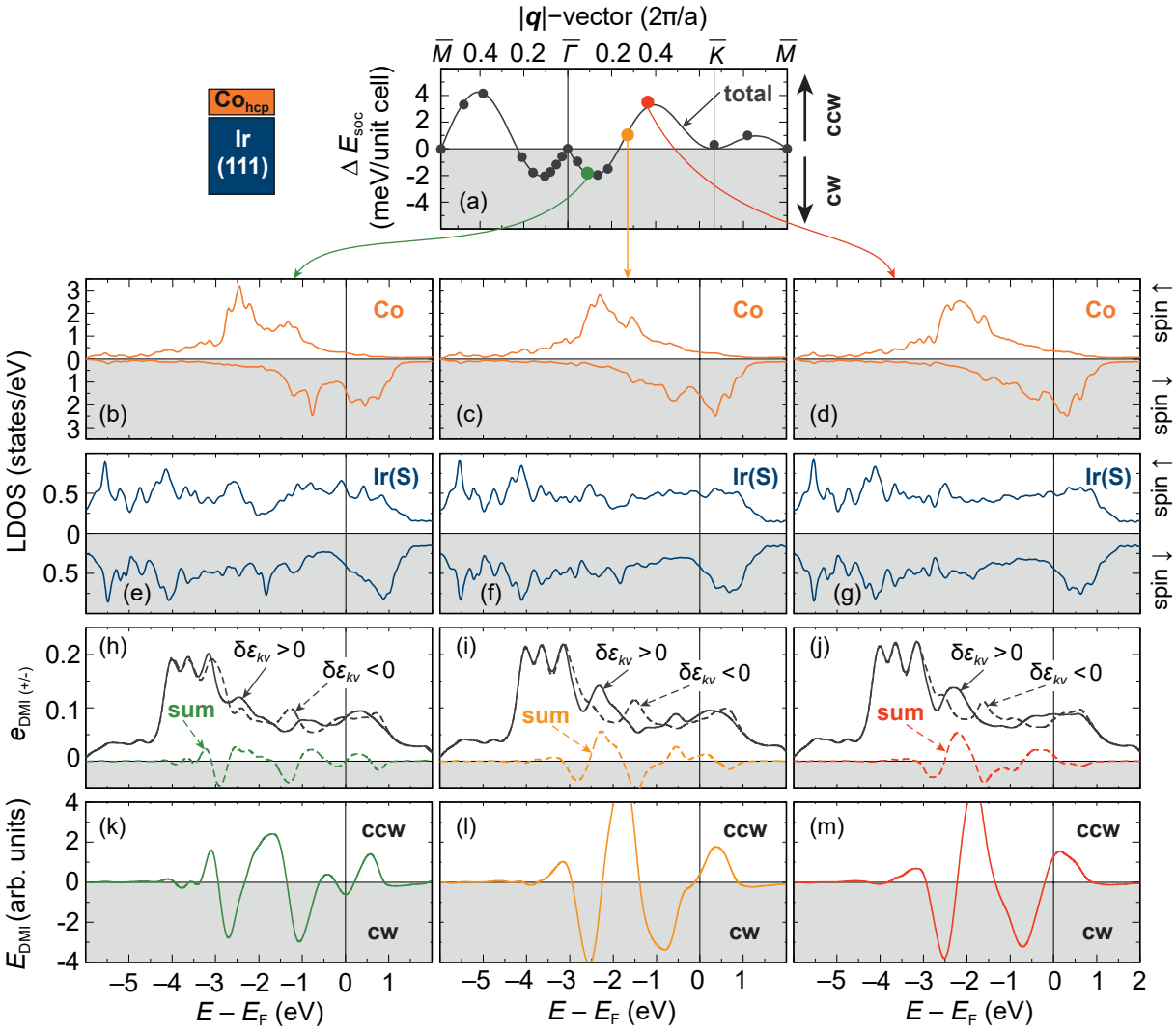

Figure 6.4 | Electronic structure analysis of three spin spiral states during the sign change of Dzyaloshinskii-Moriya interaction (DMI) for Co_{hcp}/Ir(111). (a) Total energy contribution due to spin-orbit coupling (SOC) as shown in Fig. 6.1 and 6.2. The three investigated states are marked with colours (green for the left, orange for the middle and red for right panel). (b-d) local density of states (LDOS) of the Co layer for the three marked states in (a). (e-g) LDOS of the Ir(111) surface layer Ir(S). Note the different scale from (b-d). (h-j) Energy resolved DMI contribution $e_{\mathrm{DMI}}(E-E_{\mathrm{F}})$ separated by positive (solid line, $\delta\epsilon_{k\nu} > 0$) and negative (dashed line, $\delta\epsilon_{k\nu} < 0$) energy shifts due to spin-orbit coupling (SOC). The dashed coloured curve describes the sum of the two curves. For more information, see Sec. 6.1. (k-m) Effective energy-integrated DMI energy E_{DMI}. Note that the energy resolved SOC contributions are broadened with a Gaussian function with a full width at half maximum of 0.1 eV.

In between −3 eV and −1 eV, the behaviour of the SOC contributions for the investigated spin spiral states looks qualitatively similar. Reducing the spin spiral period, at −2.5 eV the positive DMI contribution [Fig. 6.4 (h-j)] increases. This coincides with the broadening and height reduction of the largest peak in the spin ↑ channel of Co [Fig. 6.4 (b-d)]. Furthermore, when the DMI is changing from CW to CCW, a second important deviation can be noticed directly below E_F. From both the sum in and the effective DMI [Fig. 6.4 (h-j) and (k-m)], the contribution of $\delta\epsilon_{k\nu} > 0$ and thus, CCW preference of DMI increases. Summing the negative and positive contributions of $\delta\epsilon_{k\nu}$ in Fig. 6.4 (h), a small minimum at −0.25 eV occurs which is at the position of a Ir(S) state in the spin ↑ channels and also visible in the Co layer [cf. Fig. 6.4 (b,e)]. Again, these are hybridizing Co-Ir states changing their character with increasing non-collinearity.

In Fig. 6.4 (f), this spin ↑ peak at −0.25 eV in Ir(S) is almost vanished and consequently, the DMI contribution is positive. It shows the largest positive contribution at the ∼ 90° spin spiral state within a broader energy range from −0.5 eV to E_F [Fig. 6.4 (j)]. From these results, this hybridizing state in the Ir(S) layer seems to be responsible for the strong DMI frustration and the change of rotation.

6.4 Effect of DMI frustration on non-collinear magnetic structures in $\mathrm{Co_{hcp}}$/Ir(111)

So far, we described the occurrence of DMI frustration based on first-principles calculations. In the following part, its effect on non-collinear spin structures, i.e. DWs and skyrmions will be investigated. We apply spindynamics simulations on the exemplary film of $\mathrm{Co_{hcp}}$/Ir(111) where we take four different magnetic interaction parameter sets into account, ranging from the effective nearest neighbour approximation (J_eff, D_eff) to the atomistic description of the spin model (J_{ij}, D_{ij}). To see the effect coming from either exchange or DMI frustration, we combine the two descriptions (J_eff, D_{ij} and J_{ij}, D_eff). In Fig. 6.5 (a,b), we investigate DW properties (as seen in the inset), whereas in Fig. 6.5 (c,d,e) the results on single skyrmions in the FM background are shown.

DWs are energetically slightly unfavourable compared to the FM ground state [Fig. 6.5 (a)] which we also investigated previously (Ch. 5). There, the effective nearest neighbour approximation and the analytic formulas of the DW energy and width, Eqs. (5.1a) and (5.1b), respectively, has been applied.

Here, with the same magnetic interaction parameters (J_eff and D_eff) applying spindynamics simulations, we can reproduce the DW properties of Sec. 5.2, where DWs are 21 meV/nm higher in energy compared to the FM ground state [Fig. 6.5 (a)]. In relation to the previously studied films of Pt/Co/Ir(111) (Sec. 5.5) this energy scale is small.

When exchange frustration is considered (J_{ij}, D_eff), the energy slightly decreases by

about 2 meV/nm. As seen in Fig. 6.1, Co_{hcp}/Ir(111) only shows moderate exchange frustration so its impact on the DW energy is expected to be small. Reversing the frustration effects (effective nearest neighbour approximation of exchange J_{eff} and DMI frustration, D_{ij}), we see a drop of the DW energy by over 10 meV/nm. This shows that DMI frustration can affect the DW energy here much more than exchange frustration. With the atomistic description of interactions, the DW energy is the smallest, where obviously the shift from (J_{eff}, D_{ij}) to (J_{ij}, D_{ij}) is the same as for (J_{eff}, D_{eff}) to (J_{ij}, D_{eff}).

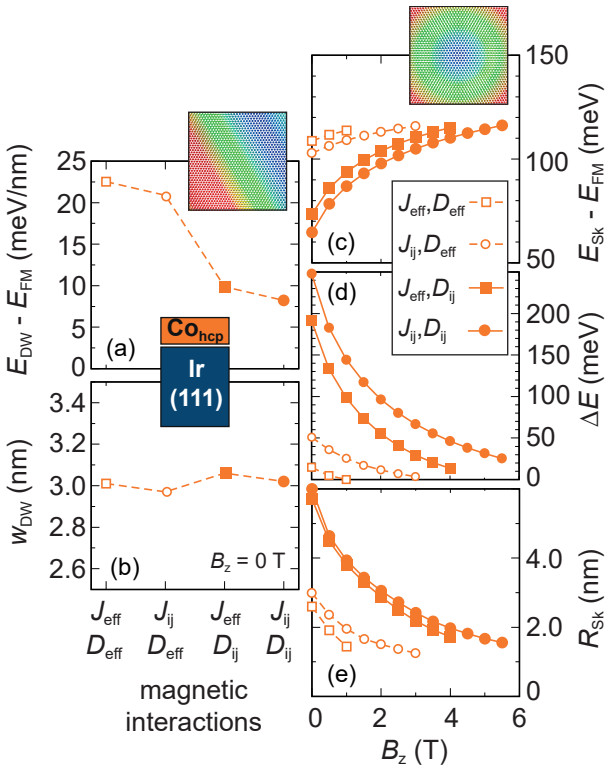

Figure 6.5 | Spindynamics simulations for Co_{hcp}/Ir(111) applying different descriptions for magnetic interactions. (a) Domain wall (DW) energies (meV/nm) without external magnetic field depending on different magnetic interaction parameter sets. (b) Domain wall (DW) width in nm. (c) Skyrmion energy of a single skyrmion with respect to the ferromagnetic (FM) state (meV) dependent on an applied magnetic field B_z (T). (d) Energy barrier ΔE (meV) for a skyrmion collapse into the FM state obtained via geodesic nudged elastic band calculations[5]. (e) Skyrmion radius (nm). Open squares denote simulations applied with the effective nearest neighbour approximation of exchange J_{eff} and Dzyaloshinskii-Moriya interaction (DMI) D_{eff}, open circles show the fully atomistic description of the exchange J_{ij} with D_{eff}, whereas filled squares correspond to J_{eff} and D_{ij}. Filled circles represent the fully atomistic description for both J_{ij} and D_{ij}. Note the different axes on the left and right. The insets show the obtained spin structures using the fully atomistic description at $B_z = 0$ T.

In Fig. 6.5 (b), the change of the DW width is presented. Regardless of the applied model, it remains almost constant at about 3 nm. From Eq. (5.1b), the DW width is only dependent on exchange and anisotropy. However, here we see a small variation in the width when changing the description of the DMI. This is unexpected, but also the variation is below 0.05 nm.

[5] Note that the energy barrier for the atomistic description does not reach zero. Due to the large damping in the spindynamics simulations, the skyrmions for larger magnetic fields are destroyed. Nevertheless, the results do not change.

Due to the small DW energy in (a), we also expect skyrmions to be metastable in the FM ground state. Fig. 6.5 (c) shows the energy cost of a single skyrmion in a FM background with respect to an applied magnetic field B_z. For all considered descriptions for the magnetic interactions, skyrmions can be metastable states in the absence of magnetic field[6]. Irrespective of the description, an energy loss of skyrmions with respect to the FM state of about $\sim 120\,\mathrm{meV}$ will not allow the stabilization of skyrmions. This can be seen when the largest skyrmion energies for all curves are taken into account where all curves show an asymptotic behaviour to that energy.

Using the effective nearest neighbour description (open squares and dashed line), the skyrmion energy at $B_z = 0\,\mathrm{T}$ is around 110 meV. When a magnetic field is applied, this energy increases due to the Zeeman interaction and consequently, skyrmions remain stable only up to 1 T where the imaginary limit of 120 meV is reached. Frustration of exchange interaction (open circles with dashed line) shifts the curve to lower energies and allows for skyrmions to be stabilized up to 3 T.

In accordance with the DWs [cf. Fig. 6.5 (a)], the energy of the skyrmion drops when we consider D_{ij} in the description. Without magnetic field, they are unfavourable by about 75 meV (J_{eff}, D_{ij} with filled squares and solid line). The energy loss with magnetic field now is larger compared to the D_{eff} case, where the limit of 120 meV is reached at 4 T. Using the atomistic description [points with solid line in Fig. 6.5 (c)], the skyrmion energy is the lowest and thus the structures are stable up to 5.5 T.

While with spindynamics the energy difference between the skyrmion (initial) state and the FM (final) state is calculated, the GNEB method gives rise to the energy of the SP (transition) state in between those states. The energy barrier of the skyrmions applying the effective nearest neighbour approximation of both exchange and DMI is about 20 meV in the absence of magnetic field [Fig. 6.5 (d)]. With exchange frustration (J_{ij}, D_{eff}), it increases to 50 meV. The enhancement of the stability is smaller than for Pd/Fe/Ir(111) [134] because $\mathrm{Co_{hcp}}$/Ir(111) shows smaller exchange frustration. When including frustration of DMI, the energy barrier can be enhanced by a factor of four. Thus, the skyrmions including frustration of DMI can be stabilized for broader range of magnetic field [Fig. 6.5 (c,d)].

This behaviour can be explained by large deviation in both skyrmion size and the different shapes of the skyrmions [135]. The skyrmion radius can differ by over a factor of two comparing the results for D_{eff} and D_{ij} [Fig. 6.5 (e)] leading to the large deviations in the energy barrier [Fig. 6.5 (d)]. As a consequence, with D_{ij}, skyrmions are more stable for a larger range of magnetic field. With the help of different test parameters of magnetic interactions, we will clarify this unexpected result of the enhanced energy barrier due to DMI frustration.

[6] We refer the stability of skyrmions also to the fact that they are not destroyed in spindynamics simulations.

6.5 DMI frustration in spindynamics

In the previous section, we noticed that the description of the DMI can have a large impact on the properties of non-collinear spin structures. Especially for skyrmions, changing from effective nearest neighbour DMI to the atomistic description leads to differently sized structures. We now want to investigate the role of DMI in more detail. Therefore we compare different artificial sets of magnetic interaction parameters of DMI while keeping the exchange at $J_{\text{eff}} = 10\,\text{meV}$ and an out-of-plane MAE at $K = -1\,\text{meV}$. The starting point of the DMI is the effective nearest neighbour $D_{\text{eff}} = -1.3\,\text{meV}$. With these interactions, it is ensured that skyrmions can be stabilized in the FM ground state for different magnetic fields. This is described below.

In Fig. 6.6, the energy dispersions for all test parameter sets are presented. The energy contribution due to SOC shows the reference parameter D_{eff} (red line) with six different atomistic parameter sets m in which seven neighbours are taken into account, D_{ij}^{m}, $m \in (1,\ldots,6)$ [Fig. 6.6 (a)].

The dispersions of D_{ij}^{m} contain different degrees of DMI frustration – the competitive DMI contributions of the next neighbours is differing. All parameter sets try to match the effective nearest neighbour approximation D_{eff} for $\mathbf{q} \to 0$ in order to see, how the skyrmion properties vary when the DMI contribution is changed for larger $\mathbf{q}$. While the region around the $\overline{\Gamma}$ point appears crucial for both energy with respect to the FM state and size of skyrmions, the larger $\mathbf{q}$ vectors might be crucial for the energy barrier because the SP structures at the transition state before the collapse of a skyrmion shows a small structure with larger angles between adjacent spins. In Fig. 6.6 (b), we analyse the energy differences of the test parameter sets with respect to D_{eff} around the $\overline{\Gamma}$ point. The deviation between the curves varies for the different D_{ij}^{m}; however, for all D_{ij}^{m} the deviations are in a very small energy window [Fig. 6.6 (b)].

It is important to recall these differences since they are crucial in the following investigation: The energy contribution due to SOC of D_{ij}^{1} (dark green dashed line) is larger than D_{eff} for small $\mathbf{q}$ so that a canting of the spin structures with small angles is preferred by D_{ij}^{1}. The opposite holds true for D_{ij}^{2} (dark blue dashed line) which is smaller than D_{eff} for $|\mathbf{q}| < 0.1\,{}^{2\pi}/_{a}$. D_{ij}^{3} (orange dashed line) also prefers more canted states with small angles. This also holds true for D_{ij}^{4} (bright green dashed line), whereas here, the preference is smaller and for states $|\mathbf{q}| > 0.1\,{}^{2\pi}/_{a}$ a canting loses energy. A more drastic change is seen for D_{ij}^{5} (bright blue dashed line), where only in a narrow region around $\overline{\Gamma}$, a canting is preferred over D_{eff}. D_{ij}^{6} (violet dashed line) shows the best agreement with D_{eff} for small $\mathbf{q}$. The deviation for large $\mathbf{q}$ on the other hand is the largest for D_{ij}^{6} among all parameter sets [Fig. 6.6 (a)].

Fig. 6.6 (c) shows the resulting full energy dispersion including exchange, DMI and MAE. For every parameter set, the FM is the ground state and we only see a very small deviation of the energy minima [Fig. 6.6 (d)]. The sets of D_{ij}^{5} and D_{ij}^{3} hold a smaller

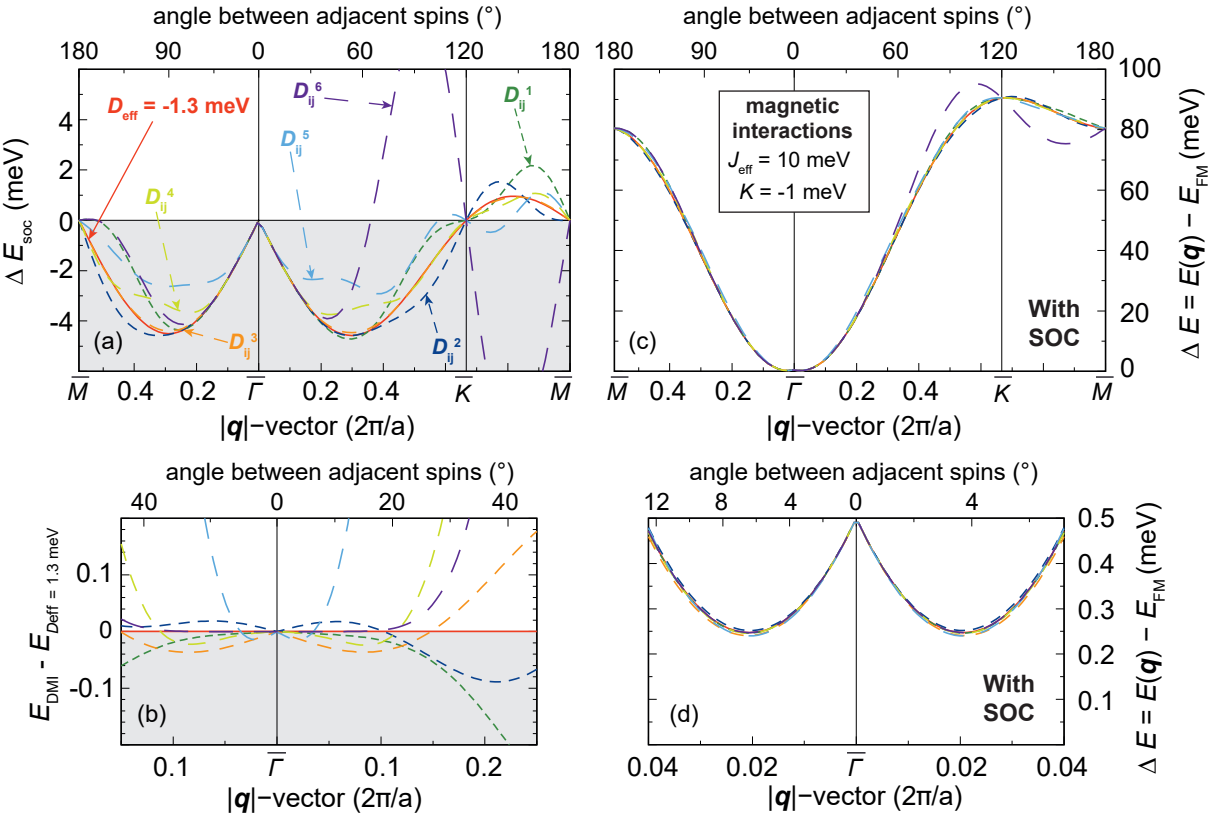

Figure 6.6 | Energy dispersions $E(\mathbf{q})$ of different magnetic interaction parameter sets for the Dzyaloshinskii-Moriya interaction (DMI). (a) Energy contribution due to spin-orbit coupling (SOC) applying the effective nearest neighbour approximation for DMI $D_{\text{eff}} = -1.3\,\text{meV}$ (red solid line) and test parameter sets using the atomistic description of D_{ij}. Each curve should match the effective nearest neighbour approximation for $\mathbf{q} \to 0$. The second x axis represents the occurring angles in the spin spirals. (b) Deviation of the dispersions of D_{ij} from D_{eff}. (c) Complete energy dispersion $E(\mathbf{q})$ including the effective nearest neighbour exchange $J_{\text{eff}} = 10\,\text{meV}$ and the uniaxial out-of-plane magnetocrystalline anisotropy energy of $K = -1\,\text{meV}$. (d) Zoom image of (c) around the minimum of the curves.

energy minimum than the reference set of D_{eff}, whereas D_{ij}^2 the energy minimum is at a larger energy. For the other sets, the minima almost match perfectly.

We perform spindynamics simulations and GNEB calculations to calculate the energy of skyrmions with respect to the FM state and energy barrier of the skyrmions for all parameter sets. The result is presented in Fig. 6.7.

For the energy of skyrmions [Fig. 6.7 (a)], very small deviations can be observed for all parameter sets. The deviations of two parameter sets are conspicuous, D_{ij}^3 (orange) and D_{ij}^5 (light blue). The former shows an energy gain compared to the reference parameter of $D_{\text{eff}} = -1.3\,\text{meV}$. This can be explained by the difference of the DMI dispersion [cf. Fig. 6.6 (b)] where for D_{ij}^3 a canting of spins gains energy. For D_{ij}^5 the opposite holds true even though for very small $\mathbf{q}$ vectors, there is a small energy gain. All other parameter sets show less deviations, even though, from Fig. 6.6 (a), the total

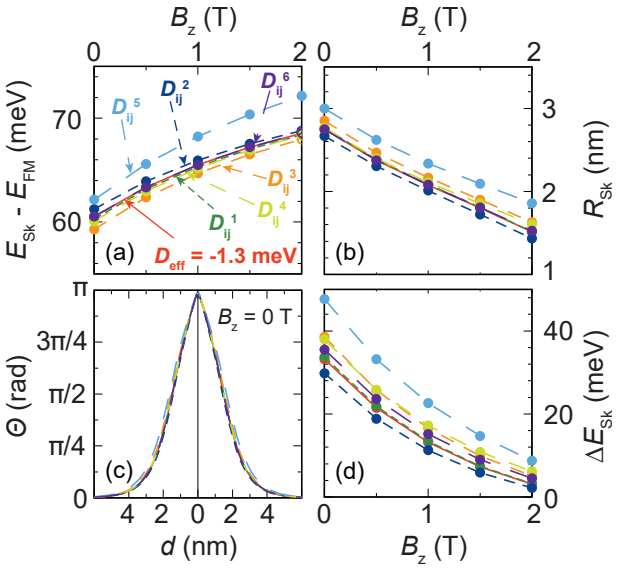

Figure 6.7 | Spindynamics simulations and geodesic nudged elastic band calculations using different magnetic interaction parameter sets for the Dzyaloshinskii-Moriya interaction. (a) Skyrmion energy of a single skyrmion with respect to the ferromagnetic (FM) state (meV) dependent on an applied magnetic field B_z(T). (b) Skyrmion radius (nm) applying the in-plane lattice constant of Ir(111). (c) Skyrmion profile for $B_z = 0$ T and (d) Energy barrier ΔE of a skyrmion for a collapse into the FM ground state. We include the effective nearest neighbour exchange $J_{\text{eff}} = 10$ meV and the uniaxial out-of-plane magnetocrystalline anisotropy energy of $K = -1$ meV.

DMI dispersion of D_{eff} and D_{ij}^3 is the least deviating one concerning the average deviation along the full $\overline{M}$-$\overline{\Gamma}$-$\overline{K}$-$\overline{M}$ direction. From that we can conclude that the results of the spindynamics simulations and the deviations of the energies is dependent on the deviation of the SOC contributions for $|\mathbf{q}| < 0.1\, 2\pi/a$. In the case of D_{ij}^6 (violet) we therefore do not observe any difference [Fig. 6.7 (a)].

The connection between the energy dispersions and the spindynamics result [Fig. 6.7 (a)] is almost opposite to that of the skyrmion radius [Fig. 6.7 (b)]. When the DMI for $|\mathbf{q}| < 0.1\, 2\pi/a$ is larger, the skyrmions increase in size. However, the radius of parameter set D_{ij}^5 shows a contradiction. D_{ij}^5 is larger for $|\mathbf{q}| < 0.04\, 2\pi/a$, a small canting of the spin structure is preferred which ends up in slightly larger skyrmions compared to D_{eff}. Exemplary, we show the skyrmion profiles in the absence of magnetic field in Fig. 6.7 (c).

We want to see how stable the skyrmions are against the collapse into the FM state and calculate the energy barrier for that process applying the GNEB method. In systems with effective nearest neighbour descriptions, the energy barrier increases with the size of skyrmions as seen comparing Fig. 6.7 (c) and (d), which is also reported in the literature, even though the shape of the skyrmion has to be taken into account [135]. The link between size and barrier can also be observed for the test parameter sets with two exceptions: The skyrmions of D_{ij}^4 are smaller than for D_{ij}^3 [Fig. 6.7 (c)], but show the same energy barrier [Fig. 6.7 (d)]. Furthermore, the descriptions of D_{eff} and D_{ij}^6 (violet) show the exact same behaviour in spindynamics [Fig. 6.7 (a,b,d)], but the energy barrier for D_{ij}^6 is slightly enhanced [Fig. 6.7 (d)]. Note that the energy scale is very small and tiny calculational errors cannot be excluded with perfect certainty.

However, this result has to be separated into several steps. First, taking D_{ij}^4 and D_{ij}^3

into account for which almost the exact energy barrier is found [Fig. 6.7 (d)], the DMI frustration for D_{ij}^4 is larger than in D_{ij}^3, i.e. the DMI contributions of different neighbours is larger. Even though for small $\mathbf{q}$, D_{ij}^4 is smaller than D_{ij}^3 [cf. bright green dashed line vs. orange dashed line in Fig. 6.6 (b)], for large $\mathbf{q}$ in Fig. 6.6 (a), it is slightly larger. When collapsing a skyrmion, the angles between adjacent spins get larger because the skyrmion shrinks in size. Since the energy differences in the energy dispersions are tiny compared to the overall energies, this effect can be seen as negligible in our calculations[7]. The same holds true when comparing D_{eff} and D_{ij}^6.

The number of neighbouring spins with large angles is very little and thus the energy deviations from different DMI parameters are negligible. Conclusively these results hold true when the descriptions of the effective nearest neighbour approximation and atomistic spin model will end up in the same ground state properties of the spindynamics simulations. However, in practice this is not possible when the underlying data for the descriptions are DFT calculations. There, these deviations will occur as seen in Fig. 6.5.

6.6 Conclusion

In this chapter we investigated the role of DMI frustration in Pt/Co/Ir interfaces. We explained that describing the DMI within the effective nearest neighbour approximation D_{eff}, can lead to wrong results of DMI when examining non-collinear states with large angles between adjacent spins. In that view, the frustration of DMI in Co/Ir(111) and Pt/Co/Ir(111) films can lead to wrong results when calculations on the DMI in these films are carried out for unsuited non-collinear spin structures. Often, the DMI is calculated from DFT supercell calculations on spin spiral states including SOC with 90° between adjacent spins. As shown here, such calculations can give wrong results when DMI frustration occurs.

The DMI frustration is mediated by the Ir(111) substrate, where especially both the hybridization of Ir and Co at the interface as well as the spin mixing in non-collinear states is taking place. In the exemplary Co_{hcp}/Ir(111), the responsible states can be narrowed down to hybridized Ir(S) states directly below the Fermi energy. These states vanish due to increasing non-collinearity changing the sign of the DMI from CW to CCW.

In Co_{hcp}/Ir(111), the frustration of DMI is shown to have a strong impact on the stability and size of DWs and skyrmions, so that within the effective nearest neighbour approximation for exchange and DMI, skyrmions are smaller by a factor of two and stable from 0 T to 1 T, while taking frustration effects into account, the stability increases up to 5.5 T where the driving mechanism for this increase is the

[7] Note that we do not gain further insight when comparing the angle distribution of the skyrmions since the results are straightforward to our interpretation. This is why the angles are not presented in this discussion.

DMI frustration.

We further presented a detailed atomistic spindynamics study on DMI frustration with respect to the stability and energy barrier of skyrmions. Since the DMI is typically a small interaction compared to the exchange, frustrated DMI does not have the large impact on both investigated properties in contrast to the large effects found due to exchange frustration [134]. When the skyrmion structures do have the same profile, the deviations of the energy barrier are vanishingly low. On the contrary, when skyrmions are stabilized due to magnetic interaction parameters based on DFT, it is highly unlikely that the profile will match and consequently the skyrmion properties can differ on a large scale.

6.7 Outlook

As presented, the DMI frustration can lead to more stable non-collinear objects such as skyrmions. However, its origin as well as effect are highly complex and should be studied in even more detail as in the present thesis. To evidently clarify the origin, more insight into the physics of the spin spiral structures is needed. This includes orbital resolved LDOS calculations to see which orbital in the electronic structure is responsible to change the sign of DMI.

It has been proposed that spin-orbit torques and orbital moments can play an important role for the DMI [186]. In order to see their impact, supercell calculations of different spin spiral states are required which are computationally demanding. The combination of such supercell calculations with those applying the generalized Bloch theorem can serve as massive tool with the deepest insight into the physics of DMI.

Furthermore, a continuative study of the impact of DMI frustration on skyrmions can be seen as promising since it cannot be excluded that – especially in GNEB calculations – a varying number of different investigated states will lead to the same result for different parameter sets. In this view, the two test parameter sets D_{eff} and D_{ij}^{6} of Sec. 6.5 are very promising since spindynamics results are completely degenerate.

6.8 Test calculations

While the results presented above are well suited to understand the physical properties of the studied systems, this chapter shows additional information about calculations and how to treat and interpret the calculations themselves. Since DFT is always relying on simplification and partial assumptions, possible errors and questions due to different approaches are discussed in the following.

In the first part, we will discuss the convergence of our calculations with respect to the thickness of our substrate. Since spin-polarization effects and changes in the magnetic moment are typically not taken into account in the classical Heisenberg model, conical spin spirals are calculated in the second part to exclude the change of magnetic moment.

6.8.1 Dependence of magnetic interactions on substrate thickness

In the sections above (Ch. 5 and Ch. 6), the results are shown for calculations with nine (for exchange and DMI, partial MAE calculations) or 13 (for some MAE calculations) Ir layers. In this section, we want to compare these results with calculations assuming five layers of Ir(111) for the substrate.

Fig. 6.8 shows the energy dispersions for Co/Ir(111) and Pt/Co/Ir(111) for all possible stackings of Co and Pt without SOC. The grey points (grey squares) and curves correspond to calculations with nine (five) Ir(111) layers. Around the FM state ($\overline{\Gamma}$ point), the energy dispersions for both kind of calculations do not deviate, so the ground state exchange energy can be well described even with five layers of Ir(111). Deviations arise when leaving the ground state for higher $\mathbf{q}$ vectors up to the AFM state. The differences in the curves will lead to small deviations in the frustration of exchange and therefore they affect the stability of non-collinear magnetic states.

As for the MAE in the previous chapters, the DMI contribution deep in the substrate is vanishing since the broken inversion symmetry is required. In our calculations, this contribution should vanish as well; however, due to the modelling of the substrate with finite number of layers, quantum well states can occur at the bottom layers. These give rise to an unphysical DMI contribution in the system.

Fig. 6.9 shows the energy contribution due to SOC for the calculated systems for both, five and nine Ir layers. In the left row the total contributions of SOC including the Ir bottom layers are presented. The latter are shown in the middle row. The SOC in the bottom layer for the thicker substrate is almost vanishing, but we see significant contributions of the bottom layer in systems with only five Ir(111) layers (middle panels in Fig. 6.9). That is why, the calculations with nine layers are taken as a good reference in this case. Especially in Co/Ir(111), this contribution could give rise to problems when interpreting the DMI.

Comparing the total DMI contribution, we do not see a trend whether systems with five layers give larger or smaller DMI. Around the FM ground state, in Fig. 6.9 (a,g,j,m),

both calculations match quite well, while for Co_{hcp}/Ir(111) in (d), the DMI calculated with a five layers substrate is significantly enhanced.

One way to handle such problems is to simply subtract the DMI contribution of the bottom layer (right panels of Fig. 6.9). Depending on the sign of the bottom layer contribution, the total DMI of the different calculations will differ more or less. Like before, there is no significant trend. For Co_{fcc}/Ir(111), the calculations with five layers seem to overestimate the DMI, while for Pt_{hcp}/Co_{fcc}/Ir(111), it seems to underestimate it.

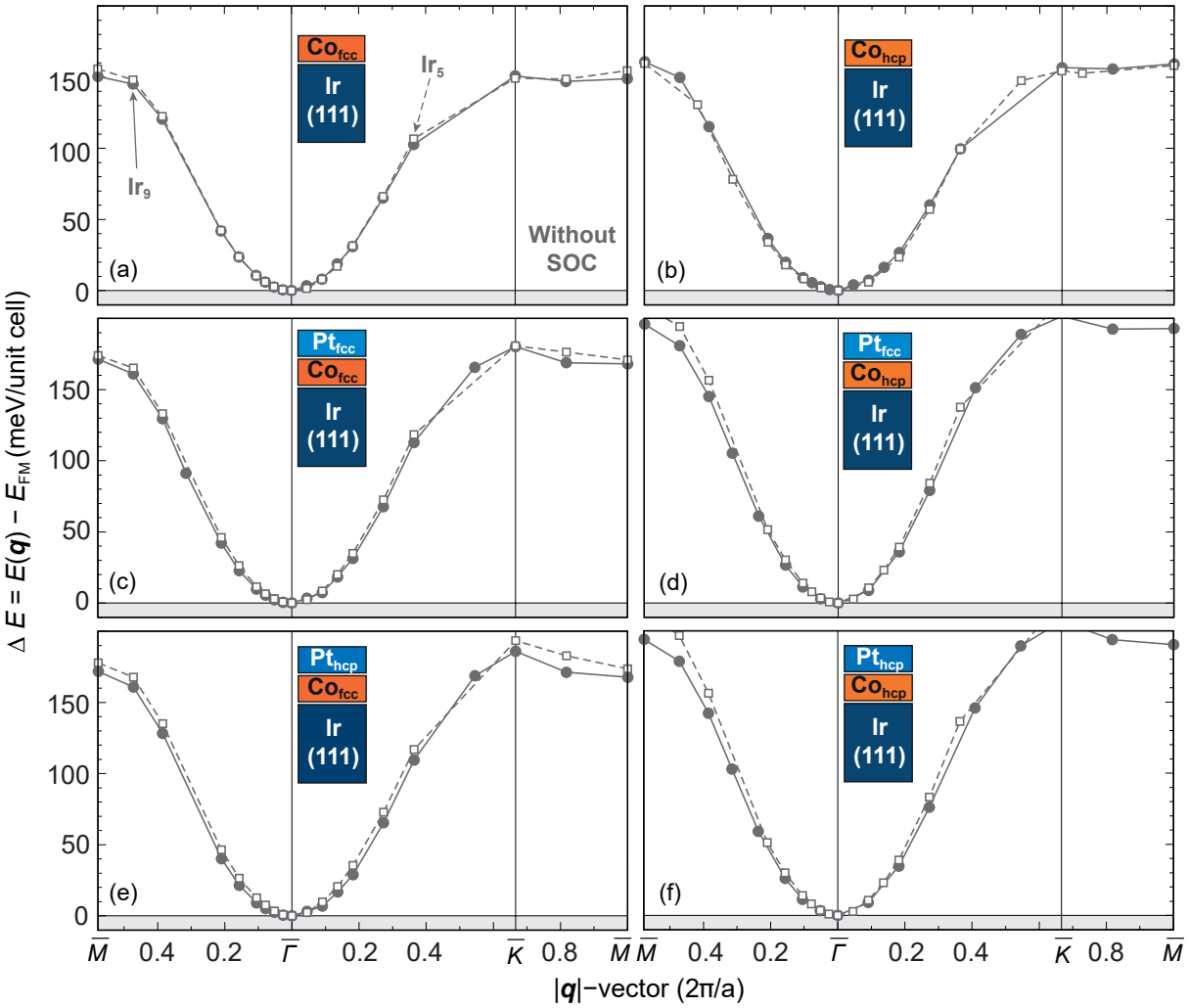

Figure 6.8 | Full energy dispersions $E(\mathbf{q})$ of flat cycloidal spin spirals for Co/Ir(111) and Pt/Co/Ir(111) without spin-orbit coupling applying different thicknesses of the Ir(111) substrate. (a) Energy dispersion along the high symmetry path $\overline{\Gamma}$-$\overline{M}$ and $\overline{\Gamma}$-$\overline{K}$-$\overline{M}$ of the two-dimensional Brillouin zone for Co_{fcc}/Ir(111). Filled points with solid lines (for calculations with nine Ir(111) layers) and open squares with dashed lines(for calculations with five Ir(111) layers) show calculated energies from DFT with respect to the ferromagnetic (FM) state. (b) Co_{hcp}/Ir(111). (c) Pt_{fcc}/Co_{fcc}/Ir(111). (d) Pt_{fcc}/Co_{hcp}/Ir(111). (e) Pt_{hcp}/Co_{fcc}/Ir(111). (f) Pt_{hcp}/Co_{hcp}/Ir(111). Note that the lines serve as guide for the eye.

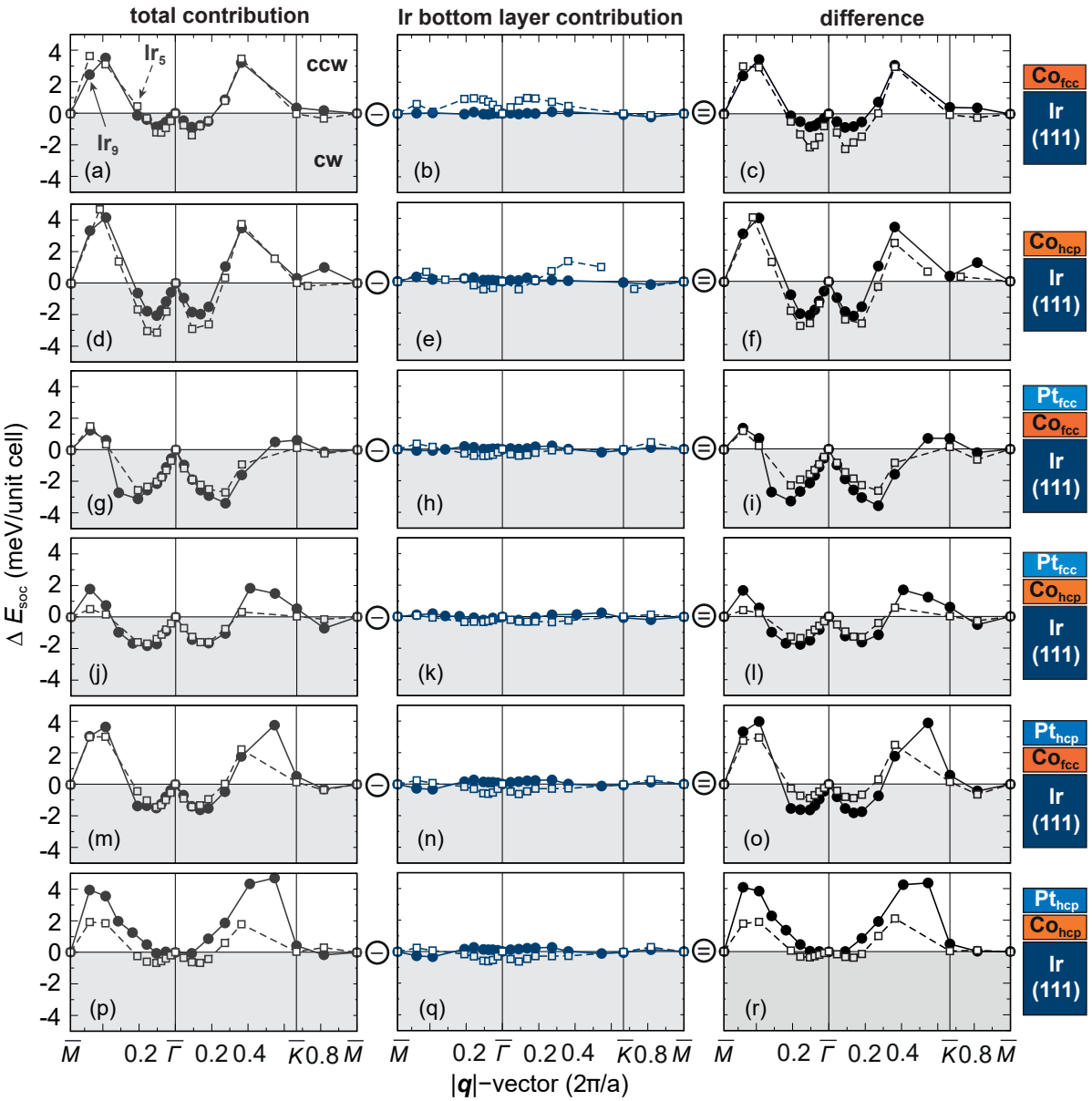

Figure 6.9 | Energy contribution due to spin-orbit coupling (SOC) to the energy dispersion of cycloidal spin spirals for Co/Ir(111) and Pt/Co/Ir(111) applying different thicknesses of the Ir(111) substrate. (a) Total SOC contribution of Co_{fcc}/Ir(111). The filled circles with solid lines represent DFT calculations with a nine Ir(111) layered substrate and open squares with dashed lines show DFT calculations with five layers of Ir(111). The lines serve as guide to the eye. (b) SOC contribution of the Ir bottom layer for Co_{fcc}/Ir(111). (c) Subtracted SOC contribution, where the contribution of the Ir bottom layer is subtracted from the total contributions. (d,e,f) Same plot as (a,b,c) for Co_{hcp}/Ir(111). Calculations on Co_{hcp}/Ir(111) with five layers of Ir(111) were performed by Bertrand Dupé[8]. (g-r) Same plots as (a,b,c) for all Pt/Co/Ir(111).

[8]Nanomat/Q-mat/CESAM, Université de Liège, B-4000 Sart Tilman, Belgium

In the beginning of Ch. 5, the problem of the vacuum boundary on the calculations has been shown for the MAE. Here, we will present the resulting values K for systems with five layers and nine layers of Ir(111). Especially for the MAE (cf. Figs. 5.2 and 5.6), it is crucial to calculate systems with more substrate layers.

Table 6.2 | Calculated values for magnetocrystalline anisotropy energy for Co/Ir(111) and Pt/Co/Ir(111) applying different thicknesses of the Ir(111) substrate. Shown are the values for calculations using a Ir(111) substrate with either five or nine layers. K is given in meV and $K < 0$ ($K > 0$) denotes an out-of-plane (in-plane) easy magnetization axis. For five layers, two to three Ir layers are taken into account and for nine layered substrate, five to six, depending on the constant region in the layers.

System	5	9
$Co_{fcc}/Ir(111)$	−1.62	−0.84
$Co_{hcp}/Ir(111)$	−2.02	−0.63
$Pt_{fcc}/Co_{fcc}/Ir(111)$	−0.03	−0.97
$Pt_{fcc}/Co_{hcp}/Ir(111)$	−0.44	−0.84
$Pt_{hcp}/Co_{fcc}/Ir(111)$	+0.11	+0.69
$Pt_{hcp}/Co_{hcp}/Ir(111)$	−0.25	+0.38

6.8.2 Conical spin spiral states

The applied Heisenberg model includes only a single magnetic atom in the unit cell. Effects of spin-polarization or induced magnetic moment of non-magnetic material or the variation of the magnetic moment in spin spiral calculations, e.g. changing the magnetic moment for different states, are not captured. Since in spin spirals, it is not obvious, which directions the moments of adjacent layers to a magnetic material will have in experiments, we apply spin spirals in all layers of the film. Assuming that the magnetic moment of the elements will not change drastically, we apply an "effective" Heisenberg model, in which we effectively include these assumptions. Here, we present spin spiral calculations where we compare flat ones ($\theta = 90°$) in which the magnetic moments vary and conical ones ($\theta = 9°$), where the magnetic moments remain constant.

Fig. 6.10 shows three exemplary systems for this investigation, where in (a-c), the SOC is neglected. We see that all spin spiral energies are in good agreement, regardless of the calculational setup. Around the FM state – when applying the effective nearest neighbour approximation – both calculations give the same result[9]. When leaving the vicinity of the ground state, deviations will appear. The same is seen in (d-f), where the SOC contribution ΔE_{SOC} is shown and the effect of DMI frustration appears.

We can address this behaviour to various reasons: Due to normalization, spin spiral states with small opening angles θ are more sensitive to small errors within the calculations. We assume the best accuracy of spin spiral energies, when the spin spiral vector $\mathbf{q}$ matches a k point in the BZ. A small deviation of $\mathbf{q}$ and k can lead to

[9] Note, that energy dispersions of spin spirals need to be normalized by $1/\sin(\pi/\theta)^2$

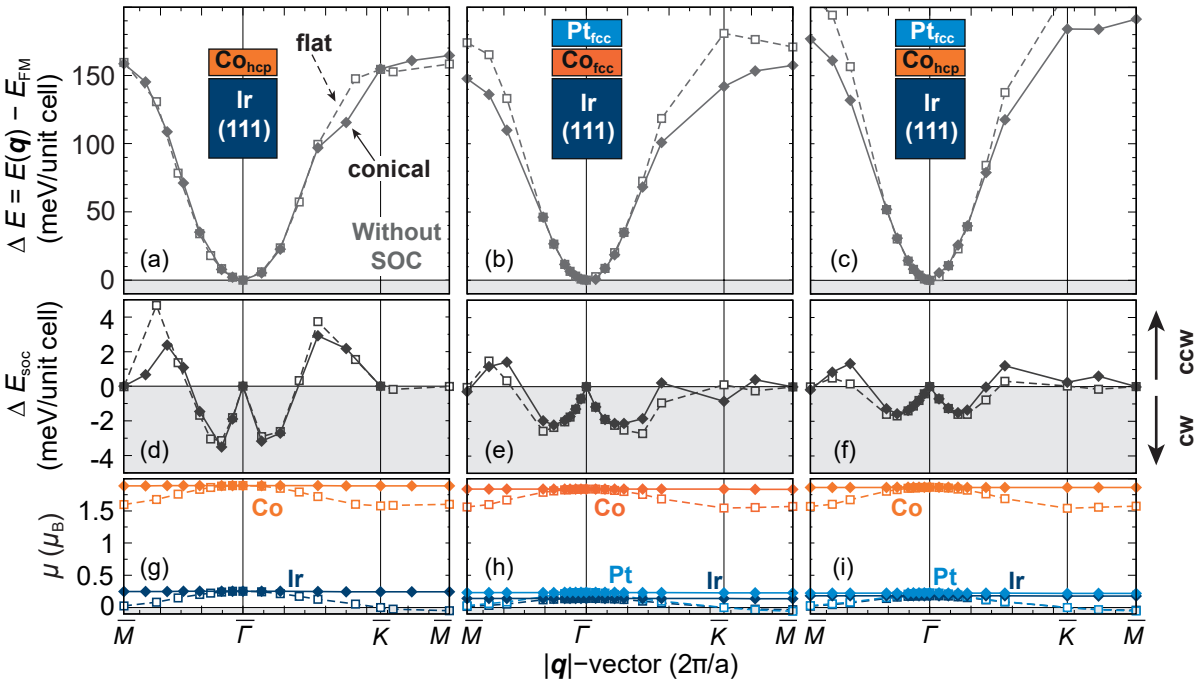

Figure 6.10 | Full energy dispersions $E(\mathbf{q})$ comparing flat cycloidal spin spirals for Co/Ir(111) and Pt/Co/Ir(111) with conical spin spiral states. (a,b,c) Energy dispersion without spin-orbit coupling (SOC) along the high symmetry path $\overline{\Gamma}$-$\overline{M}$ and $\overline{\Gamma}$-$\overline{K}$-$\overline{M}$ of the two-dimensional Brillouin zone for Co_{hcp}/Ir(111), Pt_{fcc}/Co_{fcc}/Ir(111) and Pt_{fcc}/Co_{hcp}/Ir(111), respectively. Shown are the calculated energies from DFT with respect to the ferromagnetic (FM) state of flat (open squares and dashed lines) and conical (filled diamonds with solid lines) spin spirals. The opening angle of conical spirals is $\theta = \pi/20$ while for flat ones it is $\theta = \pi/2$. Note that the energy dispersion gets rescaled by $\frac{1}{\sin(\pi/\theta)^2}$. The calculations are carried out using a substrate with five Ir(111) layers. (d,e,f) Energy contribution due to SOC. (g,h,i) Magnetic moment (μ_B) of the (Pt), Co and Ir surface layer for the two types of calculations.

small deviations in energy which are not negligible anymore, when the normalization is large. Additionally, when investigating spin spirals around the FM state, the electronic structure of flat and conical spin spirals is similar. Both calculations reveal FM states. For higher $\mathbf{q}$, conical spin spirals still are FMs, but flat spirals show large cantings between nearest neighbours ending up in real AFM states. Therefore, the electronic structure clearly differs.

In Fig. 6.10 (g-i), the magnetic moments of the topmost layers are presented. For all conical spin spiral states, it is constant due to the fact that all states are FMs. In the case of flat spin spirals, all moments are at maximum in the FM state and decrease with increasing $\mathbf{q}$. A contribution to the Stoner energy $\frac{1}{2}I\Delta\mu(\mathbf{q})^2$ could be calculated, which contributes to the exchange[10]. Here, I is the Stoner parameter and $\Delta\mu(\mathbf{q})$ the variation of the magnetic moment with respect to $\mathbf{q}$.

Contrary to the exchange, the DMI is not dependent on the Stoner energy due to an induced magnetic moment in non-magnetic layers [129]. As a consequence, we

[10]Such a calculation has been done in Ref. 129.

address the deviations in the DMI for both kinds of calculations to a different electronic structure in combination with small calculational errors which get renormalized. Since the DMI is typically small compared to the exchange, these effects will have a larger impact.

As a conclusion, both conical and flat spin spiral calculations lead to a similar descriptions of the magnetic systems in Co/Ir(111) and Pt/Co/Ir(111). Around their ground state, both give the same results, whereas for higher **q** points, they will differ. Comparing theoretical results with experiments, both kinds of calculation give reasonable insight into the ground state properties[11]. Therefore, both flat and conical spin spiral calculations should be seen as good approximation to describe a realistic ultrathin film system. For further theoretical investigations, which appear sensitive to quantitatively deviations (ground state energies, energy barriers of non-collinear states, Curie temperatures, etc.), differences will occur.

[11] Note, that in experiments, it is not a priori obvious, how non-magnetic layers would behave in a spin spiral state

Chapter 7

Tuning exchange frustration in Co films

Controlling the magnetic interactions is one of the key issues in order to stabilize non-collinear magnetic structures such as domain walls (DWs) and skyrmions. For an Fe monolayer (ML) on different hexagonal 4*d* and 5*d* transition metal (TM) substrates, it has been predicted based on density functional theory (DFT) calculations, that the magnetism can vary from strongly antiferromagnetic (AFM) to strongly ferromagnetic (FM) by filling the *d* band of the respective substrate [50].

Complex magnetic structures such as skyrmion lattices and multi-Q states are found in Fe MLs on the Ir(111) or the Rh(111) surface [29, 45]. Due to strong hybridization with the substrate, the exchange interaction is highly frustrated, i.e. the exchange beyond nearest neighbours is competing as well as higher order exchange interactions are of comparable strength.

A 4*d* TM top layer on Fe/Ir(111) or Fe/Rh(111) can further tune the magnetic interactions, leading to spin spiral ground state and isolated skyrmions in magnetic fields in Pd/Fe/Ir(111) [31, 122] or a canted up-up-down-down state in the film system of Rh/Fe/Ir(111) [44]. DFT calculations predict a long-ranged spin spiral ground state and skyrmions in a magnetic field for Pd/Fe/Rh(111) [136], where the Dzyaloshinskii-Moriya interaction (DMI) is significantly reduced compared to the respective film including an Ir(111) substrate.

Co is known as stronger FM compared to Fe because its *d* band is filled with one additional electron and only spin $\downarrow$ states occur at the Fermi energy. Therefore, the spectrum of magnetic ground states is assumed to be smaller for a Co based film. Nevertheless, based on DFT calculations, the effective nearest neighbour exchange interaction in a Co ML can vary from $\sim 30\,\mathrm{meV}$ in Co/Pt(111) [137, 138] to $\sim 17\,\mathrm{meV}$ in Co/Ir(111) [Pub. I] or $\sim 13\,\mathrm{meV}$ in Co/Ru(0001) [139]. These examples show that indeed, the magnetic interactions can be tuned in ultrathin Co films; however, a study on different materials using Co MLs is still missing.

In this chapter, we present a systematic study for different 4*d* TM MLs on Co/Ir(111) and Co/Rh(111). Since we want to recognize element dependent trends, we fill the 4*d* band from Tc to Pd, where in Fig. 7.1 all elements included in this analysis are shown.

Filling the *d* band of the top layer, we observe an increasing nearest neighbour exchange interaction, whereas for a Rh top layer, the exchange appears to be highly frustrated. Replacing the 5*d* Ir(111) substrate with its isoelectronic 4*d* equivalent, Rh(111), the exchange is similar, but the spin-orbit coupling (SOC) dependent quantities such as DMI and magnetocrystalline anisotropy energy (MAE) are reduced

significantly.

In the first part (Sec. 7.2), we analyse the trends of the structural relaxation as well as the magnetic moment. Investigations concerning magnetic ground state will be determined by performing spin spiral calculations after which we investigate the trends in the magnetic interactions (Sec. 7.3).

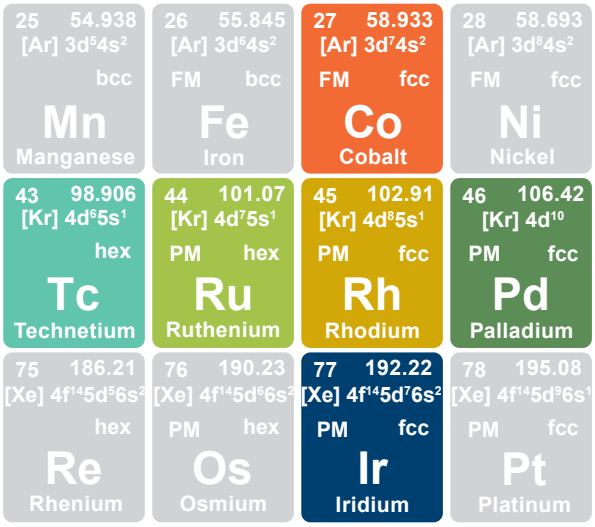

Figure 7.1 | Periodic table of elements used for 4d/Co bilayers on Ir(111) and Rh(111). Shown are the atomic numbers, mass, electronic configuration, magnetic and structural phase. The 4*d* band of the top layer on Co/(111) and Co/Rh(111) is filled from Tc to Pd. Elements in grey will be neglected in the following investigation.

7.1 Computational Details

For this study, we used the FLEUR code [47] with film geometry. We choose the theoretical equilibrium lattice parameter of bulk Ir $a_{\text{Ir-bulk}} = 7.22\,\text{a.u.}$, which was obtained within the local density approximation (LDA) [127]. For Rh, the lattice constant is relaxed to $a_{\text{Rh-bulk}} = 7.26\,\text{a.u.}$ [129], using the revised PBE version of the generalized gradient approximation (GGA) *xc* potential [140][1]. For the following calculations, the muffin tin (MT) radii are set to $R^{\text{MT}}_{4d,\,5d} = 2.31\,\text{a.u.}$, $R^{\text{MT}}_{\text{Co}} = 2.23\,\text{a.u.}$ for Ir and the 4*d* TMs and Co, respectively. If not stated differently, the energy cutoff was set to $k_{\text{max}} = 4.0\,\text{a.u.}^{-1}$. In this investigation, we restrict ourselves to only fcc stacked Co and 4*d* transition metals.

Structural relaxation The structural relaxations were performed in the FM state using a symmetric film with five layers of Ir(111) or Rh(111) adding a 4*d*/Co bilayer (BL) on both sides of the film. The forces between the uppermost layers were minimized in [111] direction up to a threshold of $F < 10^{-5}\,\text{htr/a.u.}$ while three Ir (Rh) layers in the centre of the film are kept fixed at the bulk equilibrium lattice parameter. The resulting interlayer distances (denoted as $d_{12}, d_{23}, \ldots$) are presented in Tab. 7.1. For the structural relaxation, we applied 110 *k* points for Co/Ir(111) and 240 *k* points in the irreducible wedge of the two-dimensional (2D) Brillouin zone (BZ) for all other presented films as well as the GGA *xc* functional [73].

[1] The GGA potential for Rh was used as in Ref. [129]. The lattice constant in LDA was giving larger deviations compared to the experimental one.

Table 7.1 | Relaxed interlayer distances d_{ij} (a.u.) for the film systems 4*d*/Co/Ir(111) and 4*d*/Co/Rh(111). The indices denote the respective layer in the film. d_{12} represents the distance between the 4*d* and the Co layer, d_{23}, between Co and the (111) substrate's surface layer and d_{34} between the substrate's surface and the substrate. As a reference, the relaxed interlayer bulk distance d_{bulk} is shown. Note that for Co/Ir(111) and Co/Rh(111) there is no 4*d* top layer.

System	d_{12}	d_{23}	d_{34}	d_{bulk}
Co/Ir(111)	–	4.01	4.37	4.17
Tc/Co/Ir(111)	3.89	4.12	4.39	4.17
Ru/Co/Ir(111)	3.83	4.07	4.37	4.17
Rh/Co/Ir(111)	3.89	4.06	4.35	4.17
Pd/Co/Ir(111)	4.07	3.97	4.36	4.17
Co/Rh(111)	–	3.82	4.29	4.19
Tc/Co/Rh(111)	3.83	4.11	4.34	4.19
Ru/Co/Rh(111)	3.81	4.06	4.31	4.19
Rh/Co/Rh(111)	3.87	4.05	4.29	4.19
Pd/Rh(111)	4.05	3.94	4.29	4.19

Spin spiral calculations Using the interlayer distances of the structural relaxation, self-consistent performed spin spiral calculations without SOC were performed using an asymmetric film with nine layers of Ir(111) or Rh(111). The vector **q** is chosen along the high symmetry directions $\overline{\Gamma}$-$\overline{M}$ and $\overline{\Gamma}$-$\overline{K}$ of the hexagonal 2D BZ. The energy contribution due to SOC, ΔE_{SOC} is calculated in first-order perturbation theory for every previously calculated **q** point [91, 128, 129]. For spin spiral calculations, we used the LDA [127] of the *xc* functional and 1936 *k* points in the full 2D BZ.

Magnetocrystalline anisotropy energy For the MAE, we first self-consistently converged calculations of asymmetric films with nine layers of Ir(111) or Rh(111) in the FM state in scalar-relativistic approximation. The computational settings are the same as for the spin spiral calculations described above. The values of the MAE, K are determined by applying the force theorem [80, 81], where we applied the spin quantization axis with SOC perpendicular the film plane $E_{\perp}$ and parallel to the film plane $E_{\parallel}$. The resulting energy difference is determined as $K = E_{\perp} - E_{\parallel}$.

7.2 Electronic structure and magnetic properties

Filling up the 4*d* band in ultrathin film systems 4*d*/Co/Ir(111) and 4*d*/Co/Rh(111) gives rise to trends in electronic structure variations. Fig. 7.2 presents the changes of interlayer distances after the structural relaxation in the FM state with respect to the ideal interlayer distances of the Ir(111) (black filled points with solid lines) and Rh(111) (grey circles with dashed lines) substrate ($a_{\text{Ir-bulk}}$ and $a_{\text{Rh-bulk}}$, respectively, Sec. 7.1). The absolute values can be seen in Tab. 7.1. Upon relaxing the topmost three layers in the film, Δd_{12} in (a), Δd_{23} in (b) and Δd_{34} in (c) denote the changes of distances between the 4*d* element and Co, between Co and the substrate surface layer and between the substrate surface layer and the rest of the substrate.

Independent on the two chosen substrates, the relaxation trends for the respective layer remain the same. The change of distance of the 4*d* element in Fig. 7.2 (a) is large for Tc, Ru and Rh, approaching the Co layer of about $\sim 7-9\%$. With a Rh(111)

substrate, the relaxation is about 1% larger than for Ir(111) and reaches the maximum for Ru. The trend shows a parabolic behaviour, where for Pd we only see a slight shift in $-z$-direction ($\sim 2-3\%$).

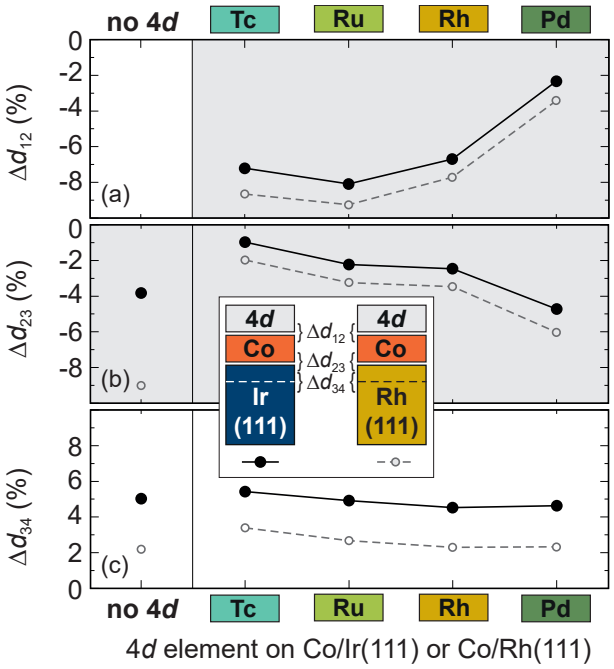

Figure 7.2 | Relaxed interlayer distance Δd (%) for 4*d*/Co/Ir(111) and 4*d*/Co/Rh(111) relative to the bulk distance of Ir(111) and Rh(111). (a) Relative distance Δd_{12} between 4*d* element and Co. Note that in the case of Co/Ir(111) and Co/Rh(111) there is no 4*d* element. (b) Δd_{23} between Co and the substrate. (c) Δd_{34} between the topmost layer of the substrate and the next substrate layer. Black points with solid lines (open grey points with dashed lines) correspond to Co/Ir(111) [Co/Rh(111)] based systems. The relaxation is done in the FM state.

For the Co layer [Fig. 7.2 (b)], a monotonic increase of the relaxation towards the substrate is seen. It ranges from 1% in Tc/Co/Ir(111) to 6% in Pd/Co/Rh(111). As in the top layer, films with a Rh(111) substrate have a stronger relaxation of about 1% compared to Ir(111). Without the 4*d* top layer, the relaxation of Co on Rh(111) is about 9% and by far the largest, whereas for Co/Ir(111) it is about 4% and in between the relaxation of Ru/Rh and Pd as 4*d* top layer. Therefore, the 4*d* top layer has a larger impact on the relaxation of Co/Rh(111) than of Co/Ir(111).

The substrate surface layer on the other hand is increasing its distance from the rest of underlying substrate [Fig. 7.2 (c)]. The difference for Ir(111) is about 5% and for Rh(111) it varies from 2% to 3%. Co can be seen as a buffer layer between the 4*d* top and the substrate layer which is why without the top layer, the relaxation of the substrate's surface layer illustrates very similar.

Fig. 7.3 shows the calculated magnetic moments of the relaxed layers, where in (a-c), the 4*d* top layer, Co and Ir(111) or Rh(111) surface layer are presented. With Rh(111) (grey circles and dashed lines), all magnetic moments are enhanced compared to the Ir(111) case.

Tc couples AFM to Co with a very small induced magnetic moment ($\sim 0.05\,\mu_B$) [Fig. 7.3 (a)]. For Ru a FM coupling to Co is induced with a slightly larger moment. The magnetic moment in the 4*d* TM increases with *d* band filling in almost every presented layer, except for the Rh top layer. Rh is isoelectronic to Co and Ir. Thus, a strong hybridization between these elements arises. The large spin susceptibility of Rh further allows for a formation of a large magnetic moment ($\sim 0.6\,\mu_B$). Replacing

Rh by Pd, the induced moment reduces to $0.3\,\mu_B$ in the 4*d* element.

Adding a 4*d* layer on top can drastically change the magnetic moment of Co due to hybridization [Fig. 7.3 (b)]. On Ir(111) and Rh(111), the Co layer exhibits a magnetic moment of $1.85 - 1.95\,\mu_B$. With Tc, the moment of Co decreases by 30% to $\sim 1.3\,\mu_B$. In Ru/Co/Ir(111) and Ru/Co/Rh(111), the value increases to $1.5\,\mu_B$ and $1.6\,\mu_B$, respectively. With Rh or Pd as top layer, Co reaches is maximum value similar to that one without 4*d* layer.

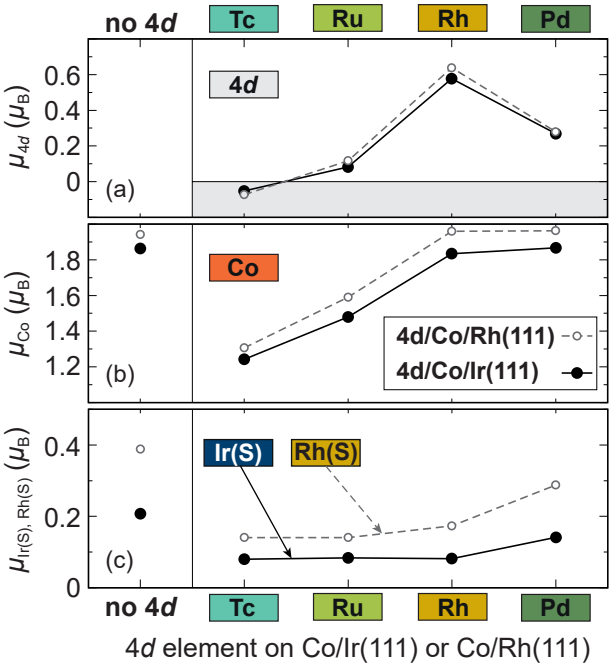

Figure 7.3 | Calculated magnetic moments (μ_B) for 4*d*/Co/Ir(111) and 4*d*/Co/Rh(111) in the ferromagnetic state. (a) 4*d* top layer. (b) Co layer. (c) Ir(111)/Rh(111) surface layer. Black points with solid lines (open grey points with dashed lines) correspond to Co/Ir(111) [Co/Rh(111)] based systems.

We also observe a significant induced magnetization in the Ir(111) and Rh(111) surface layers [Fig. 7.3 (c)]. It is twice larger in the case of Co/Rh(111), $0.4\,\mu_B$, compared to Co/Ir(111), $0.2\,\mu_B$. Rh has the largest spin susceptibility which plays a key role for the induced magnetic moments. Note that the magnetic moment reflects the electronic structure and therefore the relaxation, which is the strongest between Co and the Rh(111) surface. Due to the reduced coordination, Co induces a large moment in the surface layer of each substrate. With Tc, Ru or Rh on top, the moment in the surface of Ir(111) or Rh(111) remains almost constant at $0.1\,\mu_B$, slightly increasing for Pd.

Local density of states Deeper insight into the trends of the electronic and magnetic origin can be seen from the local density of states (LDOS) presented in Figs. 7.4 and 7.5 where the three topmost layers of each investigated film are illustrated. In Fig. 7.4 (a,b) the reference for Co/Ir(111) according to Sec. 5.2 is presented. In the Co layer, we observe narrow and large peaks with an exchange splitting of about 1.5 eV. Almost all majority spin states are occupied, whereas unoccupied states occur in the minority spin channel, established in the magnetic moment of about $1.9\,\mu_B$. For the Ir surface layer in (b) the LDOS is much broader and slightly of asymmetric shape due to hybridization with Co. Therefore, the small

magnetic moment of $0.2\,\mu_B$ is induced [cf. Fig. 7.3 (c)].

Filling the 4*d* band from Tc to Pd in the top layer [Fig. 7.4 (c,f,i,l)] the expected shift of the LDOS to more occupied states can be observed (especially in the majority spins, but also in the minority channel). At the same time, we recognize an enhanced asymmetric shape of the LDOS, depending on the hybridization with the Co layer. For the Rh top layer in (i) it appears to be at maximum which is where the largest magnetic moment is obtained [cf. Fig. 7.3 (a)].

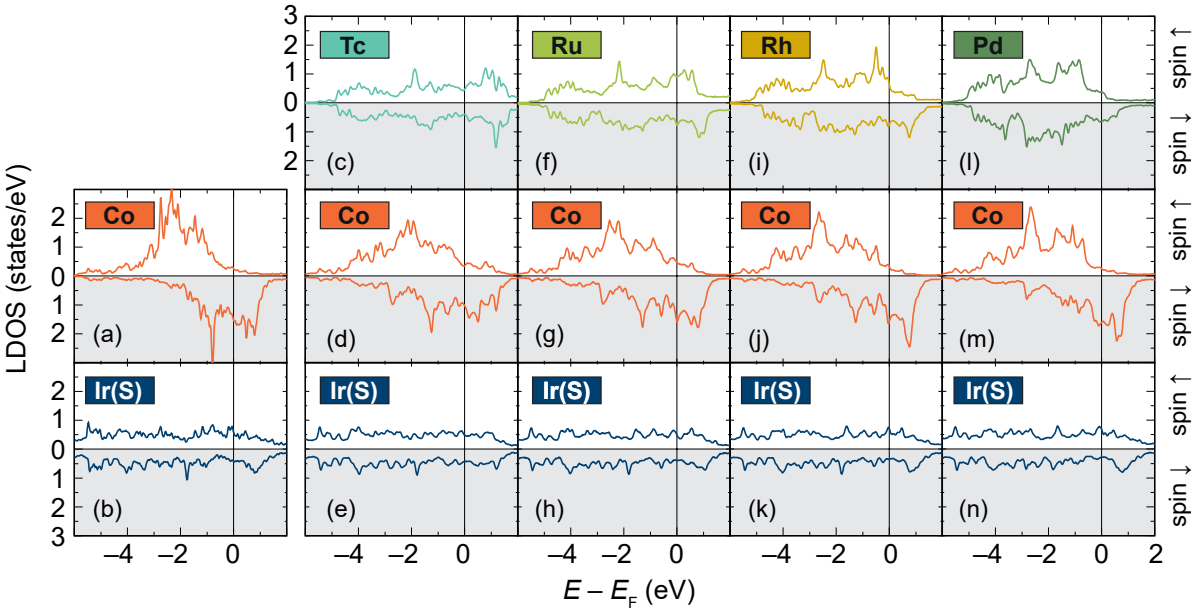

Figure 7.4 | Calculated local density of states (LDOS) for 4*d*/Co/Ir(111) films in the ferromagnetic state. (a,b) LDOS of Co/Ir(111) for Co and the Ir(111) surface layer. (c,d,e) LDOS of Tc/Co/Ir(111) for Tc, Co and the Ir(111) surface layer, respectively. (f,g,h) LDOS of Ru/Co/Ir(111). (i,j,k) LDOS of Rh/Co/Ir(111). (l,m,n) LDOS of Pd/Co/Ir(111).

In accordance with the hybridization with 4*d* top layers, the same trends are visible in the adjacent Co layers [Fig. 7.4 (d,g,j,m)]. Compared to Co/Ir(111), the LDOS is broadened slightly when an additional 4*d* layer is present as expected from hybridization effects. Note that the broadening can be seen as small since Ir(111) already broadens the LDOS of Co even without 4*d* layer as described in Sec. 5.3. However, the exchange splitting is strongly reduced due to a Tc or Ru top layer to less than 1 eV and unoccupied spin ↑ states occur. Additionally, the height of most of the significant peaks is reduced resulting in the comparably small magnetic moment of $\sim 1.3\,\mu_B$ in Tc/Co/Ir(111) [$1.5\,\mu_B$ for Ru/Co/Ir(111)].

In Rh/Co/Ir(111) the hybridization between the elements is the strongest. This is visible by the increased hybridization peak heights through the layers. In Co, the exchange splitting is close to that of Co/Ir(111), where with Rh on top, significant peak structures at the Fermi energy are noticed. Since the number of valence electrons in Rh, Co and Ir is the same, a very similar ratio of unoccupied vs. occupied states is seen in spin ↑ and ↓ channels. With Pd, the LDOS does not change a lot, but a

slight shift of the LDOS to more occupied states is visible. Therefore, the magnetic moment in the Co layer for Rh/Co and Pd/Co BL on Ir(111) is almost the same.

For the Ir(111) surface layer [Fig. 7.4 (b,e,h,k,n)], the LDOS looks very similar for all systems showing small variations in hybridization peaks and asymmetry. Here, the 4*d* top layer has a small impact since it is the second adjacent layer. Nevertheless, an increasing asymmetric shape of the LDOS appears when filling the 4*d* band of the top layer. Additionally, different hybridization peaks occur in Ir(S) which go through all three presented layers. Note that the height of these peaks is also determined by the distance between the layers. Comparing Rh/Co/Ir(111) with Pd/Co/Ir(111), we see similar heights in the unoccupied spin ↓ channel at 1 eV in both Co and Ir(S), but it is larger in the Rh top layer than in Pd.

Replacing the substrate by Rh(111), all trends described before remain the same. Since we replace a 5*d* element by its isoelectronic 4*d* euivalent, the surface of the substrate holds a reduced band width in all elements. As a consequence, all magnetic moments are enhanced with a Rh(111) substrate [cf. Fig. 7.3]. The relaxation of films with Rh(111) appear to be stronger [cf. Fig. 7.2] and the hybridization peaks in these films are enhanced compared to 4*d*/Co/Ir(111) films.

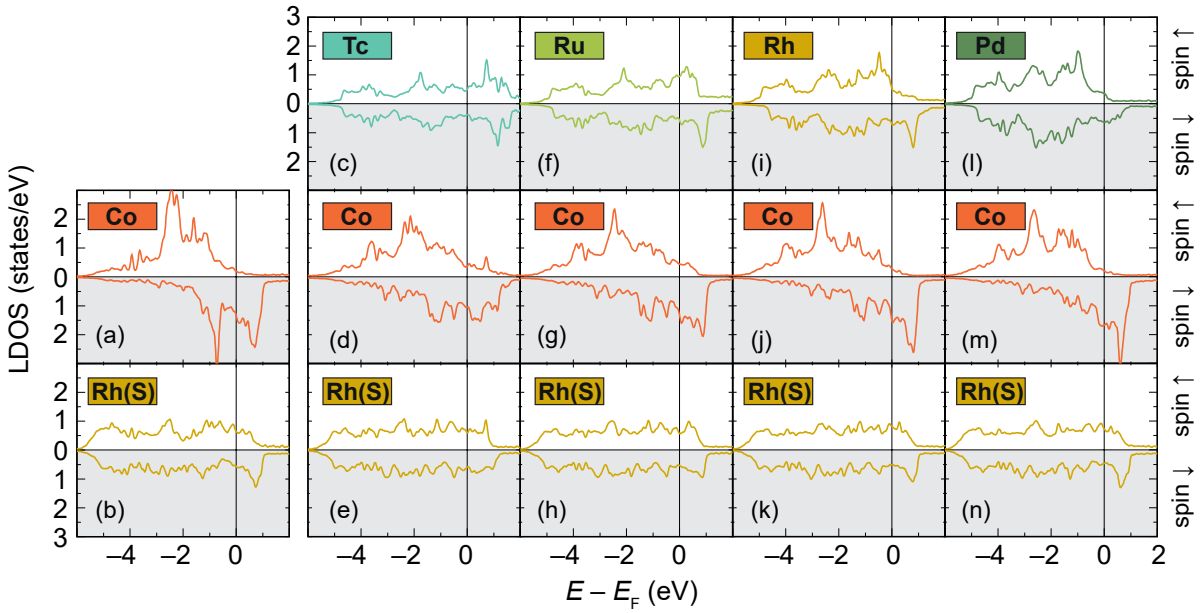

Figure 7.5 | Calculated local density of states (LDOS) for 4*d*/Co/Rh(111) films in the ferromagnetic state. (a,b) LDOS of Co/Rh(111) for Co and the Rh(111) surface layer. (c,d,e) LDOS of Tc/Co/Rh(111) for Tc, Co and the Rh(111) surface layer, respectively. (f,g,h) LDOS of Ru/Co/Rh(111). (i,j,k) LDOS of Rh/Co/Rh(111). (l,m,n) LDOS of Pd/Co/Rh(111).

Despite of small differences, the electronic structure in 4*d*/Co/Ir(111) and 4*d*/Co/Rh(111) looks expectedly similar, concerning the relaxation, magnetic moments and LDOS. That is why, we further do not expect large differences in the magnetic behaviour in these systems, which will be presented in the next section.

7.3 Describing magnetic interactions

The previous description has shown the properties of the films in the FM state. We include non-collinear spin spiral states to scan a wider magnetic phase space. Therefore, Fig. 7.6 shows the calculated energy dispersion $E(\mathbf{q})$ along the whole high symmetry path $\overline{M}$-$\overline{\Gamma}$-$\overline{K}$-$\overline{M}$ of the hexagonal 2D BZ. All calculations (points) include SOC. For the description (lines) the atomistic spin model beyond nearest neighbours is used including exchange interaction, DMI and MAE. On the left, Co/Ir(111) based films are presented and on the right, Co/Rh(111) films are shown. The smaller panels (b,d) are a zoom around the FM region ($\overline{\Gamma}$ point). For all presented films, a FM ground state is predicted.

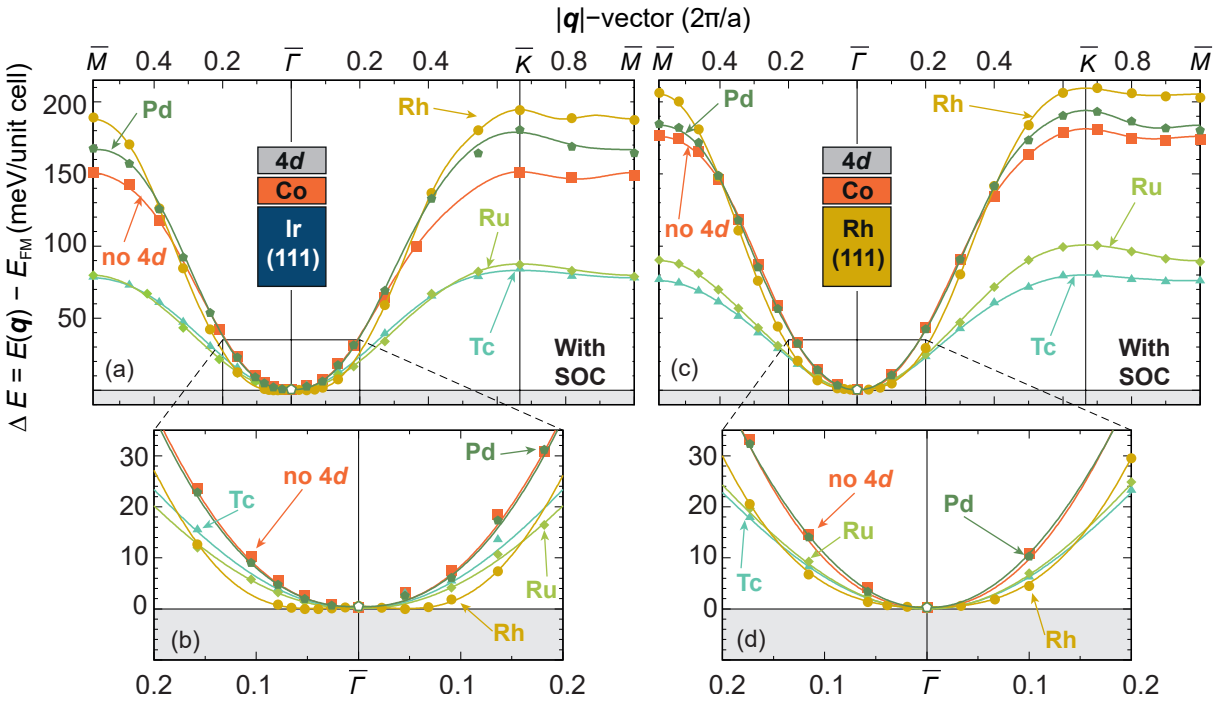

Figure 7.6 | Full energy dispersions $E(\mathbf{q})$ of flat cycloidal spin spirals for 4*d*/Co/Ir(111) and 4*d*/Co/Rh(111) including spin-orbit coupling (SOC). (a) Energy dispersions of Co/Ir(111) based films along the high symmetry path $\overline{\Gamma}$-$\overline{M}$ and $\overline{\Gamma}$-$\overline{K}$-$\overline{M}$ of the two-dimensional Brillouin zone. All points show calculated energies from DFT with respect to the ferromagnetic (FM) state, whereas lines represent the mapping to the atomistic spin model of the Heisenberg exchange beyond nearest neighbours, Dzyaloshinskii-Moriya interaction beyond nearest neighbours and the magnetocrystalline anisotropy energy. (b) Zoom area around the $\overline{\Gamma}$ point of (a). (c) Energy dispersions of Co/Rh(111) based films and (d) Zoom area around the $\overline{\Gamma}$ point of (c). Note that all stackings are presumed to be fcc.

In Co/Ir(111) [red squares and lines in Fig. 7.6 (a,b)], we see small exchange frustration (cf. Ch. 5 and Pub. I). This can be recognized by $E \sim q^2$ which corresponds to perfectly FM order. In this system, the nearest neighbour exchange J_1 is the dominant as expected for a strong FM. Consequently, the AFM states at the BZ boundaries are $\sim 150\,\mathrm{meV/Co}$ higher in energy compared to the FM ground state.

Adding the 4*d* layer on top, we modify the energy dispersions. With Tc or Ru, the AFM states at the BZ boundaries are only 80 meV/Co higher in energy than the FM state at the $\overline{\Gamma}$ point. Tc/Co/Ir(111) and Ru/Co/Ir(111) show almost the same energy dispersions. A decrease of the total energy differences between the high symmetry states at $\overline{\Gamma}$, $\overline{K}$ and $\overline{M}$ is assumed to reflect large exchange frustration; however, the curve is almost of perfect parabolic shape around the $\overline{\Gamma}$ point which is a sign for small frustration effects. The hybridization of Co with elements having less valence electrons (Tc, Ru) gives rise to a weaker FM coupling because spin ↑ states occur at E_F (cf. Fig. 7.4). Therefore the magnetic moments in the Co layer is reduced (Fig. 7.3) which corresponds to the Stoner criterion (cf. Sec. 4.1 and Ref. 92).

Replacing Tc or Ru by Pd the FM order is strengthened. We observe almost the same energy dispersion as in Co/Ir(111) [Fig. 7.6 (b)] while the AFM states lose about 20 meV/Co more compared to Co/Ir(111). We expect Pd/Co/Ir(111) to be a stronger FM with less exchange frustration than Co/Ir(111).

In Rh/Co/Ir(111), the magnetism behaves qualitatively different from the other presented films. We especially see the largest energy differences between AFM and FM states among all investigated films [Fig. 7.6 (a)]. This could lead to the assumption Rh/Co/Ir(111) is a very strong FM. A closer look around the FM state in [Fig. 7.6 (b)] reveals an exceptionally flat energy dispersion which does not show the quadratic parabolic shape as the film systems. Here, the energies of spin spiral states with $\mathbf{q}$ vectors up to $0.1\,{}^{2\pi}/_{a}$ appear to be nearly degenerate allowing spin structures to cant up to 10° with almost no energy cost. Both features give rise to a strongly exchange frustrated system, which will be discussed in much more detail in the next chapter (Ch. 8).

Replacing the Ir(111) substrate by Rh(111), all investigated films tend towards stronger FM structures. In Fig. 7.6 (c), the energy differences between FM state ($\overline{\Gamma}$) and AFM states ($\overline{K}$, $\overline{M}$) are increased due to the presence of Rh(111). Co/Rh(111) shows a slightly steeper energy dispersion than Co/Ir(111) which can be explained by a smaller exchange frustration.

The 4*d* top layers Tc and Ru will reduce the total energy differences in Co/Rh(111) by over a factor of two and weaken the FM order. The same has been observed for Co/Ir(111). They also show the same quadratic behaviour of $E(\mathbf{q})$ around the FM as in Tc/Co/Ir(111) or Ru/Co/Ir(111) [Fig. 7.6 (d)]. Hence, the magnetism for the four films should appear very similar.

The strong FM behaviour of Co/Rh(111) will not be affected by a Pd top layer. The energy dispersions of Pd/Co/Rh(111) and Co/Rh(111) are almost on top of each other. Note that the LDOS of Pd/Co/Rh(111) and Co/Rh(111) around E_F (Fig. 7.5) almost match, emphasizing the similarity in these films within a FM ground state.

Again, Rh as a top layer has a strong impact on the magnetic behaviour of Co/Rh(111). The energy differences between FM and AFM states are the largest of all investigated films and $E(\mathbf{q})$ is exceptionally flat around $\overline{\Gamma}$ [Fig. 7.6 (d)]. A canting of magnetic

moments costs little energy which shows the frustration of magnetic interactions due to the strong hybridization of the involved elements. Despite of these observations, the FM state is the distinct ground state. This is different to Rh/Co/Ir(111) where the energy cost for a small canting is zero showing an even more frustrated film than Rh/Co/Rh(111).

From these results, we can predict two films to be the most promising ones which could stabilize non-collinear structures such as skyrmions: Rh/Co/Ir(111) and Rh/Co/Rh(111). All the other systems show more FM behaviour; however, due to small energy differences between FM and AFM states with Tc and Ru on top, non-collinear structures could also be observed in these films. In the following, we will discuss the magnetic interactions which result from these energy dispersions in more details.

Exchange interaction For the exchange interaction, we compare the atomistic spin model beyond nearest neighbour with the effective nearest neighbour approximation. Such a comparison gives insight in the degree of frustration in Co films and shows limitations using a description of energy dispersions with J_{eff}.

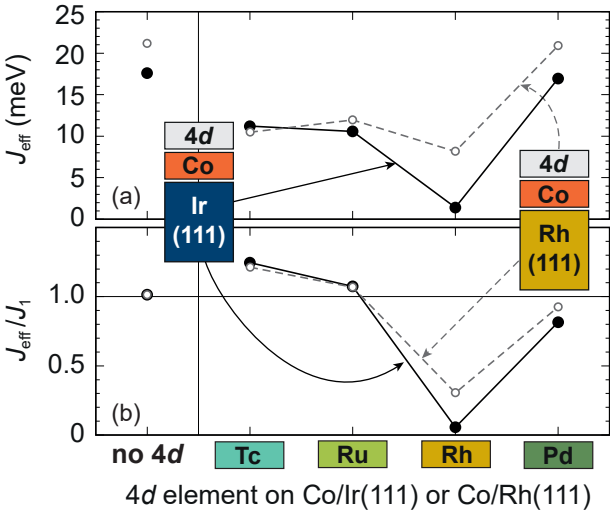

Figure 7.7 | Obtained values of exchange interaction in 4*d*/Co/Ir(111) and 4*d*/Co/Rh(111) mapping the effective nearest neighbour approximation of the spin model to the DFT results. (a) J_{eff} (meV). (b) Ratio J_{eff}/J_1. For a ratio of 1, the two descriptions are matching whereas for different ratios more exchange frustration is expected. Black points with solid lines (open grey points with dashed lines) correspond to Co/Ir(111) [Co/Rh(111)] based systems.

Therefore, in Fig. 7.7 (a) the variation of the effective nearest neighbour exchange interaction is shown. J_{eff} can be tuned on a wide range of about 20 meV, where for almost all Co/Rh(111) films, we observe larger J_{eff}. The effective exchange increases from 18 meV in Co/Ir(111) to 21 meV in Co/Rh(111). For the latter, Co appears to be a stronger FM. This is expected due to the Stoner energy because we observed a smaller bandwidth in the LDOS and a larger magnetic moment in Co (cf. Figs. 7.3 and 7.5). With Tc or Ru on top of the two films, the exchange drops to about 10 meV whereas with Pd, it is similar to the uncovered systems.

For the very flat energy dispersions in Fig. 7.6, J_{eff} drops to 8 or even to 1 meV in the case of Rh/Co/Rh(111) and Rh/Co/Ir(111), respectively. Comparing J_{eff} with the nearest neighbour exchange J_1 of the fully atomistic model is seen as a direct indication of the degree of exchange frustration. J_1 represents the energy difference between

the FM state at the $\overline{\Gamma}$ point with the AFM states and $\overline{M}^2$ whereas J_{eff} represents the quadratic behaviour of the energy dispersion for $\mathbf{q} \to 0$. A ratio of $J_{\text{eff}}/J_1 \sim 1$ therefore is exemplary for the accordance of the two descriptions and a sign for small exchange frustration in the film.

In Fig. 7.7 (b), this ratio is plotted, where we observe small exchange frustration for almost all films with exception of Rh/Co/Ir(111) and Rh/Co/Rh(111). There, the ratio drops below 0.5 (for Rh/Co/Ir(111) even below 0.1). The films are strongly exchange frustrated and the description of the effective nearest neighbour approximation only holds true for a very narrow region around the FM state. For Rh/Co/Ir(111) the description fails.

For a detailed analysis, Fig. 7.8 presents the strength of the exchange interaction up to the third nearest neighbour (all magnetic interactions are listed in Tab. 7.2 and 7.3). Comparing the strengths and signs of J_i is a direct evaluation for exchange frustration. In (a), the nearest neighbour exchange is shown, whereas in (b,c), the strength of the second and third one is presented. Positive values denote a FM order between two spins and negative ones correspond to AFM order.

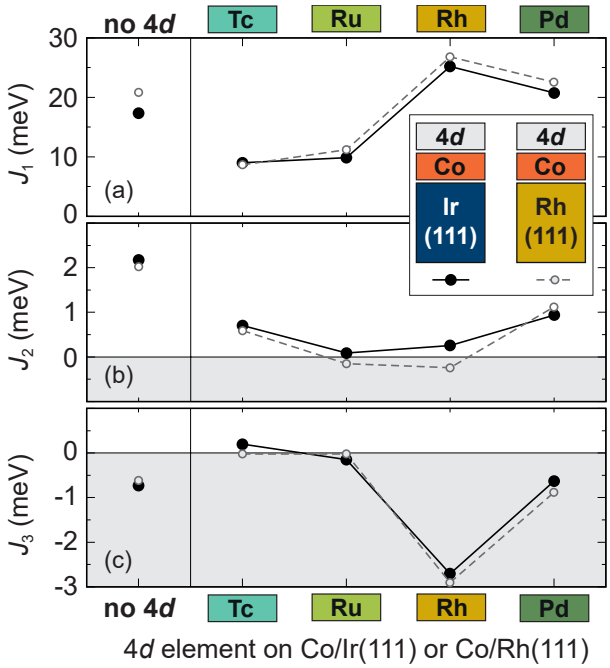

Figure 7.8 | Obtained values of exchange interaction J_i for the three nearest neighbours in 4*d*/Co/Ir(111) and 4*d*/Co/Rh(111) mapping the atomistic spin model to the DFT results. (a,b,c) Strength of J_i for $i = 1, 2, 3$ respectively. All energies are given in meV. Black points with solid lines (open grey points with dashed lines) correspond to Co/Ir(111) [Co/Rh(111)] based systems.

For Co/Rh(111) and Co/Ir(111), $J_1 = 21\,\text{meV}$ and $18\,\text{meV}$, is strongly FM, whereas $J_2 \sim \frac{1}{10}J_1$ and J_3 is smaller than -5% of J_1. Consequently both systems show small exchange frustration since beyond nearest neighbours, J_i is too weak to compete with J_1. Taking this into account, the frustration of Co/Rh(111) is smaller than that of Co/Ir(111).

[2] Note that J_1 is determined by the mapping of the fully atomistic spin model to $E(\mathbf{q})$ and not by the exact energy difference of the collinear states.

With Tc or Ru, the nearest neighbour exchange interaction drops to $J_1 < +10\,\text{meV}$ due to the small energy differences in $E(\mathbf{q})$. However, despite of J_2 for the Tc top layer (which has the same sign as J_1), the interactions beyond the first neighbour do not exceed about 5% of J_1. Co/Ir(111) and Co/Rh(111) films with a Tc or Ru top layer cannot be seen as typically exchange frustrated where the next neighbours compete with J_1. However, due to the small exchange interaction itself, other magnetic interactions such as DMI can compete with the exchange to form the magnetic ground state.

Rh/Co/Ir(111) and Rh/Co/Rh(111) films behave significantly different: we see the largest FM nearest neighbour exchange ($\sim +25\,\text{meV}$), especially $J_3 \sim -\frac{1}{10}J_1$ showing the strong exchange frustration in this system. Note that for Rh/Co/Ir(111) ten and for Rh/Co/Rh(111) six neighbours are required to describe $E(\mathbf{q})$ (Tab. 7.2 and 7.3) emphasizing the observations.

With Pd as top layer, the FM order is strengthened similar to Co/Ir(111) and Co/Rh(111) since J_1 is the largest interaction, whereas $J_3 \sim 0.05\,J_1$. The FM state is further stabilized by J_2. With the exception of Rh as top layer, we can recognize an increase of J_1 and a parabolic shape of J_2 when filling the 4*d* band in the top layer. The third neighbour's exchange interaction changes from FM to stronger AFM order [3].

Dzyaloshinskii-Moriya interaction With D_{eff} as linear approximation at $\mathbf{q} \to 0$, we evaluate the strength of the DMI (Fig. 7.9). We notice a smaller DMI for films with a Rh(111) substrate compared to Ir(111) due to a smaller SOC constant. D_{eff} in Co/Ir(111) is about three times larger than for Co/Rh(111) both preferring clockwise (CW) rotation of long-period spin spiral states. With 4*d* top layer, these differences occur to be smaller, increasing from Tc to Pd. For Tc, D_{eff} is comparably large and counterclockwise (CCW) rotating spin spirals are preferred, whereas due to *d* band filling, CW rotation is favoured with increasing strength.

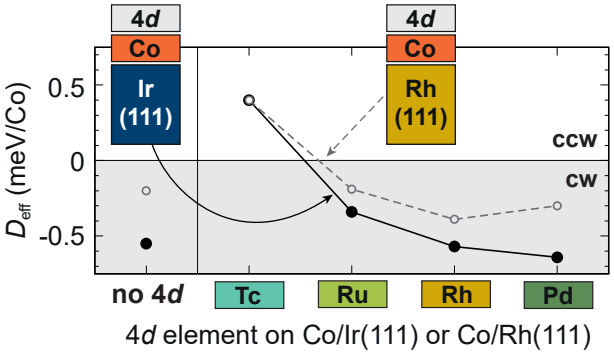

Figure 7.9 | Calculated strength of Dzyaloshinskii-Moriya interaction (DMI) in effective nearest neighbour approximation D_{eff} for 4*d*/Co/Ir(111) and 4*d*/Co/Rh(111). Negative values denote clockwise (CW) preference of rotation while positive values denote a counterclockwise (CCW) rotation. Black points with solid lines (open grey points with dashed lines) correspond to Co/Ir(111) [Co/Rh(111)] based systems. The strength of D_{eff} is determined by a linear fit around $\mathbf{q} \to 0$.

[3] Note that the qualitative behaviour of J_3 matches the ratio J_{eff}/J_1 in Fig. 7.7.

Because of the mapping process for D_{eff} it is a sensitive value strongly dependent on the choice of region around the $\overline{\Gamma}$ point. In the following, we analyse the DMI in more detail. In Fig. 7.10, the energy contribution due to SOC ΔE_{SOC} is presented along the high symmetry directions of the calculated energy dispersions. Black points correspond to the DFT calculated total contributions, where the solid lines are the fits to the DMI beyond nearest neighbours.

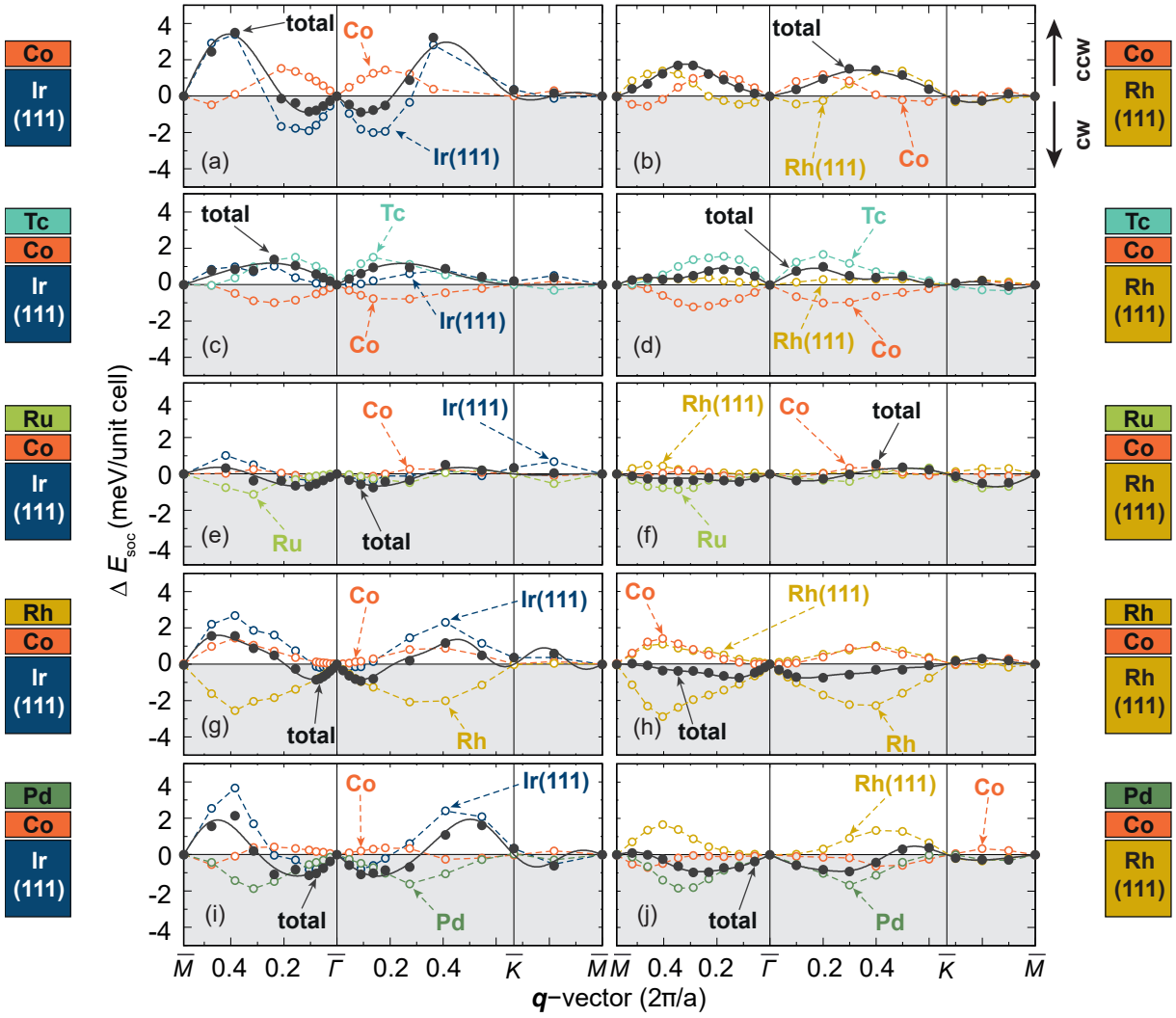

Figure 7.10 | Element resolved energy contribution due to spin-orbit coupling (SOC) to the energy dispersion of cycloidal spin spirals for 4*d*/Co/Ir(111) and 4*d*/Co/Rh(111). The filled black points correspond to the DFT calculations while the solid black lines are the fits to the atomistic spin model of the Dzyaloshinskii-Moriya interaction (DMI). Open points (dashed lines represent a guide for the eye) represent the respective element in the shown film system where positive values denote counterclockwise (CCW) rotation and negative values clockwise (CW) rotation. (a,c,e,g,i) Co/Ir(111) based films and (b,d,f,h,j) Co/Rh(111) based films. Note that the Ir(111) and Rh(111) contributions of ΔE_{SOC} are the sums of all Ir or Rh layers of the respective substrate.

All open circles (dashed lines serve as guide to the eye) show the respective contributions of the elements. The substrate's contribution to SOC is the sum of all substrate layers, denoted as Ir(111) or Rh(111). On the left side Co/Ir(111) based systems and on the right side Co/Rh(111) based systems are shown. We observe the same trend described previously for Fig. 7.9. Dispersions with Ir(111) substrate increase their amplitude compared to the ones with Rh(111), where we observe the largest values without 4*d* top layer. Tc/Co/Ir(111) and Tc/Co/Rh(111) prefer CCW rotating spin spirals, all other films with 4*d* top layer show a frustration of DMI, i.e. CW preference around $\overline{\Gamma}$ and CCW for larger **q**.

The qualitative trend of the total SOC contributions with Ir(111) is very similar to the ones with Rh(111), where for the latter, the amplitude is smaller. Irrespective of the substrate, ΔE_{SOC} for Co and 4*d* top layers are almost the same. Since the two substrates are isoelectronic, we conclude that the electronic structure is decisive for the sign of the DMI and the strength is not only mediated by the SOC constant of the non-magnetic element. This is further supported by the contributions of Ir(111) and Rh(111) to SOC which particularly differ in magnitude.

The latter observation is the reason for Co/Ir(111) [Fig. 7.10 (a)] preferring CW rotation around $\overline{\Gamma}$ whereas Co/Rh(111) [Fig. 7.10 (b)] favours CCW rotating states. The Rh(111) contribution smaller than the one of Co one while Ir(111) is exceeding the Co contribution. Additionally, for Rh/Co/Rh(111), we see how the DMI behaves for a Co ML sandwiched between the same element: both surface and substrate qualitatively exhibit the same SOC contribution with opposite sign; however, the Rh surface provides a stronger contribution due to the stronger relaxation top layer.

Magnetocrystalline anisotropy energy The second interaction due to SOC which we study is the strength of the uniaxial MAE (Fig. 7.11). The MAE constant K is negative (positive) for an out-of-plane (in-plane) easy axis. As for the DMI in Fig. 7.9, K is smaller for all films with Rh(111) substrate.

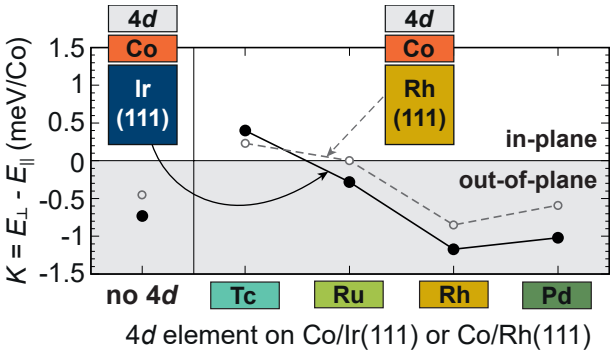

Figure 7.11 | Calculated strength of uniaxial magnetocrystalline anisotropy energy K for 4*d*/Co/Ir(111) and 4*d*/Co/Rh(111). Negative values correspond to an out-of-plane easy axis and positive values denote an in-plane easy axis. Black points with solid lines (open grey points with dashed lines) correspond to Co/Ir(111) [Co/Rh(111)] based systems.

Co/Ir(111) is strongly out-of-plane FM with about −0.7 meV. With Rh(111), the value drops to −0.2 meV. It is in correspondence with a previous study on $\mathrm{Co_{hcp}}$/Rh(111) [141]. As the DMI undergoes a change of rotational preference from CCW to CW with the 4*d* top layer from Tc to Ru, the MAE changes from in-plane to out-of-plane. Note that for Ru/Co/Rh(111), due to computational precision, K is very small so both in-

plane or out-of-plane MAEs could be favoured[4]. Filling the d band of the top layer to Rh or Pd increases the MAE, where for Rh/Co/Ir(111), the maximum of −1.1 meV is reached [−1.0 meV for Pd/Co/Ir(111)]. With Rh(111), K is reduced by about 50% in these films.

All discussed magnetic interactions are presented in Tab. 7.2 and 7.3.

7.4 Conclusion

In this chapter, we demonstrated how we can tune the magnetic properties in Co/Ir(111) and Co/Rh(111) films. Adding different 4d TM top layers (Tc, Ru, Rh, Pd), the effective nearest neighbour exchange interaction J_{eff} is varied over a wide range from 1 − 22 meV. A large frustration of exchange can be achieved by adding the isoelectronic 4d element Rh on either Co/Ir(111) or Co/Rh(111). All other films appear to have a strongly FM ground state with small exchange frustration, although with Tc or Ru, the FM order can be weakened due to their less filled 4d band. The impact on the exchange interaction by replacing Ir(111) with Rh(111) appears as rather small.

However, the SOC dependent quantities such as DMI and MAE are significantly lower for Co/Rh(111) films than in Co/Ir(111) based films and still show the same trends. The electronic structure is crucial for both DMI and MAE even though these quantities are mediated by SOC. Exchanging 5d elements and 4d isoelectronic elements can therefore be a sophisticated way to control the magnetic interactions.

Among all films, Rh/Co/Ir(111) and Rh/Co/Rh(111) appear as most promising in order to host non-collinear spin structures, such as DWs and skyrmions. The highly frustrated exchange interaction in these films can prevent non-trivial magnetic structures to be stable and not be destroyed into the FM ground state.

[4]The dipolar interaction favours the in-plane order and contributes to the MAE.

Table 7.2 | Obtained values for magnetic interactions in (4*d*)/Co/Ir(111) mapping the atomistic spin model to the results of DFT calculations. All values of the i-th neighbour exchange J_i, Dzyaloshinskii-Moriya interaction constants D_i and uniaxial magnetocrystalline anisotropy energy K are given in meV. $J > 0$ ($J < 0$) represents ferromagnetic (antiferromagnetic) order, $D > 0$ ($D < 0$) clockwise (counterclockwise) rotation and $K > 0$ ($K < 0$) denotes an in-plane (out-of-plane) easy axis. As a comparison, the effective nearest neighbour exchange and DMI, J_{eff} and D_{eff}, are presented.

Parameter	4*d* monolayer on Co/Ir(111)				
	no 4*d*	Tc	Ru	Rh	Pd
J_1	+17.372	+9.0164	+9.866	+25.180	+20.756
J_2	+2.176	+0.706	+0.088	+0.254	+0.938
J_3	−0.729	+0.200	−0.149	−2.706	−0.630
J_4	+0.081	–	–	−0.634	−0.154
J_5	−0.874	–	–	−0.237	−0.606
J_6	–	–	–	+0.095	–
J_7	–	–	–	+0.016	–
J_8	–	–	–	+0.273	–
J_9	–	–	–	+0.030	–
J_{10}	–	–	–	−0.281	–
J_{eff}	+17.614	+11.229	+10.586	+1.408	+16.944
D_1	−0.678	−0.294	+0.004	−0.294	−0.207
D_2	+0.271	−0.066	+0.100	+0.106	+0.311
D_3	+0.434	–	+0.089	+0.294	+0.303
D_4	–	–	–	−0.033	−0.089
D_5	–	–	–	−0.022	+0.021
D_6	–	–	–	+0.038	+0.040
D_7	–	–	–	+0.088	–
D_{eff}	−0.55	+0.40	−0.34	−0.57	−0.64
K	−0.73	+0.40	−0.28	−1.17	−1.02

Table 7.3 | Obtained values for magnetic interactions in (4*d*)/Co/Rh(111) mapping the atomistic spin model to the results of DFT calculations. All values of the i-th neighbour exchange J_i, Dzyaloshinskii-Moriya interaction constants D_i and uniaxial magnetocrystalline anisotropy energy K are given in meV. $J > 0$ ($J < 0$) represents ferromagnetic (antiferromagnetic) order, $D > 0$ ($D < 0$) clockwise (counterclockwise) rotation and $K > 0$ ($K < 0$) denotes an in-plane (out-of-plane) easy axis. As a comparison, the effective nearest neighbour exchange and DMI, J_{eff} and D_{eff}, are presented.

Parameter	4*d* monolayer on Co/Rh(111)				
	no 4*d*	Tc	Ru	Rh	Pd
J_1	+20.869	+8.640	+11.192	+26.813	+22.578
J_2	+2.019	+0.593	−0.154	−0.238	+1.125
J_3	−0.616	−0.025	−0.024	−2.903	−0.884
J_4	−0.067	+0.125	+0.016	−0.338	−0.321
J_5	−0.767	–	+0.173	−0.280	−0.596
J_6	–	–	–	–	+0.040
J_7	–	–	–	–	+0.239
J_8	–	–	–	–	–
J_9	–	–	–	–	–
J_{10}	–	–	–	–	–
J_{eff}	+21.168	+10.483	+11.962	+8.147	+20.897
D_1	−0.419	−0.179	+0.014	+0.145	+0.154
D_2	+0.002	−0.041	+0.132	+0.013	+0.138
D_3	+0.078	−0.010	−0.072	+0.070	+0.026
D_4	−0.005	−0.043	+0.024	+0.005	−0.043
D_5	+0.081	−0.028	–	+0.012	−0.004
D_6	−0.023	−0.012	–	−0.001	+0.019
D_7	−0.005	+0.026	–	+0.019	+0.012
D_{eff}	−0.20	+0.40	−0.19	−0.39	−0.30
K	−0.45	+0.23	+0.00	−0.85	−0.59

Chapter 8

Detection of isolated zero field sub-10 nm skyrmions in ultrathin Co films

The stabilization of magnetic skyrmions has been predicted based on a micromagnetic model more than 20 years ago [24, 25]. Since their first experimental observation in different class of materials [26, 28, 29, 31] they are envisioned to be used in novel storage and logic devices [2, 3, 8, 142]. Therefore, the requirements on both material and the structures itself are vast and thus, the research is still ongoing to find the perfect skyrmionic system.

Being suitable for applications, skyrmions should be small and stable at room temperature without applying an external magnetic field [3]. Furthermore, the detection of such structures is crucial for simple device fabrication. It has been proposed that the all-electrical readout of magnetic bits is beneficial [34]. A key aspect for stabilizing such skyrmions in magnetic systems is the controlled interplay of mainly the exchange interaction, Dzyaloshinskii-Moriya interaction (DMI) and magnetocrystalline anisotropy energy (MAE) [143, 144].

In the recent past, some of the features such as room temperature stabilization have been accomplished in multilayer systems, confined magnetic structures, compensated ferrimagnets or synthetic antiferromagnets (AFMs) [35–40, 145, 146]. However, even though the skyrmions occur either in remanence, i.e. after the application and reduction of a magnetic field, are too large in size or have not been observed with electrical measurements.

In the previous chapter, we presented an overview on which combination of materials can be potentially interesting to stabilize complex magnetic structures such as skyrmions. Rh/Co/Ir(111) appears to be the most promising film due to a large exchange frustration, moderate DMI and large MAE.

Here, we present a detailed description for Rh/Co/Ir(111), in which we predict nm-sized skyrmions to be stable without applying a magnetic field. Measurements from experimental colleagues in Hamburg confirm the occurrence of such small skyrmions together with atomic-scale domain walls (DWs) for small temperatures. They appear – in contrast to other skyrmion systems – in a ferromagnetic (FM) surrounding in the virgin state and can be detected with a non-magnetic scanning tunnelling microscopy (STM) tips due to a large non-collinear magnetoresistance (NCMR) at the Fermi energy. The NCMR effect has first been found for Pd/Fe/Ir(111), but at an energy far from E_F [147, 148]. We recently published our findings in Pubs. II and III.

This chapter is structured as follows: In Secs. 8.2 and 8.3, we provide a detailed analysis of the strong frustration effects in Rh/Co/Ir(111) describing the magnetism. Performing spindynamics simulations for Rh_{fcc}/Co/Ir(111) skyrmions are predicted to be stable in this film (Sec. 8.4). Triggered by our prediction, experiments have been performed at the University of Hamburg which are partially presented in Sec. 8.7. They reveal stable skyrmions in the hcp stacked Rh layer on Co/Ir(111). Due to some intermixing in the experiments, the magnetic properties might be slightly affected. We therefore present calculations on the inverted stacked Co/Rh/Ir(111) to get a rudimentary insight about intermixing (Sec. 8.6). Working out the DMI being the most affected quantity due to intermixing, we reduce this interaction for Rh_{hcp}/Co/Ir(111) in our calculations and present spindynamics and geodesic nudged elastic band (GNEB) calculations on non-collinear structures in Sec. 8.7. In Sec. 8.8, we explain the properties of the non-collinear states in Rh_{hcp}/Co/Ir(111) being detected by electronic structure measurements. Furthermore, we applied various test calculations on Rh/Co/Ir(111) to see the robustness of both data and analysis which are finally presented in Sec. 8.10.

8.1 Computational Details

For this study, we used the FLEUR code [47] with film geometry. We choose the theoretical equilibrium lattice parameter of bulk Ir $a_{\text{Ir-bulk}} = 7.22\,\text{a.u.}$, which has been obtained within the local density approximation (LDA) [127]. For the following calculations, the muffin tin (MT) radii were set to $R^{\text{MT}}_{\text{Rh,Ir}} = 2.31\,\text{a.u.}$, $R^{\text{MT}}_{\text{Co}} = 2.23\,\text{a.u.}$ for Rh, Ir and Co, respectively. If not stated differently, the energy cutoff was set to $k_{\text{max}} = 4.0\,\text{a.u.}^{-1}$. We investigate fcc and hcp stacking possibilities of the Rh surface layer.

Structural relaxation The structural relaxations were performed in the FM state using a symmetric film with five layers of Ir(111) and a Rh/Co bilayer (BL) on both sides of the film. The forces between the layers were minimized in [111] direction up to a threshold of $10^{-5}\,\text{htr/a.u.}$ while three Ir layers in the centre of the film are kept fixed at the bulk equilibrium lattice parameter. The resulting interlayer distances (denoted as $d_{12}, d_{23}, \ldots$) are presented in Tab. 8.1. For the structural relaxation, we applied 240 k points in the irreducible wedge of the two-dimensional (2D) Brillouin zone (BZ) as well as the generalized gradient approximation (GGA) exchange correlation (xc) functional [73]. The same calculations were done for the film of Co/Rh/Ir(111) to get insight into a film where the BL shows inverted order. In Sec. 8.10.3, we present calculations with a different xc potential where the robustness of our data is emphasized.

Spin spiral calculations Applying the interlayer distances of the structural relaxation, we self-consistently performed spin spiral calculations without spin-orbit coupling (SOC) using an asymmetric film with nine layers of Ir(111). The vector $\mathbf{q}$ is chosen along the high symmetry directions $\overline{\Gamma}$-$\overline{M}$ and $\overline{\Gamma}$-$\overline{K}$ of the hexagonal 2D BZ.

Table 8.1 | Relaxed interlayer distances d_{ij} (a.u.) for Rh/Co/Ir(111) and Co/Rh/Ir(111). d_{12} represents the distance between the Rh and the Co layer, d_{23}, between Co [Rh in the case of Co/Rh/Ir(111)] and the Ir(111) surface layer and d_{34} between the Ir(111) surface and the substrate. The interlayer distance for Ir(111) bulk is 4.17 a.u.

System	d_{12}	d_{23}	d_{34}
Rh_{fcc}/Co/Ir(111)	3.89	4.06	4.35
Rh_{hcp}/Co/Ir(111)	3.88	4.02	4.41
Co_{fcc}/Rh/Ir(111)	3.85	4.32	4.28
Co_{hcp}/Rh/Ir(111)	3.84	4.30	4.29

The energy contribution due to SOC, ΔE_{SOC}, is calculated in first-order perturbation theory for every previously calculated $\mathbf{q}$ point [91, 128, 129]. For spin spiral calculations, we used the LDA *xc* functional [127] and 1936 k points in the full 2D BZ. In order to obtain full convergence of spin spiral states (Sec. 8.10.1) around the $\overline{\Gamma}$ point, we increased the energy cutoff to $k_{\mathrm{max}} = 4.3\,\mathrm{a.u.}^{-1}$ and applied up to 10000 k points in the full 2D BZ.

Magnetocrystalline anisotropy energy For the MAE, we first self-consistently converge calculations of asymmetric films with 9 layers of Ir(111) in the FM state in scalar-relativistic approximation. The computational settings are the same as for the spin spiral calculations described above. The values of the MAE, K are determined by applying the force theorem [80, 81], where we applied the spin quantization axis with SOC perpendicular the film plane $E_{\perp}$ and parallel to the film plane $E_{\parallel}$. The resulting energy difference is determined as $K = E_{\perp} - E_{\parallel}$.

Vacuum density of states and magnetoresistance We compare the tunnelling anisotropic magnetoresistance (TAMR) and NCMR from Rh/Co/Ir(111) with experimental observations. Therefore, we calculate the vacuum local density of states (LDOS) 3 Å above the surface of the film. The computational setup was taken from spin spiral calculations and the resulting magnetoresistance (MR) is calculated via

$$MR = \frac{\mathrm{LDOS}_{\mathrm{FM}} - \mathrm{LDOS}_{\mathrm{spiral}}}{\mathrm{LDOS}_{\mathrm{FM}}} \tag{8.1}$$

Spindynamics simulations The magnetic interaction parameters which are obtained by mapping the atomistic spin model to our density functional theory (DFT) results are used to perform spindynamics simulations to scan a wider phase space of magnetic states including skyrmions and antiskyrmions. We compare the structures with the FM ground state and numerically solve the Landau-Lifshitz equation by applying the semi-implicit integrator as proposed in Ref. 149. The simulations are carried out with various damping parameters of $\alpha \in [0.05, 1]$ and a time step of 0.1 fs where we used $1.5 - 5.0 \times 10^6$ timesteps to relax the structures. For Rh_{fcc}/Co/Ir(111), we present results from a hexagonal lattice of 100×100 spins, whereas for Rh_{hcp}/Co/Ir(111), a 70×70 lattice has been used. The magnetic moment of both films is set to $2.5\,\mu_{\mathrm{B}}$.

In order to compare the diameter of skyrmions and antiskyrmions with experiments, we present m_z profiles which are defined as

$$m_z(x,y) = \cos(\theta(r)) \tag{8.2}$$

where

$$\theta(r) = \pi - \arcsin\left[\tanh\left(\frac{r-c}{\Delta/2}\right)\right] - \arcsin\left[\tanh\left(\frac{r+c}{\Delta/2}\right)\right] \tag{8.2a}$$

and

$$r = \sqrt{(x-x_0)^2 + (y-y_0)^2} \tag{8.2b}$$

The diameter is the distance from the centre of the skyrmion to the two points of the profile at which $m_z = 0$.

Note that the procedure for the skyrmion diameter is deviating from that for the DW width w, where the slope at the reversal point of the profile is taken into account, so that

$$\theta(\mathbf{r}) = 2\arctan\left[\exp\left(\frac{(r-c)}{\Delta}\right)\right], \tag{8.3}$$

where $\theta(r)$ defines the angle of the spin in the wall and c is the centre position of the DW and Δ is attributed to the width of the DW.

Geodesic nudged elastic band method calculations Starting from the relaxed spin structures from spindynamics, we calculate the minimum energy path (MEP) for annihilation processes of skyrmions and antiskyrmions into the FM state. For this purpose we apply the GNEB method [119]. The generated discrete path consists of images from the local minimum (skyrmion, antiskyrmion) into the global minimum (FM) and is systematically brought into the MEP. For Rh_{fcc}/Co/Ir(111), we use 30 images along the MEP whereas for Rh_{hcp}/Co/Ir(111), 20 images are taken into account. To determine the height and position of the saddle point (SP), the energy barrier, we apply the climbing image technique [120, 121].

8.2 Exchange and DMI frustration in Rh/Co/Ir(111)

In order to describe the magnetic properties, we calculate the energy dispersion $E(\mathbf{q})$ of flat, cycloidal spin spiral states presented in Fig. 8.1. Points represent DFT calculations and lines are fits to the atomistic spin model including exchange beyond nearest neighbours (without SOC), DMI and MAE (with SOC). The light red curve shows the film of Co_{fcc}/Ir(111) as reference as it has been presented in Ch. 6 and 7.

Co/Ir(111) holds small exchange frustration and $E \sim \mathbf{q}^2$ where we see a FM ground state. Experiments have shown out-of-plane FM domains with small DWs as described in Ch. 5 and Pub. I. With a Rh layer on top, the energy dispersion shows significant differences at the $\overline{\Gamma}$ point and at the edges of the 2D BZ, $\overline{M}$ and $\overline{K}$, which has been partially described previously (Ch. 7).

Due to the large energies at the AFM states, Co/Ir(111) and Rh/Co/Ir(111) show a large nearest neighbour exchange interaction J_1, which is a typical characteristic for strong

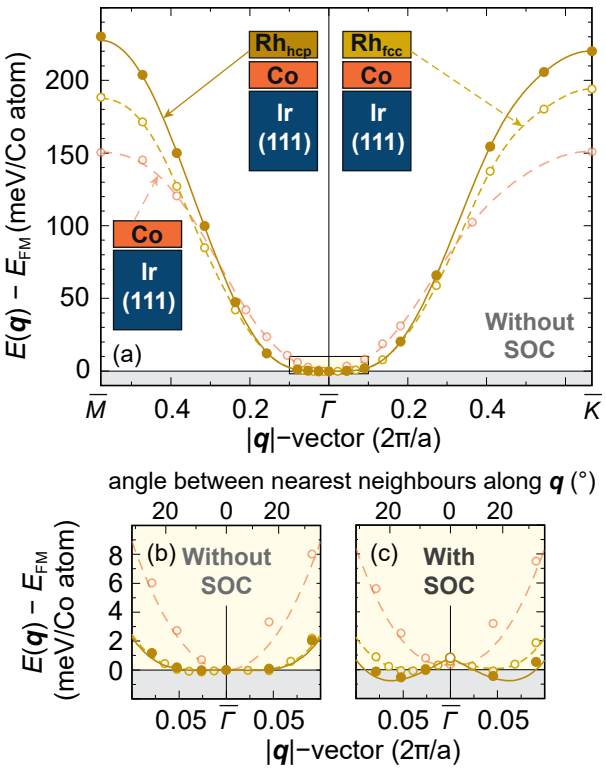

Figure 8.1 | Full energy dispersions $E(\mathbf{q})$ of flat cycloidal spin spirals for Rh/Co/Ir(111). (a) Energy dispersion without spin-orbit coupling (SOC) along the high symmetry path $\overline{\Gamma}$-$\overline{M}$ and $\overline{\Gamma}$-$\overline{K}$ of the two-dimensional Brillouin zone. Filled and open circles for Rh_{hcp}/Co/Ir(111) and Rh_{fcc}/Co/Ir(111), respectively, show calculated energies from DFT with respect to the ferromagnetic (FM) state, whereas lines [solid for Rh_{hcp}/Co/Ir(111) and dashed for Rh_{fcc}/Co/Ir(111)] represent the mapping to the atomistic spin model of the Heisenberg exchange beyond nearest neighbours. As a reference, the energy dispersion of the film system Co_{fcc}/Ir(111) is shown. (b) Zoom image of (a) around $\overline{\Gamma}$ [shown as rectangle in (a)]. (c) Zoom image as (b) including SOC. The atomistic spin models for the description now contains exchange, Dzyaloshinskii-Moriya interaction (DMI) beyond nearest neighbours and the uniaxial magnetocrystalline anisotropy energy. The figure has been adapted from Pub. II.

FMs. All obtained magnetic interactions of Rh/Co/Ir(111) are presented in Tab. 8.2. In fact, upon adding a Rh_{hcp} layer on Co/Ir(111) J_1 increases by up to 10 meV which is emphasized by higher energies of the states at the BZ boundaries [Fig. 8.1 (a)]. This could lead to the assumption that Rh/Co/Ir(111) is an even more prototypical FM film system.

However, for small $\mathbf{q}$ vectors, the energy dispersion does not exhibit the $\mathbf{q}^2$ behaviour as Co/Ir(111) [Fig. 8.1 (b)]. $E(\mathbf{q})$ is extremely flat and neglecting SOC, a canting of about 20° between nearest neighbours does not cost any energy. This is only seen for systems with large exchange frustration and thus, the mapping of the curve requires ten neighbours $(J_1,\ldots,J_{10})$ for the exchange to capture this shape. In Sec. 8.10.1, we show that even six neighbours are not sufficient.

When including SOC, collinear states are preferred by the strong out-of-plane MAE, $K = -1.2$ meV for Rh_{fcc} and $K = -1.6$ meV for Rh_{hcp}, whereas a canting is induced by the DMI. Due to the presence of SOC, spin spiral states and the FM state are almost energetically degenerate and small distortions will have a decisive impact on the magnetic ground state [Fig. 8.1 (c)]. For Rh_{fcc}, the magnetic interactions propose a FM ground state [dashed line in Fig. 8.1 (c)], whereas the DFT calculations show a tiny

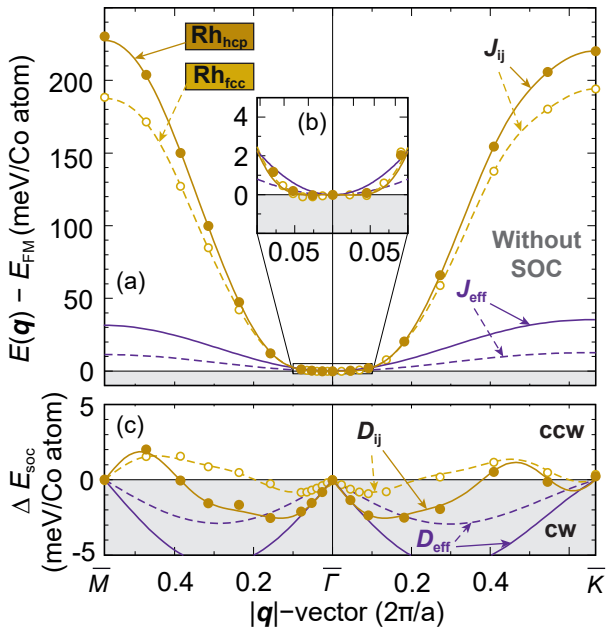

Figure 8.2 | Energy dispersions $E(\mathbf{q})$ of flat cycloidal spin spirals for Rh/Co/Ir(111) comparing the atomistic spin model with the effective nearest neighbour approximation. (a) Energy dispersion without spin-orbit coupling (SOC) along the high symmetry path $\overline{\Gamma}$-$\overline{M}$ and $\overline{\Gamma}$-$\overline{K}$ of the two-dimensional Brillouin zone. (b) Zoom image at $|\mathbf{q}| \to 0$. (c) Energy contribution due to SOC where positive values denote counterclockwise (CCW) rotation and negative values clockwise (CW) rotation. Filled and open circles for Rh_{hcp}/Co/Ir(111) and Rh_{fcc}/Co/Ir(111), respectively, show calculated energies from DFT with respect to the ferromagnetic (FM) state, whereas lines [solid for Rh_{hcp}/Co/Ir(111) and dashed for Rh_{fcc}/Co/Ir(111)] represent the fits to either the fully atomistic spin model J_{ij} for the Heisenberg exchange in (a,b) and D_{ij} for the Dzyaloshinskii-Moriya interaction in (c). The purple curves correspond to the respective fits to the effective nearest neighbour approximation J_{eff} in (a,b) and D_{eff} in (c). The figure has been adapted from the supplemental material of Pub. II.

spin spiral minimum (open circles); however, the deviations are beyond the accuracy of the calculations. In the case of Rh_{hcp}, a long-ranged spin spiral state occurs as ground state in both DFT and the atomistic spin model, where the energy differences between FM and spin spirals are below 1 meV/Co atom.

While the effective nearest neighbour approximation (similar to the micromagnetic model) can describe the magnetism in typical FMs such as Co/Ir(111), we analyse this model in detail for Rh/Co/Ir(111). The descriptions of the fully atomistic spin model (J_{ij}, D_{ij}) based on DFT calculations are compared with the effective nearest neighbour approximation (J_{eff}, D_{eff}) of both exchange and DMI in (Fig. 8.2). When applying J_{eff}, for both stackings (dashed lines correspond to fcc stacking of Rh, solid lines to the hcp stacking) the obtained energy dispersions differ by far from those using J_{ij} [Fig. 8.2 (a)]. Especially around the AFM states ($\overline{M}$ and $\overline{K}$ points) the energy differences between the two descriptions are about 200 meV/Co atom.

Even around the $\overline{\Gamma}$ point [Fig. 8.2 (b)], we see a slight deviation between the two models. However, the qualitative trend is differing because no matter how small J_{eff}

	Rh_{fcc}	Rh_{hcp}
J_1	+25.1802	+29.2169
J_2	+0.2538	+0.8550
J_3	−2.7064	−4.0687
J_4	−0.6335	−0.4136
J_5	−0.2375	−0.5804
J_6	+0.0950	−0.1268
J_7	+0.0162	+0.0055
J_8	+0.2727	+0.0468
J_9	+0.0299	+0.0478
J_{10}	−0.2814	−0.1586
J_{eff}	+1.4080	+3.9100
D_1	−0.2935	+0.1303
D_2	+0.1064	+0.3816
D_3	+0.2944	+0.3741
D_4	−0.0330	−0.0277
D_5	−0.0217	−0.2388
D_6	+0.0383	−0.0564
D_7	+0.0876	+0.1784
D_{eff}	+0.8333	+1.6345
K	−1.1660	−1.6350

Table 8.2 | Obtained values for magnetic interactions in Rh/Co/Ir(111) mapping the atomistic spin model to the results of DFT calculations. All values of the i-th neighbour exchange J_i, Dzyaloshinskii-Moriya interaction (DMI) constants D_i and uniaxial magnetocrystalline anisotropy energy K are given in meV. $J > 0$ ($J < 0$) represents ferromagnetic (antiferromagnetic) order, $D > 0$ ($D < 0$) clockwise (counterclockwise) rotation and $K > 0$ ($K < 0$) denotes an in-plane (out-of-plane) easy axis. As a comparison, the effective nearest neighbour exchange and DMI, J_{eff} and D_{eff}, are presented. Note that J_{eff} and D_{eff} are strongly dependent on the fitting region around $\mathbf{q} < |0.1|\,2\pi/a$. In order to reproduce the following spindynamics simulations, four digits are presented.

is, it will always show a $\mathbf{q}^2$ behaviour. Only $J_{\text{eff}} \sim 0\,\text{meV}$ will capture the energetically degenerate spin spiral states within $|\mathbf{q}| < 0.05\,2\pi/a$. Note with improving the nearest neighbour approximation around the $\overline{\Gamma}$ point, the deviations at the BZ boundaries will be worsened and vice versa. With the effective nearest neighbour description, in Rh/Co/Ir(111) the interpretation would give a physically wrong picture[1]. In Sec. 8.10.4, we can also determine effective parameters from DW properties.

For the DMI [Fig. 8.2 (c)], D_{eff} and D_{ij} describe the obtained contribution ΔE_{SOC} around the $\overline{\Gamma}$ point for $|\mathbf{q}| < 0.1\,2\pi/a$ in a similar way. For larger $\mathbf{q}$, the DFT calculations show a drastic change of the behaviour and even CCW spin spiral states with a short period are preferred. As described in Ch. 6, the DMI is strongly frustrated in accordance to the exchange and seven neighbours are required to capture the dispersion of ΔE_{SOC}. For Rh/Co/Ir(111), it is necessary to apply the fully atomistic spin model in order to adequately describe the energies of non-collinear spin structures.

More details on the DMI can be seen in Fig. 8.3, where the element resolved energy contributions due to SOC are shown for Rh/Co/Ir(111). For both stackings, the Rh top layer has a decisive contribution preferring CW rotating spin spiral states along the complete high symmetry paths of the 2D BZ. Especially Rh_{hcp} [Fig. 8.3 (b)] shows

[1] Note that J_{eff} and D_{eff} are strongly dependent on the fitting region around $\mathbf{q} \to 0$. For both stackings of Rh, we could obtain the same J_{eff}.

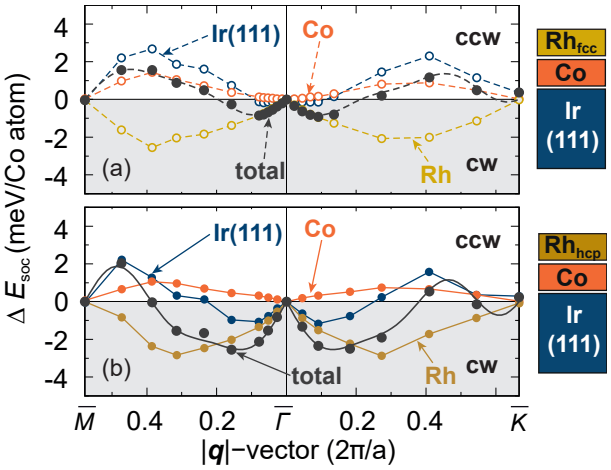

Figure 8.3 | Element resolved energy contribution due to spin-orbit coupling (SOC) to the energy dispersion of cycloidal spin spirals for Rh/Co/Ir(111). (a) Contribution due to SOC for Rh_{fcc}/Co/Ir(111) where positive values denote counterclockwise (CCW) rotation and negative values clockwise (CW) rotation. The black points show calculated values from DFT calculations and the black line is the fit to the atomistic spin model of the Dzyaloshinskii-Moriya interaction. Coloured points/lines represent the SOC contribution of the respective element. Note that the Ir(111) contribution (dark blue) of ΔE_{SOC} is the sum of all Ir layers. The coloured lines serve as guide to the eye. (b) Contribution due to SOC for Rh_{hcp}/Co/Ir(111).

a larger contribution around $\overline{\Gamma}$. The Ir(111) substrate prefers CW rotating states for small **q**, but CCW rotation for higher **q** vectors. Its contribution around the $\overline{\Gamma}$ point is also higher for the hcp stacking of Rh. In both films, the Co can be neglected when determining the DMI around the FM state, but its contribution increases for larger **q** vectors. Therefore, in particular the competition of ΔE_{SOC} between Rh and Ir(111) substrate is the driving mechanism of the DMI frustration in Rh/Co/Ir(111).

8.3 Magnetic and electronic properties

The magnetic interactions of Rh/Co/Ir(111) are strongly frustrated. Since the classical model of spin interactions does neither take into account an induced magnetization nor a change in the magnetic moment along the energy dispersion, we have to make sure that our interpretation of the magnetism holds true when such effects occur. The Stoner contribution (cf. Sec. 4.1) can change the energies of the different states which has also been analysed in Ref. 129. Within the small energies in Rh/Co/Ir(111), this could lead to different ground states.

In Fig. 8.4, the magnetic moment is presented for the topmost three elements of Rh/Co/Ir(111). Open circles with dashed lines correspond to the fcc stacking in the Rh layer and points with solid lines to Rh_{hcp}/Co/Ir(111). For all elements, the magnetic moment in the film of Rh_{hcp}/Co/Ir(111) is larger. Consequently, Rh_{hcp}/Co/Ir(111) shows a stronger FM behaviour where AFM states are higher in energy (cf. Fig. 8.1).

The change of magnetic moment in both Rh and Co in Fig. 8.4 (a,b) is comparably

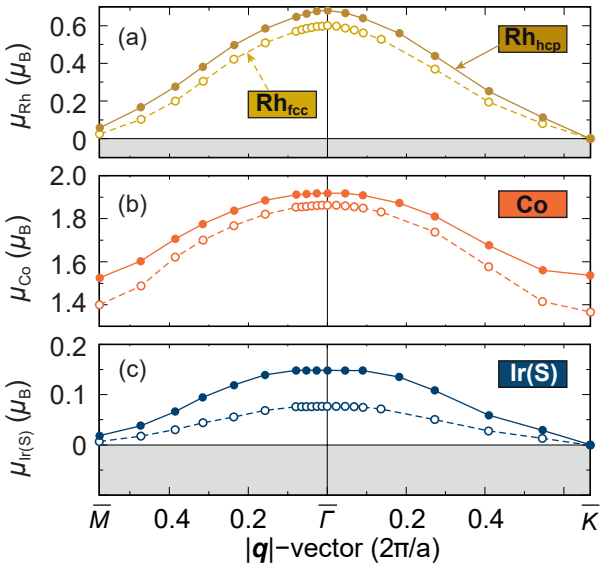

Figure 8.4 | Calculated magnetic moment (μ_B) for spin spirals in Rh/Co/Ir(111). (a) Magnetic moment of the Rh top layer. Points and solid lines correspond to Rh_{hcp}/Co/Ir(111) and open circles with dashed lines to Rh_{fcc}/Co/Ir(111). The lines serve as guide to the eye. (b) Magnetic moment of Co. (c) Magnetic moment of the Ir(111) surface layer Ir(S).

large, about $0.6\,\mu_B$ for Rh and $0.4\,\mu_B$ for Co comparing the high symmetry points $\overline{\Gamma}$ with $\overline{M}$ or $\overline{K}$. In the narrow region of the ground state $\mathbf{q} \to 0$, all magnetic moments show a constant behaviour. We conclude that the Stoner energy will not affect our interpretation of the ground states. Test calculations on conical spin spirals have been carried out (cf. Sec. 8.10), where without change of the magnetic moment almost the exact same energy dispersion (especially in the FM region) is obtained and supports our approach.

We analyse the electronic structure in more detail comparing the LDOS in the FM states. In Fig. 8.5, the LDOS is presented for the topmost three layers where the shaded areas show reference LDOS. For Rh, this is a Rh unsupported monolayer with the lattice constant of Ir(111), whereas for the Co layer, the reference film of Co_{fcc}/Ir(111) is used. The shaded area of Ir shows the LDOS of a middle layer in the Ir(111) of Rh/Co/Ir(111).

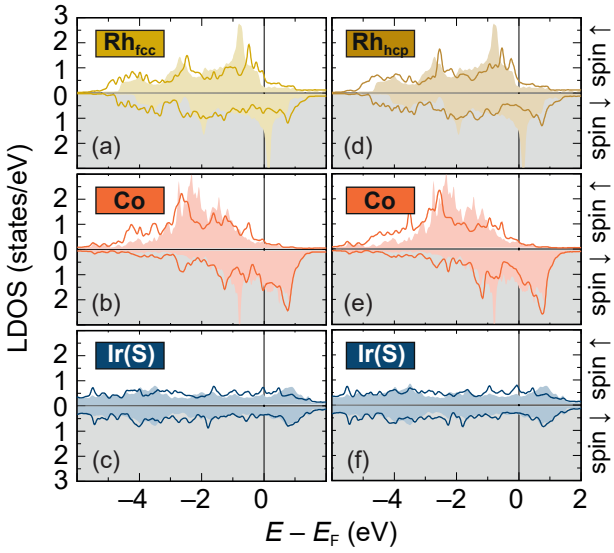

Figure 8.5 | Calculated local density of states (LDOS) for Rh/Co/Ir(111) in the ferromagnetic state. (a,b,c) LDOS of Rh_{fcc}/Co/Ir(111) for Rh, Co and the Ir(111) surface layer, respectively. (d,e,f) LDOS of Rh_{hcp}/Co/Ir(111). The shaded areas in (a,d) show the comparison of an Rh unsupported monolayer using the in-plane lattice constant of Ir(111), while for (b,e) the contributions of the Co areas are taken from the film systems of Co_{fcc}/Ir(111) (Fig. 5.4). For Ir, a layer in the middle of the calculated Ir(111) substrate is taken in (c,f).

The differences between shaded areas and lines only occur due to the strong hybridization between the three elements and we see large peaks in Rh/Co/Ir(111) which are absent in the reference LDOS.

Around the Fermi energy, a significant difference between the two stacking orders of Rh is observed. Only for Rh_{fcc}/Co/Ir(111) [Fig. 8.5 (a,b)] a peak in both spin $\uparrow$ and spin $\downarrow$ channels is present. For Rh_{hcp}/Co/Ir(111), this peak in the minority spin channel is shifted to higher energies and the peak of the majority spin channel does not appear. Consequently, the magnetic moments of both Rh and Co for Rh_{hcp}/Co/Ir(111) are larger. The LDOS of the Ir surface layer looks similar for both stackings where the large hybridization peaks with Co and Rh around E_F are observed.

8.4 Prediction of skyrmions and antiskyrmions in Rh_{fcc}/Co/Ir(111)

To see the consequences of frustration in Rh/Co/Ir(111), we use the obtained magnetic interaction parameters from the atomistic spin model and perform spindynamics simulations on Rh_{fcc}/Co/Ir(111) solving the Landau-Lifshitz equation.

We first consider a DW in the absence of magnetic field, since the interactions show a FM ground state (lines in Fig. 8.1). Due to the very small energies in $E(\mathbf{q})$, DWs will cost small energy: +2 meV/nm compared to the FM state. This energy difference is one order of magnitude lower than the DW energy for Co_{fcc}/Ir(111) (Ch. 5), where the occurrence of DWs has been confirmed by experiments in Pub. I. Due to the very flat energy dispersion and the large out-of-plane anisotropy, the DWs are exceptionally thin. From simulations, we obtain a DW width of $w = 1.4$ nm, which is half the width of the DWs for Co/Ir(111).

The small DW energy allows for a stabilization of other non-collinear magnetic structures. In fact, both skyrmions and antiskyrmions are metastable over a wide range of applied magnetic field and especially without applying a magnetic field (8.6). Note that in contrast to other ultrathin film systems that host skyrmions such as Pd/Fe/Ir(111) [31, 122] or Co/Ru(0001) [139], the magnetic ground state here is the FM state. Therefore, no magnetic field is needed to trigger a transition from a spin spiral ground state to the skyrmion state.

In Fig. 8.6 (a), the profile of both antiskyrmion (grey) and skyrmion (yellow) in the absence of magnetic field is shown, where the lines are the fit to Eq. (8.2). For both profiles, the fit is good; however, due to the small size of the antiskyrmion, Eq. (8.2) is at the limit of description. In their centre antiskyrmion and skyrmion exhibit a continuous rotation of the spins.

Comparing the energy of these spin structures with the FM ground state at $B_z = 0$ T the skyrmion is only 0.05 meV/Co atom higher in energy [Fig. 8.6 (b)]. In accordance with the literature [134, 150, 151], due to the presence of DMI, antiskyrmions are more unfavoured (0.25 meV/Co atom at $B_z = 0$ T). When a magnetic field is applied,

the Zeeman interaction prefers collinear order in the direction of magnetic field. Consequently, the energy of (anti-) skyrmions rises, but the energy loss is small so that the structures are stable beyond the presented range of magnetic field.

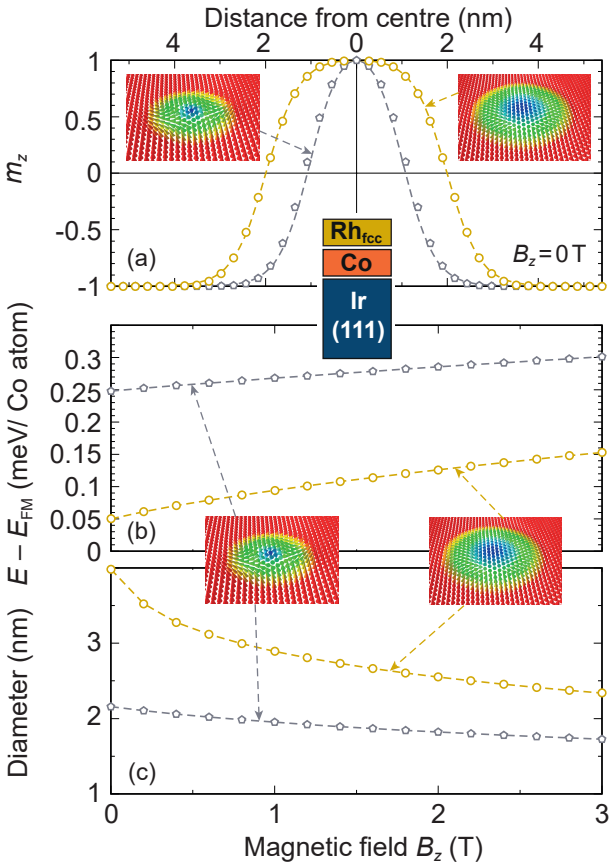

Figure 8.6 | Spindynamics simulations on skyrmions and antiskyrmions for Rh_{fcc}/Co/Ir(111). (a) (Anti-) skyrmion profile m_z in the absence of external magnetic field. The grey points (curves) correspond to antiskyrmions (sketch upper left) and yellow points (curves) to skyrmions (sketch upper right). Note that the profile is reversed compared to the sketches where red spins have a positive z-component and blue spins a negative one. (b) Energy difference of (anti-) skyrmions in meV/Co atom with respect to the ferromagnetic (FM) ground state depending on an applied magnetic field. (c) (Anti-) skyrmion diameter in nm dependent on the magnetic field. The diameter is the distance from the centre of the skyrmion to the two points of the profile at which $m_z = 0$ in (a).

We have already shown that both structures are small even in the absence of magnetic field [cf. Fig. 8.6 (a)]. In Fig. 8.6 (c), the (anti-) skyrmion diameter is plotted over the applied magnetic field. B_z will force spins to align along the z direction and hence the skyrmions get smaller with increasing field. Antiskyrmions are not strongly affected by an applied magnetic field. From 0 – 3 T, its diameter reduces by about 0.5 nm, whereas the change for the skyrmion is more than 1.5 nm for the presented range of magnetic field.

The combination of large exchange frustration where small cantings between spins do not cost any energy and the large MAE in Rh_{fcc}/Co/Ir(111) is the key for stabilizing skyrmions and antiskyrmions without external magnetic field on the nm scale. We further expect even more complex structures such as higher order skyrmions and antiskyrmions to be stable in Rh/Co/Ir(111), similar to the study in Ref. 150. Even though, Co is known as strong FM, the magnetic properties of Rh/Co/Ir(111) show very unique behaviour which can give rise to further studies on this film system.

8.5 Experimental observation of atomic-scale domain walls and skyrmions in Rh_{hcp}/Co/Ir(111)

Motivated by our theoretical predictions, experiments on Rh/Co/Ir(111) have been performed by Marco Perini at the University of Hamburg under the supervision of André Kubetzka and Kirsten von Bergmann in the lab of Prof. Roland Wiesendanger[2].

As described in Ch. 5, Co is growing pseudomorphically in fcc stacking from the Ir(111) step edges (cf. Ref. [130] and Pubs. I and II). Above the Co, Rh forms compact pseudomorphic islands where both stacking possibilities of Rh (fcc and hcp) can be observed. Due to some lateral displacements in the topography and dI/dU signal, the measurements reveal some degree of intermixing between the Rh and the Co. However, Rh and Co are isoelectronic and a quantification of the intermixing is not possible. More details about the experimental procedures and results can be seen in Ref. 130 and Pub. II.

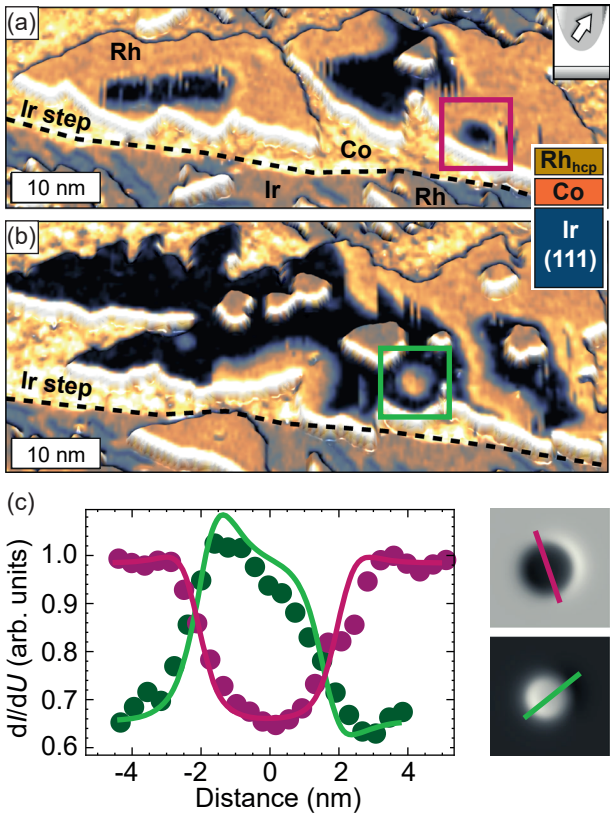

Figure 8.7 | Spin-polarized scanning tunnelling microscopy measurements of Rh_{hcp}/Co/Ir(111) in the virgin state without magnetic field. (a,b) Perspective views of the topography colourized with the simultaneously measured spin-resolved dI/dU signal. The inset in the upper right of (a) shows the direction of the magnetic Cr tip. The ferromagnetic domains are identified by their two-stage contrast. Scanning parameters: $U = -250\,\mathrm{mV}$, $I = 800\,\mathrm{pA}$, $B = 0\,\mathrm{T}$, $T = 4.2\,\mathrm{K}$. (c) dI/dU signal (dots) across the skyrmions of (a,b) in the coloured boxes. The line profiles (lines) are taken along the directions shown in the right sketches. The figure has been adapted from Pub. II.

The fcc stacking of Rh on Co/Ir(111) shows strong out-of-plane FM behaviour for each island. In Fig. 8.7, STM images of Rh_{hcp} islands on Co/Ir(111) are presented in the virgin state, i.e. no manipulation was done.

The large contrast [dark and white in Fig. 8.7 (a,b)] shows oppositely magnetized FM domains, which are separated by very thin DWs (blue rim around the domains). In

[2]Institute of Applied Physics and and Interdisciplinary Nanoscience Center Hamburg, University of Hamburg, Jungiusstrasse 11, 20355 Hamburg, Germany

the coloured boxes [purple in Fig. 8.7 (a), green in (b)] we can recognize small round shaped objects – skyrmions which occur in both magnetization directions. Note that this is the first time that skyrmions spontaneously appear as stable objects in a film without any manipulation (electric or magnetic field). From the size scale in the lower left, we can estimate the skyrmions to be smaller than 5 nm.

Taking the $\mathrm{d}I/\mathrm{d}U$ signal over the skyrmions within the direction as shown in the sketches on the right side, the skyrmion profile can be measured [Fig. 8.7 (c)]. The resulting diameter of the skyrmions is 4.3 nm and 3.5 nm, where the agreement between the measurements (points) and the fitted profile (lines) is reasonable. Note that an asymmetric shape of the profile is expected due to effects of tunnelling MR and NCMR (cf. supplemental material of Pub. II). The mean width of the observed DWs is $w = 0.8\,\mathrm{nm}$.

Comparing the experimentally measured film of Rh/Co/Ir(111), the magnetism with both stackings fcc and hcp appears slightly more FM than it is predicted from our DFT calculations. Nevertheless, such changes take place on a very small energy scale (note that +1 meV in both energy dispersions end up in the right description) and we want to analyse the comparison in more detail. In the following, we therefore discuss how we interpret the occurring intermixing and how small changes in the lattice parameters or DFT calculations can have an impact on the analysis of Rh/Co/Ir(111).

8.6 Swapping Rh and Co – a 100% intermixed film system

Both films of Rh/Co/Ir(111) show a slightly more FM behaviour in the experiments than it has been obtained based on the DFT calculations. We can address this deviation to two facts. First, our calculations show very small energy differences which can be overcome by small distortions such as a different number of Ir(111) layers and structural properties. Here, the *xc* potential which is a correction to the self-energy also plays a role since it can lead to different energies on such a scale. Second, Rh, Co are isoelectronic and from experiments it cannot be unambiguously distinguished between the elements when a small degree of intermixing occurs.

A theoretical description of intermixing within the full potential linearized augmented planewave (FLAPW) method with film geometry requires the application of large supercells for which the computational effort for this study is unreasonable[3]. However, in order to get an idea, we investigated the film of Co/Rh/Ir(111), where we consider the two stackings fcc and hcp in the Co top layer and only fcc stacking of Rh. Applying the results of the structural relaxation of Sec. 8.1, we perform equivalent spin spiral calculations for Co/Rh/Ir(111) as for Rh/Co/Ir(111).

In Fig. 8.8, $E(\mathbf{q})$ is shown for Co/Rh/Ir(111) where the film of $\mathrm{Rh_{fcc}}$/Co/Ir(111) is

[3] Note that with DFT codes using the Korringa-Kohn-Rostoker method, intermixing can be introduced in a more sophisticated way.

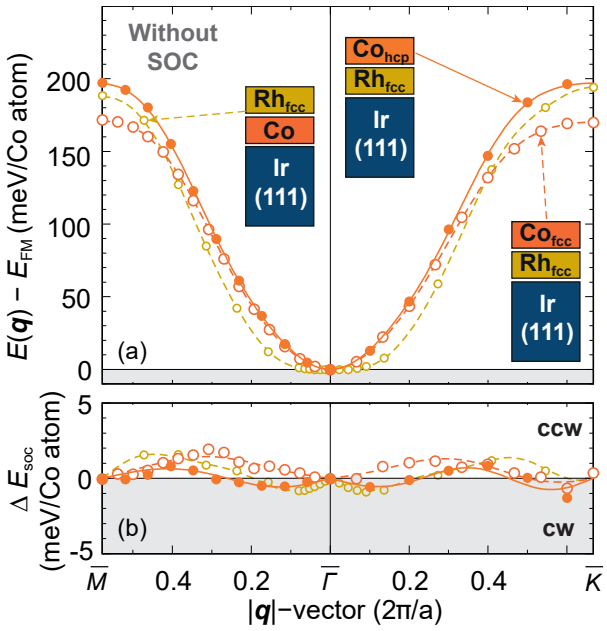

Figure 8.8 | Full energy dispersions $E(\mathbf{q})$ of flat cycloidal spin spirals for Co/Rh/Ir(111). (a) Energy dispersion without spin-orbit coupling (SOC) along the high symmetry path $\overline{\Gamma}$-$\overline{M}$ and $\overline{\Gamma}$-$\overline{K}$ of the two-dimensional Brillouin zone. Orange filled circles [Co_{hcp}/Rh/Ir(111)] and open circles [Co_{fcc}/Rh/Ir(111)] show calculated energies from DFT with respect to the ferromagnetic (FM) state, whereas lines [solid for Co_{hcp}/Rh/Ir(111) and dashed for Co_{fcc}/Rh/Ir(111)] represent the mapping to the atomistic spin model of the Heisenberg exchange beyond nearest neighbours. As reference, the film of Rh_{fcc}/Co/Ir(111) (yellow circles and dashed lines) is shown. (b) Energy contribution due to SOC where the lines are the fit to the Dzyaloshinskii-Moriya interaction beyond nearest neighbours. Positive (negative) values correspond to counterclockwise (CCW) [clockwise (CW)] rotation. The obtained values are presented in Tab. 8.3.

presented as a reference. Without SOC, all films show similar energy differences between the FM state at the $\overline{\Gamma}$ point and AFM states at the BZ boundaries [Fig. 8.8 (a)]. That is why, J_1 compares very well between the different films. All obtained magnetic interactions for Co/Rh/Ir(111) are presented in Tab. 8.3.

However, for small $\mathbf{q}$ vectors, both films of Co/Rh/Ir(111) show a $\mathbf{q}^2$ behaviour and less exchange frustration than the reference system. As a consequence, for both Co_{fcc}/Rh/Ir(111) and Co_{hcp}/Rh/Ir(111) only seven neighbours of J_{ij} are required to describe the DFT results. When considering a small degree of intermixing, we believe that the exchange of Rh/Co/Ir(111) is slightly less frustrated compared to the ideal system.

The energy contribution due to SOC for Co/Rh/Ir(111) around the $\overline{\Gamma}$ point is very small [Fig. 8.8 (b)]. In fact, for Co_{fcc} the DMI slightly prefers CCW rotational spin spirals and Co_{hcp} CW rotation. We therefore see a smaller DMI for Co/Rh/Ir(111) compared to Rh/Co/Ir(111). In the real sample of Rh/Co/Ir(111), the DMI will be smaller than predicted by our DFT calculations.

This assumption is supported by Ref. 152, where it has been shown that in Co/Pt multilayers, the DMI will be reduced due to a small intermixing at the Co/Pt interface. Furthermore, self-consistent DMI calculations have revealed that the

Table 8.3 | Obtained values for magnetic interactions for Co/Rh/Ir(111) mapping the atomistic spin model to the results of DFT. All values of the i-th neighbour exchange J_i and Dzyaloshinskii-Moriya interaction (DMI) constants D_i are given in meV. $J > 0$ ($J < 0$) represents ferromagnetic (antiferromagnetic) order, $D > 0$ ($D < 0$) clockwise (counterclockwise) rotation. As a comparison, the effective nearest neighbour exchange and DMI, J_{eff} and D_{eff}, are presented. Note that J_{eff} and D_{eff} are strongly dependent on the fitting region around $\mathbf{q} \to 0$.

	Co_{fcc}	Co_{hcp}
J_1	+19.928	+23.495
J_2	+2.126	+1.377
J_3	−0.868	−1.487
J_4	−0.284	−0.353
J_5	−0.560	−0.183
J_6	+0.193	+0.165
J_7	+0.211	+0.287
J_{eff}	+20.713	+22.353
D_1	−0.310	−0.064
D_2	−0.137	−0.008
D_3	+0.105	+0.108
D_4	+0.029	−0.089
D_5	−	−0.080
D_{eff}	−0.121	+0.310

treatment of ΔE_{SOC} in first order perturbation can overestimate the DMI by up to 20 – 30 % [129, 138].

The findings above show that intermixing will stabilize the FM order in Rh/Co/Ir(111) due to both reduction of exchange frustration and DMI.

8.7 Zero field skyrmions and the chimera collapse mechanism in Rh_{hcp}/Co/Ir(111)

From the analysis above, the DMI appears as most sensitive interaction due to intermixing. We have also shown previously (cf. Sec. 8.2) that small distortions will affect the calculated ground state due to the extremely small energy differences (cf. Fig. 8.1). In Rh_{hcp}/Co/Ir(111), we therefore reduce the DMI by 50 % in order to obtain the FM ground state as in the experiment. Such a reduction can be addressed to both intermixing and treatment of first order perturbation theory in SOC based spin spiral calculations.

According to Sec. 8.4, we perform spindynamics simulations to see whether we can stabilize non-collinear spin structures. With the large MAE in Rh_{hcp}/Co/Ir(111), we expect slightly smaller structures compared to Rh_{fcc}/Co/Ir(111). In Fig. 8.9 (a), the m_z profile at $B_z = 0\,\text{T}$ is shown for a DW (green), skyrmion (yellow) and an antiskyrmion (grey), respectively[4].

A DW costs about 4.4 meV/nm and can be seen as nearly energetically degenerate with the FM state explaining the large amount of DWs in the Rh/Co/Ir(111) islands of the

[4] Note that due to the extraordinary energy dispersion for Rh/Co/Ir(111), it is possible to stabilize much more complex structures.

experiment as well as their meandering shape (Fig. 8.7). From our simulations, the DWs have a width of 1.3 nm, which is slightly larger than in experiments neglecting constrictions and other distortions. Therefore, our theoretical results are in excellent agreement with the experimental observations.

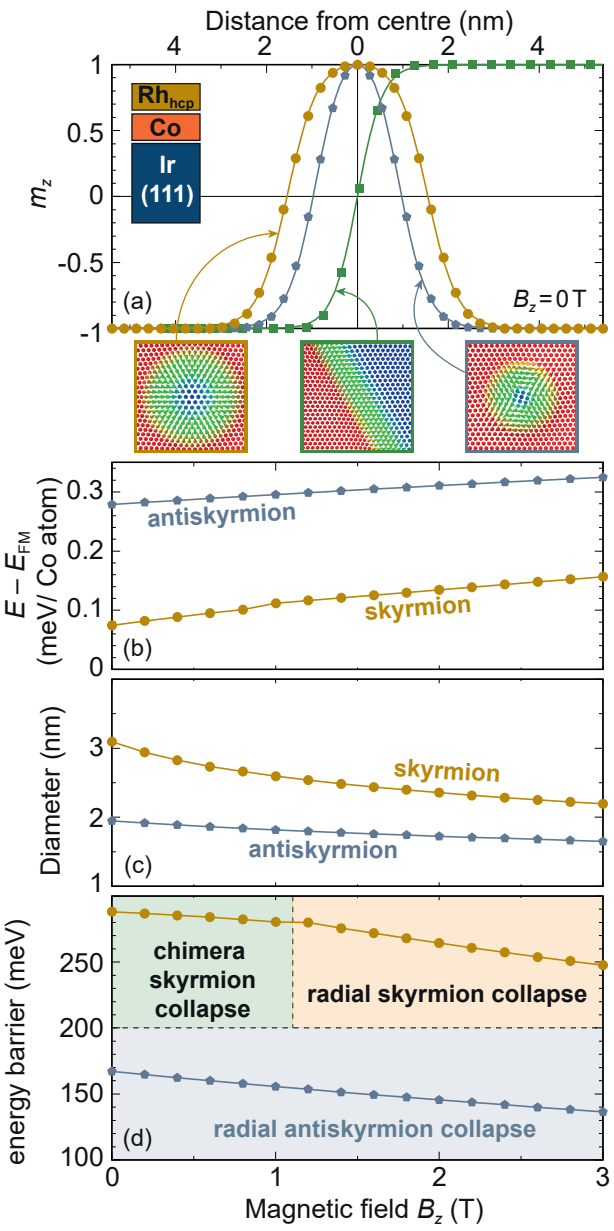

Figure 8.9 | Calculated properties of non-collinear skyrmions, antiskyrmions and a domain wall (DW) for Rh_{hcp}/Co/Ir(111). (a) Profile m_z for a single skyrmion (yellow points and line), antiskyrmion (grey points and line) and DW (green squares and line) stabilized in the absence of an external magnetic field. The lines are fits to the points using Eq. (8.2) (Eq. (8.3) for the DW). The sketches underneath show the respective structures, where colours denote the out-of-plane magnetization direction (red upwards, blue downwards). Note that the profile is inverted compared to the sketches. (b) Energy difference of antiskyrmions and skyrmions in meV/Co atom with respect to the ferromagnetic (FM) ground state depending on an applied magnetic field. (c) (Anti-) skyrmion diameter in nm dependent on the magnetic field. The diameter is the distance from the centre of the skyrmion to the two points of the profile at which $m_z = 0$. (d) Energy barrier with respect to the initial state from geodesic nudged elastic band (GNEB) method calculations for antiskyrmions and skyrmions collapsing into the FM state. Shown are the saddle point energies for skyrmions and antiskyrmions dependent on the magnetic field. The coloured areas denote the different collapse mechanisms.

Both skyrmion and antiskyrmion appear very small and exhibit a continuous rotation of spins in the centre. This is in accordance with measurements presented in Sec. 8.5. We observe small deviations for the fitted profiles (lines) which occur due to frustration of magnetic interactions [Fig. 8.9 (a)]. Estimating the width of the profile as the distance between the points at which $m_z = 0$, the skyrmion diameter is slightly above 3 nm and matches the experimental measurements very well.

Due to the very small energy cost of a single skyrmion compared to the FM state

skyrmions can be stable in a FM background even for magnetic fields beyond 3 T [Fig. 8.9 (b)]. The same holds true for antiskyrmions where the DMI leads to an increase of the energy with respect to the FM state[5]. The small energy differences are a direct consequence of the flat energy dispersion around the FM state (cf. Fig. 8.1). A small canting of spins does not cost energy and thus, skyrmions, DWs and antiskyrmions can be metastable states within a FM ground state.

Fig. 8.9 (c) shows the field dependent size of both skyrmions and antiskyrmions. For $B_z = 0$ T, the profile can be seen in (a). The presence of DMI leads to a compression in the antiskyrmion and furthermore to a slightly asymmetric shape. Applying a magnetic field, these structures cannot be shrunk largely as seen from the almost constant behaviour of the diameter – the size of the antiskyrmion is limited before collapsing into the FM state. Skyrmions appear larger and their field dependent contraction is enhanced for small magnetic fields compared to the antiskyrmions. However, the change in diameter still is less than 1 nm over 3 T [Fig. 8.9 (c)]. Note that in the experiments, the skyrmions also show only a small size dependence with the applied magnetic field (see [130] and Pub. II).

In order to understand why such small (anti-) skyrmions can be stabilized over a large range of magnetic field, we perform GNEB calculations for a collapse the non-collinear spin structures into the FM state. The resulting MEP and its SP represents the energy barrier preventing skyrmions and antiskyrmions to vanish into the FM background. In Fig. 8.9 (d), the SP energies, the energy barrier with respect to the initial state, for both types of structures are presented.

An energy barrier of 0 meV would lead to a spontaneous collapse of a non-collinear spin structure into the FM ground state. For skyrmions and antiskyrmions; however, we see a very large energy barriers above 100 meV even for large magnetic fields. Compared to the prototypical skyrmion film system of Pd/Fe/Ir(111) [134, 153], the energy barrier in Rh/Co/Ir(111) for skyrmions is about 100 meV larger and for the antiskyrmions the difference is about 150 meV showing the exceptional magnetic properties of Rh/Co/Ir(111).

We see two different gradients in the curve and a kink analysing the energy barrier for skyrmions around 1 T [Fig. 8.9 (d)]. This kink arises due to different collapse mechanisms for skyrmions where for $B_z > 1$ T, the skyrmions shrink in size radial symmetrically [134, 153] (yellow shaded area in the background). For $B_z < 1$ T a different collapse mechanism occurs which we denote as chimera skyrmion collapse (green shaded area). For antiskyrmions, only one collapse mechanism is obtained (grey shaded area).

We analyse these different collapse paths in more detail. In Fig. 8.10, the energies along the MEPs of skyrmions are presented where in (a,c), the chimera skyrmion collapse corresponds to magnetic fields below 1 T [cf. Fig. 8.9 (d)] for the green shaded area. The filled points show the energy of the respective image along the MEP where the

[5] Note that in the absence of DMI, skyrmions and antiskyrmions are energetically degenerate.

length of the MEP is given as reaction coordinate.

Starting from the initial skyrmion state (Sk), the energy for several images does not change. For the whole collapse mechanism presented in App. B, this is due to a shift of the skyrmion on the lattice without any deformation, a so-called translation mode [153, 154]. The energy further increases steeply to the SP energy and afterwards a plateau with almost constant energy is observed until the FM ground state is reached.

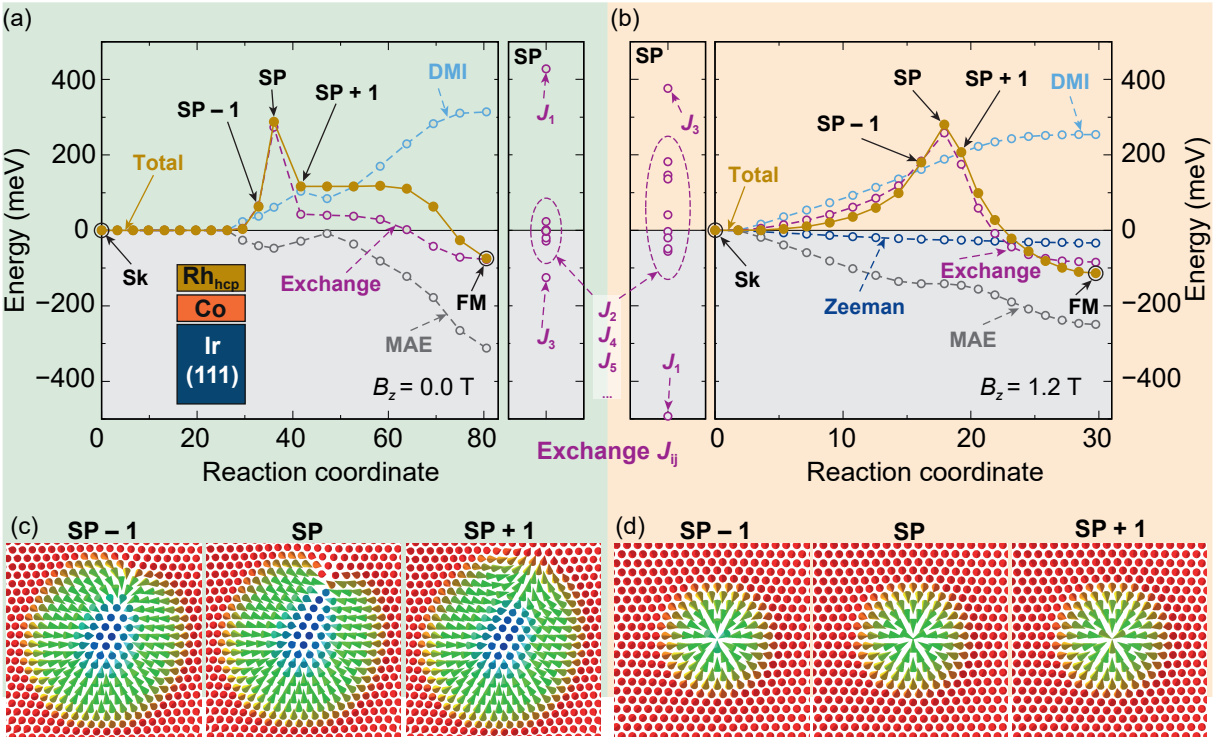

Figure 8.10 | Minimum energy paths (MEPs) for two mechanisms of skyrmion collapses into the ferromagnetic (FM) state for Rh_{hcp}/Co/Ir(111). (a) Total energy (yellow points) and interaction resolved energy contributions along the MEP of the skyrmion (Sk) collapsing into the FM state at $B_z = 0\,T$ via the transition of the chimera skyrmion. Magenta circles show the sum of exchange contributions. Light blue circles are the sum of the Dzyaloshinskii-Moriya interaction (DMI) contribution and grey circles denote the magnetocrystalline anisotropy energy (MAE) contribution. All lines serve as guide to the eye and the colour of the shaded background area corresponds to shaded area in Fig. 8.9 (d) for magnetic fields below 1 T. The right panel shows the decomposition for all included neighbours of exchange interaction energy at the saddle point (SP). (b) Same plot as in (a) for the radial symmetric collapse mechanism at a field of 1.2 T. Additionally, the Zeeman interaction (blue circles) arises. (c) Three zoomed images before and after the SP for the chimera collapse mechanism as marked in (a). All complete MEPs images are presented in App. B. (d) Three zoomed images of the spin structures before and after the SP for the radial symmetric collapse mechanism as marked in (b). Colours denote the out-of-plane magnetization direction of the Co atoms (red upwards, blue downwards). The figure has been adapted from Pub. II.

In Fig. 8.10 (c), the simulated spin structures for three points, before the SP (denoted as SP-1) at the SP and after the SP (denoted as SP+1) are sketched. At SP-1, the

skyrmion is slightly deformed where in the upper right, we see an irregular shape which opens up at the SP structure. Here, the topological charge vanishes and the following structure at SP+1 is called chimera skyrmion [150] which can collapse into the FM state.

Due to the transition via the chimera skyrmion, the energy barrier can lower the energy barrier compared to the standard radial collapse mechanism [cf. Fig. 8.9 (d)]. The energy of the MEP for the radial symmetric collapse is presented in Fig. 8.10 (b). Around the SP, the skyrmion is shrunk in size and at the SP three spins in the centre of the skyrmion are pointing towards each other and tilting out-of-plane at SP+1 [Fig. 8.10 (d)].

Comparing the SP structures [Fig. 8.10 (c,d)] of both collapse mechanisms, the most striking difference is the size of the skyrmions. The chimera skyrmion has a similar size as the initial skyrmion, but for the radial symmetric collapse, the SP structure is about twice smaller. Therefore, the magnetic interactions have a different impact on the energy barrier.

The exchange energies exhibit the same SP energy as the total energy barrier [magneta circles in Fig. 8.10 (a,b)]. In the smaller panels aside, the exchange contributions at the SP are resolved for the different neighbours in the film (J_1,...,J_{10}). J_1 strongly prefers FM alignment and in case of the chimera collapse, the SP structure is large hosting a lot of canted spins [Fig. 8.10 (c)]. The energy barrier from J_1 consequently is very large. J_3 on the other hand prefers AFM alignment as presented in Tab. 8.2. In relation to the initial, perfectly round shaped skyrmion state, the SP structure of the chimera collapse shows more AFM alignment in the upper right and thus J_3 reduces the energy barrier. The contributions of all other neighboured exchange interactions are visible in the encircled area and have a minor contribution.

The exchange for the radial symmetric collapse exhibits the opposite behaviour [Fig. 8.10 (b)]. The SP structure shows a larger FM region than the initial skyrmion state [Fig. 8.10 (d)] and consequently J_1 reduces the energy barrier whereas J_3 has an increasing effect [small panel in Fig. 8.10 (b)]. The analysis of J_2,J_4,J_5,... in the encircled area therefore is straightforward.

Despite these resolved differences, the sum of all exchange contributions gives rise to very similar energy barrier and thus, the frustrated exchange interaction itself cannot explain the occurring chimera skyrmion collapse mechanism. Note that frustrated exchange interaction is unambiguously necessary to induce the chimera collapse mechanism because in the nearest neighbour approximation, J_{eff} prefers the radial symmetric collapse mechanism according to J_1. The chimera collapse only can take place because the DMI contributions have a different impact on the energy barrier [bright blue circles of Fig. 8.10 (a,b)]. The larger SP structure for the chimera collapse costs less DMI energy than the smaller SP structure of the radial symmetric collapse mechanism where less spins are canted.

Neglecting the DMI would always favour the radial collapse because for an

out-of-plane MAE, the smaller SP structure in Fig. 8.10 (b) is energetically more favourable than the one of the chimera collapse. Due to the larger size of the chimera skyrmion structures, more spins show an in-plane component. Those in-plane spins are the reason why the MAE increases almost up to zero energy compared to the initial skyrmion state which is not present for the radial collapse [Fig. 8.10 (a)]. Obviously, the MAE is always competing with the DMI when the energy barrier is formed. With a larger MAE in Rh/Co/Ir(111), the chimera collapse mechanism becomes unfavourable. Due to the applied magnetic field additionally the Zeeman interaction prefers collinear states and therefore reduces the energy barrier [dark blue circles in Fig. 8.10 (b)].

For completeness, we analyse the collapse mechanism of an antiskyrmion (Fig. 8.11). The energy barrier is smaller than for skyrmions because of the low DMI contribution [bright blue circles of Fig. 8.11 (a)][6].

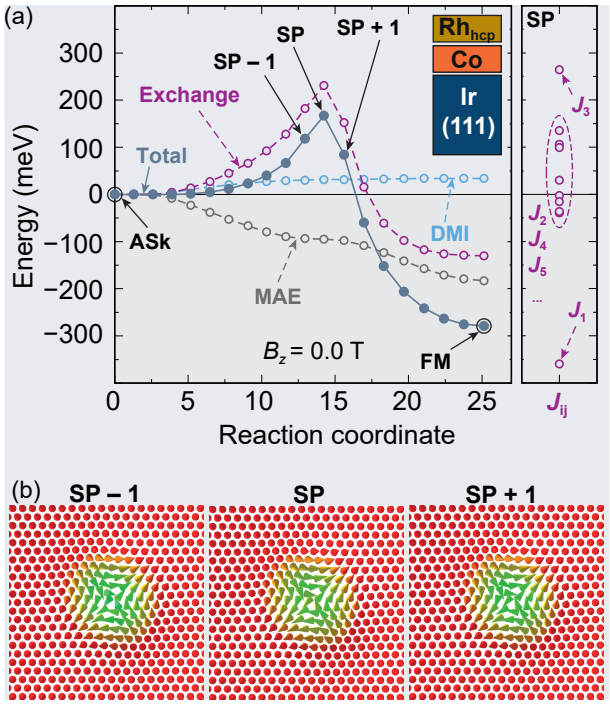

Figure 8.11 | Minimum energy paths (MEPs) for an antiskyrmion collapse into the ferromagnetic (FM) state for Rh_{hcp}/Co/Ir(111). (a) Total energy (grey filled points) and interaction resolved energy contributions along the MEP of the antiskyrmion (ASk) collapsing into the FM state at B_z) = 0 T. Magenta circles show the sum of exchange contributions. Light blue circles are the sum of the Dzyaloshinskii-Moriya interaction (DMI) contribution and grey circles denote the magnetocrystalline anisotropy energy (MAE) contribution. All lines serve as guide to the eye and the colour of the shaded background area corresponds to the shaded area in Fig. 8.9 (d) for all magnetic fields. (b) Three zoomed images before and after the SP for the antiskyrmion collapse mechanism as marked in (a). All complete MEPs images are presented in App. B. Colours denote the out-of-plane magnetization direction (red upwards, blue downwards).

The impact of exchange frustration is similar to the radial symmetric collapse mechanism for skyrmions, where due to the reduced size of the antiskyrmion around the SP in Fig. 8.11 (b), the FM exchange constants such as J_1 reduces the energy barrier whereas AFM constants such as J_3 are contributing to a larger barrier (see

[6]Note that in the absence of DMI, the energy barrier of skyrmions and antiskyrmions are the same.

smaller panel on the right side). Similar to the skyrmion case, the MAE constantly gains energy on the MEP to the FM ground state.

The experimental observations of occurring skyrmions in a FM virgin state (Ref. 130 and Pub. II) can be explained, based on our DFT calculations and atomistic spindynamics simulations presented here. It is driven by the interplay of large exchange frustration, moderate DMI and large MAE. Due to the flat energy dispersion around the $\overline{\Gamma}$ point, the energy cost of skyrmions is very small. The large energies for the AFM states enhance the energy barrier preventing skyrmions to collapse into the collinear FM state.

8.8 Non-collinear tunnelling magnetoresistance in Rh_{hcp}/Co/Ir(111)

In the previous part, we explained the interplay of magnetic interactions of Rh/Co/Ir(111) and the experimental observation of nano-scale skyrmions in Rh_{hcp}/Co/Ir(111). Interestingly, the measurements revealed that it is not necessary to use a magnetic tip in STM experiments in order to resolve the small magnetic structures. Two possible effects, the TAMR [155] as well as the NCMR [147] can be responsible for detecting small non-collinear magnetic structures within an electrical measurement procedure. STM simulations have shown both TAMR and NCMR contributions need to be included to resolve the experimental observations (Pubs. II and III).

In order to understand the origin of the NCMR allowing an electrical read-out of non-collinear structures, we compare experimental $\mathrm{d}I/\mathrm{d}U$ spectra with DFT calculated vacuum LDOS which are directly proportional within the Tersoff-Hamann model of STM [156]. In Fig. 8.12 (a), a sample area with three FM domains (dark contrast and brighter contrast in the middle) separated by two DWs (brightest contrast) is shown, where spin-averaged $\mathrm{d}I/\mathrm{d}U$ spectra are taken at the marked areas (green points for the DWs and grey points for oppositely magnetized FM domains).

Comparing the two spectra [green line for the DW and grey line for the FM domains in Fig. 8.12 (b)], two significant differences occur. The peak at the Fermi energy in the FM curve is shifted to higher energies and has lower intensity for the DW. The opposite is observed for the second peak around −0.3 V for the FM state which is shifted to lower energies. These deviations lead to a very large MR at the Fermi level, which is defined as

$$MR = \frac{\mathrm{d}I/\mathrm{d}U_{\mathrm{FM}} - \mathrm{d}I/\mathrm{d}U_{\mathrm{DW}}}{\mathrm{d}I/\mathrm{d}U_{\mathrm{FM}}} \tag{8.4}$$

It is about 20 % and within a broad energy range [Fig. 8.12 (c)]. This allows for a detection of DWs and skyrmions using transport measurements with planar tunnel junctions which is often anticipated for spintronic applications [34].

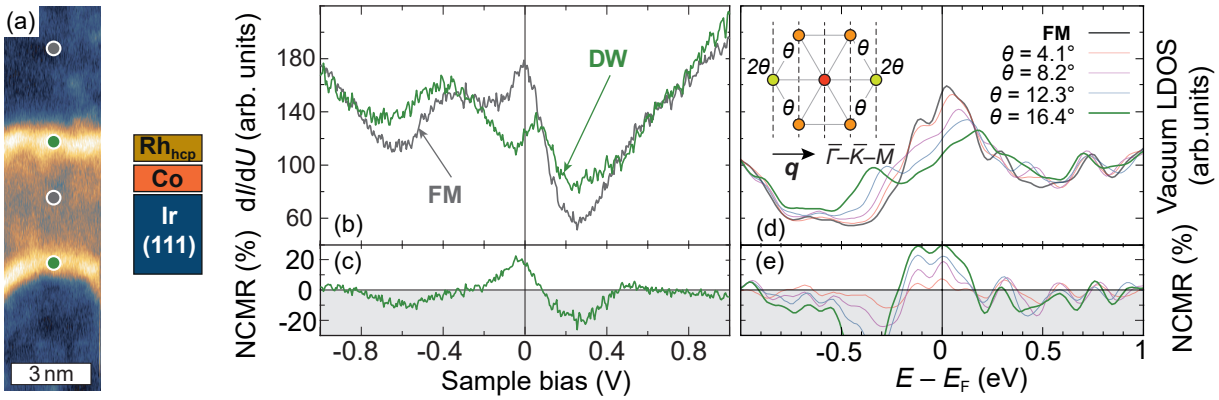

Figure 8.12 | Comparison of non-collinear magnetoresistance (NCMR) from experiments with calculations in Rh_{hcp}/Co/Ir(111). (a) Spin-resolved dI/dU map of Rh_{hcp}/Co/Ir(111) with three ferromagnetic (FM) domains separated by two domain walls (DWs). The measurements are performed at −250 mV. (b) Spin-averaged dI/dU spectra for the FM region (grey line) as taken from the grey points in (a). The DW (green line) was measured at the green points in (a). (c) NCMR in % calculated from Eq. (8.1) where both dI/dU spectra of are taken into account. (d) DFT calculated vacuum local density of states (LDOS) 3 Å above the surface for different spin spiral states where **q** is chosen along the $\overline{\Gamma}$-$\overline{K}$-$\overline{M}$ direction of the hexagonal two-dimensional Brillouin zone. The grey line corresponds to the FM state and the angle θ between nearest neighbours is increased for the coloured curves. The inset shows the sketch of the hexagonal atomic lattice with the spin spiral propagation direction and the respective angles for each neighbouring spins. (e) Calculated NCMR from Eq. (8.1) using the vacuum LDOS of (d). Note that the theoretical zero lines are aligned with experimental ones. The figure has been adapted from Pub. III.

Taking the Tersoff-Hamann model into account [156], we have calculated the vacuum LDOS 3 Å above the surface comparing different states [Fig. 8.12 (d)]. In the FM state, the vacuum LDOS is in good agreement with the dI/dU spectrum of this state (grey curve). The most significant peak arises at E_F and also a second peak is present for lower energies. For computational reasons, we locally approximate the experimentally measured DW with homogeneous spin spiral states. The LDOS is shown for different canting angles θ between adjacent spins [Fig. 8.12 (d)] where spin spiral states along the $\overline{\Gamma}$-$\overline{K}$-$\overline{M}$ direction are shown. Therefore, in the inset, the propagation as well as the occurring angles of the neighbouring spins in the hexagonal lattice is shown.

We successively increase the angle θ observing a trend in the change of vacuum LDOS. The main peak at E_F shifts to larger energies and the intensity reduces, while the smaller peak is shifted to lower energies, where its significance gets enhanced for larger angles. Taking the experimental DW width of ~ 0.8 nm into account as well as the Ir(111) lattice constant, $\theta = 16.4°$ is the most reasonable comparing our spin spiral calculation with the DW. Here, we also observe a good agreement for the vacuum LDOS (green curve) and the dI/dU signal.

Taking Eq. (8.1) into account, we calculate the NCMR contribution for Rh_{hcp}/Co/Ir(111) of the LDOS for the presented spin spiral states [Fig. 8.12 (e)]. With

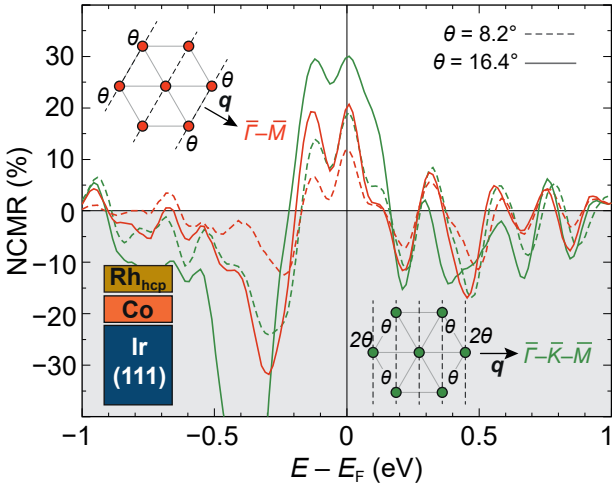

Figure 8.13 | Calculated non-collinear magnetoresistance (NCMR) for Rh_{hcp}/Co/Ir(111) applying spin spirals in different directions of the two-dimensional (2D) Brillouin zone (BZ). In green, the NCMR is shown for spin spirals along the $\overline{\Gamma}$-$\overline{K}$-$\overline{M}$ direction of the 2D BZ corresponding to Fig. 8.12 (e) and in red, the same calculations are shown for spin spirals propagating along the $\overline{\Gamma}$-$\overline{M}$ direction. Solid lines show spin spiral states for an angle of $\theta = 16.4°$ between nearest neighbours and dashed lines with $\theta = 8.2°$. The insets show the respective sketch of the hexagonal atomic lattice with the spin spiral propagation direction and the respective angles for each neighbouring spins. The figure has been adapted from the supplemental material of Pub. III.

increasing angle, the NCMR increases simultaneously where around E_F, it reaches about 25 %. This is in very good agreement with the experimentally observed one [Fig. 8.12 (c)], despite of the approximation of the measured DW with a homogeneous spin spiral. Furthermore, we can reproduce the qualitative behaviour of the NCMR, which shows negative values for both higher and lower energies. We would like to emphasize the good quality of agreement compared to the ones found in the literature [147].

It can be further confirmed by also taking spin spiral states into account which propagate into the other high symmetry direction of the hexagonal 2D BZ[7]. In Fig. 8.13 we compare the NCMR for two angles θ for both $\overline{\Gamma}$-$\overline{K}$-$\overline{M}$ (green lines) and $\overline{\Gamma}$-$\overline{M}$ (red lines) directions. The insets show the differences of the spin spiral propagation, where in $\overline{\Gamma}$-$\overline{K}$-$\overline{M}$ direction, two spins occur with a canting of 2θ, this is not the case for the $\overline{\Gamma}$-$\overline{M}$ direction, where in addition, the wave front has different distance.

This is the reason why the NCMR is scaled differently in both high symmetry directions. We especially see a factor of two arising in the NCMR - both 16.4° of the $\overline{\Gamma}$-$\overline{M}$ spin spiral and 8.2° spiral of the $\overline{\Gamma}$-$\overline{K}$-$\overline{M}$ direction show the same NCMR. The factor is the same as the mean angle between one atom and its six nearest neighbours, which is $2/3\theta$ in $\overline{\Gamma}$-$\overline{M}$ and $4/3\theta$ in $\overline{\Gamma}$-$\overline{K}$-$\overline{M}$ direction [147, 148]. We therefore conclude that the quantitative deviation between experiment and theory is even smaller when

[7] Note that the propagation direction of DWs in the experiment is not fixed to one crystallographic direction.

considering the effect of different propagation directions.

In our calculations presented above, SOC is neglected. However, the TAMR based on SOC can also have a large impact on detecting non-collinear structures. We therefore apply the quantization axis in both in-plane and out-of-plane direction for the FM state and calculate the TAMR in the same way as in Eq. (8.1). The result is shown in Fig. 8.14 as black line and compared to the NCMR presented above. The TAMR shows a strongly varying behaviour and is always lower than 10 % and thus has a negligible contribution to the signal which is obtained for the detection of the spin structures in the experiment.

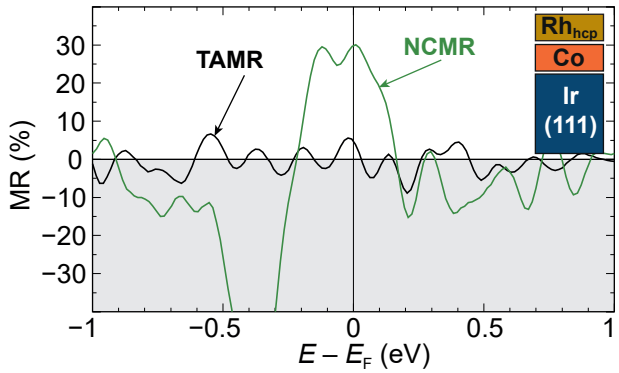

Figure 8.14 | Calculated tunnelling anisotropic magnetoresistance (TAMR) and non-collinear magnetoresistance (NCMR) for Rh$_{hcp}$/Co/Ir(111). The TAMR (black line) is obtained from local density of states (LDOS) of the ferromagnetic (FM) state with applying the spin quantization axis out-of-plane and in-plane, respectively. The NCMR is obtained from LDOS comparing FM state with a spin spiral state along $\overline{\Gamma}$-$\overline{K}$ and an angle $\theta = 16.4°$ as shown in Fig. 8.12 (d,e). The figure has been adapted from the supplemental material of Pub. III.

In order to understand the origin of the strong electronic contrast, we analyse the LDOS of both the Rh and Co atom. The complete orbital resolved LDOS for these atoms can be found in App. C. Rh exhibits a large magnetic moment of about $0.6\,\mu_B$ stemming from hybridization with the adjacent Co layer (Sec. 8.3). Due to the strong delocalization of p orbitals, we find that the vacuum LDOS in the FM state around the Fermi energy to be governed by the contribution of the minority p_z states of the Rh surface [Figs. 8.12 (d) and 8.15 (a)]. The majority d_{xz} states only have a minor contribution in the vacuum since they are strongly localized.

When tilting the spins in the Rh/Co BL, we see the exact same behaviour in the minority p_z states as in the vacuum LDOS. The large peak at E_F is shifted to higher energies and reduced in height [lower panel in Fig. 8.15 (a)]. Another peak below the Fermi level arises when the angle between spins increases (green line for a spin spiral with $\theta = 16.4°$). Due to the canting of the spins, spin mixing can occur which is absent in collinear configurations. We find the majority d_{xz} state located at $-0.25\,\text{eV}$ compared to E_F [grey line in the upper panel of Fig. 8.15 (a)]. This peak shifts to lower energies and reduces in height with increasing the angle between adjacent spins. These effects can also be observed for the Co layer (Fig. C.1); however, they appear more clearly in the Rh.

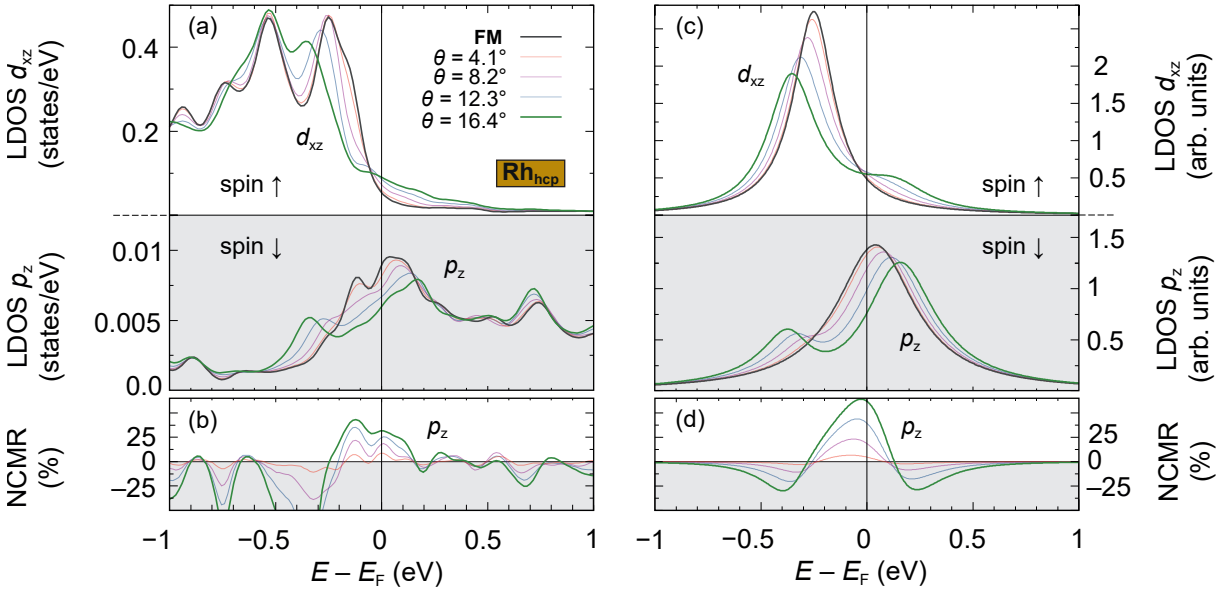

Figure 8.15 | Comparison between DFT calculated local density of states (LDOS) of majority d_{xy} and minority p_z spin states for the Rh surface and a simplified tight binding model for Rh_{hcp}/Co/Ir(111). (a) DFT calculated LDOS of the majority d_{xy} orbital (upper panel) of the Rh surface for different spin spiral states where **q** is chosen along the $\overline{\Gamma}$-$\overline{K}$-$\overline{M}$ direction of the hexagonal two-dimensional Brillouin zone. The grey line corresponds to the FM state and the angle θ between nearest neighbours is increased for the coloured curves corresponding to Fig. 8.12 (d,e). The lower panel shows the LDOS for the p_z orbital for the respective states. Note the two different y-axes due to delocalization of p orbitals. (b) Calculated NCMR from the p_z LDOS in (a) of the Rh surface. (c) LDOS as in (a) obtained from a simplified two-state tight binding model. (d) Calculated NCMR from the p_z LDOS in (b) for the tight binding model. The figure has been adapted from Pub. III.

In Fig. 8.15 (b), we have calculated the NCMR for only the minority p_z LDOS. Around E_F, we see that it agrees well with both experimentally observed and calculated NCMR from vacuum LDOS. Therefore, we can conclude that the electrical detection of skyrmions and DWs in Rh/Co/Ir(111) is mediated by the minority p_z states.

To see the effect of spin mixing in a more detailed way, we apply a simplified tight-binding model which can be solved analytically with a Green function $G(E)$:

$$\left[E \cdot \mathbb{1}_2 - \begin{pmatrix} \epsilon^{\uparrow} & -t(\theta) \\ -t(\theta) & \epsilon^{\downarrow} \end{pmatrix} - \begin{pmatrix} -i\gamma^{\uparrow} & 0 \\ 0 & -i\gamma^{\downarrow} \end{pmatrix}\right] G(E) = \mathbb{1}_2 \tag{8.5}$$

where

$$t(\theta) = -t_0 \sin \theta/2 \tag{8.5a}$$

is the hopping parameter for the two states depending on the angle between the two spin quantization axes. The two diagonal elements of the matrix

$$\Sigma = \begin{pmatrix} -i\gamma^{\uparrow} & 0 \\ 0 & -i\gamma^{\downarrow} \end{pmatrix} \tag{8.5b}$$

occur due to hybridization and account for the peak broadening.

Solving Eq. (8.5) gives rise to the LDOS in the two spin channels, defined by the diagonal elements of the Green's function:

$$n_\sigma(E) = -(1/\pi)\,\mathfrak{Im}\left[G_{\sigma\sigma}(E)\right] \tag{8.6}$$

We determine the energies and widths of the peaks by fitting Lorentzian curves to the DFT data of Fig. 8.15 (a) in the FM state. For the majority d_{xz} state, we obtain $\epsilon^{\uparrow} = E_F - 0.25\,\mathrm{eV}$, $\gamma^{\uparrow} \approx 0.12\,\mathrm{eV}$ and for the minority p_z state $\epsilon^{\downarrow} = E_F + 0.04\,\mathrm{eV}$, $\gamma^{\uparrow} \approx 0.22\,\mathrm{eV}$. The hopping matrix element [Eq. (8.5a)] $t_0 = 1.5\,\mathrm{eV}$ and is chosen so that for $\theta = 16.4°$, the peak position of the model agrees with the one of the DFT calculation.

The obtained LDOS for both majority and minority states can be seen in Fig. 8.15 (c), where the main features of the DFT calculations are reproduced. For the grey lines, no spin mixing is observed and the curves behave as undisturbed Lorentzians. We also observe the same peak shifts as in (a). The peak of the d_{xz} state shifts to lower energy and decreases in height, whereas a small peak structure occurs at $E_F + 0.1\,\mathrm{eV}$. The latter only can arise from the spin mixing with the minority p_z state. The main peak of the p_z state shifts to higher energies and also reduces in height. Due to the mixing with the d_{xz} state now the second peak at $E_F - 0.4\,\mathrm{eV}$ arises, which is in excellent agreement with DFT calculations. Note that the simplified model cannot capture all effects of hybridization, but the similarities show that it can indeed capture the essential physics of this spin mixing.

Furthermore, we can calculate the NCMR from the tight binding model of the p_z LDOS [Fig. 8.15 (d)]. The qualitative behaviour not only matches the DFT calculations, but also the experimental observations. We therefore can conclude that the spin mixing of majority d_{xz} state and minority p_z state are evidently responsible for the large NCMR at the Fermi level, allowing for all-electrical readout of non-collinear magnetic structures in Rh/Co/Ir(111).

8.9 Conclusion

In this chapter we studied the ultrathin film Rh/Co/Ir(111). Since the three elements are isoelectronic, strong hybridization between them was found leading to a exceptionally large degree of frustration effects in Co. Despite a FM ground state, a canting between adjacent spins of up to 20° almost costs no energy.

The combination of exchange frustration, moderate DMI and large out-of-plane MAE allow for a stabilization of zero field, sub 5 nm skyrmions as well as atomic-scale DWs. Experiments at the university of Hamburg could confirm the magnetic properties of Rh/Co/Ir(111) where for the first time, ultra-small skyrmions have been stabilized in the virgin state without applying a magnetic field at a temperature of 4 K.

However, due to large energy barrier obtained from GNEB calculations, we suggest the skyrmions to be stable at higher temperatures. We believe that our findings can be

transferred to more applicable multilayer systems composed of a repeated Rh/Co/Ir sandwich structure. Such a transfer has already been shown for Pd/Fe/Ir(111) [157]. DFT calculations already show promising results [158].

Furthermore, we were able to explain the observation of skyrmions and DWs with a non-magnetic electrode due to a large NCMR of about 20 % at the Fermi energy. The effect is governed by the minority p_z states of the Rh surface and is mediated by spin mixing with the majority d_{xz} orbital. Before our observation, such an effect was only seen in Fe-based material [147].

8.10 Test calculations

In the discussion above, we emphasized the complex magnetism in the presented film system. We want to show here that our interpretation of the film is robust and have performed various test calculations which are presented in the following.

8.10.1 Convergence of spin spiral states and the atomistic spin model beyond nearest neighbours

The description of Rh/Co/Ir(111) is dependent on very small energy differences below 1 meV and that small distortions can affect the magnetic ground state. Therefore it is important to check the convergence of the calculations, especially around the FM state.

In Fig. 8.16 (a) we show the calculations where we converged the energies of the spin spiral states using different computational setups. The standard accuracy with which we calculate most of the energy dispersions serves as benchmark because for energies around 1 meV, the states can be seen as converged. The setup is therefore as described in Sec. 8.1 consists of an energy cutoff $k_{\max} = 4.0\,\text{a.u.}^{-1}$ and 1936 k points in the full 2D BZ [black circles and lines in Fig. 8.16 (a,b)].

We increase both, $k_{\max}$ and the number of k points (red circles and lines) where in $\overline{\Gamma}$-$\overline{M}$ direction, the spin spiral states calculated with the standard setup reveal the same energies and the deviation is below 0.3 meV/Co atom. In $\overline{\Gamma}$-$\overline{K}$ direction, we observe an interesting feature which can only be solved by including either a different set of k points or a different spin spiral state. First, the spin spiral state for $|\mathbf{q}| \sim 0.1\,{}^{2\pi}/_{a}$ is fully converged where black and red circles lie above each other. But a deviation remains for other states, e.g. at $|\mathbf{q}| \sim 0.05\,{}^{2\pi}/_{a}$. Here, the deviation is about 2 meV/Co atom and would change the interpretation of the magnetic ground state.

Since both $\mathbf{q}$ and k are reciprocal lattice vectors, the description of a spin spiral state is most accurate when the Kohn-Sham equations are solved exactly at this point, i.e. when $k = \mathbf{q}$. In $\overline{\Gamma}$-$\overline{M}$ direction, the coordinates of $\mathbf{q}$ seem to match k, but for certain $\mathbf{q}$ points in $\overline{\Gamma}$-$\overline{K}$ direction, this is not the case and a calculational error is seen. Even when we consider a large basis set as chosen for the red curve.

By further increasing the number of k points to 100×100 (green circles and lines), we see convergence of the spin spiral states for $\mathbf{q} \to 0$. Note that for less frustrated systems, the energy differences are on a different scale and do not necessarily require such a large degree of accuracy which is computationally demanding.

In Fig. 8.16 (b), we see the same effect as described before on the SOC contribution. In $\overline{\Gamma}$-$\overline{M}$ direction, the energies appear as converged, but in $\overline{\Gamma}$-$\overline{K}$ direction we see fluctuations in energy even in the red curve. The DMI therefore is strongly dependent on the chosen k point set and converges for 10000 k points.

When including the accurately obtained points of (a) into $E(\mathbf{q})$, the dispersion behaves flatter than before. This has consequences for the mapping of the Heisenberg exchange interaction parameters J_{ij}. In Fig. 8.16 (c), two fitting curves are presented with two

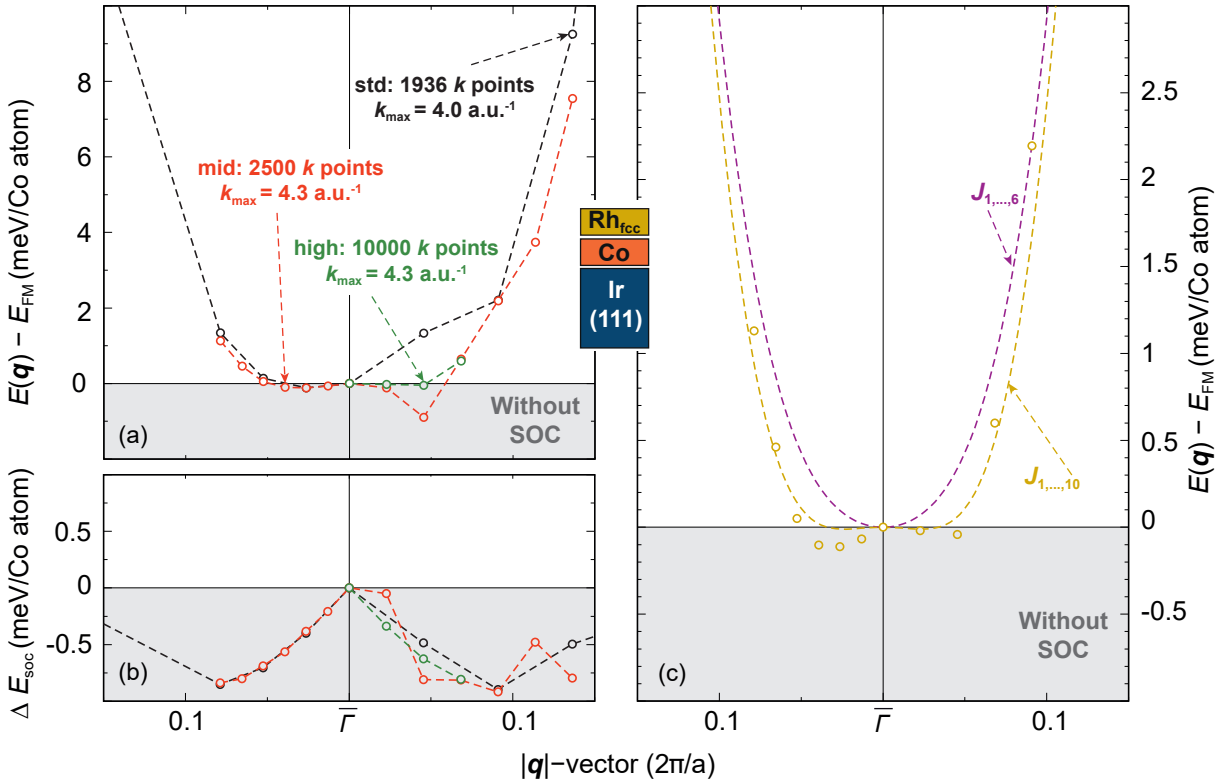

Figure 8.16 | Convergence of energy dispersion $E(\mathbf{q})$ for Rh_{fcc}/Co/Ir(111) at $\mathbf{q} \to 0$. (a) Energy dispersion without spin-orbit coupling (SOC). Black circles and lines show the DFT obtained energies applying the standard accuracy with an energy cutoff of $k_{max} = 4.0\,a.u.^{-1}$ and 1936 k points in the full two-dimensional (2D) Brillouin zone (BZ). In red, the mid-level accuracy is applied with $k_{max} = 4.3\,a.u.^{-1}$ and 2500 k points where the highest accuracy is achieved with $k_{max} = 4.3\,a.u.^{-1}$ and 10000 k points (green). Note that the standard setup can be seen as high convergence in typical calculations and that the energy differences here are very small. The lines serve as guide to the eye. (b) Energy contribution due to SOC for the points in (a). (c) Convergence for the fit of the Heisenberg exchange interaction J_{ij} applying six nearest neighbours (purple line) or ten neighbours (yellow line). The points represent the DFT calculations with the highest accuracy from (a). Note the extremely small energy difference in (c).

different amounts of nearest neighbours which are taken into account. We want to emphasize that the energy scale in (c) is extremely small.

Before including the highly accurate points, a fit with six nearest neighbours showed very reasonable agreement with the DFT results. However, with including J_6, the FM state is the lowest in energy, which does not hold true for the DFT calculations. We even see a small spin spiral energy minimum without SOC which is smaller than 0.2 meV/Co atom. This trend requires ten neighbours of exchange parameters and is the reason why in Tab. 8.2, J_{10} has a comparably large value when compared to J_9, J_8, J_7, J_6. We can conclude that the strong exchange frustration in the film is only captured when including ten neighbours for the exchange interaction.

8.10.2 Conical spin spiral states

When successively tilting the spins from the FM state into the AFM state in a Co layer, the electronic structure changes for the different states. The hybridization between to neighbouring spins is large in the FM state and vanishes in the AFM state. Due to these changes, the magnetic moment of the magnetic elements in all our spin spiral calculations can vary on significant scale. Since in the Heisenberg model, the magnetic moment is assumed to be constant, we have to take into account the effect and moreover consider an energy contribution of the Stoner energy due to the change of the magnetic moment.

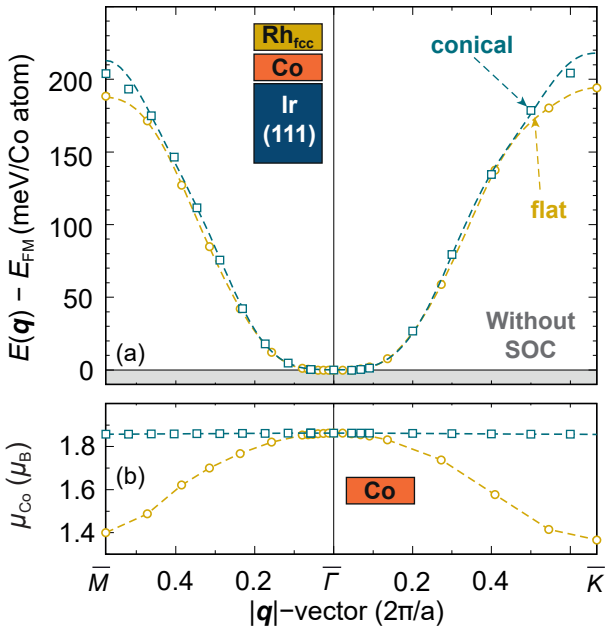

Figure 8.17 | Full energy dispersions $E(\mathbf{q})$ comparing flat cycloidal spin spirals for Rh_{fcc}/Co/Ir(111) with conical spin spiral states. (a) Energy dispersion without spin-orbit coupling (SOC) along the high symmetry path $\overline{\Gamma}$-$\overline{M}$ and $\overline{\Gamma}$-$\overline{K}$ of the two-dimensional Brillouin zone. Open circles (flat spin spirals) and squares (conical spin spirals) show calculated energies from DFT with respect to the ferromagnetic (FM) state, whereas lines represent the mapping to the atomistic spin model of the Heisenberg exchange beyond nearest neighbours. The opening angle of conical spirals is $\theta = \pi/20$ while for flat ones it is $\theta = \pi/2$. Note that the energy dispersions has been rescaled by $\frac{1}{\sin(\pi/\theta)^2}$. (b) Magnetic moment ($\mu_B$) of the Co layer for the two types of calculations in (a). For flat spin spirals, the moment changes with $\mathbf{q}$ whereas for conical spirals it remains constant. The same holds true for the Rh top layer.

Considering Rh adjacent to the magnetic layer, the induced magnetic moment can be strong as shown in Fig. 8.4. Such a moment is not captured as well in the Heisenberg model. We therefore apply a more effective Heisenberg model where in our calculations these effects occur. Considering the AFM states in the magnetic layer, an adjacent non-magnetic layer such as Rh which sits in between two or three magnetic atoms will not be spin polarized due to symmetry effects of neighbouring positive and negative magnetic moments. This is why in the Rh layer, we also observe a large change of magnetic moment with increasing $\mathbf{q}$ vector in Fig. 8.4. Consequently, such a change would also contribute to the Stoner energy.

We can interpret, check and analyse our data in more detail when seeing the energy contributions of the effects. Therefore, we calculate the energy dispersion of conical

spin spiral states where we apply the same **q** vectors. In the case of flat spin spiral states, we scan a phase space from FM to AFM states, but conical spin spirals are close to the FM state, regardless of **q**. This is why in conical spin spiral states, the LDOS does not change that drastically with **q** and therefore, the magnetic moment is constant. After rescaling the energies of spin spirals by $\frac{1}{\sin(\pi/\theta)^2}$, where θ is the opening angle of the spiral, we can compare the energy dispersions of the two types of spin spiral calculations. Note that before the rescaling, the energy differences of the conical spin spiral states are very small and consequently very small errors in the energy will be rescaled as well. To obtain a reasonable comparison between flat and conical states, the computational accuracy for the latter has to be drastically increased.

In Fig. 8.17, we compare the two kinds of calculations for $\mathrm{Rh_{fcc}}$/Co/Ir(111) where we applied an energy cutoff of $k_{\max} = 4.0\,\mathrm{a.u.}^{-1}$ and 10000 k points in the full 2D BZ for the self-consistently calculated conical spin spirals. Since the energy differences around the $\overline{\Gamma}$ point are very small, such a test calculation is very important to interpret the DFT results.

In (a), the energies of both conical and flat spin spirals are almost perfectly aligned where we observe perfect agreement around the magnetic ground state. As expected in (b), due to the conical spin spiral states, the magnetic moment remains constant for both the Rh (not shown) and the Co layer. We therefore conclude that our interpretation of the DFT data is valid and the results appear as robust. This is supported by the obtained magnetic interaction parameters in Tab. 8.4.

Table 8.4 | Obtained values for magnetic interactions in Rh/Co/Ir(111) mapping the atomistic spin model to the results of the DFT test calculations. All values of the i-th neighbour exchange J_i, Dzyaloshinskii-Moriya interaction (DMI) constants D_i and uniaxial magnetocrystalline anisotropy energy K are given in meV. $J > 0$ ($J < 0$) represents ferromagnetic (antiferromagnetic) order, $D > 0$ ($D < 0$) clockwise (counterclockwise) rotation and $K > 0$ ($K < 0$) denotes an in-plane (out-of-plane) easy axis. For $\mathrm{Rh_{fcc}^{con}}$, the obtained results from conical spin spirals calculated for $\mathrm{Rh_{fcc}}$/Co/Ir(111) are shown and for $\mathrm{Rh_{hcp}^{mix\text{-}rel}}$, the values are obtained from the results of the spin spiral calculation of $\mathrm{Rh_{hcp}}$/Co/Ir(111) with a different relaxation (Sec 8.10.3) .

	$\mathrm{Rh_{fcc}^{con}}$	$\mathrm{Rh_{hcp}^{mix\text{-}rel}}$
J_1	+28.7800	+26.5946
J_2	−0.9711	+1.2953
J_3	−4.1568	−2.9503
J_4	+0.4507	−0.5047
J_5	+0.4110	−1.5183
J_6	+0.0262	−1.2350
J_7	−1.5241	+1.3674
J_8	+0.8008	−1.2147
J_9	+0.4739	−0.1361
J_{10}	−0.2034	+0.0989
D_1	–	+0.2605
D_2	–	+0.3662
D_3	–	+0.4932
D_4	–	−0.0733
D_5	–	−0.2615
D_6	–	−0.1480
D_7	–	+0.2554
K	–	−1.6600

8.10.3 Influence of *xc* potential on DFT results

Due to the small energies which define the magnetic ground state in Rh/Co/Ir(111), small deviations can affect the formation of the occurring magnetic structures. We therefore consider a different *xc* potential in order to structurally relax the film of Rh_{hcp}/Co/Ir(111) and recalculate the energy dispersion[8].

While the structural relaxation in the main part was performed using the GGA *xc* potential, we apply a mixture of GGA+LDA potential dependent on the described element. For Co, GGA was used and for Rh and Ir the LDA *xc* potential. We obtain slightly different values for the structural relaxation, which can be compared to Tab. 8.1. For the mixed potential, the relaxed interlayer distances are $d_{12} = 3.80\,\text{a.u.}$, $d_{23} = 3.94\,\text{a.u.}$, $d_{34} = 4.35\,\text{a.u.}$

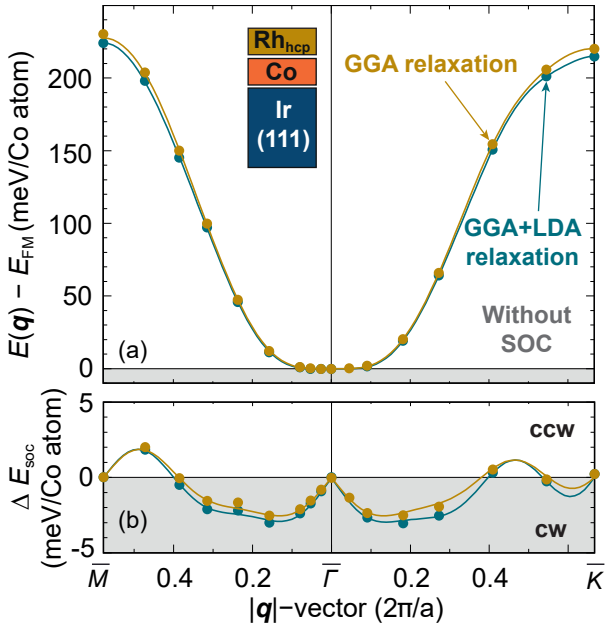

Figure 8.18 | Full energy dispersions $E(\mathbf{q})$ of flat cycloidal spin spirals for Rh_{hcp}/Co/Ir(111) applying two different structural relaxations. (a) Energy dispersion without spin-orbit coupling (SOC) along the high symmetry path $\bar{\Gamma}$-$\bar{M}$ and $\bar{\Gamma}$-$\bar{K}$ of the two-dimensional Brillouin zone. Points show calculated energies from DFT with respect to the ferromagnetic (FM) state, whereas lines represent the mapping to the atomistic spin model of the Heisenberg exchange beyond nearest neighbours. (b) Energy contribution due to SOC where the lines are the fit to the Dzyaloshinskii-Moriya interaction beyond nearest neighbours.

We perform spin spiral calculations the same way as described in Sec. 8.1 where the result can be seen in Fig. 8.18. The energy dispersion without SOC for both relaxations can be seen as equivalent, concerning the fact that the deviations are negligible. Different interlayer distances therefore will not affect the key result of the frustrated exchange interaction. In Fig. 8.18 (b), ΔE_{SOC} seems to be slightly affected where due to the closer distances between the layers with the mixed potential, the DMI is slightly increasing. On the other hand, we expect the DMI to be reduced when increasing those distances. We also calculated the MAE, which remains unaffected by a different structural relaxation. We obtain $K = -1.66\,\text{meV/Co atom}$ which is only $0.03\,\text{meV/Co atom}$ enhanced compared to the previous relaxation. All obtained magnetic interactions are presented in Tab. 8.4.

[8] Note that the different *xc* potential is only used to obtain a different structural relaxation. Further calculations were performed the same way as presented above within the LDA *xc* potential.

From this test calculation, we see that exchange and MAE will not be affected by different structural properties. The DMI on the contrary is strongly dependent on the interlayer distances between the layers and we can reduce the DMI by increasing the distance or the other way around. Due to this observation, we only reduce the DMI in Sec. 8.7 to reveal the FM ground state which was proposed by the experiment.

8.10.4 Determining magnetic interactions from domain wall properties

When experimental observations without DFT are analysed, the occurring magnetic structures as itself are taken into account to get an idea of the ratio between exchange, MAE and DMI on a micromagnetic level [159]. We want to transfer this method examining DWs which have been obtained from spindynamics simulations applying the fully atomistic spin model. The results are compared to the values which are obtained from DFT applying both effective nearest neighbour approximation and atomistic spin model. Therefore, an assertion is possible whether such an approach from theory or experiment gives rise to a good understanding of the magnetism in the system. From the DW energy

$$\Delta E_{\text{DW-FM}} = \frac{4}{a}\sqrt{2|J_{\text{eff}}K|} - \frac{2}{a}\pi\sqrt{3}|D_{\text{eff}}| \tag{8.7a}$$

and width

$$w = 2a\sqrt{\frac{3J_{\text{eff}}}{2|K|}} \tag{8.7b}$$

we extract J_{eff} and D_{eff} by assuming the given MAE from DFT calculations. Starting from DW width, we determine the effective nearest neighbour exchange constant J_{DW} and taking the DW energy into account, we calculate the effective DMI D_{DW}[9].

Table 8.5 | Calculated values for nearest neighbour exchange and Dzyaloshinskii-Moriya interaction (DMI) from domain wall (DW) properties for Rh/Co/Ir(111). We use the DW width w in nm, K from Tab. 8.2 and Eq. (8.7b) to determine the exchange J_{DW} in meV. The DW energy $\Delta E_{\text{DW-FM}}$ [Eq. (8.7a)] is applied to further obtain the DMI D_{DW} in meV. The DWs were calculated with spindynamics applying the fully atomistic spin model.

Film on Co/Ir(111)	w	$\Delta E_{\text{DW-FM}}$	J_{DW}	D_{DW}
Rh_{fcc}	1.42	+2.01	+5.376	+1.252
Rh_{hcp}	1.27	+4.42	+6.030	+1.522

We compare exchange and DMI obtained from the DW properties with the effective nearest neighbour exchange and DMI obtained by DFT calculations in Tab. 8.2. The deviations are more or less drastic which is mostly dependent on the fitting region of J_{eff} to the DFT points. While J_{eff} can vanish for $\mathbf{q} \to 0$ and can have the same magnitude as the DMI or even less, J_{DW} shows FM coupling which is larger than the DMI. Both

[9] Note that in Pub. II, J_{DW} is denoted in the Supplementary Material as J_{eff}.

descriptions fail to give the right physical understanding especially due to the large energy differences between FM and AFM states which are obtained via DFT.

Approaching the values from experimental point of view, we can only determine the exchange J_{exp} since only the DW width is given. In $\mathrm{Rh_{hcp}}$/Co/Ir(111), the DWs are smaller than the ones from spindynamics simulations. A width of 0.8 nm will lead to an exchange of $J_{\mathrm{exp}} = +1.3$ nm and gives a similar picture as J_{eff}.

Concerning the DMI, for $\mathrm{Rh_{hcp}}$/Co/Ir(111), D_{DW} agrees with D_{eff}, whereas for $\mathrm{Rh_{fcc}}$/Co/Ir(111), $D_{\mathrm{DW}} \sim 1.5 D_{\mathrm{eff}}$. From the DWs, we are able to extract the magnetic interactions in a more stable way compared to the fitting of DFT points, when we deal with highly exchange frustrated films[10]. Note that the DW profile applying the fully atomistic spin model and the effective parameters which are extracted by the DW will match. Even though the same holds true for magnetic skyrmions, the stability of skyrmions will be estimated clearly in a wrong way. For the film of Rh/Co/Ir(111) we would like to emphasize the unconditional requirement of the atomistic spin model describing the magnetism.

[10] For stronger FM films, both methods will come to more similar values.

Part III

Strongly frustrated antiferromagnetic Manganese

Chapter 9

Magnetic moment quenching through hybridization and frustration - Mn double layer on W(001)

Antiferromagnets (AFMs) have recently gained attention due to their promising intriguing properties to use them in spintronic devices and applications [160]. Compared to ferromagnetic (FM) structures, they possess beneficial properties such as faster spindynamics, insensitivity to magnetic fields as well as vanishing stray fields [5, 161, 162].

In particular, Mn is an AFM material that holds a wide spectrum of structural and magnetic properties, depending on the prevalent conditions [163]. α– and β–Mn e.g. show a cubic structure with complex unit cells being stable up to large temperatures [164], but for stabilizing face centred cubic (fcc) γ– and body centred cubic (bcc) δ–Mn, temperatures close to the melting point are required. A different route towards stable γ– and δ–Mn is epitaxial growth of Mn on suitable substrates [48, 165–170].

When grown on W substrates, complex magnetic structures can appear due to strong hybridization between Mn and W. A pseudomorphic Mn monolayer (ML) on W(110) e.g. forms a cycloidal AFM spin spiral, which is induced by the Dzyaloshinskii-Moriya interaction (DMI) [171]. The double layer (DL) Mn on W(110) also prefers AFM order between nearest neighbours, but the competition of DMI and higher order exchange interactions forces this system into a conical spin spiral ground state [46]. On the W(001) surface, the Mn ML exhibits FM nearest-neighbour exchange interaction; however, the DMI stabilizes a spin spiral ground state [43].

In this chapter, we revisit the magnetism of a Mn DL on W(001). Previous density functional theory (DFT) calculations have revealed a FM ground state for this system [172], but experiments unwind the magnetic ground state to be a $c(2\times2)$ AFM. Our DFT calculations can confirm the measurements and indicate that the Mn interface layer behaves as dead magnetic layer (DML). The concept of DMLs was suggested in the past [173–175] (see Ref. 176 for a review), but the magnetic moments have been either in local AFM order [177] or reduced due to oxidation at the interface or surface [178]. We recently published our findings in Pub. IV.

This chapter is structured as follows: In the first part (Sec. 9.1), we shed light into the previous DFT calculations from Ref. 172, in which a systematic study is made for Mn MLs on W substrates. In the second part (Sec. 9.2), the experimental results from the

University of Würzburg are presented. In Sec. 9.4 we describe the magnetic ground state properties of Mn/Mn/W(001) where the last two Secs. 9.5 and 9.6 are dedicated to the verification of the dead Mn interface layer.

9.1 Previous study on Mn/Mn/W(001)

In 2005, Dennler and Hafner published a complete DFT study on up to three Mn MLs on W(100) and W(110) [172]. The most important results on the investigated Mn/Mn/W(100) are presented in Tab. 9.1. In their study, the FM order is lowest in energy; however, a stabilization of a $c(2\times2)$ AFM state in the system was not possible. The layered antiferromagnetic (LAFM) state is unfavourable by about 44 meV/Mn. For the FM state, the Mn interface layer [Mn(I)] has a large relaxation towards the substrate ($\Delta d_{23} = -18.5\,\%$) while in the LAFM state, it is the surface Mn(S) layer ($\Delta d_{12} = -16.6\,\%$). The magnetic moments of Mn(S) in both states are similar and reach a large value of $\sim 3.9\ \mu_B$ ($\sim 3.8\ \mu_B$) for the FM (LAFM) state. In Mn(I), the magnetic moment is twice as large in the LAFM state ($\sim 2.5\ \mu_B$) as in the FM state ($\sim 1.3\ \mu_B$).

	FM	LAFM
ΔE	0	+ 44
Δd_{12}	−6.6	−16.6
Δd_{23}	−18.5	−7.5
Δd_{34}	+2.1	−2.0
$\mu_{\mathrm{Mn(S)}}$	+3.87	−3.76
$\mu_{\mathrm{Mn(I)}}$	+1.31	+2.51
$\mu_{\mathrm{W(S)}}$	−0.22	−0.25

Table 9.1 | Previous results obtained from DFT calculations on Mn/Mn/W(001) taken from [172]. Energy difference ΔE (meV/Mn) between magnetic states, change of interlayer distances Δd (%) with respect to the interlayer distance $d_{100} = 1.59\,\text{Å}$ and magnetic moment (μ_B) of the topmost three layers in the system.

9.2 Experimental observation of a $c(2\times2)$ antiferromagnetic ground state

The experimental measurements were performed by Martin Schmitt at the University of Würzburg in the laboratory of Prof. Dr. Matthias Bode[1]. Fig. 9.1 shows the spin-polarized scanning tunnelling microscopy (SP-STM) measurements on the Mn DL on W(001), where the $p(1\times1)$ electronic structure is visible in the spin-averaged scanning tunnelling microscopy (STM) image [Fig. 9.1 (a)]. The measured periodicity of the (1×1) is $312\pm30\,\text{pm}$ and confirms pseudomorphic growth of bcc Mn on W(001). With magnetic contrast, the SP-STM image exhibits a $\sqrt{2}\times\sqrt{2}$ superstructure, rotated by 45° which is compatible with the $c(2\times2)$ AFM state [Fig. 9.1 (b)]. Here, the image looks like an unusual grid of linear elevations in which dark holes are embedded. Fig. 9.1

[1] Physikalisches Institut, Experimentelle Physik II, Universität Würzburg, Am Hubland, 97074 Würzburg, Germany

(c) presents the measured dI/dU spectrum over a large range of energy. Below the Fermi level and up to 0.3 eV, the spectrum is flat without any features in the spectrum whereas in the unoccupied states, two large peaks arise.

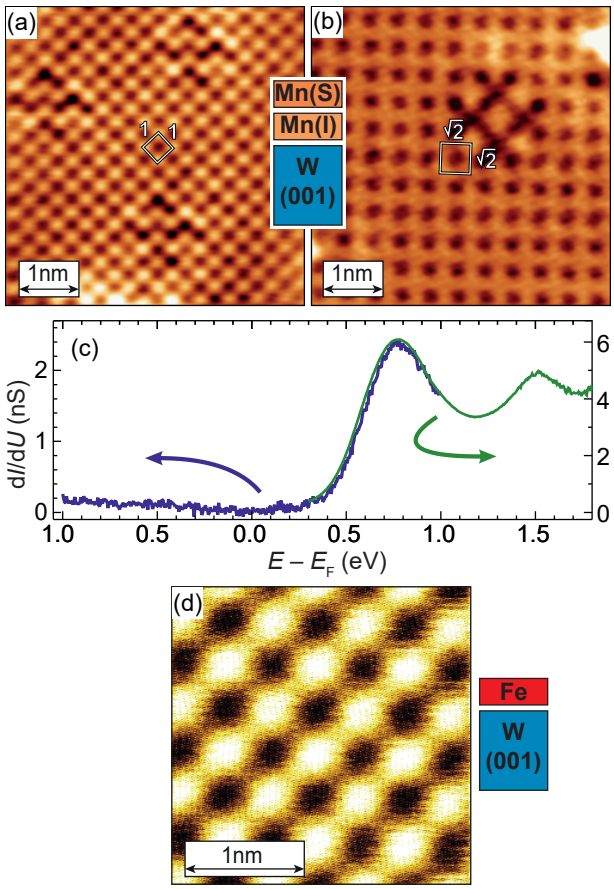

Figure 9.1 | Spin-polarized scanning tunnelling microscopy (SP-STM) measurements of Mn/Mn/W(001) compared to Fe/W(001) [179]. (a) Spin averaged data with chemical $p(1 \times 1)$ unit cell; Scan parameters: W tip, $U = 10\,\text{mV}$, $I = 5\,\text{nA}$. (b) Magnetic resolution with enlarged $c(2 \times 2)$ magnetic unit cell which indicates antiferromagnetic (AFM) order; Scan parameters: Fe/W tip, $U = 10\,\text{mV}$, $I = 3\,\text{nA}$. (c) dI/dU spectrum measurements on Mn/Mn/W(001); Stabilization parameters: $U = 1\,\text{V}$, $I = 1\,\text{nA}$ (blue line), $U = 0.3\,\text{V}$, $I = 0.5\,\text{nA}$ (green line). (d) SP-STM measurement on Fe/W(001) showing a $c(2 \times 2)$ AFM superstructure for comparison; $U = 500\,\text{mV}$, $I = 2\,\text{nA}$, $B = 2.5\,\text{T}$. Note that despite Mn/Mn/W(001) and Fe/W(001) show the same ground state, the SP-STM images (b) and (d) look different. The figures in (a,b,c) have been adapted from Pub. IV while the picture in (d) has been adapted from [179].

We can compare the SP-STM image of Mn/Mn/W(001) with that one of Fe/W(001) [Fig. 9.1 (d)], where a $c(2 \times 2)$ AFM ground state has also been observed [179]. Despite of the same magnetic ground state in the top layer, the images look different. For Fe/W(001), a distinctive checkerboard pattern with bright and dark squares can be observed, which is absent in Mn/Mn/W(001). Our calculations will show that this can be explained by a dead magnetic interface Mn layer.

9.3 Computational details

For this study, we used the FLEUR code [47] with film geometry. We choose the experimental lattice constant of bulk W $a_{\text{W-bulk}} = 5.981\,\text{a.u.}$ For the following calculations, the muffin tin (MT) radii were set to $R^{\text{MT}}_{\text{Mn}} = 2.25\,\text{a.u.}$, $R^{\text{MT}}_{\text{W}} = 2.50\,\text{a.u.}$ for Mn and W, respectively. We added W 5p semi-core states as local p orbitals to the basis set and the energy cut-off was set to $k_{\text{max}} = 4.0\,\text{a.u.}^{-1}$

Structural relaxation We assumed three collinear states for the structural relaxation: FM, LAFM and $c(2 \times 2)$ AFM state. For each we used a symmetric film with nine layers

of W(001) and the Mn DL on both sides of the film. The forces between the three uppermost layers were minimized in [001] direction until they reached the threshold of 10^{-5} htr/a.u.. Seven W layers in the middle of the film are kept fixed at the bulk equilibrium lattice (denoted as $d_{\text{W-bulk}}$). The resulting interlayer distances (denoted as $d_{12}, d_{23}, \ldots$) and magnetic moments are presented in Tab. 9.2. We applied 289 k points in 1/4 of the two-dimensional (2D) Brillouin zone (BZ) and the generalized gradient approximation (GGA) exchange correlation (xc) potential [73].

	FM	LAFM	$c(2\times 2)$ AFM
d_{12}	2.80	2.53	2.74
d_{23}	2.46	2.77	2.50
d_{34}	3.10	3.00	3.10

Table 9.2 | Relaxed interlayer distances d_{ij} (a.u.) for Mn/Mn/W(001). Three collinear states are chosen: ferromagnetic (FM) state, layered antiferromagnetic (LAFM) state and checkerboard $c(2\times 2)$ antiferromagnetic (AFM) state. The interlayer distance for W(001) bulk is $d_{\text{W-bulk}} = 2.99$ a.u.

Spin spiral calculations We support our calculations on collinear states by scanning the magnetic phase space for more magnetic states. Performing spin spiral calculations without spin-orbit coupling (SOC), we used an asymmetric film with eight layers of W(001) and the Mn DL on one side. The interlayer distances were set according of the structural relaxations, in the FM and $c(2\times 2)$ AFM state[1]. The vector $\mathbf{q}$ is chosen along the high symmetry directions $\overline{\Gamma}$-$\overline{M}$ and $\overline{\Gamma}$-$\overline{X}$ of the quadratic 2D BZ and the energy contributions due to SOC ΔE_{SOC} are calculated in first-order perturbation theory for every previously calculated $\mathbf{q}$ point [91, 128, 129]. We applied the local density approximation (LDA) xc potential [127] and 2304 k points in the full 2D BZ.

Magnetocrystalline anisotropy energy The magnetocrystalline anisotropy energy (MAE) is determined by self-consistently converging an asymmetric film with eight layers of W(001) with the Mn DL on one side in the FM and $c(2\times 2)$ AFM state in scalar-relativistic approximation. The calculational settings are the same as for the spin spiral calculations described above. The values of the MAE (K) are obtained by applying the force theorem [80, 81], where we applied the spin quantization axis with SOC perpendicular to the film plane $E_{\perp}$ and parallel to the film plane $E_{\parallel}$. The resulting energy difference, the MAE is defined as $K = E_{\perp} - E_{\parallel}$.

(Spin-polarized) Scanning tunnelling microscopy and (vacuum) local density of states calculations Comparing experimental with theoretical results, we performed SP-STM images and vacuum local density of states (LDOS) calculations. We used self-consistently converged calculations with the symmetric film from the structural relaxation described above. In order to obtain convincing results, we applied the GGA [73] as well the LDA [127] xc potentials. The SP-STM simulations are done at a distance of ~ 3 Å above the film surface for different energy ranges: ($E_{\text{F}} - 0.1$ V,

[1] Note that the energy dispersion in the LAFM state could not be converged for large $\mathbf{q}$.

$E_F - 0.05\,V$, $E_F - 0.01\,V$, $E_F + 0.01\,V$, $E_F + 0.05\,V$, $E_F + 0.1\,V$). For all energy ranges, the simulations look similar as well as for different distances above the surface (not shown in the thesis). All LDOS calculations were performed with a dense k-point mesh of 1225 points in 1/4 in the quadratic 2D BZ of the $c(2\times2)$ unit cell. In the vacuum, the distance of ~ 3 Å is chosen.

Calculations on stabilization of a magnetic moment in the Mn interface layer We can stabilize a magnetic moment in the Mn interface layer in the $c(2\times2)$ AFM state by increasing the distance of Mn(I) to the W(001) surface. We therefore use the relaxed interlayer distances in the $c(2\times2)$ AFM state and increase d_{23} by Δd. Since the distance between Mn(S) and Mn(I) is kept constant at the value of d_{12}, it is increased in the same way as the interface layer. We choose the increasing steps of Δd to 0.1 a.u.

9.4 $c(2\times2)$ antiferromagnetic ground state

The results of our DFT calculations are summarized in Tab. 9.3 and can be compared to the previously obtained results (cf. Tab. 9.1). The total energy differences, relaxed interlayer distances and magnetic moments in the FM and LAFM state are in good agreement with those published in Ref. 172. In the FM state, the Mn surface shows a moderate approach of about 6 % compared to the W(001) bulk interlayer distance. For the Mn interface layer, the relaxation towards the W substrate is larger by a factor of 3, which is a result of a very strong the Mn-W hybridization.

When Mn(S) and Mn(I) couple antiferromagnetically (i.e. the LAFM state), the relaxation of the surface (about 16 %) and interface layer (about 7 %) show the opposite behaviour compared to the FM state. Therefore, the magnetic moment in Mn(S) is higher in the FM state than in the LAFM state ($3.8\,\mu_B$ vs. $3.7\,\mu_B$). It is a consequence of the reduced coordination at the surface rather than the strong hybridization with the underlying element resulting in the different relaxations: A varying relaxation of 10 % changes $\mu_{Mn(S)}$ only by about 3 %.

Table 9.3 | DFT calculated results for Mn/Mn/W(001) in three collinear states after structural relaxation. Energy difference ΔE (meV/Mn) between magnetic states, change of interlayer distances Δd (%) with respect to the W-bulk distance $d_{\text{W-bulk}} = 2.99$ a.u. and magnetic moment (μ_B) of the topmost three layers in the system.

	FM	LAFM	$c(2\times2)$ AFM
ΔE	+45.6	+91.9	0
Δd_{12}	−6.4	−15.5	−8.6
Δd_{23}	−17.8	−7.4	−16.4
Δd_{34}	+3.7	+0.3	+3.7
$\mu_{Mn(S)}$	+3.81	−3.70	±3.70
$\mu_{Mn(I)}$	+1.18	+2.38	±0.00
$\mu_{W(S)}$	−0.19	−0.25	±0.03

For Mn(I), the hybridization with the non-magnetic W substrate has a large impact. In the FM state, the magnetic moment is reduced by a factor of three compared to the surface layer. This is rather surprising because the magnetic moment of a 3d

transition metal with half filled bands is expected to be larger. The Mn interface layer behaves similar to a non-magnetic transition metal (TM) material with large spin susceptibility. In contrast to the surface Mn layer, the relaxation affects the magnetic moments strongly. In the LAFM state, the Mn(I) layer has 10 % smaller relaxation towards W compared to the FM state and its magnetic moment is reduced slightly ($2.4\,\mu_B$). The magnetic moment is almost twice as large as for the FM state. From these results, we conclude that the Mn-W hybridization plays a crucial role for the magnetism of the Mn interface layer.

Our DFT calculations reveal the $c(2\times2)$ AFM state as lowest in energy by ~ 45 meV/Mn compared to the FM state (90 meV/Mn lower than the LAFM, Tab. 9.3). The interlayer distances between FM and AFM state are similar; however, the magnetic moment of the interface layer in the AFM state vanishes completely. According to the Mn(I) layer in the FM state, this is expected from a non-magnetic TM layer due to the checkerboard symmetry of the surface layer. In this case, the interface Mn layer is a DML.

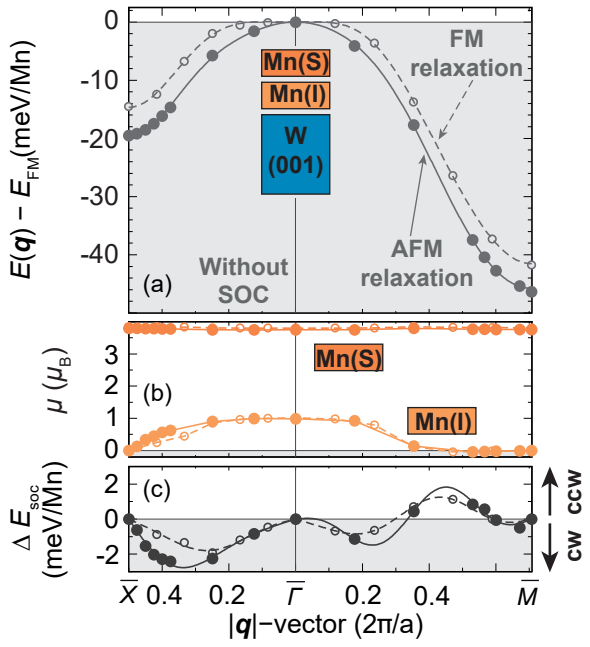

Figure 9.2 | Full energy dispersions $E(\mathbf{q})$ of flat cycloidal spin spirals for Mn/Mn/W(001) applying two different structural relaxations. (a) Energy dispersion without spin-orbit coupling (SOC) along the high symmetry path $\overline{\Gamma}$-$\overline{X}$ and $\overline{\Gamma}$-$\overline{M}$ of the two-dimensional Brillouin zone. Open circles (for structural relaxation in the ferromagnetic (FM) state) and filled points (for the structural relaxation in the $c(2\times2)$ antiferromagnetic (AFM) state) show the DFT calculated energies with respect to the FM state, whereas lines (dashed for FM relaxation and solid for AFM relaxation) represent the mapping to the atomistic spin model of the Heisenberg exchange beyond nearest neighbours. (b) Magnetic moment of the Mn surface and Mn interface layer. (c) Energy contribution due to SOC where the lines are the fit to the Dzyaloshinskii-Moriya interaction beyond nearest neighbours. The figure has been adapted from the supplemental material of Pub. IV.

We perform spin spiral calculations to scan a greater phase space of magnetic states than the collinear ones described above. The result can be seen in Fig. 9.2, where we gradually tilt the spins from the FM into the $c(2\times2)$ and $p(2\times1)$ AFM state applying

the FM and $c(2\times2)$ AFM relaxations of Tab. 9.2[2]. Without SOC the $c(2\times2)$ AFM state as lowest in energy for all three relaxations and the intra-layer FM order is most unfavourable [Fig. 9.2 (a)]. Despite of using a different *xc* potential, the energy differences and magnetic moments [Fig. 9.2 (b)] are in good agreement with the collinear ones (cf. Tab. 9.3). For all investigated spin spiral states, the magnetic moment of the Mn surface layer is constant at about 3.8 μ_B. The magnetic moment of the Mn interface layer at $\overline{\Gamma}$ is strongly dependent on the interlayer distance and is vanishing at the edge of the SOC for the FM and $c(2\times2)$ AFM relaxation ($\overline{M}$ and $\overline{X}$). In $\overline{\Gamma}$-$\overline{M}$ direction, $\mu_{\mathrm{Mn(I)}}$ is vanishing for angles $\varphi > 90°$ between adjacent spins. Both collinear and non-collinear calculations predict a $c(2\times2)$ AFM ground state of Mn/Mn/W(001) with a DML of the Mn(I) layer.

From the magnetic interactions, strong frustration of exchange and DMI is expected (Tab. 9.4). For all assumed relaxations, the AFM nearest-neighbour exchange interaction is smaller than |7| meV. Despite the small exchange interactions, the DMI only has a negligible contribution to affect the $c(2\times2)$ AFM ground state. In a Mn DL, the 3*d*-5*d* DMI forming interface is not at the surface and its magnitude is reduced [129]. Additionally, we find a strong out-of-plane MAE for both the FM and $c(2\times2)$ AFM state which further stabilizes the collinear order (Tab. 9.4).

Table 9.4 | Obtained values for magnetic interactions for Mn/Mn/W(001) mapping the atomistic spin model to the DFT calculations. All values of the i-th neighbour exchange J_i, Dzyaloshinskii-Moriya interaction constants D_i and uniaxial magnetocrystalline anisotropy energy K are given in meV. $J > 0$ ($J < 0$) represents ferromagnetic (antiferromagnetic) order, $D > 0$ ($D < 0$) clockwise (counterclockwise) rotation and $K > 0$ ($K < 0$) denotes an in-plane (out-of-plane) easy axis.

Mn/Mn/W(001)							
FM	J_1	J_2	J_3	J_4	J_5	J_6	K
	−5.65	+0.76	+0.51	+0.30	+0.09	−0.13	−0.52
	D_1	D_2	D_3	D_4	D_5	D_6	D_7
	−0.54	+0.08	−0.20	+1.00	−1.18	−1.18	+0.57
$c(2\times2)$ AFM	J_1	J_2	J_3	J_4	J_5	J_6	K
	−6.14	+0.41	+0.43	+0.31	−0.07	−0.20	−0.81
	D_1	D_2	D_3	D_4	D_5	D_6	D_7
	−0.98	−0.63	+0.09	+2.07	−3.00	−3.68	+1.45

Local density of states The LDOS of Mn can be changed drastically due to the hybridization with the W(001) substrate [Fig. 9.3]. The shaded areas of the Mn layers indicate the LDOS of free-standing Mn DL without the W(001) substrate. For the free-standing DLs, the areas look similar and we see a large exchange splitting for all

[2]For the FM and $c(2\times2)$ AFM relaxation, the $\overline{\Gamma}$ point represents a FM configuration with same orientation in Mn(S) and Mn(I). Note, that higher **q** spin spiral states in the LAFM relaxation and orientation could not be stabilized.

three states [Fig. 9.3 (a,b,d,e,g,h)]. Due to the presence of the W(001) substrate (lines in Fig. 9.3), the LDOS of the Mn surface changes significantly and the peak visible in the free-standing DLs at the Fermi energy in the minority spin states almost vanishes for the FM and $c(2\times2)$ AFM state [Fig. 9.3 (a,d,g)]. For the LAFM state, the magnetic moment of Mn(S) has an opposite sign which is why here, the peak at E_F occurs in the majority states [Fig. 9.3 (d)]. When Mn/Mn/W(001) is in LAFM order, localized *d* states are still present at the Fermi level.

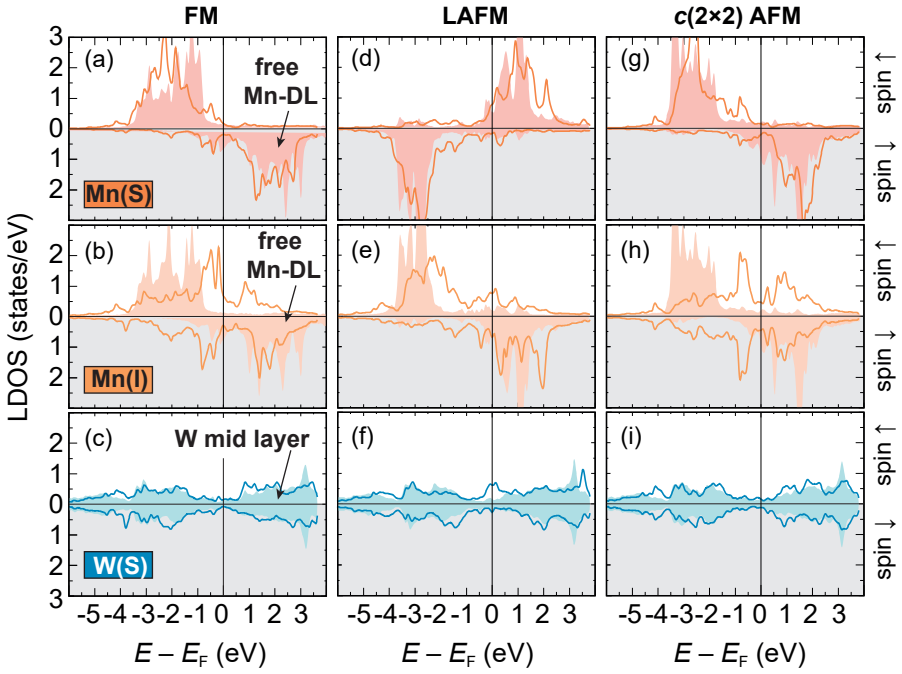

Figure 9.3 | Calculated local density of states (LDOS) for Mn/Mn/W(001). (a,b,c) LDOS for Mn surface layer Mn(S), Mn interface layer Mn(I) and W(001) surface layer W(S) in the ferromagnetic (FM) state. (d,e,f) LDOS as in (a,b,c) in the layered antiferromagnetic (LAFM) state. (g,h,i) LDOS in the $c(2\times2)$ antiferromagnetic (AFM) state. The shaded areas for Mn show the comparison of free-standing Mn double layers (DLs) without W(001) substrate in the respective magnetic state. For W, a layer in the middle of the calculated W(001) substrate is taken. Note that all states are calculated within their structural relaxation and for the LAFM state, Mn(S) has an opposite magnetic moment.

The LDOS of the Mn interface layer is presented in Fig. 9.3 (b,e,h). The exchange splitting is reduced for all three states compared to Mn(S), where the largest splitting remains in the LAFM state. This is in correspondence with the magnetic moment (Tab. 9.3): Since the distance between Mn(I) and W(001) is the largest in the LAFM, their hybridization is the smallest among the three collinear states and therefore the magnetic moment is larger than in the FM and $c(2\times2)$ AFM case.

In the FM state, unoccupied majority states occur which arise from the Mn-W hybridization [Fig. 9.3 (b)]. The double-peak structure at around 1 eV is visible in the shaded LDOS of the W substrate; however, it is smaller than for the W(001) surface layer [Fig. 9.3 (c)]. W(S) is lifted from the rest of the substrate and in combination

with the approach of the Mn(I) layer, the strong hybridization leads to the large peak structure. Furthermore, the peak is also present in the Mn surface layer in panel (a). Such a behaviour is observed for a large range of energies in the majority and minority spin channels.

Flipping every second spin into an AFM configuration of the Mn(S) layer will increase the exchange splitting for each spin compared to the FM case because the hybridization between two adjacent spins in the layer is absent. In combination with the strong hybridization of the substrate, the magnetic moment in Mn(I) is quenched (cf. Tab. 9.3 and Fig. 9.2). Its LDOS is symmetric and we see large hybridization peaks going from Mn(S) to Mn(I) into the W(S) layer [Fig. 9.3 (g,h,i)]. In order to understand the quenching of the moment, it is important to consider the geometry in the $c(2\times 2)$ AFM state. In Mn(I), every spin has the same distance to both a positive and a negative magnetic moments of the surface. This leads to a strong frustration of the Mn(I) layer.

9.5 Detection of a dead magnetic layer

The DFT calculations presented above predict a vanishing magnetic moment of the Mn interface layer in the $c(2\times 2)$ AFM ground state of the Mn(S) layer. However, since DFT calculations use different approximations in practice, we cannot be sure that this is necessarily true. Unfortunately, with state-of-the-art experimental techniques, it is not possible to resolve the magnetism of the interface layer of Mn experimentally. Therefore, we compare theoretical results with experiments which provide strong evidence that indeed, the $c(2\times 2)$ AFM ground state can be explained by a dead magnetic interface layer.

Taking the Tersoff-Hamann model into account, we can compare $\mathrm{d}I/\mathrm{d}U$ spectrum to the vacuum LDOS [156]. Fig. 9.4 shows the calculated vacuum LDOS for the three assumed collinear states. The comparable $\mathrm{d}I/\mathrm{d}U$ spectrum is seen in Fig. 9.1.

In the $c(2\times 2)$ AFM state the qualitative behaviour of the $\mathrm{d}I/\mathrm{d}U$ spectrum is reproduced, where around the Fermi energy, no features are visible and above E_F, two significant peaks occur [Fig. 9.4 (a)]. The quantitative deviations can be attributed to the use of the *xc* functional which only is an approximation to the self-energy. In the FM state [Fig. 9.4 (b)], features are also absent around E_F; however, the peak structure above E_F looks qualitatively different to the $\mathrm{d}I/\mathrm{d}U$ signal [cf. Fig. 9.1 (c)]. When the two Mn layers show an opposite magnetization direction [LAFM state in Fig. 9.4 (c)], states in the vicinity of the Fermi level occur. Even though larger peaks arise at energies which match the peak positions from experiments better than in the FM and $c(2\times 2)$ AFM state, a third peak is visible which holds the largest height. From comparison of vacuum LDOS with $\mathrm{d}I/\mathrm{d}U$ spectrum, the $c(2\times 2)$ AFM state shows the best agreement, supporting the total energy calculations of the previous chapter[3].

[3] Note, that from SP-STM experiments, the ground state in Mn(S) is $c(2\times 2)$ AFM.

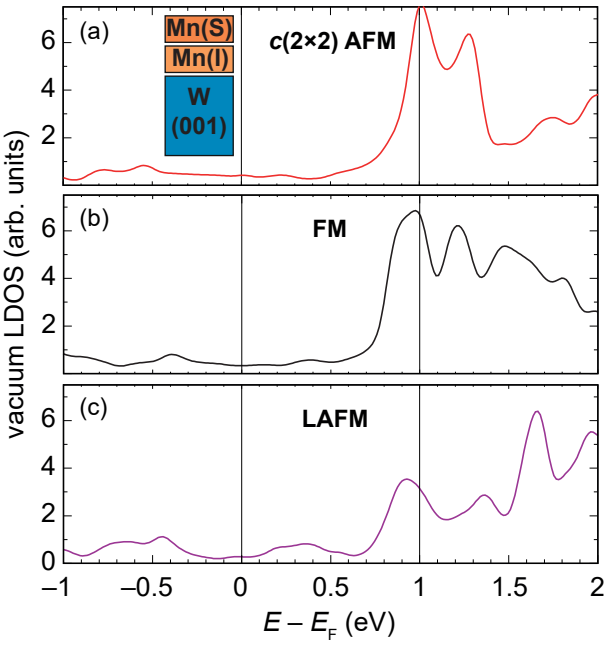

Figure 9.4 | Calculated vacuum local density of states (LDOS) for Mn/Mn/W(001). (a) Vacuum LDOS in the $c(2 \times 2)$ antiferromagnetic (AFM) state. (b) Ferromagnetic (FM) state. (c) Layered antiferromagnetic (LAFM) state. The calculations were performed 3 Å above the surface. The figure has been adapted from Pub. IV.

Stronger evidence for the $c(2 \times 2)$ AFM state with vanishing magnetic moment in the Mn(I) layer can be seen by comparing SP-STM measurements with simulations. Such simulations are presented in Fig. 9.5. In (a), the STM simulation shows the $p(1 \times 1)$ electronic contrast seen in Fig. 9.1 (a). Here, the black (white) contrast indicates the Mn surface (Mn interface) as shown in the sketch. As a result, the Mn(I) atoms show the maximum contrast and the Mn(S) atoms display the minima, so it is possible to image both the Mn surface and the Mn interface layer. Similar subsurface imaging technique has been reported before [180, 181].

Including magnetic contrast with an assumed tip polarization of 0.5 in Fig. 9.5 (b), we can reproduce the unconventional SP-STM contrast of the experiment [cf. Fig. 9.1 (b)]. The unit cell changes from $p(1 \times 1)$ to $c(2 \times 2)$ and the maxima now indicate magnetic moments pointing upwards. The minima are magnetic moments pointing downwards. Note that it is also high between magnetized surface atoms at the position of Mn(I).

The contrast in the SP-STM images can be explained by the d_z^2-like behaviour of the Mn(I) atoms for both spin $\uparrow$ and spin $\downarrow$ channels which is visible in the charge density plots of Fig. 9.5 (c,d). On the contrary, strongly spin-polarized states are visible in the surface layer showing a completely different contribution into the vacuum. The majority spin states in Fig. 9.5 (c) are governed by the Mn interface layer, whereas the minority spin states in Fig. 9.5 (d) show the maximum from the surface layer at 3 Å above the surface. Note, that the LDOS in Fig. 9.3 exhibits only few d-like states in the vicinity of the Fermi level due to the large exchange splitting in Mn(S). As a consequence, the electronic contrast [Fig. 9.5 (e)] shows the maxima at the positions of the Mn(I) layer and the magnetic contrast is dominated by the magnetic surface atoms [Fig. 9.5 (f)].

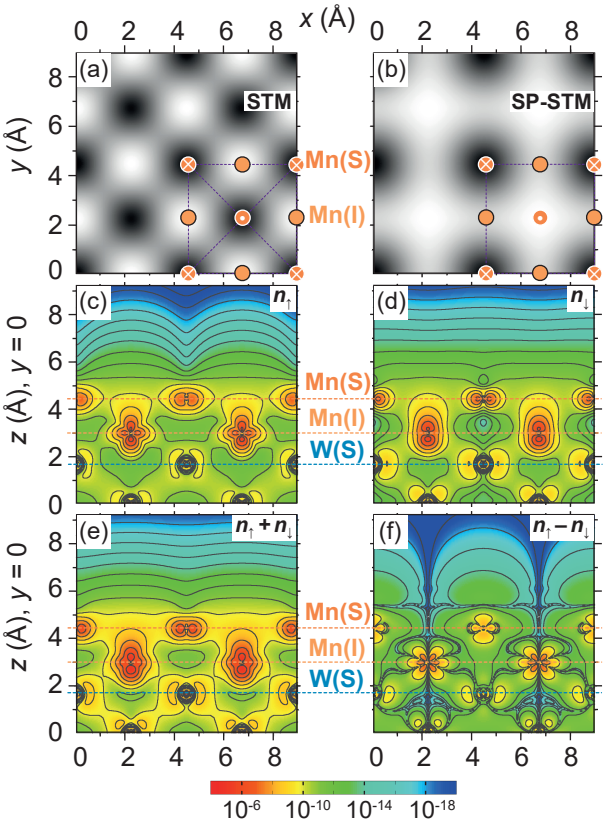

Figure 9.5 | DFT calculated spin-polarized scanning tunnelling microscopy (SP-STM) images at $U = +10$ mV and charge density for Mn/Mn/W(001) in the $c(2 \times 2)$ antiferromagnetic (AFM) state. (a) STM simulation at 3 Å above the film surface. The Mn surface Mn(S) and interface Mn(I) atoms are illustrated by orange circles, where in the Mn(S), the white crosses and dots denote down- and upwards pointing magnetic moments. Note, that we find an out-of-plane easy magnetization direction. (b) SP-STM simulation with assumed tip spin polarization of 0.5. (c,d) Cross-section plots through the spin-up and spin-down partial charge density in the energy range $[E_F, E_F + 0.01\ \text{eV}]$. (d) Electron density and (e) magnetization density plots as in (c). The figure has been adapted from Pub. IV.

In the SP-STM images presented above, the spin polarisation is far below 100% (in simulations, it is assumed to be 50%), since it can be simulated by the sum of both the magnetic and the electronic contribution to the tunnelling current. However, it is possible to disentangle these contributions not only in simulations, but in experiments as shown for Fe/W(001) [179].

Scanning the same area of a sample with oppositely magnetized tip magnetization directions, a magnetic surface will show a reversed contrast in the SP-STM. Such a procedure is presented in Fig. 9.6 (a,b), where dark (bright) spots in panel (a) are visible as bright (dark) spots in panel (b). The contrast is reversed due to a tip switching event. While the magnetic contrast can be eliminated by summing the two images (a) + (b) as presented in Fig. 9.6 (c), its electronic contrast is vanishing by subtracting them as shown in Fig. 9.6 (d). As already described in Sec. 9.2, the unit cell in the electronic contrast is rotated by 45° to the magnetic unit cell [Fig. 9.6 (c) and (d)].

In Fig. 9.6 (a-c), a defect structure is visible in the middle of every image which serves as a scanning reference. Its origin is non-magnetic since it is absent in (d), where only magnetic contrast is presented.

In the top right corner of every experimental image, the respective SP-STM simulation (corresponding to Fig. 9.5) is shown. Experiments and simulations are in excellent agreement, emphasizing the good theoretical description of the $c(2 \times 2)$ AFM ground state. Since the ground state forms a DML in the Mn interface layer, this is a strong evidence of its existence.

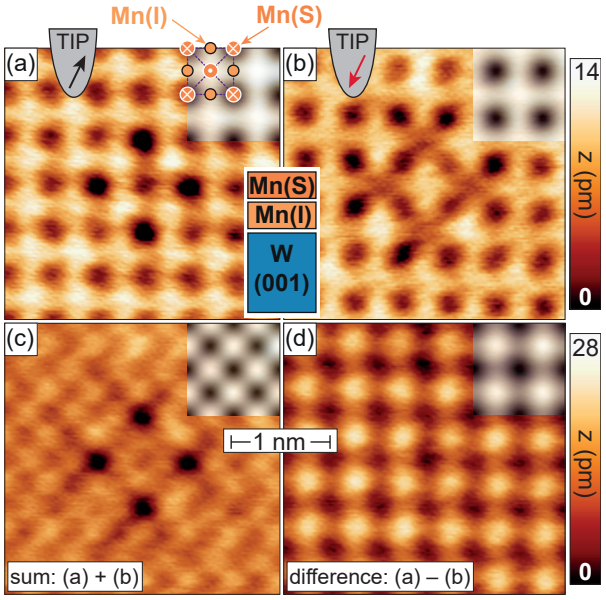

Figure 9.6 | Comparison of spin-polarized scanning tunnelling microscopy (SP-STM) measurements and simulations at $U = +10\,\mathbf{mV}$, $I = 3\,\mathbf{nA}$ for Mn/Mn/W(001) in the $c(2 \times 2)$ antiferromagnetic (AFM) state. (a) SP-STM images with positive perpendicular tip magnetization. (b) SP-STM images after tip switching. (c) Sum and (d) difference of SP-STM images of (a) and (b). The SP-STM simulations are performed with DFT according to Fig. 9.5. Note that the defect structure in the middle of the images (a-c) serves as reference which is non-magnetic since it is absent in (d). The figure has been adapted from Pub. IV.

9.6 Artificial stabilization of a magnetic moment in the Mn interface layer

Further verification of the existence of the DML presented above can be gained by analysing results when the Mn(I) layer holds a magnetic moment. When artificially increasing the Mn DL distance from the substrate (d_{23} with fixed d_{12} from Tab. 9.2), the Mn-W hybridization reduces and hence, a magnetic moment in the Mn(I) layer can be stabilized.

In Fig. 9.7, we present the results obtained with both the GGA and LDA *xc* functionals, which are consistent. Leaving the structurally relaxed equilibrium distance between the Mn DL and W substrate, the energy increases monotonically [Fig. 9.7 (a)]. Upon lifting the Mn DL, the magnetic moment of the Mn surface layer remains constant around $\pm 3.8\,\mu_B$ [Fig. 9.7 (b)]. In the Mn interface layer on the other hand, a magnetic moment can be stabilized by increasing d_{23} by more than 0.10 Å for GGA (0.15 Å for LDA). For a magnetic material, it is expected that the formation of a magnetic moment gains energy (Ref. 179); however, in Mn/Mn/W(001) the energy is increasing monotonically.

We further investigate the SP-STM contrast at the threshold of its formation 3 Å above the surface for vanishing magnetic moment [Fig. 9.7 (c)], small magnetic moment [Fig. 9.7 (d)] and increasing magnetic moment of Mn(I) [Fig. 9.7 (e)], respectively. For both GGA and LDA *xc* potential, the SP-STM contrast looks the same and only if the Mn interface layer is a DML, we recognize the unusual contrast pattern which is visible in the experiments (cf. Fig. 9.1). Even with a small magnetic moment, the magnetic contrast changes into a striped pattern which is enhanced by larger moments in the interface layer [Fig. 9.7 (d,e)].

Fig. 9.7 (f-h) shows how the vacuum LDOS varies due to the change of the magnetic

moment described above. When the DL is slightly lifted from the relaxed distance, the two significant peaks, above E_F in Fig. 9.4 (c) come closer. The vacuum LDOS look alike and even with a small magnetic moment in Mn(I), no states are visible around the Fermi level [Fig. 9.7 (f,g)]. The electronic structure seems to react more sensitive on the change of interlayer distance than on a formation of a small magnetic moment.

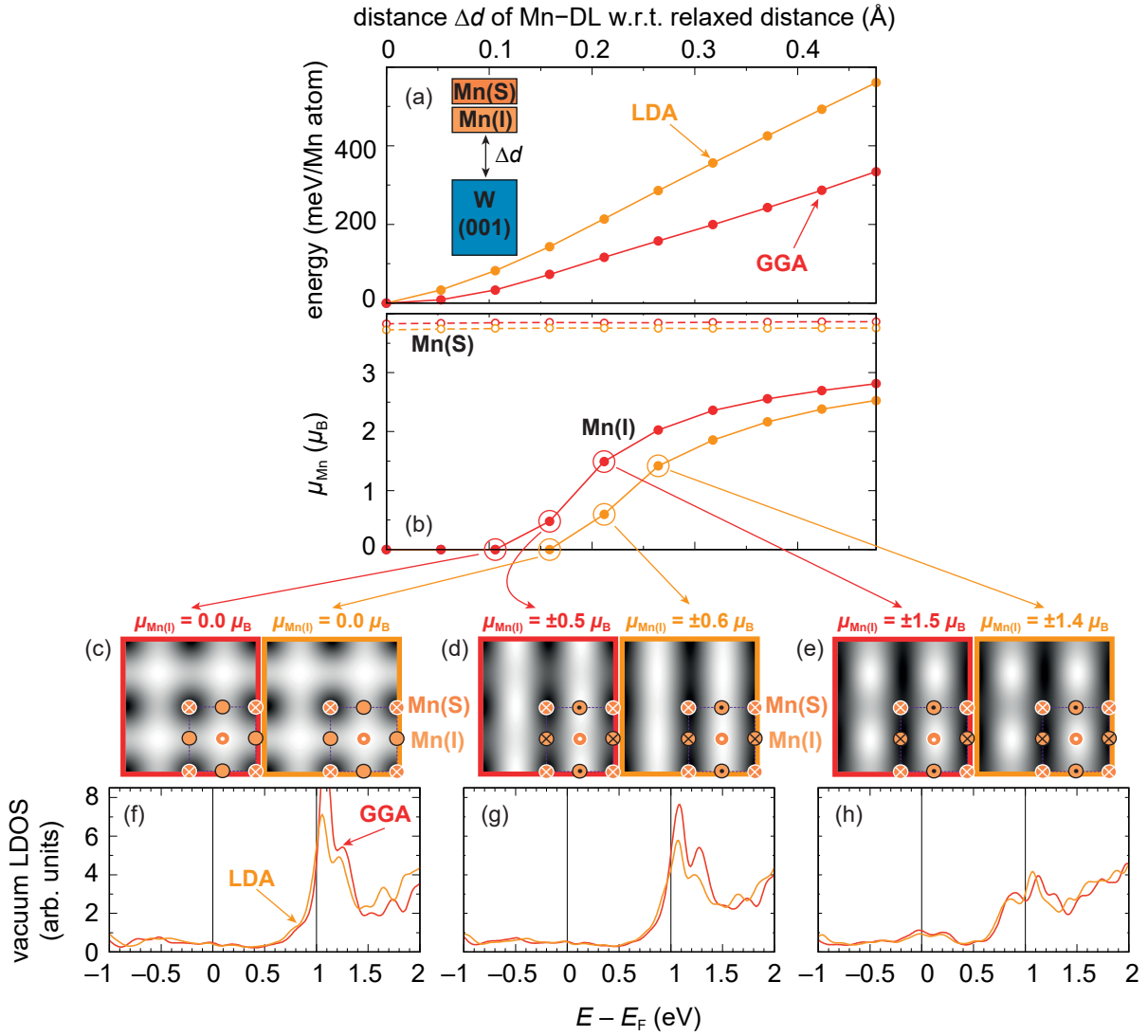

Figure 9.7 | DFT calculated results upon artificially increasing the distance of the Mn double layer from the W substrate for Mn/Mn/W(001) in the $c(2 \times 2)$ antiferromagnetic (AFM) state. (a) Total energy difference. (b) Calculated magnetic moment for the Mn surface layer Mn(S) and interface layer Mn(I). (c,d,e) Spin-polarized scanning tunnelling microscopy simulations 3 Å above the film surface at $U = +10\,\text{mV}$ for three different distances Δd marked in (b). The sketches show the magnetic unit cells. (f,g,h) Calculated vacuum local density of states for the states (c,d). Note that the starting point is the structurally relaxed interlayer distance in the $c(2 \times 2)$ AFM state from Tab. 9.2. The magnetic state in the interface layer is assumed to be $c(2 \times 2)$ AFM.

However, when a larger magnetic moment is stabilized in the interface Mn layer, the vacuum LDOS changes drastically and states occur around E_F [Fig. 9.7 (h)]. The two

significant peaks around 1 eV are dropping in height. A formation of a magnetic interface layer therefore would not only change the SP-STM contrast, but also give rise to a different dI/dU spectra in the experiments. From these calculations we conclude that the experimental observations can be explained by a dead magnetic interface Mn layer[4].

In Fig. 9.8 (a,b), the SP-STM images are shown for a small and large magnetic moment of the Mn interface layer, respectively. Furthermore, the cross-section plots of the charge densities are presented [Fig. 9.8 (c-f)]. Comparing these with Fig. 9.5, the d_z^2-orbital character of Mn(I) reduces for increasing magnetic moment. Note that STM simulations and measurements are performed in the vicinity of the Fermi energy. When a magnetic moment appears, the d states are moved from E_F due to exchange splitting. Since these states are responsible for the unusual contrast in the experiment, their reduction at E_F leads to a different contrast in the SP-STM, which is a consequence of the reduced Mn-W hybridization.

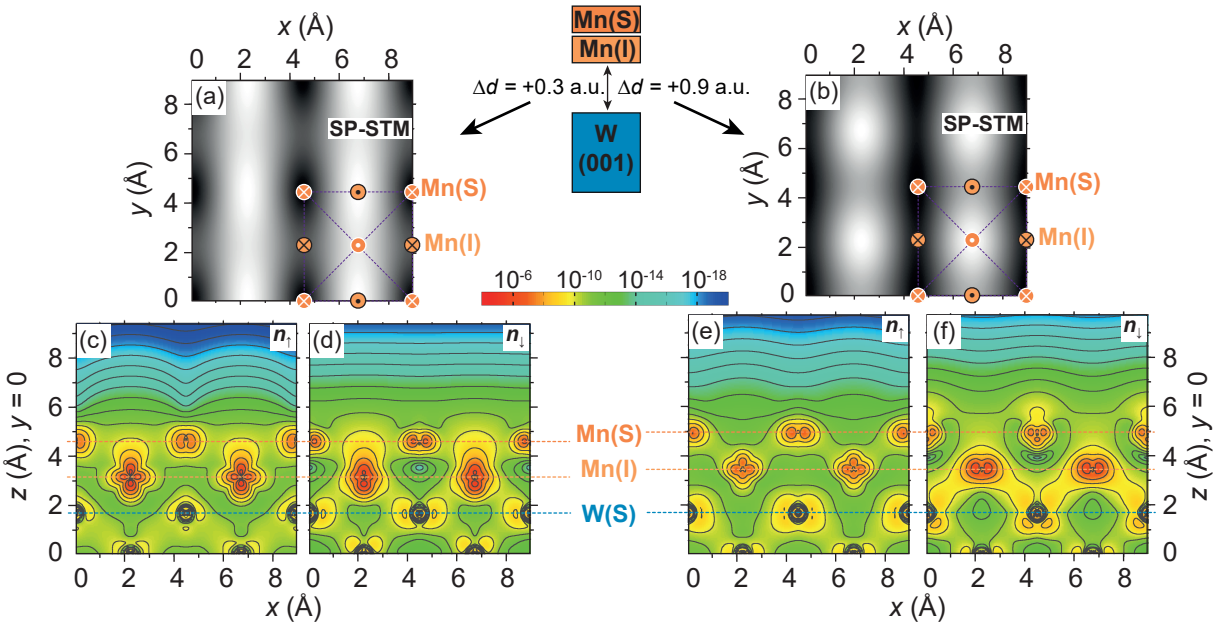

Figure 9.8 | DFT calculated spin-polarized scanning tunnelling microscopy (SP-STM) images at U = +10 mV and charge density for Mn/Mn/W(001) in the $c(2 \times 2)$ antiferromagnetic (AFM) state including a magnetic moment in the Mn interface layer. (a,b) SP-STM simulation at 3 Å above the film surface for increased interlayer distance of 0.3 Å [0.9 Å in (d)]. The resulting magnetic moments of Mn(I) are $\pm 0.5\,\mu$B and $\pm 1.5\,\mu$B, respectively. (c-f) Cross-section plots through spin-up and down partial charge densities in the energy range of [E_F, E_F + 0.01 eV] for the two cases in (a,b). The magnetic state in the interface layer is assumed to be $c(2 \times 2)$ AFM.

[4]We exclude other magnetic states from SP-STM, e.g combining a $c(2 \times 2)$ Mn(S) layer with a FM Mn(I) layer would lead to ferrimagnetic structure. This would give a $c(2 \times 2)$ superstructure in the non-magnetic STM due to the change of the electronic structure of ↑ and ↓ spins [171].

9.7 Conclusion

In this chapter we have unravelled the magnetic ground state of a Mn DL on W(001). A $c(2 \times 2)$ AFM state is stabilized in the Mn surface layer whereas the Mn interface layer occurs to be magnetically dead. SP-STM measurements are in excellent agreement with DFT calculations which show that both the hybridization between Mn interface and W(001) surface and the frustration of the checkerboard AFM state in the surface layer are crucial to transfer the magnetic behaviour of the Mn interface layer into one of a non-magnetic TM with a large spin susceptibility. Due to the combination of experiment and theory it is possible to image and analyse the Mn interface layer. Whereas in the Mn top layer, only very few *d*-like states are present at the Fermi energy, d_{z^2}-like in the Mn interface penetrate into the vacuum leading to a strong contrast of surface and interface layer in STM images. Our example further presents the vast magnetic phases of Mn grown on TM substrates.

Chapter 10

Competition of higher order exchange interactions: Mn/Re(0001)

In the previous chapters we analysed the magnetism of ultrathin films applying the extended atomistic Heisenberg model parametrized from density functional theory (DFT), where besides frustration of exchange and Dzyaloshinskii-Moriya interaction (DMI) beyond nearest neighbours, the magnetocrystalline anisotropy energy (MAE) was taken into account. The descriptions were sufficient for the films above, which were shown to be in good agreement with experimental observations.

When dealing with small energy differences and large frustration effects, interactions which are often neglected due to their small energy can be decisive to form the magnetic ground state. In this view, the dipolar interaction typically has a negligible contribution in ultra-thin films, similar as the anisotropic symmetric exchange (ASE). The latter describes the anisotropic part of the dipolar interaction, denoted as pseudo-dipolar interaction and arises due to the spin-orbit coupling (SOC) as the DMI and the MAE [116, 117].

Furthermore, in films such as Rh/Fe/Ir(111) [44] and Fe/Rh(111) [45, 110], even exchange frustration is not sufficient to describe the occurring multi-Q states. With a superposition of different spin spiral (single-Q) states, multi-Q states can be formed which are energetically degenerate within the Heisenberg exchange interaction – irrespective of the degree of frustration. When the total energies of multi-Q and single-Q states obtained via DFT are deviating, another class of magnetic interactions, higher order exchange interactions (HOIs) beyond the pairwise interactions have been taken into account to shed light into the mechanism forming complex magnetic structures with exciting new properties. This was successfully done for the above mentioned films, but also for the skyrmion lattice in Fe/Ir(111) [29] or the conical spin spiral ground state in Mn/Mn/W(110) [46].

For the film system of Mn/Cu(111), a highly complex magnetic structure was proposed based on DFT about 20 years ago, which holds a superposition of three row-wise antiferromagnetic (RW-AFM) states. This so called triple-Q or 3Q state exhibiting a tetrahedron angle ($\sim 109°$) between adjacent spins was explained by a distinct HOI, the 4-spin interaction [182]. In this film, it especially arises due to the increased interatomic distance of Mn atoms on the Cu(111) surface. However, up to now this state could be not confirmed in experiments.

In this chapter, we investigate the magnetic film of a Mn monolayer (ML) on the

Re(0001) surface. While both RW-AFM state and 3Q state are predicted for different systems in the past [49, 50], our collaborators of the University of Hamburg demonstrate its occurrence in the fcc and hcp stacking of the Mn top layer.

Our DFT calculations reveal that driven by frustrated exchange interaction, the RW-AFM state is the lowest among all single-Q states for both fcc and hcp Mn/Re(0001). Calculating the total energy differences to the 3Q states, very small energies arise which are at the limit of DFT calculations and where slight distortions can affect the magnetic ground state. Despite these small energies, the HOI are comparably large. We find the ASE and the dipolar interaction to be responsible for coupling the spins of the RW-AFM in Mn_{fcc}/Re(0001) to the atomic lattice and suggest a distorted, non-ideal 3Q state as ground state for Mn_{hcp}/Re(0001). Even though the literature holds various spin models, such as interactions arising due to non-vanishing topological orbital moments [183–186], none of the known can explain the obtained DFT results so far.

The chapter is structured as follows: first (Sec. 10.1), experimental observations are presented which have been performed at the University of Hamburg. In Sec. 10.3, we show spin spiral energy dispersions and higher order states and conclude that both exchange and HOI are highly frustrated. The electronic structure of the ground states is discussed in Sec. 10.4. We shed light onto the effect of ASE in Mn/Re(0001) (Sec. 10.5) as well as canting the spins from the perfect tetrahedron angles of the 3Q state in Sec. 10.6.

10.1 Experimental observation of RW-AFM and 3Q states

The experiments were motivated by the prediction of large DMI in Mn/Re(0001) [187][1]. They were performed by Jonas Spethmann under the supervision of André Kubetzka and Kirsten von Bergmann in the lab of Prof. Roland Wiesendanger[2]. On the Re(0001) surface, the growth of Mn is prevalent in fcc, while the hcp stacking of Mn can only be induced by growing Co before the Mn. Co covers the step edges and then allows Mn to align in hcp areas. For further information see Ref. 51 and Pub V. In Fig. 10.1 close views are presented of areas with Mn_{fcc}/Re(0001) in (a) and Mn_{hcp}/Re(0001) in (b).

For Mn_{fcc}, an Fe coated W tip is used and a stripe pattern is observed which possesses three rotational domains. From the distance between the stripes which is exactly two atomic rows, measurements reveal a RW-AFM as ground state. Since the contrast between the rotational domains is different (high contrast in the lower left and low contrast in the upper right), experimentalists conclude the easy axis is in-plane. Furthermore we see a strong coupling of the spins to the magnetic rows where only

[1] André Kubetzka, private communication

[2] Institute of Applied Physics and and Interdisciplinary Nanoscience Center Hamburg, University of Hamburg, Jungiusstrasse 11, 20355 Hamburg, Germany

three possible rotations are allowed.

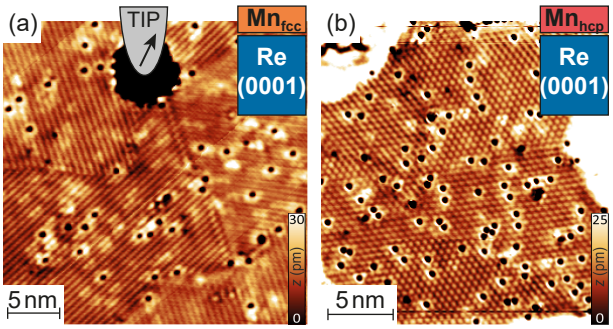

Figure 10.1 | Spin-polarized scanning tunnelling microscopy measurements on Mn/Re(0001). (a) Image on the row-wise antiferromagnet of Mn_{fcc}/Re(0001); Fe-coated W tip and $U = -20\,\mathrm{mV}$, $I = 7.5\,\mathrm{nA}$, $T = 8\,\mathrm{K}$, $B = 0\,\mathrm{T}$. (b) Image on the 3Q state of Mn_{hcp}/Re(0001); Cr tip and $U = -30\,\mathrm{mV}$, $I = 7.0\,\mathrm{nA}$, $T = 4\,\mathrm{K}$, $B = 0\,\mathrm{T}$. The figure has been adapted from Pub. V.

The spin-resolved scanning tunnelling microscopy (STM) image of Mn_{hcp}/Re(0001) is shown in Fig. 10.1 (b), where the white areas in the upper left and middle right are due to the adjacent Co areas. These measurements were performed with a Cr tip with arbitrary magnetization direction. Compared to (a), we do not see a striped pattern, but a hexagonal superstructure. The structure reveals four atoms in the magnetic unit cell which are in accordance to the three-dimensional 3Q state. A closer look shows that not every region looks qualitatively the same and different rotational domains appear. This can be seen as similar to the fcc stacking of Mn. Further measurements indicate that the 3Q state might not be in perfect prototypical shape with one complete out-of-plane component. When rotating all spins by a constant angle, different versions of the 3Q state can occur (Fig. 10.2).

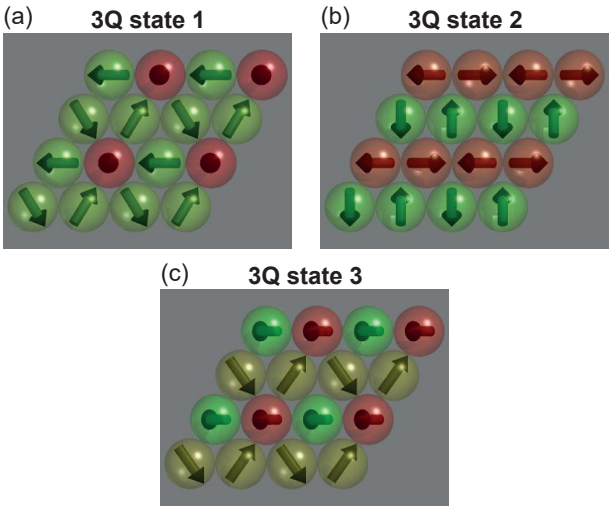

Figure 10.2 | Different configurations of 3Q states. Shown are three configurations which could give rise to the experimental observation in Fig. 10.1 (b). (a) 3Q state 1 with one spin completely out-of-plane giving rise to perfect hexagonal pattern in the scanning tunnelling microscopy (STM). (b) 3Q state 2 would give rise to striped pattern in STM. (c) 3Q state 3 would show a distorted hexagonal pattern in STM. Red spins are pointing upwards and green spins point downwards. Images by courtesy of André Kubetzka.

Both experimentally observed magnetic states are studied theoretically in the recent past, but did not occur in measurements up to now. Since a change of the stacking order in the top layer results in two different complicated magnetic ground states, the film of Mn/Re(0001) is assumed to contain complex physics which we try to analyse via DFT in the following part.

10.2 Computational Details

In this study, we used the FLEUR code [47] with film geometry. We took the lattice parameters a, c from Ref. 188 as reference where they were obtained in DFT calculations applying the generalized gradient approximation (GGA) exchange correlation (xc) potential [73]. The in-plane parameter is $a_{\mathrm{NN}} = 5.24\,\mathrm{a.u.}$ whereas the out-of-plane component is $c = 8.47\,\mathrm{a.u.}$ Our spin-polarized calculations are performed with muffin tin (MT) radii of $R^{\mathrm{MT}}_{\mathrm{Mn}} = 2.35\,\mathrm{a.u.}$, $R^{\mathrm{MT}}_{\mathrm{Re}} = 2.40\,\mathrm{a.u.}$ for Mn and Re, respectively. If not stated differently, the energy cutoff was set to $k_{\mathrm{max}} = 4.0\,\mathrm{a.u.}^{-1}$.

Structural relaxation In order to find the equilibrium distance between the layers, we structurally relaxed symmetric films consisting of nine Re(0001) layers where a Mn ML is placed on both sides of the film. The RW-AFM state was applied in the Mn layers. Between the topmost layers (denoted as $d_{12}, d_{23}, \ldots$) we minimized the forces in [111] direction up to a threshold of $10^{-5}\,\mathrm{htr/a.u.}$ while five Re(0001) layers in the centre of the film are kept fixed at the bulk equilibrium lattice parameter. The resulting interlayer distances are presented in Tab. 10.1. We applied 144 k points for in the irreducible wedge of the Brillouin zone (BZ) for and the GGA xc functional [73].

	$\mathrm{Mn_{fcc}}$	$\mathrm{Mn_{hcp}}$
ΔE	0	+27.4
d_{12}	4.155	4.136
d_{23}	4.141	4.144
d_{34}	4.316	4.325
μ_{Mn}	±3.31	±3.30
$\mu_{\mathrm{Re(S)}}$	±0.047	±0.035
$\mu_{\mathrm{Re(S-1)}}$	±0.027	±0.045

Table 10.1 | Computational results for Mn/Re(0001) in the row-wise antiferromagnetic state after structural relaxation. Energy difference ΔE (meV/Mn) between the two stackings of Mn, fcc and hcp. Relaxed interlayer distances d_{ij} (a.u.) for the topmost layers and magnetic moment (μ_{B}) of the topmost three layers in the system. d_{12} represents the distance between the Mn and Re layer, d_{23}, between the Re surface layer and subsurface layer and d_{34} between the Re subsurface layer and layer underneath.

Spin spiral calculations We performed self-consistent spin-spiral calculations to compare the total energies of single-Q states [49]. We chose an asymmetric film of six Re(0001) and a Mn ML on one side of the film. As stated below, we applied the same film setup for the multi-Q states. Test calculations revealed that a film with nine layers will not change the energy dispersion. Applying the interlayer distances from structural relaxation, the $\mathbf{q}$ vector is chosen in $\overline{M}$-$\overline{\Gamma}$-$\overline{K}$-$\overline{M}$ direction of the hexagonal two-dimensional (2D) BZ. The energy contribution due to SOC, ΔE_{SOC} is calculated for every converged spin spiral state in first-order perturbation theory [91, 128, 129]. We applied the local density approximation (LDA) xc potential [127] and 1936 k points in the full 2D BZ. For the evaluation of spin spiral calculations, we mapped the atomistic spin model of the exchange interaction to the DFT results without SOC and the DMI to ΔE_{SOC}.

Multi-Q states We compare the single-Q spin spiral states to those which occur due to a superposition of spin spirals, so-called multi-Q states. These are the up-up-down-down $(\uparrow\uparrow\downarrow\downarrow)$[3] in both high symmetry directions $\overline{\Gamma}$-$\overline{M}$ and $\overline{\Gamma}$-$\overline{K}$ and the 3Q states [50, 189]. We set the $\uparrow\uparrow\downarrow\downarrow$ states in relation to the ferromagnetic (FM) equivalents and the 3Q states to the respective RW-AFM states. Every multi-Q state is calculated in its own supercell which are presented in App. D. To be consistent with single-Q calculations, we apply an asymmetric film with six Re(0001) layers and the Mn ML on top of the film and more than 1000 k points in the full BZ are used for all calculations as well as the LDA *xc* potential [127].

When including HOIs driven by the energy differences of single-Q and multi-Q states, the exchange constants J_i which are obtained from spin spiral calculations have to be updated (denoted as J_i') since the mapping of $E(\mathbf{q})$ is done neglecting HOIs [45, 190]:

$$J_1' = J_1 - Y_1 \tag{10.1a}$$

$$J_2' = J_2 - Y_1 \tag{10.1b}$$

$$J_3' = J_3 - B_1/2 \tag{10.1c}$$

Magnetocrystalline anisotropy energy We calculated the MAE by self-consistently converging an asymmetric film with nine layers of Re(0001) with the Mn ML on one side in RW-AFM state including SOC. The values of the MAE (K) are determined by applying the spin quantization axis with SOC perpendicular to the film plane $E_\perp$ and parallel to the film plane $E_\parallel$. The in-plane direction is $\pi = 0°$ from Fig. 10.6 in the left panel. The resulting energy difference, the MAE is defined as $K = E_\perp - E_\parallel$. For the MAE, we applied an energy cutoff of $k_{\max} = 4.1\,\text{a.u.}^{-1}$ and 1914 k points in the full 2D BZ.

Anisotropic symmetric exchange interaction energy Correspondent to the MAE, we apply the spin quantization in different in-plane directions, where starting from $\phi = 0°$ to $\phi = 90°$ from Fig. 10.6. The self-consistent calculations were performed with the same settings as for the MAE described before.

Transformation of 2Q to 3Q to 1Q state In order to determine the magnetic ground state in Mn/Re(0001) we consider distorted 3Q states as possible solutions. This is why we successively cant spins from different multi-Q states into a single-Q state. Starting from a 3Q state [Fig. 10.2 (c)], we rotate two spins in the in-plane direction and two spins in the out-of-plane direction with approx ±5° per step. By rotating in different directions, we end up in the 2Q state and the RW-AFM state. All resulting energy differences are energetically degenerate within the classical Heisenberg model as we have checked numerically.

We have performed these kind of calculations for a Mn unsupported monolayer (UML) using three different lattice constants. Since we want to see the influence of the Re(0001) substrate on these states, we use the lattice constant of

[3] The respective single-Q states of the $\uparrow\uparrow\downarrow\downarrow$ are a superposition of left-and right rotating 90° spin spiral states in the $\overline{\Gamma}$-$\overline{M}$ and $\overline{\Gamma}$-$\overline{K}$ directions.

Re(0001) which we refer to as $a_{\mathrm{Re}(0001)}$. Furthermore, we reproduce the energy difference between 3Q and 1Q state with the lattice constant of Cu(111) taken from Ref. 182 using the theoretically determined in-plane lattice constant of Cu[4], denoted as $a_{\mathrm{Cu}(111)\text{-theo}} = 4.702\,\mathrm{a.u.}$ We increase this lattice constant to the experimental one assigned as $a_{\mathrm{Cu}(111)\text{-exp}} = 4.750\,\mathrm{a.u.}$ For calculations with the Mn UMLs, we use 128 k points in one half of the 2D BZ and an energy cutoff of $k_{\mathrm{max}} = 3.7\,\mathrm{a.u.}^{-1}$.

Repeating these calculations for the complete films of Mn/Re(0001), we apply an asymmetric film with six layers of Re(0001) and the Mn ML on top of the film. The computational setup consists of 722 k points in one half of the 2D BZ and an energy cutoff of $k_{\mathrm{max}} = 4.0\,\mathrm{a.u.}^{-1}$.

10.3 Competition of higher order exchange interactions from first-principles

The experimental observations of Sec. 10.1 reveal the RW-AFM state in $\mathrm{Mn_{fcc}}$/Re(0001) and in case of $\mathrm{Mn_{hcp}}$/Re(0001) it is a superposition of three RW-AFM, the 3Q state. We first perform spin spiral calculations in order to scan the phase space of single-Q states. The results neglecting SOC can be seen in Fig. 10.3 (a), where the circles (points) show the DFT calculated energies of $\mathrm{Mn_{fcc}}$ ($\mathrm{Mn_{hcp}}$) and the lines are due to the fit of the Heisenberg exchange interaction beyond nearest neighbours.

Without SOC, for both stackings, the RW-AFM is the lowest in energy which only occurs due to the frustration of exchange interaction. Note that without $J_2, J_3, \ldots$ the 120° Néel state at the $\overline{K}$ point would be the energy minimum. All resulting values for the pairwise magnetic interactions can be seen in Tab. 10.2. Since the second neighbour J_2 prefers antiferromagnetic (AFM) order with a comparably large value ($J_2/J_1 > 1/5$ for both stackings of Mn), the RW-AFM state can be favoured.

According to Ref. 187 the DMI in Mn/Re(0001) is predicted to be large and in combination with our results this would change the magnetic ground state from collinear to non-collinear. However, from Fig. 10.3 (b), the SOC contribution in the films is only large around the FM state and small around the RW-AFM[5]. Consequently, the DMI is not strong enough to have a decisive impact on the RW-AFM ground state in the films.

We self-consistently calculate the MAE by considering the RW-AFM state and applying the spin quantization axis in and out of the plane. For both $\mathrm{Mn_{fcc}}$ and $\mathrm{Mn_{hcp}}$, we find a large MAE preferring an in-plane magnetization direction as suggested by the experiment ($K \sim +1\,\mathrm{meV/Mn\ atom}$ for both Mn stackings) and could already explain the magnetic ground state of $\mathrm{Mn_{fcc}}$/Re(0001), but not the occurring 3Q state in $\mathrm{Mn_{hcp}}$.

[4]Note that in the publication the lattice constant is not presented. Thus it is taken from the PhD thesis of Philipp Kurz [68].

[5]Note that we reproduce the strength of DMI from Ref. 187 when considering the region around the $\overline{\Gamma}$ point.

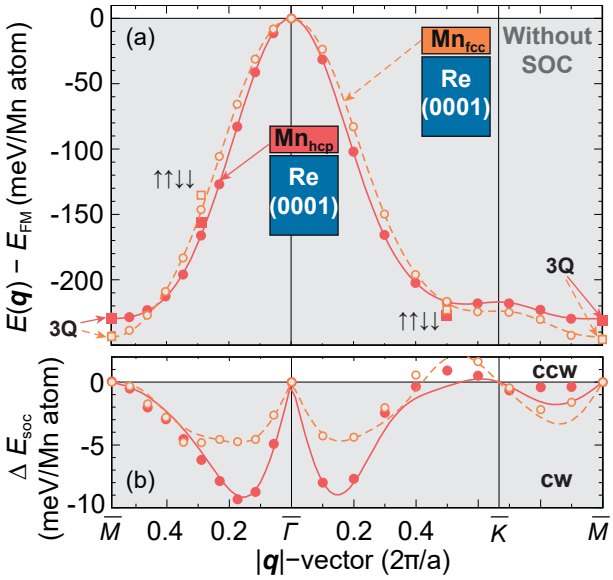

Figure 10.3 | Full energy dispersions $E(\mathbf{q})$ of flat cycloidal spin spirals for Mn/Re(0001). (a) Energy dispersions without spin-orbit coupling (SOC) along the high symmetry path $\overline{\Gamma}$-$\overline{M}$ and $\overline{\Gamma}$-$\overline{K}$ of the two-dimensional Brillouin zone. Orange circles [for Mn_{fcc}/Re(0001)] and red points [for Mn_{hcp}/Re(0001)] show calculated energies from DFT with respect to the ferromagnetic (FM) state, whereas lines (dashed for Mn_{fcc} and solid for Mn_{hcp}) represent the mapping to the atomistic spin model of the Heisenberg exchange beyond nearest neighbours. The energies of multi-Q states (↑↑↓↓ and 3Q states) are displayed open and filled squares, respectively. (b) Energy contribution due to SOC where the lines are the fit to the Dzyaloshinskii-Moriya interaction beyond nearest neighbours. of Mn_{fcc}/Re(0001) (circles and dashed lines) and Mn_{hcp}/Re(0001) (points and solid lines) in $\overline{M}$-$\overline{\Gamma}$-$\overline{K}$-$\overline{M}$ direction.

Table 10.2 | Obtained values for magnetic interactions in Mn/Re(0001) mapping the atomistic spin model without higher order exchange interactions to the DFT calculations of single-Q states. All values of the i-th neighbour exchange J_i, Dzyaloshinskii-Moriya interaction (DMI) constants D_i and uniaxial magnetocrystalline anisotropy energy K are given in meV. $J > 0$ ($J < 0$) represents ferromagnetic (antiferromagnetic) order, $D > 0$ ($D < 0$) clockwise (counterclockwise) rotation and $K > 0$ ($K < 0$) denotes an in-plane (out-of-plane) easy axis. Note that the values of J_1, J_2, J_3 need to be modified according to Eq. (10.1) when HOI are included to the spin model.

Mn_{fcc}	J_1	J_2	J_3	J_4	J_5	J_6	J_7
	−24.68	−5.67	+0.10	−0.38	+0.18	−0.049	+0.23
	D_1	D_2	D_3	D_4	D_5	D_6	D_7
	+0.69	+0.97	−0.16	+0.014	−0.042	+0.064	+0.078
Mn_{hcp}	J_1	J_2	J_3	J_4	J_5	J_6	J_7
	−21.19	−6.72	−2.00	−0.62	+0.12	−0.36	+0.16
	D_1	D_2	D_3	D_4	D_5	D_6	D_7
	+1.21	+1.02	+0.19	+0.30	−0.047	+0.13	+0.0067

Therefore, we compare the energies of a perfect 3Q state and its respective RW-AFM, denoted as $\Delta E_{\overline{M}}^{3Q}$ in Tab. 10.3. For both stackings, the 3Q state is preferred over the RW-AFM by less than 1 meV. Taking the MAE into account which prefers collinear states over non-collinear ones, the energy is even smaller by about 0.3 meV. Within our accuracy, 3Q and 1Q state are energetically degenerate and small deviations e.g. in relaxation, lattice parameter or number of assumed Re layers in the substrate will affect the theoretical result. These results do not give rise to a unambiguous conclusion why in Mn_{fcc} the single-Q state and in Mn_{hcp} the triple-Q state is preferred. However, in both films, both states are possible from our calculations.

Applying the Heisenberg exchange interaction beyond nearest neighbours cannot explain an energy difference between a 1Q and a 3Q state. In such a case, HOIs have to be considered as it is suggested in Ref. 182. There, the magnetic ground state of a Mn ML on Cu(111) was investigated via DFT and a large energy difference of $\Delta E_{\overline{M}}^{3Q} \sim -17$ meV/Mn atom has been found. This energy difference was explained by the 4-spin interaction, where $\Delta E_{\overline{M}}^{3Q} = E_{3Q} - E_{1Q} = {}^{32}/_{3}\, K_1$.

Considering the small energy differences can give rise to a negligible contribution of this HOI in Mn/Re(0001). However, we further calculate two different superpositions of spin spiral states, the $\uparrow\uparrow\downarrow\downarrow$ states in $\overline{\Gamma}$-$\overline{K}$ and $\overline{\Gamma}$-$\overline{M}$ direction [44, 45, 50, 110, 189], respectively. The energy differences between these higher order states and their respective single-Q state are presented in Tab. 10.3. With all three calculated energy differences of multi-Q states, we are not only able to consider the 4-site 4-spin interaction (K_1), but also the biquadratic (B_1) and 3-site 4-spin interaction (Y_1) from Eq. (10.2) as suggested in Ref. 110 and 45.

$$\Delta E_{\overline{\mathrm{M}}}^{3Q} = E_{\overline{\mathrm{M}}}^{3Q} - E_{\overline{\mathrm{M}}}^{1\mathrm{Q}} = \frac{16}{3}(2K_1 + B_1 - Y_1) \tag{10.2a}$$

$$\Delta E_{\overline{\mathrm{M}}/2}^{\uparrow\uparrow\downarrow\downarrow} = E_{\overline{\mathrm{M}}/2}^{\uparrow\uparrow\downarrow\downarrow} - E_{\overline{\mathrm{M}}/2}^{1Q} = 4(2K_1 - B_1 - Y_1) \tag{10.2b}$$

$$\Delta E_{3\overline{\mathrm{K}}/4}^{\uparrow\uparrow\downarrow\downarrow} = E_{3\overline{\mathrm{K}}/4}^{\uparrow\uparrow\downarrow\downarrow} - E_{3\overline{\mathrm{K}}/4}^{1\mathrm{Q}} = 4(2K_1 - B_1 + Y_1) \tag{10.2c}$$

Table 10.3 | Calculated higher order exchange interactions for Mn/Re(0001). DFT calculated total energy differences between the multi-Q states and their corresponding spin spiral states according to Eq. (10.2) (a-c) (meV/Mn atom) and obtained values for the higher-order exchange constants (meV). B_1, Y_1, K_1 are the biquadratic, 3-site 4-spin and 4-site 4-spin interaction, respectively.

System	$\Delta E_{\overline{M}}^{3Q}$	$\Delta E_{\overline{M}/2}^{\uparrow\uparrow\downarrow\downarrow}$	$\Delta E_{3\overline{K}/4}^{\uparrow\uparrow\downarrow\downarrow}$	B_1	Y_1	K_1
Mn_{fcc}	−0.7	+11.9	−6.4	−1.56	−2.29	−0.43
Mn_{hcp}	−0.4	+9.7	−10.2	−1.25	−2.49	−0.66

Despite the previous assumption of small HOIs, they appear to be comparably large as seen in Tab. 10.3 in nearest neighbour approximation. All HOIs have the same sign and compete with each other concerning the energy difference between the RW-AFM and the 3Q state [Eq. (10.2a)]. This is referred to a frustration of HOI. But even such a frustration of HOI cannot fully explain the experimental observation which is why we analyse the electronic structure and consider different effects in more detail in the following.

10.4 Electronic structure in Mn/Re(0001)

We want to achieve a more detailed description of the electronic structure and compare the local density of states (LDOS) for Mn/Re(0001) in Fig. 10.4. In the left column, the LDOS of the RW-AFM state is shown for Mn_{fcc}/Re(0001) and in the right column, three calculations are presented for Mn_{hcp}/Re(0001). For the Mn_{fcc} layer, we observe the typically large exchange splitting [Fig. 10.4 (a)]. The magnetic moment consequently is very large (cf. Tab. 10.1).

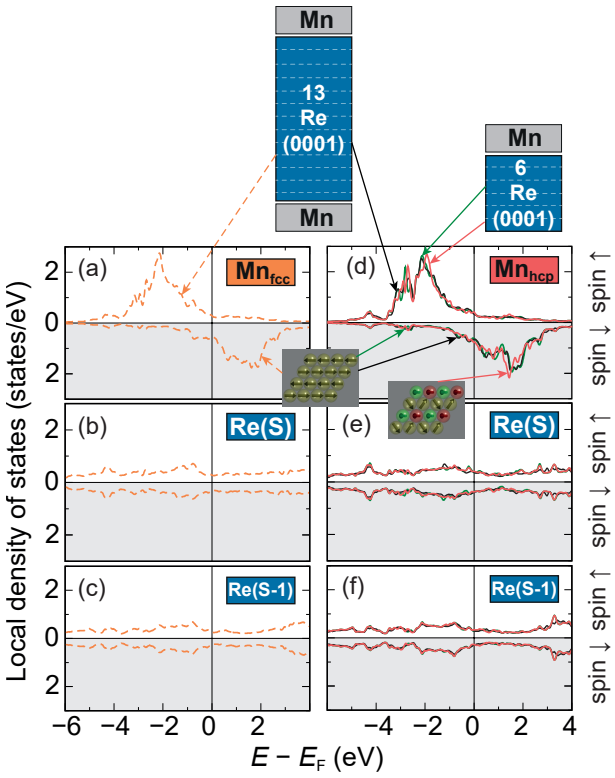

Figure 10.4 | Calculated local density of states (LDOS) for Mn/Re(0001). (a,b,c) LDOS in the row-wise antiferromagnetic (RW-AFM) state of Mn_{fcc}/Re(0001) obtained with a symmetric film with 13 layers of Re(0001) in between two Mn monolayers (MLs) (See sketch above the panels). (d,e,f) LDOS for Mn_{hcp}/Re(0001) for three calculations: the 3Q (red lines) and RW-AFM state (green lines) are calculated with an asymmetric film consisting of the Mn ML on top of a six layers Re(0001) substrate and of the RW-AFM state is calculated with the symmetric film consisting of 13 layers Re(0001) in between two Mn MLs (black lines) as in (a,b,c). Images of the spin structures by courtesy of André Kubetzka.

Due to the RW-AFM state, the induced magnetic moment of the substrate is expected to be small which is visible due to the almost perfectly symmetric shape of the Re(S) and Re(S-1) layer [Fig. 10.4 (b,c)]. However, the energy gain of a spin-polarized compared to a non-spin-polarized substrate in the RW-AFM state is about 3 meV/Mn atom[6] and

[6]This value has been obtained comparing two RW-AFM where for one the spin polarization in the Re substrate is allowed and for the other it is suppressed.

thus this small induced magnetic moment in Re(0001) can play an important role to form the magnetic ground state.

The LDOS for Mn_{hcp}/Re(0001) looks very similar to that one of the fcc stacking of Mn. This is expected since the deviation in the stacking will at first affect the subsurface layer of the substrate. For Mn_{hcp} three different kinds of calculations are compared. For a symmetric film with 13 layers of Re as shown in the sketch, the electronic structure can be seen as converged, but the computational effort for calculating a 3Q state in such a setup is too high. As for the energy dispersion $E(\mathbf{q})$ in Fig. 10.3, we calculated the 3Q state in an asymmetric film with six layers of Re(0001). To see whether the electronic structure is converged, we compare the RW-AFM state in this setup (green line) with that one of the symmetric film (black line). Despite minor deviations, both LDOS agree very well and the film setup with six layers are converged [Fig. 10.4 (d)].

The red line shows the LDOS of the 3Q state. For all presented layers, the electronic structure in the 3Q state is very similar to the one of the RW-AFM. Since the 3Q state is a superposition of three RW-AFM states, this is expected. The most important deviations between 3Q and 1Q state occur around the Fermi energy. At E_F, small peaks arise in the case of the 3Q state in both spin ↑ and spin ↓ channels which are absent in the RW-AFM state.

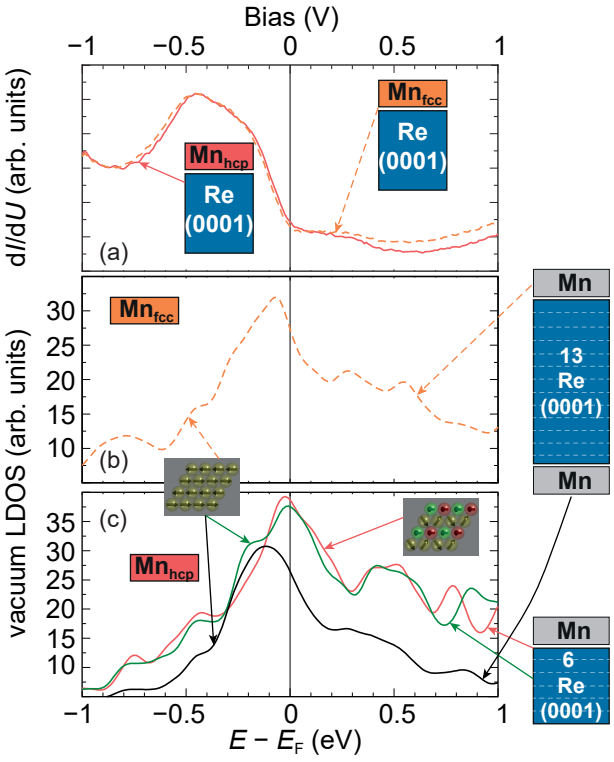

Figure 10.5 | Comparison of experimental dI/dU spectra with calculated vacuum local density of states (LDOS) for Mn/Re(0001). (a) Experimental dI/dU spectrum of the Mn monolayer (ML) on Re(0001) for both stackings. (b) Calculated vacuum LDOS in the row-wise antiferromagnetic (RW-AFM) for Mn_{fcc}/Re(0001) obtained with a symmetric film consisting of 13 layers of Re(0001) in between two Mn MLs (see sketch on the right). (c) Calculated vacuum LDOS for Mn_{hcp}/Re(0001) for three calculations: the 3Q (red lines) and RW-AFM state (green lines) are calculated with an asymmetric film consisting of the Mn ML on top of a six layers Re(0001) substrate and of the RW-AFM state is calculated with the symmetric film consisting of 13 layers Re(0001) in between two Mn MLs (black lines). The calculations are performed at 3 Å above the surface. Images of the spin structures by courtesy of André Kubetzka.

Furthermore, the minority spins in the unoccupied region slightly differs and the peaks are shifted to lower energies. These features can be decisive for the 3Q state being energetically favourable by small energy difference.

Comparing the experimentally measured dI/dU signal with the calculated vacuum LDOS, we can estimate how good the description of our films are with respect to the experimentally prepared sample. Fig. 10.5 shows this comparison with the same states we discussed in Fig. 10.4.

The dI/dU signal for both stackings of Mn shows one significant, broad peak below E_F without any other features [Fig. 10.5 (a)]. For the DFT calculations, similar results are obtained, whereas the peak positions occur closer to the Fermi energy [Fig. 10.5 (c,d)]. As in the experiment, the deviations between $\mathrm{Mn_{fcc}}$ and $\mathrm{Mn_{hcp}}$ are very small and we further observe that with a thicker substrate [black line in Fig. 10.5 (c)], the main peak shifts to lower energies. The theoretical description of the experimental dI/dU spectrum can be seen as good even though the small deviations can also manifest in small energy differences.

10.5 Coupling magnetic states to the lattice - anisotropic symmetric exchange

Previously we showed the complexity of finding the magnetic ground state of Mn/Re(0001) due to the frustration of the different HOIs. However, the considered interactions up to now cannot fully explain the coupling of spins to the atomic lattice. Note that in measurements on $\mathrm{Mn_{fcc}}$, three rotational domains of the RW-AFM state have been observed.

One possibility to mediate such a coupling is the dipolar interaction which is often neglected in ultra-thin films and AFM states. Such a simplification is reasonable for most of the systems since the energy contribution of the dipole-dipole interaction typically is too small to have decisive impact and can be effectively added to the MAE. The energy contribution can be estimated by taking the calculated magnetic moment into account (cf. Tab. 10.1) and thus, configurations with spin quantization axes parallel to the rows is preferred by about 0.14 meV/Mn atom.

Additionally, SOC will couple the spins to the magnetic rows. In this case, the ASE will lead to an energy gain for a particular arrangement of spins. We calculate the energy differences between different configurations where the spin quantization axis is rotated from $\phi = 0°$ to 90° so it is aligned in four high symmetry directions of the 2DBZ (Fig. 10.6 left panel).

For $\mathrm{Mn_{fcc}}$/Re(0001), we find an energy difference of about 0.1 meV/Mn atom which is mediated by the ASE. Both dipole-dipole interaction and ASE contribute on the same energy scale and try to align the spins to the atomic lattice as it is observed in the experiment.

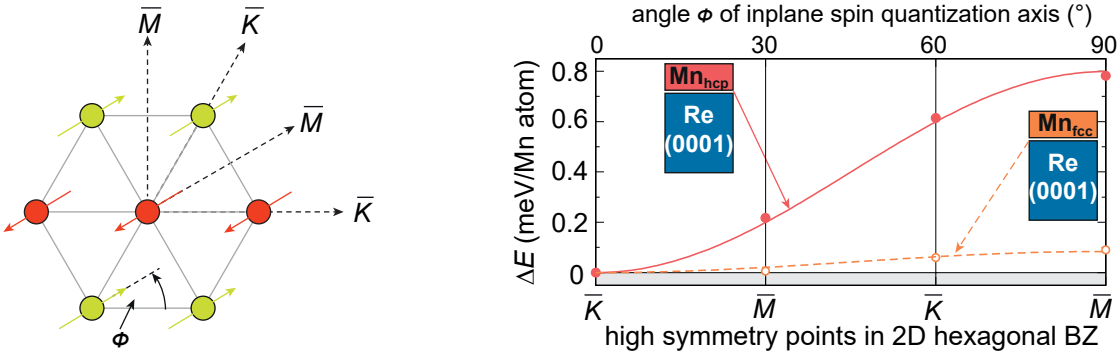

Figure 10.6 | Self-consistent calculations on in-plane rotation of spin-quantization axis for Mn/Re(0001). Left: Sketch of row-wise antiferromagnetic state applying different in-plane spin-quantization axes for anisotropic symmetric exchange (ASE) interaction. The angle ϕ denotes the orientation of spins w.r.t. the atomic lattice and is rotated from 0° to 90° to obtain the pseudo dipolar interaction on the right. Points show DFT calculated results whereas the lines are the fit to the ASE.

For completeness, we calculated the ASE for Mn_{hcp}/Re(0001). Taking the nearest neighbour into account, $J_1^{ASE} = 0.2\,meV$ the ASE is an order of magnitude larger than that one of Mn_{fcc}/Re(0001). In combination with the dipolar interaction, this would lead to a strong coupling between spins and lattice. However, the calculations are carried out in the collinear RW-AFM state where these interactions are the strongest. We want to investigate how the particular 3Q state from experiment looks like.

For a non-collinear spin structure such as the 3Q state, the dipole-dipole contribution reduces to 0.01 meV in order to distinguish between the three different 3Q orientations from Fig. 10.2. In the same way, the ASE favours a certain 3Q state by only 0.07 meV. Both contributions sum up to 0.08 meV to favour the prototypical 3Q state with its out-of-plane component over the 3Q with two in-plane components [Fig. 10.2 (a) and (c)]. Note that this only holds true if the 3Q states possesses a perfect tetrahedron angle between the spins. In the following, we will show that the ASE and dipolar interaction in Mn_{hcp}/Re(0001) are not strong enough to explain the experimental observation.

10.6 Conversion of Multi-Q states

As stated before, the magnetic ground state of Mn_{fcc} can clearly identified from experiments to be an in-plane RW-AFM state (cf. Sec. 10.1). Such a clear declaration is not possible for Mn_{hcp} since rotational domains occur as well, maybe mediated by SOC or by other interactions which are not yet considered. The question therefore remains how exactly such a 3Q state looks like and how it can be described. From a computational point of view, it is very demanding to cant spins out of a perfect state by angles of more than $\sim 1°$ using spin-orbit torques. Motivated by the experimentally proposed 3Q state, we consider the 3Q state with two spins lying completely in the plane [Fig. 10.7 (a)].

When the out-of-plane components of the red and green spins are rotated with the

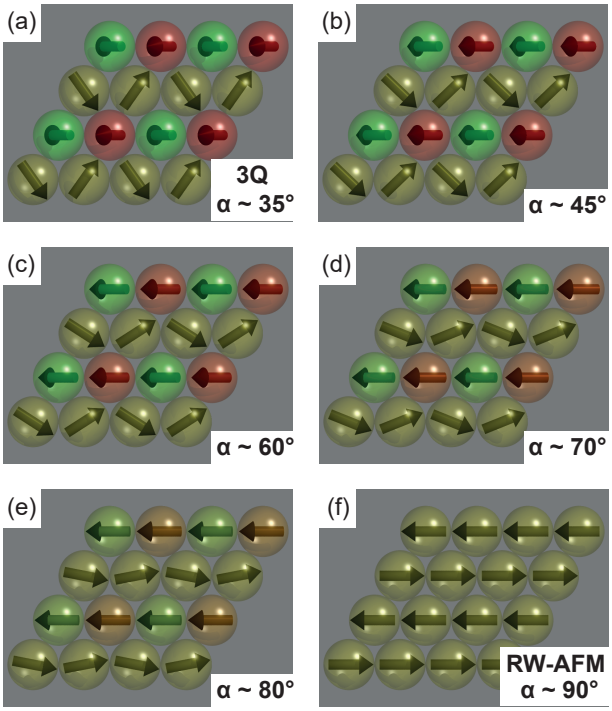

Figure 10.7 | Sketches of magnetic states upon converting a 3Q state into a 1Q state. Red coloured spins have an out-of-plane direction pointing towards the reader, green ones show a direction into the plane. Yellow spins have no out-of-plane component. (a) Rotated 3Q state with two spins in the plane. All spins in the unit cell are rotated with $\pm\alpha$ to reduce both the out-of-plane components of red and green spins parallel to the in-plane component of the yellow spins in order to achieve the in-plane row-wise antiferromagnetic state in (f). (b-e) are canted 3Q states on the path of this conversion. The rounded angles α are provided with respect to the 2Q state as it will be calculated below. Images by courtesy of André Kubetzka.

same angles as the yellow ones to align in one direction (b-e), the 3Q state can be continuously transformed into the RW-AFM state (f). A rotation of the spins in another direction would end up in the 2Q state. A similar path was suggested for three-dimensional (3D) systems in Ref. 186, where the authors explain the occurring energy dispersions with topological-chiral interactions.

The total energy on the whole path is calculated for an Mn UML with different in-plane lattice constants (Fig. 10.8). Even though the UML is assumed to be a simple model system, features are observed, which cannot be explained by state-of-the-art magnetic interactions and even by topological-chiral interactions from Ref. 186.

First, we compare the HOIs in Mn/Re(0001) with those in Mn/Cu(111) [182]. The energy dispersion with the same computational setup for the Mn UML as in Ref. 182 is shown in Fig. 10.8 (a). The energy difference between 3Q and RW-AFM states can be reproduced; however, we find a small energy minimum at the 2Q state (orange points in Fig. 10.8). Such an energy minimum was excluded in Ref. 182 due to symmetry arguments based on the biquadratic and 4-site 4-spin interaction which were the only HOIs taken into account. Therefore, the 2Q state was not considered in Ref. 182.

When slightly increasing the lattice constant of the Mn UML, the energy difference between 3Q state and RW-AFM vanishes while the 2Q state gains energy [green points in Fig. 10.8 (a)]. Now, a local minimum occurs which can be seen as distorted 3Q state. The in-plane lattice constant of Re(0001) is larger than that of Cu(111) and thus, the distance between the atoms in the Mn UML increases (blue points in Fig. 10.8). Compared to the Mn UML with experimental Cu(111) lattice, the 2Q state only gains about 4 meV/Mn atom, but the energy gain of the RW-AFM is by far larger

and more than 22 meV. This shows how sensitive the magnetic ground state of a Mn UML behaves with different lattice constants.

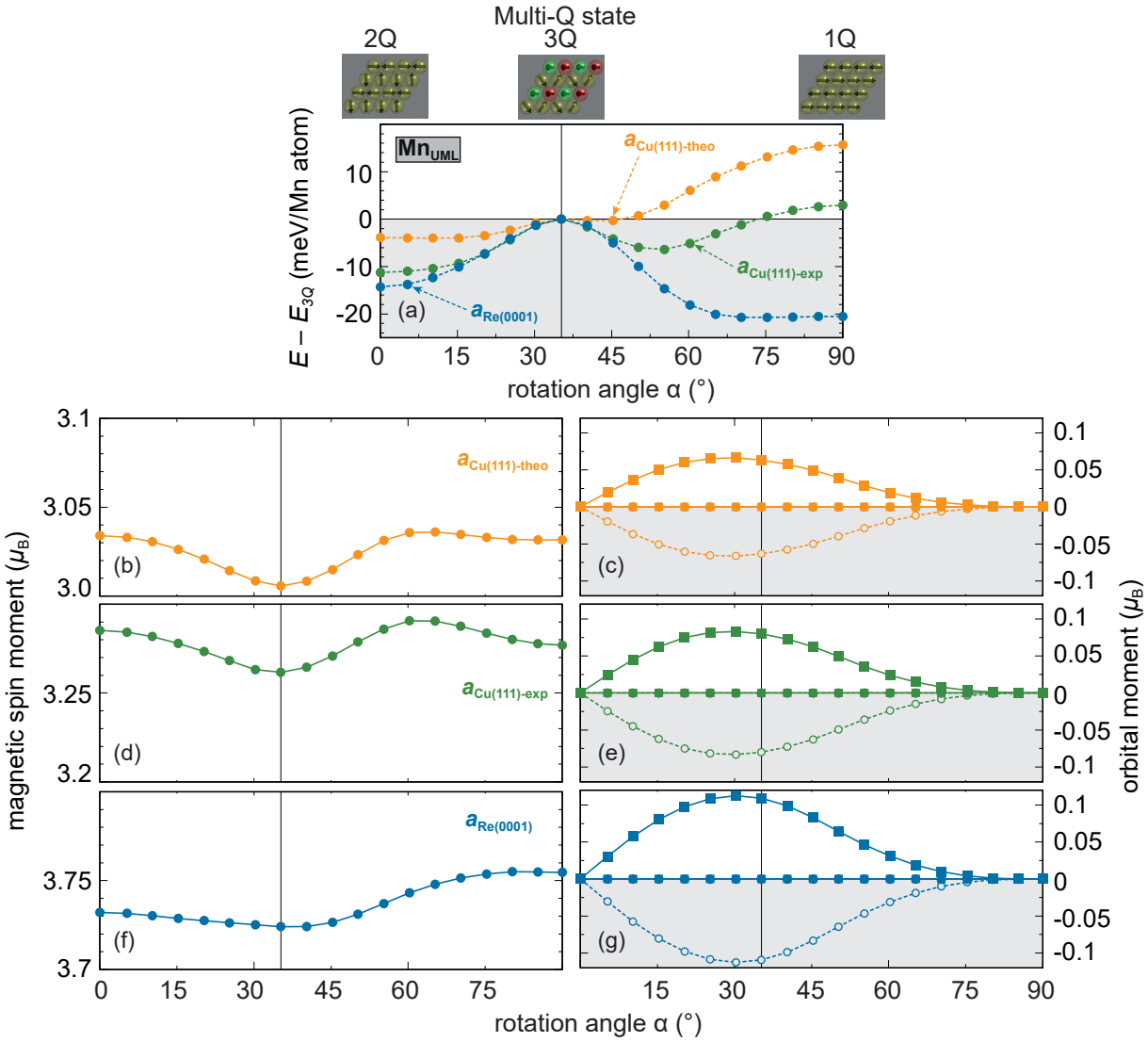

Figure 10.8 | DFT DFT results on the continuous transformation of multi-Q states in Mn unsupported monolayers. (a) Energy with respect to the 3Q state. (b,c) Magnetic and orbital moment for the Mn UML applying the theoretically obtained lattice constant of Cu(111), $a_{\text{Cu(111)-theo}} = 4.70\,\text{a.u.}$, respectively. (d,e) Magnetic and orbital moment for the Mn UML with an experimental lattice constant of Cu(111), $a_{\text{Cu(111)-exp}} = 4.75\,\text{a.u.}$. (f,g) Magnetic and orbital moment for the Mn UML with the Re(0001) lattice constant used for the film system, $a_{\text{Re(0001)}} = 5.42\,\text{a.u.}$ The spins are successively rotated from 3Q into 2Q and into the RW-AFM state as presented in the insets and according to Fig. 10.7. Note that the four curves for the orbital moments represent the four spins in the unit cell (the orbital moments of two spins are constantly 0) and the sum of all orbital moments in one layer of each state vanishes completely. For further details, see text and Sec. 10.2. All lines serve as guide for the eye. Images of the spin structures by courtesy of André Kubetzka.

We compare the behaviour of magnetic spin moments (Fig. 10.8 left panels) and orbital moments (Fig. 10.8 right panels) of the Mn UMLs to gain more insight into driving mechanisms of the energy dispersions. The variation of both magnetic and orbital moment is small, where an increase of the mean moments for the different UMLs is stemming from an increased nearest neighbour distance a_{NN} due to the reduced hybridization. It is according to the Stoner criterion [92].

The magnetic moment exhibits minima in the 3Q state for every dispersion [Fig. 10.8 (b,d,f)]. In the case of the Mn UMLs with experimental Cu(111) and Re(0001) lattice constant [Fig. 10.8 (d,f)], the increasing and decreasing magnetic moments correspond with the energy gain and loss in (a), respectively. However, this trend is not observed for the Mn UML at $a_{\mathrm{Cu(111)\text{-}theo}}$. The orbital moment for the 2Q and 1Q states are vanishing in each spin, whereas in the 3Q state, it is close to the maximum [Fig. 10.8 (c,e,g)] and the shape of the curves is perfectly symmetric. From both magnetic spin and orbital moment, we do not observe clear features which can explain the exhibited total energy dispersions for the 2Q-3Q-1Q transformation. Furthermore, since the complex behaviour of the total energy arise in the absence of SOC, HOIs which are beyond the previously known could give information on the obtained results.

Comparing the energy difference $\Delta E_{\overline{M}}^{3\mathrm{Q}}$ (cf. Tab. 10.3) with the energy difference for the Mn UML on the lattice constant of Re(0001) [cf. Fig. 10.8 (a)], a large discrepancy is observed. The presence of Re(0001) reduces the energy from 21 meV/Mn atom to −0.4 meV/Mn atom for $\mathrm{Mn_{hcp}}$ and −0.7 meV/Mn atom for $\mathrm{Mn_{fcc}}$. This is in stark contrast to the study on Mn/Cu(111), where for film and UML this energy difference varies only slightly [182] and emphasizes the importance of the hybridization between Mn and Re(0001) for the formation of the magnetic ground state.

Therefore, the energy dispersion due to the transformation of 2Q to 3Q to 1Q state from Fig. 10.8 will look very different. The result for the film system is presented in Fig. 10.9, where for completeness the fcc stacking of Mn is also presented. For both films, the total energy range is lower than 4 meV/Mn atom and the curves show energy maxima in the RW-AFM state whereas a local minimum for the 2Q states is exhibited. Contrary to the Mn UML of Fig. 10.8 is the gradient of the curves at the 2Q and 3Q states. While for the UML the gradients of the curves at the 2Q and 3Q states vanish

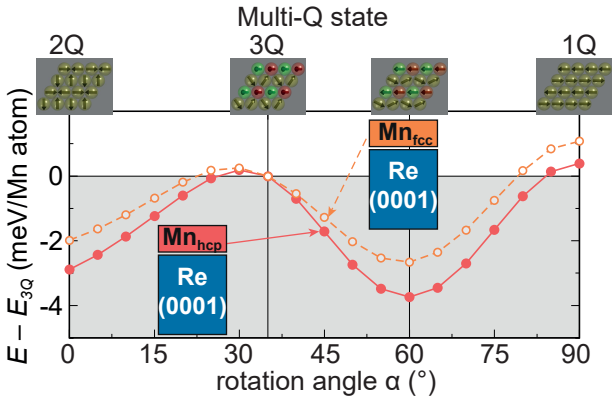

Figure 10.9 | DFT calculated total energy differences for the continuous transformation of multi-Q states in Mn/Re(0001). The spins are successively rotated from 3Q into 2Q and into the row-wise antiferromagnetic state as presented in the insets and according to Fig. 10.7. The lines serve as guide for the eye. Images of the spin structures by courtesy of André Kubetzka.

[cf. Fig. 10.8 (a)], this is not the case for the Mn/Re(0001) film system. So far, there is no explanation for such a behaviour.

As it has been shown previously, the RW-AFM and 3Q states can be considered as energetically degenerate within our DFT accuracy (cf. Sec. 10.3). However, a distortion of the 3Q state with a rotation of about 20° gains up to 4 meV/Mn atom. A similar result has been obtained with DFT calculations by S. Haldar using the VASP code. The same observation is made for Mn_{fcc}/Re(0001). For the latter, experiments revealed a RW-AFM ground state. As stated before, it is not a priori clear what kind of higher order exchange interaction can explain the presented DFT results. Promising candidates are sixth order terms such as the bicubic interaction which can appear for systems with $S = 3/2$ (i.e. $\mu \approx 3\,\mu_B$) [110].

Test calculations carried out with different spin polarization of the Re(0001) substrate[7] can affect the energies in a way that a 2Q state is preferred over the distorted 3Q state. Taking this effect into account, we want to see whether the Stoner energy can explain the theoretically predicted ground state for Mn_{hcp}/Re(0001). Fig. 10.10 presents the change of the magnetic moment (left panels) for each layer in the film. The states are fully converged, so that the moment of every atom in the unit cell has the same magnitude.

All changes of magnetic moments are on a very small scale, around $10^{-3}\,\mu_B$ which are an order of magnitude smaller than for the Mn UML. For the Mn layer, the smallest magnetic moment is observed in the 3Q state from where it increases monotonically [Fig. 10.10 (a)]. The Mn layer in the 2Q state has the largest spin moment, but around the energy minimum we do not observe any noticeable differences. The induced magnetic moment of the Re(0001) surface layer [Re(S), Fig. 10.10 (c)] shows a qualitatively similar behaviour to the energy dispersion; however, the spin moment is larger for the 2Q state than for the canted 3Q state.

Similar trends are observed for all other layers, i.e. we cannot see a deviation that would explain an energy minimum of the canted 3Q state over the 2Q state by only taking the Stoner energy into account. We further investigate the topological orbital moment (TOM) (right panels of Fig. 10.10) since it appeared to be crucial for 3D systems with similar energy paths [186] and can appear from non-collinearity in spin structures in the absence of SOC [183, 185]. For every spin in the unit cell, the TOM is slightly different, but their sum will always vanish. In the film system, the orbital moments do not vanish in the 2Q and 1Q state as in the Mn UML and also there is no symmetric behaviour. As for the magnetic spin moment, the changes of TOM are very small and we do not observe any features that are prominent to favour a canted 3Q state. Note that the TOM vanishes for the Re layers in the middle of the substrate [Re(S-1), Re(S-2), Re(S-3) in Fig. 10.10 (f,h,j)], but their contribution rises at the

[7] The Re(0001) moments are not canted according to the Mn surface layer, but have collinear out-of-plane direction. Typically the deviation with calculations where the Re(0001) moments are canted w.r.t. the Mn surface layer are very small, but here they can change the qualitative trends.

bottom [Re(S-4), Re(B) in Fig. 10.10 (l,n)] due to the vacuum boundary.

From our investigation, we cannot impeccably explain the energy minima of a distorted 3Q state in the DFT calculations for both stackings of Mn/Re(0001). The state-of-the-art magnetic spin models come to the limits explaining these energy dispersions and therefore the analysis is not finalized yet. HOIs that occur in sixth order perturbation of the Hubbard model for $S = 3/2$ particles, such as bicubic terms might describe the DFT results, but so far, these have not yet been studied in models. Also it is not clear by DFT calculations, why experiments reveal the RW-AFM state for Mn_{fcc} and the 3Q state for Mn_{hcp}. However, taking all our tests into account it is not surprising that different relaxations, *xc* potentials and layer thicknesses will affect the DFT predictions on the same energy scale.

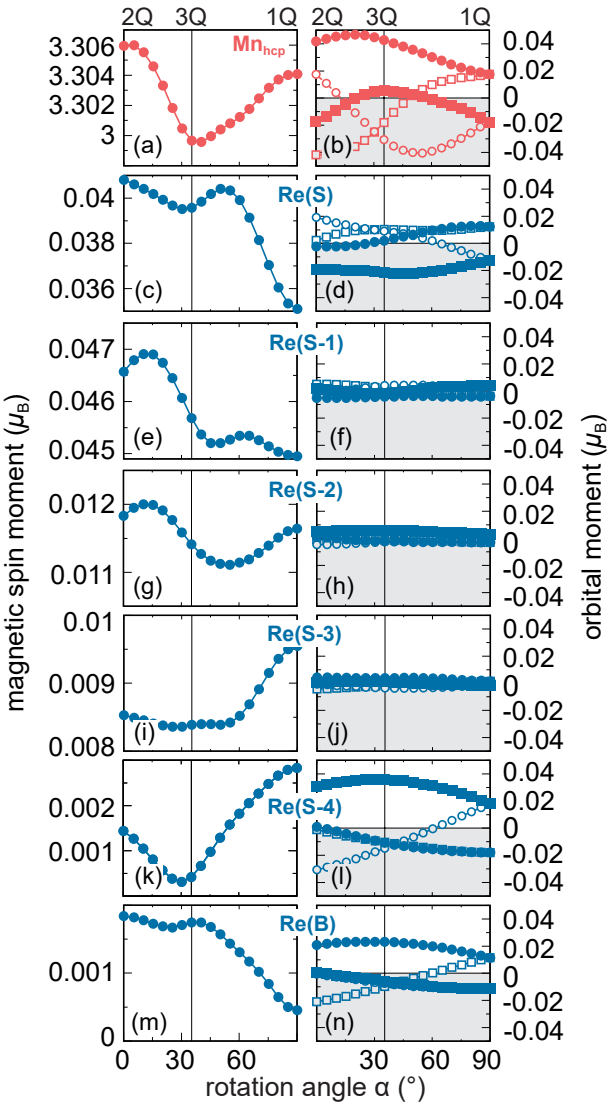

Figure 10.10 | DFT calculated change of magnetic spin moment and orbital moment for the continuous transformation of multi-Q states in Mn_{hcp}/Re(0001). The left row shows the magnetic spin moments (in μ_B) of all layers and the right row the orbital moments (in μ_B). (a,b) Mn_{hcp} layer. (c,d) Re(0001) surface layer denoted as Re(S). (e,f) Re(0001) subsurface layer denoted as Re(S-1). (g,h) Re(S-2). (i,j) Re(S-3). (k,l) Re(S-4). (m,n) Bottom layer of the Re(0001) film denoted as Re(B). Note that the four curves for the orbital moments represent the four spins in the unit cell and the sum of all orbital moments in one layer of each state vanishes completely. All calculations are done neglecting spin-orbit coupling and the orbital moment only arises due to the canting of the moments.

10.7 Conclusion

In this chapter, we analyse and explain the experimental observation of the RW-AFM and the 3Q state in both fcc and hcp stacking of a Mn ML on the Re(0001) surface, respectively. Although a large DMI has been predicted based on DFT in Mn/Re(0001) [187], our DFT calculations show negligible DMI contributions around the magnetic ground states.

Among all spin spiral (single-Q) states for both fcc and hcp Mn, the RW-AFM is the lowest in energy – driven by frustration of the Heisenberg exchange interaction. The occurring HOIs show a large energy contribution, where strong frustration of HOIs results in very small energy differences between RW-AFM and 3Q states which are obtained by DFT. In Mn/Re(0001), small distortions can prefer one state over the other.

For Mn_{fcc} we find that the dipolar in combination with the ASE interaction aligns the spins along the magnetic rows, whereas for different 3Q states in Mn_{hcp}/Re(0001) both interactions are comparably small to prefer a distinct 3Q state. Based on DFT, the experimentally observed 3Q state in Mn_{hcp} could show a distortion towards the RW-AFM state, which is found as an energy minimum by transforming the 3Q state into the RW-AFM state. Up to now this finding cannot be explained by state-of-the-art magnetic spin models, but HOIs in sixth order perturbation from the Hubbard model for $S = 3/2$ particles [110] which are not yet included in spin models might explain the obtained DFT results.

Chapter 11

Summary

In this thesis, density functional theory (DFT) calculations based on the full potential linearized augmented planewave method were performed to study complex collinear and non-collinear spin structures in ultrathin Co and Mn films. The magnetism in the systems is driven by strong frustration of magnetic interactions which are obtained by mapping total energy calculations on an atomistic spin model. The results are used in spindynamics simulations to analyse the magnetic properties of non-collinear spin structures such as domain walls (DWs), skyrmions and antiskyrmions. The calculations in this work are compared to spin-polarized scanning tunnelling microscopy (SP-STM) measurements from experimental collaborators and demonstrate how the synergy of experiment and theory is used to understand complex magnetic structures.

Triggered by the prominent Pt/Co/Ir interfaces for which additive Dzyaloshinskii-Moriya interaction (DMI) effects are predicted in multilayer films [35, 36], the DMI is studied in pseudomorphic Co monolayers (MLs) and Pt/Co bilayers (BLs) on Ir(111). It is pointed out that a DMI enhancement from Co/Ir(111) to Pt/Co/Ir(111) does not occur due to additive effects when a Co ML is sandwiched between Pt and Ir. On the contrary, the DMI is completely driven by either the Pt/Co or the Co/Ir interface and is strongly dependent on the stacking of the Pt/Co BL. For a Co double layer between both Pt and Ir(111) on the other hand, the additive effects can be confirmed emphasizing the importance of interlayer hybridization effects and Co film thickness on the DMI in magnetic films. SP-STM experiments from the group of Prof. Wiesendanger (University of Hamburg) on DWs in the films are in good agreement with the calculations and support our results (Pub. I).

The DMI further is found to be more complex in these transition metal interfaces and the occurrence of DMI frustration is explained – an effect which so far has been neglected in the field. Hybridization and spin mixing at the Co/Ir interface lead to a dependence of the rotational sense on the spin spiral period and a sign change of the DMI. When DFT calculations on this interaction are carried out for unsuitable spin spiral states, wrong predictions on both strength and sign are the consequences.

While for Fe it has been shown that the magnetic phase space in ultrathin films is very large, Co is assumed to behave more resistant to hybridization with different elements. However, we demonstrate that the nearest neighbour exchange interaction of Co/Ir(111) can be varied from weakly ferromagnetic (FM) to strongly FM when filling the d band of an additional 4d layer ranging from Tc, Ru, Rh to Pd. When

Ir(111) is replaced by its 4*d* equivalent Rh(111), we observe equivalent trends on the exchange, but all spin-orbit coupling (SOC) dependent quantities – DMI and magnetocrystalline anisotropy energy (MAE) – are reduced due to the smaller SOC constant of Rh. The study provides a strategy to control the magnetic interactions in magnetic films.

From this analysis, Rh/Co/Ir(111) shows an extraordinarily flat energy dispersion of spin spirals around the FM state. A canting of spins of up to 20° does not cost energy. At the same time, antiferromagnetic (AFM) states are high in energy and thus, both features indicate exceptionally large exchange frustration for a Co film. Taking strong out-of-plane MAE and moderate DMI into account, Rh/Co/Ir(111) can be seen as a prototypical film where skyrmions on the scale of 3 – 4 nm can be stable even in the absence of an external magnetic field. This is demonstrated by atomistic spindynamics simulations based on the DFT calculations. Indeed, measurements from our experimental colleagues in Hamburg confirmed this prediction in Rh_{hcp}/Co/Ir(111) (Fig. 11.1). It is the first time that nm-sized skyrmions are stable in the virgin state without applying a magnetic field (Pub. II).

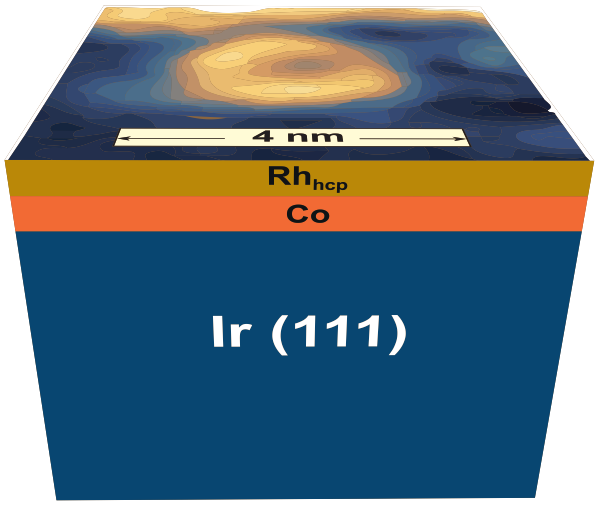

Figure 11.1 | Scanning tunnelling microscopy image of a skyrmion in Rh_{hcp}/Co/Ir(111) without magnetic field. Differential conductance map where the object is visible due to the non-collinear magnetoresistance contrast. Scan parameters: Cr-bulk tip, $U = -250\,\mathrm{mV}$, $I = 800\,\mathrm{pA}$, $B = 0\,\mathrm{T}$, $T = 4.2\,\mathrm{K}$. The experimental figure has been adapted from Pub. II.

We further predict more complex spin structures such as antiskyrmions to be metastable states in this film system. The energy barrier protecting the (anti-) skyrmions from vanishing into the FM ground state is very large. For small magnetic fields, the radial symmetric collapse mechanism which is commonly assumed based on simulations [134, 153] becomes unfavourable and a novel transition via a chimera skyrmion state is found (Fig. 11.2). This collapse could be observed in very recent experiments on Pd/Fe/Ir(111) [191].

In order to read out skyrmions or DWs for potential spintronic applications, it is envisioned to not only rely on magnetic detection techniques [34]. In Rh/Co/Ir(111), we find a large non-collinear magnetoresistance of about 20 %. This effect has been discovered for an Fe ML for skyrmions at large bias voltages [147, 148]. Here, it occurs at the Fermi energy and in Co – a material which is widely used in applications. This allows for the detection of both skyrmions and DWs in tunnel

junctions with non-magnetic tips (Fig. 11.1). Based on both DFT and a simplified tight binding model we explain the effect by spin mixing of a minority p_z and a majority d_{xz} state (Pub. III).

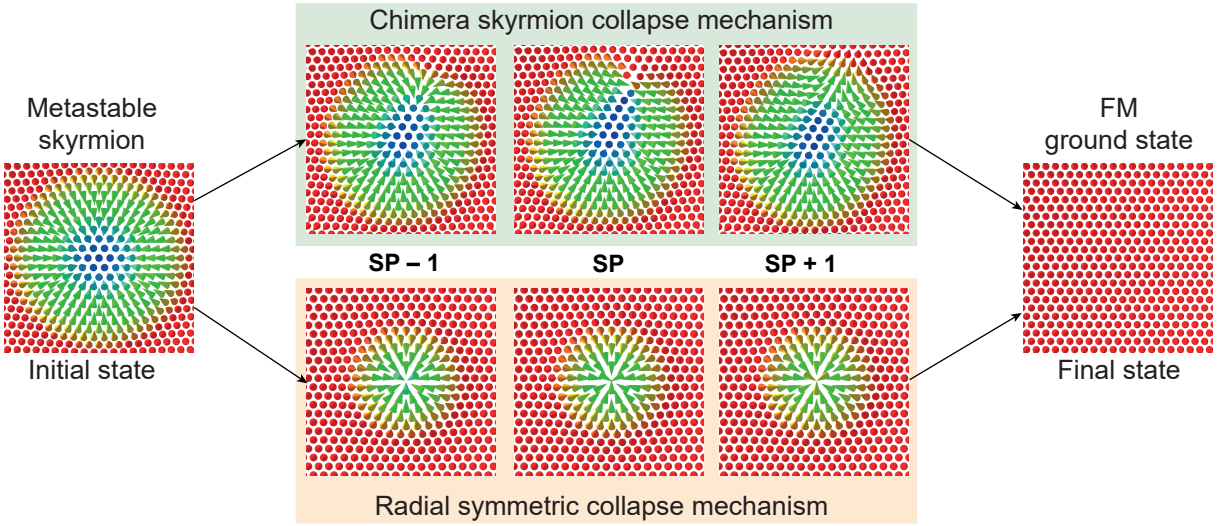

Figure 11.2 | Collapse mechanisms of a single skyrmion into the ferromagnetic (FM) state for Rh_{hcp}/Co/Ir(111). The transition from a metastable skyrmion (initial state, left sketch) into the FM ground state (final state, right sketch) can take place via two collapse mechanisms which are shown in the middle. the colours show the magnetic moments of the Co atoms and denote the out-of-plane magnetization direction (red upwards, blue downwards). In the chimera skyrmion collapse (upper sketches), the skyrmion deforms at the right top (SP-1 structure) and transforms into the chimera skyrmion at SP+1 with a topological charge of 0. The lower panels show the radial symmetric collapse mechanism where the skyrmion shrinks in size and at the saddle point (SP), three centred spins point towards each other and tilt out of the plane at SP+1. For details see Sec. 8.7.

Regardless of the complexity of the systems above, their magnetic ground state is FM. AFM systems have recently attracted a lot of attention because they are predicted to have superior properties for spintronic applications [5, 6, 161, 162, 192]. Mn is a prototypical AFM material that holds a wide spectrum of both structural and magnetic properties.

We revisit the magnetism of Mn/Mn/W(001) for which a FM ground state was predicted based on previous DFT calculations [172]. However, experiments from the group of Prof. Bode (University of Würzburg) revealed a collinear checkerboard $c(2\times2)$ AFM ground state. This ground state is confirmed by our DFT calculations, but surprisingly, only coincides with the Mn subsurface layer fully losing its magnetic moment – a so-called dead magnetic layer (DML). The concept of DMLs was frequently claimed to occur in the past [173–176], but could always be disproven so far [177, 178].

Here, the strong hybridization with the W(001) surface in combination with the frustration due to the symmetric AFM state from the Mn top layer fully quenches the magnetic moment of the Mn subsurface layer. The excellent agreement between

SP-STM measurements and simulations based on DFT calculations verify the occurrence of a DML (Fig. 11.3) and further allow for imaging the dead magnetic subsurface Mn atoms (Pub. IV).

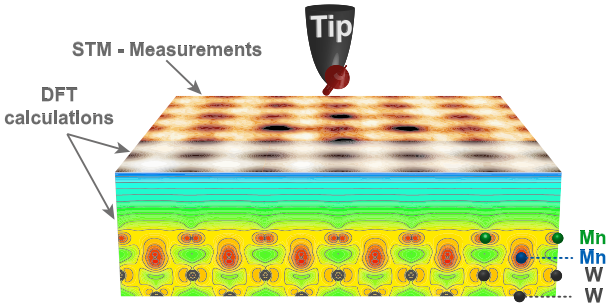

Figure 11.3 | Combined measured and calculated spin-polarized scanning tunnelling microscopy (SP-STM) image of the $c(2 \times 2)$ antiferromagnetic state for Mn/Mn/W(001). The background shows the measured SP-STM images with positive perpendicular tip magnetization. The SP-STM simulations with assumed tip spin polarization of 0.5 in the are performed according to Fig. 9.5 with the cross-section plots through up and down channels of the charge density at [E_F, E_F + 0.01 eV]. Scan parameters: $U = +10\,\mathrm{mV}$, $I = 3\,\mathrm{nA}$.

About 20 years ago, a ML of Mn on Cu(111) has been predicted to exhibit a three-dimensional 3Q state based on DFT calculations [49]. The 3Q state is a superposition of three row-wise antiferromagnetic (RW-AFM) states [Fig. 11.4 (a,b)]. Both states have been studied theoretically [49, 50, 189], but could not be observed experimentally before.

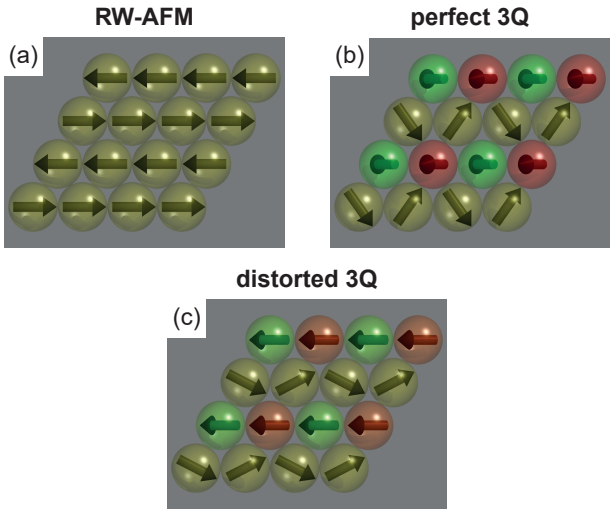

Figure 11.4 | Magnetic states in Mn/Re(0001). (a) Row-wise antiferromagnetic (RW-AFM) state which is observed in Mn_{fcc}/Re(0001). (b) Perfect 3Q state which can be constructed by a superposition of three RW-AFM states. The angle between adjacent spins is the tetrahedron angle ($\sim 109°$). (c) Distorted 3Q state suggested as magnetic ground state for Mn_{hcp}/Re(0001). The colours denote the out-of-plane spin component (red upwards, green downwards). Images by courtesy of André Kubetzka (University of Hamburg).

Recently, SP-STM experiments performed in the group of Prof. Wiesendanger (University of Hamburg) verified the existence of the RW-AFM and the 3Q state in fcc and hcp stacking of a Mn ML on Re(0001), respectively. Based on DFT, we show in this thesis that the hybridization between Mn and the Re(0001) surface plays a decisive role resulting in both degeneracy of the two magnetic states and large competing higher order exchange interactions (HOIs). The experimentally observed coupling of the AFM rows in Mn_{fcc} to the underlying lattice can be explained by the

addition of the dipolar interaction and the anisotropic symmetric exchange (ASE) (Pub. V).

However, for the experimentally proposed 3Q state in Mn_{hcp}/Re(0001), the coupling due to dipole-dipole interaction and ASE to prefer a distinct 3Q state over another is too weak. DFT calculations presented here suggest a distorted 3Q state as a possible ground state [Fig. 11.4 (c)]. It appears due to an in-plane canting of the 3Q state in the direction of the RW-AFM state[1] in calculations without SOC. Therefore, it could be driven by HOIs beyond those which are considered so far.

In conclusion, DFT calculations are performed to study complex spin structures where the combined approach with subsequent spindynamics simulations serves as a powerful tool to understand, explain and predict complex magnetism in ultrathin films. Ultrathin films are best suited comparing theory with experimental SP-STM measurements due to their film quality and the resulting well defined interfaces. The agreement between theory and experiment can be used e.g. to verify complex interfacial phenomena as it has been shown for the DML in Mn/Mn/W(001). It further provides deep understanding of occurring non-collinear structures such as DWs and skyrmions as it has been demonstrated for Rh/Co/Ir(111). For the highly complex example of Mn/Re(0001), the experimental observations triggered the addition of typically underestimated interactions in the applied spin model where still, a distorted 3Q state is desired to be explained based on interactions beyond the previously known.

[1] Similar DFT results have been obtained by S. Haldar using the code VASP.

Bibliography

[1] S. S. P. Parkin, M. Hayashi, and L. Thomas, *Magnetic Domain-Wall Racetrack Memory*, Science **320**, 190 (2008).

[2] N. S. Kiselev, a. N. Bogdanov, R. Schäfer, and U. K. Rößler, *Chiral skyrmions in thin magnetic films: new objects for magnetic storage technologies?*, Journal of Physics D: Applied Physics **44**, 392001 (2011).

[3] A. Fert, V. Cros, and J. Sampaio, *Skyrmions on the track*, Nature Nanotechnology **8**, 152 (2013).

[4] S. Parkin and S.-H. Yang, *Memory on the racetrack*, Nature Nanotechnology **10**, 195 (2015).

[5] T. Jungwirth, X. Marti, P. Wadley, and J. Wunderlich, *Antiferromagnetic spintronics*, Nature Nanotechnology **11**, 231 (2016).

[6] M. B. Jungfleisch, W. Zhang, and A. Hoffmann, *Perspectives of antiferromagnetic spintronics*, Physics Letters A **382**, 865 (2018).

[7] F. Büttner, I. Lemesh, and G. S. D. Beach, *Theory of isolated magnetic skyrmions: From fundamentals to room temperature applications*, Scientific Reports **8**, 4464 (2018).

[8] R. Wiesendanger, *Nanoscale magnetic skyrmions in metallic films and multilayers: a new twist for spintronics*, Nature Reviews Materials **1**, 16044 (2016).

[9] J. Grollier, D. Querlioz, K. Y. Camsari, K. Everschor-Sitte, S. Fukami, and M. D. Stiles, *Neuromorphic spintronics*, Nature Electronics , 1 (2020).

[10] A. Thiaville, S. Rohart, É. Jué, V. Cros, and A. Fert, *Dynamics of Dzyaloshinskii domain walls in ultrathin magnetic films*, EPL (Europhysics Letters) **100**, 57002 (2012).

[11] D. Claudio-Gonzalez, A. Thiaville, and J. Miltat, *Domain Wall Dynamics under Nonlocal Spin-Transfer Torque*, Physical Review Letters **108**, 227208 (2012).

[12] I. Mihai Miron, G. Gaudin, S. Auffret, B. Rodmacq, A. Schuhl, S. Pizzini, J. Vogel, and P. Gambardella, *Current-driven spin torque induced by the Rashba effect in a ferromagnetic metal layer*, Nature Materials **9**, 230 (2010).

[13] D. Bhowmik, L. You, and S. Salahuddin, *Spin Hall effect clocking of nanomagnetic logic without a magnetic field*, Nature Nanotechnology **9**, 59 (2014).

[14] S. Emori, U. Bauer, S.-M. Ahn, E. Martinez, and G. S. D. Beach, *Current-driven dynamics of chiral ferromagnetic domain walls*, Nature Materials **12**, 611 (2013).

[15] P. P. J. Haazen, E. Murè, J. H. Franken, R. Lavrijsen, H. J. M. Swagten, and B. Koopmans, *Domain wall depinning governed by the spin Hall effect*, Nature Materials **12**, 299 (2013).

[16] A. Hrabec, V. Křižáková, S. Pizzini, J. Sampaio, A. Thiaville, S. Rohart, and J. Vogel, *Velocity Enhancement by Synchronization of Magnetic Domain Walls*, Physical Review Letters **120**, 227204 (2018).

[17] J. Cao, Y. Chen, T. Jin, W. Gan, Y. Wang, Y. Zheng, H. Lv, S. Cardoso, D. Wei, and W. S. Lew, *Spin orbit torques induced magnetization reversal through asymmetric domain wall propagation in Ta/CoFeB/MgO structures*, Scientific Reports **8**, 1355 (2018).

[18] O. Alejos, V. Raposo, L. Sanchez-Tejerina, and E. Martinez, *Efficient and controlled domain wall nucleation for magnetic shift registers*, Scientific Reports **7**, 11909 (2017).

[19] A. van den Brink, S. Cosemans, S. Cornelissen, M. Manfrini, A. Vaysset, W. Van Roy, T. Min, H. J. M. Swagten, and B. Koopmans, *Spin-Hall-assisted magnetic random access memory*, Applied Physics Letters **104**, 012403 (2014).

[20] W. Zhao, Y. Zhang, T. Devolder, J. Klein, D. Ravelosona, C. Chappert, and P. Mazoyer, *Failure and reliability analysis of STT-MRAM*, Microelectronics Reliability **52**, 1848 (2012).

[21] P. Lai, G. P. Zhao, H. Tang, N. Ran, S. Q. Wu, J. Xia, X. Zhang, and Y. Zhou, *An Improved Racetrack Structure for Transporting a Skyrmion*, Scientific Reports **7**, 45330 (2017).

[22] D. Zhu, W. Kang, S. Li, Y. Huang, X. Zhang, Y. Zhou, and W. Zhao, *Skyrmion Racetrack Memory With Random Information Update/Deletion/Insertion*, IEEE Transactions on Electron Devices **65**, 87 (2018).

[23] W. Koshibae, Y. Kaneko, J. Iwasaki, M. Kawasaki, Y. Tokura, and N. Nagaosa, *Memory functions of magnetic skyrmions*, Japanese Journal of Applied Physics **54**, 053001 (2015).

[24] A. Bogdanov and D. Yablonskii, *Thermodynamically stable "vortices" in magnetically ordered crystals. The mixed state of magnets*, Zh. Eksp. Teor. Fiz **95**, 178 (1989).

[25] A. Bogdanov and A. Hubert, *Thermodynamically stable magnetic vortex states in magnetic crystals*, Journal of Magnetism and Magnetic Materials **138**, 255 (1994).

[26] S. Mühlbauer, B. Binz, F. Jonietz, C. Pfleiderer, A. Rosch, A. Neubauer, R. Georgii, and P. Boni, *Skyrmion Lattice in a Chiral Magnet*, Science **323**, 915 (2009).

[27] W. Münzer, A. Neubauer, T. Adams, S. Mühlbauer, C. Franz, F. Jonietz, R. Georgii, P. Böni, B. Pedersen, M. Schmidt, A. Rosch, and C. Pfleiderer, *Skyrmion lattice in the doped semiconductor $Fe_{1-x}Co_xSi$*, Physical Review B **81**, 041203 (2010).

[28] X. Z. Yu, Y. Onose, N. Kanazawa, J. H. Park, J. H. Han, Y. Matsui, N. Nagaosa, and Y. Tokura, *Real-space observation of a two-dimensional skyrmion crystal*, Nature **465**, 901 (2010).

[29] S. Heinze, K. von Bergmann, M. Menzel, J. Brede, A. Kubetzka, R. Wiesendanger, G. Bihlmayer, and S. Blügel, *Spontaneous atomic-scale magnetic skyrmion lattice in two dimensions*, Nature Physics **7**, 713 (2011).

[30] X. Z. Yu, N. Kanazawa, Y. Onose, K. Kimoto, W. Z. Zhang, S. Ishiwata, Y. Matsui, and Y. Tokura, *Near room-temperature formation of a skyrmion crystal in thin-films of the helimagnet FeGe*, Nature Materials **10**, 106 (2011).

[31] N. Romming, C. Hanneken, M. Menzel, J. E. Bickel, B. Wolter, K. von Bergmann, A. Kubetzka, and R. Wiesendanger, *Writing and Deleting Single Magnetic Skyrmions*, Science **341**, 636 (2013).

[32] N. Nagaosa and Y. Tokura, *Topological properties and dynamics of magnetic skyrmions*, Nature Nanotechnology **8**, 899 (2013).

[33] W. Jiang, G. Chen, K. Liu, J. Zang, S. G. te Velthuis, and A. Hoffmann, *Skyrmions in magnetic multilayers*, Physics Reports **704**, 1 (2017).

[34] T. L. Monchesky, *Detection with unpolarized currents*, Nature Nanotechnology **10**, 1008 (2015).

[35] C. Moreau-Luchaire, C. Moutafis, N. Reyren, J. Sampaio, C. A. F. Vaz, N. Van Horne, K. Bouzehouane, K. Garcia, C. Deranlot, P. Warnicke, P. Wohlhüter, J.-M. George, M. Weigand, J. Raabe, V. Cros, and A. Fert, *Additive interfacial chiral interaction in multilayers for stabilization of small individual skyrmions at room temperature*, Nature Nanotechnology **11**, 444 (2016).

[36] A. Soumyanarayanan, M. Raju, A. L. Gonzalez Oyarce, A. K. C. Tan, M.-Y. Im, A. P. Petrović, P. Ho, K. H. Khoo, M. Tran, C. K. Gan, F. Ernult, and C. Panagopoulos, *Tunable room-temperature magnetic skyrmions in Ir/Fe/Co/Pt multilayers*, Nature Materials **16**, 898 (2017).

[37] S. D. Pollard, J. A. Garlow, J. Yu, Z. Wang, Y. Zhu, and H. Yang, *Observation of stable Néel skyrmions in cobalt/palladium multilayers with Lorentz transmission electron microscopy*, Nature Communications **8**, 14761 (2017).

[38] O. Boulle, J. Vogel, H. Yang, S. Pizzini, D. de Souza Chaves, A. Locatelli, T. O. Mente, A. Sala, L. D. Buda-Prejbeanu, O. Klein, M. Belmeguenai, Y. Roussigné, A. Stashkevich, S. M. Chérif, L. Aballe, M. Foerster, M. Chshiev, S. Auffret, I. M. Miron, and G. Gaudin, *Room-temperature chiral magnetic skyrmions in ultrathin magnetic nanostructures*, Nature Nanotechnology **11**, 449 (2016).

[39] P. Ho, A. K. Tan, S. Goolaup, A. G. Oyarce, M. Raju, L. Huang, A. Soumyanarayanan, and C. Panagopoulos, *Geometrically Tailored Skyrmions at Zero Magnetic Field in Multilayered Nanostructures*, Physical Review Applied **11**, 024064 (2019).

[40] L. Caretta, M. Mann, F. Büttner, K. Ueda, B. Pfau, C. M. Günther, P. Hessing, A. Churikova, C. Klose, M. Schneider, D. Engel, C. Marcus, D. Bono, K. Bagschik, S. Eisebitt, and G. S. D. Beach, *Fast current-driven domain walls and small skyrmions in a compensated ferrimagnet*, Nature Nanotechnology **13**, 1154 (2018).

[41] A. K. Nandy, N. S. Kiselev, and S. Blügel, *Interlayer Exchange Coupling: A General Scheme Turning Chiral Magnets into Magnetic Multilayers Carrying Atomic-Scale Skyrmions*, Physical Review Letters **116**, 177202 (2016).

[42] M. Bode, M. Heide, K. von Bergmann, P. Ferriani, S. Heinze, G. Bihlmayer, A. Kubetzka, O. Pietzsch, S. Blügel, and R. Wiesendanger, *Chiral magnetic order at surfaces driven by inversion asymmetry*, Nature **447**, 190 (2007).

[43] P. Ferriani, K. von Bergmann, E. Y. Vedmedenko, S. Heinze, M. Bode, M. Heide, G. Bihlmayer, S. Blügel, and R. Wiesendanger, *Atomic-Scale Spin Spiral with a Unique Rotational Sense: Mn Monolayer on W(001)*, Physical Review Letters **101**, 027201 (2008).

[44] N. Romming, H. Pralow, A. Kubetzka, M. Hoffmann, S. von Malottki, S. Meyer, B. Dupé, R. Wiesendanger, K. von Bergmann, and S. Heinze, *Competition of Dzyaloshinskii-Moriya and Higher-Order Exchange Interactions in Rh / Fe Atomic Bilayers on Ir(111)*, Physical Review Letters **120**, 207201 (2018).

[45] A. Krönlein, M. Schmitt, M. Hoffmann, J. Kemmer, N. Seubert, M. Vogt, J. Küspert, M. Böhme, B. Alonazi, J. Kügel, H. A. Albrithen, M. Bode, G. Bihlmayer, and S. Blügel, *Magnetic Ground State Stabilized by Three-Site Interactions: Fe / Rh (111)*, Physical Review Letters **120**, 207202 (2018).

[46] Y. Yoshida, S. Schröder, P. Ferriani, D. Serrate, A. Kubetzka, K. von Bergmann, S. Heinze, and R. Wiesendanger, *Conical Spin-Spiral State in an Ultrathin Film Driven by Higher-Order Spin Interactions*, Physical Review Letters **108**, 087205 (2012).

[47] *www.flapw.de* (2020).

[48] M. Bode, M. Hennefarth, D. Haude, M. Getzlaff, and R. Wiesendanger, *Growth of thin Mn films on W(110) studied by means of in-situ scanning tunnelling microscopy*, Surface Science **432**, 8 (1999).

[49] P. Kurz, F. Förster, L. Nordström, G. Bihlmayer, and S. Blügel, *Ab initio treatment of noncollinear magnets with the full-potential linearized augmented plane wave method*, Physical Review B **69**, 24415 (2004).

[50] B. Hardrat, A. Al-Zubi, P. Ferriani, S. Blügel, G. Bihlmayer, and S. Heinze, *Complex magnetism of iron monolayers on hexagonal transition metal surfaces from first principles*, Physical Review B **79**, 094411 (2009).

[51] J. Spethmann, *Magnetische Schichten auf Re(0001)*, Masterthesis, University of Hamburg (2018).

[52] M. Born and R. Oppenheimer, *Zur Quantentheorie der Molekeln*, Annalen der Physik **389**, 457 (1927).

[53] R. G. Parr, *Density Functional Theory of Atoms and Molecules*, edited by K. Fukui and B. Pullman (Springer Netherlands, Dordrecht, 1980).

[54] E. Engler and R. M. Dreizler, *Density Functional Theory An Advanced Course* (Springer-Verlag Berlin Heidelberg, 2011).

[55] D. M. Probert, *Electronic Structure: Basic Theory and Practical Methods, by Richard M. Martin* (Taylor and Francis, 2011).

[56] W. Koch and M. Holthausen, *A Chemist's Guide to Density Functional Theory* (Wiley, 2015).

[57] J. Kohanoff, *Electronic Structure Calculations for Solids and Molecules: Theory and Computational Methods* (Cambridge University Press, 2006).

[58] D. Sholl and J. Steckel, *Density Functional Theory: A Practical Introduction* (Wiley, 2009).

[59] K. Capelle, *A bird's-eye view of density-functional theory*, Brazilian Journal of Physics **36**, 1318 (2006).

[60] P. Hohenberg and W. Kohn, *Inhomogeneous Electron Gas*, Physical Review **136**, B864 (1964).

[61] W. Kohn and L. J. Sham, *Self-Consistent Equations Including Exchange and Correlation Effects*, Physical Review **140**, A1133 (1965).

[62] U. von Barth and L. Hedin, *A local exchange-correlation potential for the spin polarized case. i*, Journal of Physics C: Solid State Physics **5**, 1629 (1972).

[63] M. M. Pant and A. K. Rajagopal, *Theory of inhomogeneous magnetic electron gas*, Solid State Communications **10**, 1157 (1972).

[64] L. Neel, *L'approche à la saturation de la magnétostriction*, Journal de Physique et le Radium **15**, 376 (1954).

[65] D. D. Koelling and B. N. Harmon, *A technique for relativistic spin-polarised calculations*, Journal of Physics C: Solid State Physics **10**, 3107 (1977).

[66] G. Baym, *Lectures On Quantum Mechanics* (CRC Press, 2018).

[67] E. Abate and M. Asdente, *Tight-Binding Calculation of 3d Bands of Fe with and without Spin-Orbit Coupling*, Physical Review **140**, A1303 (1965).

[68] P. Kurz, *Non-Collinear Magnetism at Surfaces and in Ultrathin Films*, Ph.D. thesis, Rheinisch-Westfälische Technische Hochschule Aachen (2000).

[69] D. J. Singh and L. Nordstrom, *Planewaves, Pseudopotentials and the LAPW Method: Second Edition* (Springer US, 2006).

[70] P. A. M. Dirac, *Note on Exchange Phenomena in the Thomas Atom*, Mathematical Proceedings of the Cambridge Philosophical Society **26**, 376385 (1930).

[71] I. I. Mazin, M. D. Johannes, L. Boeri, K. Koepernik, and D. J. Singh, *Problems with reconciling density functional theory calculations with experiment in ferropnictides*, Physical Review B **78**, 085104 (2008).

[72] P. Haas, F. Tran, and P. Blaha, *Calculation of the lattice constant of solids with semilocal functionals*, Physical Review B **79**, 085104 (2009).

[73] Y. Zhang and W. Yang, *Comment on "Generalized Gradient Approximation Made Simple"*, Physical Review Letters **80**, 890 (1998).

[74] C. G. Broyden, *A Class of Methods for Solving Nonlinear Simultaneous Equations*, Mathematics of Computation **19**, 577 (1965).

[75] D. G. Anderson, *Iterative Procedures for Nonlinear Integral Equations*, Journal of the ACM **12**, 547560 (1965).

[76] G. P. Srivastava, *Broyden's method for self-consistent field convergence acceleration*, Journal of Physics A: Mathematical and General **17**, L317 (1984).

[77] D. D. Johnson, *Modified Broyden's method for accelerating convergence in self-consistent calculations*, Physical Review B **38**, 12807 (1988).

[78] M. Weinert, E. Wimmer, and A. J. Freeman, *Total-energy all-electron density functional method for bulk solids and surfaces*, Physical Review B **26**, 4571 (1982).

[79] A. Mackintosh and O. Andersen, *Electrons at the Fermi surface*, ed. M. Springford, Cambridge Univ. Press, London , 149 (1980).

[80] A. Oswald, R. Zeller, P. J. Braspenning, and P. H. Dederichs, *Interaction of magnetic impurities in Cu and Ag*, Journal of Physics F: Metal Physics **15**, 193 (1985).

[81] A. I. Liechtenstein, M. I. Katsnelson, V. P. Antropov, and V. A. Gubanov, *Local spin density functional approach to the theory of exchange interactions in ferromagnetic metals and alloys*, Journal of Magnetism and Magnetic Materials **67**, 65 (1987).

[82] D. R. Hamann, *Semiconductor Charge Densities with Hard-Core and Soft-Core Pseudopotentials*, Physical Review Letters **42**, 662 (1979).

[83] E. Wimmer, H. Krakauer, M. Weinert, and A. J. Freeman, *Full-potential self-consistent linearized-augmented-plane-wave method for calculating the electronic structure of molecules and surfaces:* O_2 *molecule*, Physical Review B **24**, 864 (1981).

[84] S. Blügel and G. Bihlmayer, *Full-Potential Linearized Augmented Planewave Method* (2006).

[85] N. J. Higham, *Cholesky factorization*, WIREs Computational Statistics **1**, 251 (2009).

[86] F. Bloch, *Über die Quantenmechanik der Elektronen in Kristallgittern*, Zeitschrift für Physik **52**, 555 (1929).

[87] O. K. Andersen, *Linear methods in band theory*, Physical Review B **12**, 3060 (1975).

[88] D. D. Koelling and G. O. Arbman, *Use of energy derivative of the radial solution in an augmented plane wave method: application to copper*, Journal of Physics F: Metal Physics **5**, 2041 (1975).

[89] H. Krakauer, M. Posternak, and A. J. Freeman, *Linearized augmented plane-wave method for the electronic band structure of thin films*, Physical Review B **19**, 1706 (1979).

[90] W. Ning, C. Kailai, and W. Dingsheng, *Work Function of Transition-Metal Surface with Submonolayer Alkali-Metal Coverage*, Physical Review Letters **56**, 2759 (1986).

[91] M. Heide, G. Bihlmayer, and S. Blügel, *Describing DzyaloshinskiiMoriya spirals from first principles*, Physica B: Condensed Matter **404**, 2678 (2009).

[92] E. C. Stoner, *Collective electron ferromagnetism II. Energy and specific heat*, Proceedings of the Royal Society of London. Series A. Mathematical and Physical Sciences **169**, 339 (1939).

[93] O. Gunnarsson, *Band model for magnetism of transition metals in the spin-density-functional formalism*, Journal of Physics F: Metal Physics **6**, 587 (1976).

[94] J. F. Janak, *Uniform susceptibilities of metallic elements*, Physical Review B **16**, 255 (1977).

[95] G. Binnig, H. Rohrer, C. Gerber, and E. Weibel, *Tunneling through a controllable vacuum gap*, Applied Physics Letters **40**, 178 (1982).

[96] G. Binnig, H. Rohrer, C. Gerber, and E. Weibel, *Surface Studies by Scanning Tunneling Microscopy*, Physical Review Letters **49**, 57 (1982).

[97] J. Bardeen, *Tunnelling from a Many-Particle Point of View*, Physical Review Letters **6**, 57 (1961).

[98] C. J. Chen, *Theory of scanning tunneling spectroscopy*, Journal of Vacuum Science & Technology A **6**, 319 (1988).

[99] C. J. Chen, *Microscopic view of scanning tunneling microscopy*, Journal of Vacuum Science & Technology A **9**, 44 (1991).

[100] C. J. Chen, *Introduction to scanning tunneling microscopy*, Vol. 4 (Oxford University Press on Demand, 1993).

[101] S. Heinze, *First-Principles Theory of Scannin Tunneling Microscopy Applied to Transition-Metal Surfaces*, Phd thesis, Universität Hamburg (2000).

[102] D. Wortmann, S. Heinze, P. Kurz, G. Bihlmayer, and S. Blügel, *Resolving Complex Atomic-Scale Spin Structures by Spin-Polarized Scanning Tunneling Microscopy*, Physical Review Letters **86**, 4132 (2001).

[103] S. Heinze, *Simulation of spin-polarized scanning tunneling microscopy images of nanoscale non-collinear magnetic structures*, Applied Physics A **85**, 407 (2006).

[104] O. Eriksson, A. Bergman, L. Bergqvist, and J. Hellsvik, *Atomistic spin dynamics: Foundations and applications* (Oxford university press, 2017).

[105] J. Hubbard and B. H. Flowers, *Electron correlations in narrow energy bands*, Proceedings of the Royal Society of London. Series A. Mathematical and Physical Sciences **276**, 238 (1963).

[106] A. H. MacDonald, S. M. Girvin, and D. Yoshioka, $\frac{t}{U}$ *expansion for the Hubbard model*, Physical Review B **37**, 9753 (1988).

[107] M. A. Ruderman and C. Kittel, *Indirect Exchange Coupling of Nuclear Magnetic Moments by Conduction Electrons*, Physical Review **96**, 99 (1954).

[108] T. Kasuya, *A Theory of Metallic Ferro- and Antiferromagnetism on Zener's Model*, Progress of Theoretical Physics **16**, 45 (1956).

[109] K. Yosida, *Magnetic Properties of Cu-Mn Alloys*, Physical Review **106**, 893 (1957).

[110] M. Hoffmann and S. Blügel, *Systematic derivation of realistic spin models for beyond-Heisenberg solids*, Physical Review B **101**, 024418 (2020).

[111] I. Dzyaloshinsky, *A thermodynamic theory of weak ferromagnetism of antiferromagnetics*, Journal of Physics and Chemistry of Solids **4**, 241 (1958).

[112] T. Moriya, *Anisotropic Superexchange Interaction and Weak Ferromagnetism*, Physical Review **120**, 91 (1960).

[113] A. Crépieux and C. Lacroix, *DzyaloshinskyMoriya interactions induced by symmetry breaking at a surface*, Journal of Magnetism and Magnetic Materials **182**, 341 (1998).

[114] A. Fert and P. M. Levy, *Role of Anisotropic Exchange Interactions in Determining the Properties of Spin-Glasses*, Physical Review Letters **44**, 1538 (1980).

[115] S. Blundell, *Magnetism in Condensed Matter* (Oxford University press 2003, New York, 2001).

[116] J. B. Staunton, B. L. Gyorffy, J. Poulter, and P. Strange, *A relativistic RKKY interaction between two magnetic impurities-the origin of a magnetic anisotropic effect*, Journal of Physics C: Solid State Physics **21**, 1595 (1988).

[117] D. Smith, *New mechanisms for magnetic anisotropy in localised S-state moment materials*, Journal of Magnetism and Magnetic Materials **1**, 214 (1976).

[118] R. Mondal, M. Berritta, and P. M. Oppeneer, *Relativistic theory of spin relaxation mechanisms in the Landau-Lifshitz-Gilbert equation of spin dynamics*, Physical Review B **94**, 144419 (2016).

[119] P. F. Bessarab, V. M. Uzdin, and H. Jónsson, *Method for finding mechanism and activation energy of magnetic transitions, applied to skyrmion and antivortex annihilation*, Computer Physics Communications **196**, 335 (2015).

[120] G. Henkelman, B. P. Uberuaga, and H. Jónsson, *A climbing image nudged elastic band method for finding saddle points and minimum energy paths*, The Journal of Chemical Physics **113**, 9901 (2000).

[121] G. Henkelman and H. Jónsson, *Improved tangent estimate in the nudged elastic band method for finding minimum energy paths and saddle points*, The Journal of Chemical Physics **113**, 9978 (2000).

[122] B. Dupé, M. Hoffmann, C. Paillard, and S. Heinze, *Tailoring magnetic skyrmions in ultra-thin transition metal films*, Nature Communications **5**, 4030 (2014).

[123] H. Yang, A. Thiaville, S. Rohart, A. Fert, and M. Chshiev, *Anatomy of Dzyaloshinskii-Moriya Interaction at* Co/Pt *Interfaces*, Physical Review Letters **115**, 267210 (2015).

[124] G. J. Vida, E. Simon, L. Rózsa, K. Palotás, and L. Szunyogh, *Domain-wall profiles in* Co/Ir_n*/Pt(111) ultrathin films: Influence of the Dzyaloshinskii-Moriya interaction*, Physical Review B **94**, 214422 (2016).

[125] H. Yang, O. Boulle, V. Cros, A. Fert, and M. Chshiev, *Controlling Dzyaloshinskii-Moriya Interaction via Chirality Dependent Atomic-Layer Stacking, Insulator Capping and Electric Field*, Scientific Reports **8**, 12356 (2018).

[126] G. Chen, A. T. N'Diaye, Y. Wu, and A. K. Schmid, *Ternary superlattice boosting interface-stabilized magnetic chirality*, Applied Physics Letters **106**, 062402 (2015).

[127] S. H. Vosko, L. Wilk, and M. Nusair, *Accurate spin-dependent electron liquid correlation energies for local spin density calculations: a critical analysis*, Canadian Journal of Physics **58**, 1200 (1980).

[128] B. Zimmermann, M. Heide, G. Bihlmayer, and S. Blügel, *First-principles analysis of a homochiral cycloidal magnetic structure in a monolayer Cr on W(110)*, Physical Review B **90**, 115427 (2014).

[129] S. Meyer, B. Dupé, P. Ferriani, and S. Heinze, *Dzyaloshinskii-Moriya interaction at an antiferromagnetic interface: First-principles study of Fe/Ir bilayers on Rh(001)*, Physical Review B **96**, 094408 (2017).

[130] M. Perini, *Nanoscale non-collinear magnetic structures in Co-based epitaxial ultrathin films*, Phd thesis, Hamburg (2018).

[131] T. Okubo, S. Chung, and H. Kawamura, *Multiple-q States and the Skyrmion Lattice of the Triangular-Lattice Heisenberg Antiferromagnet under Magnetic Fields*, Physical Review Letters **108**, 017206 (2012).

[132] A. O. Leonov and M. Mostovoy, *Multiply periodic states and isolated skyrmions in an anisotropic frustrated magnet*, Nature Communications **6**, 8275 (2015), 1501.02757 .

[133] E. A. S. Oliveira, R. L. Silva, R. C. Silva, and A. R. Pereira, *Effects of second neighbor interactions on skyrmion lattices in chiral magnets*, Journal of Physics: Condensed Matter **29**, 205801 (2017).

[134] S. von Malottki, B. Dupé, P. F. Bessarab, A. Delin, and S. Heinze, *Enhanced skyrmion stability due to exchange frustration*, Scientific Reports **7**, 12299 (2017).

[135] A. Varentsova, M. Potkina, S. von Malottki, S. Heinze, and P. Bessarab, *Interplay between size and stability of magnetic skyrmions*, Nanosystems: Physics, Chemistry, Mathematics **9**, 356 (2018).

[136] S. Haldar, S. von Malottki, S. Meyer, P. F. Bessarab, and S. Heinze, *First-principles prediction of sub-10-nm skyrmions in Pd/Fe bilayers on Rh(111)*, Physical Review B **98**, 060413 (2018).

[137] E. Simon, L. Rózsa, K. Palotás, and L. Szunyogh, *Magnetism of a Co monolayer on Pt(111) capped by overlayers of* 5*d elements: A spin-model study*, Physical Review B **97**, 134405 (2018).

[138] B. Zimmermann, G. Bihlmayer, M. Böttcher, M. Bouhassoune, S. Lounis, J. Sinova, S. Heinze, S. Blügel, and B. Dupé, *Comparison of first-principles methods to extract magnetic parameters in ultrathin films: Co/Pt(111)*, Physical Review B **99**, 214426 (2019).

[139] M. Hervé, B. Dupé, R. Lopes, M. Böttcher, M. D. Martins, T. Balashov, L. Gerhard, J. Sinova, and W. Wulfhekel, *Stabilizing spin spirals and isolated skyrmions at low magnetic field exploiting vanishing magnetic anisotropy*, Nature Communications **9**, 1015 (2018).

[140] Y. Zhang and W. Yang, *Comment on "Generalized Gradient Approximation Made Simple"*, Physical Review Letters **80**, 890 (1998).

[141] A. Lehnert, S. Dennler, P. Błoński, S. Rusponi, M. Etzkorn, G. Moulas, P. Bencok, P. Gambardella, H. Brune, and J. Hafner, *Magnetic anisotropy of Fe and Co ultrathin films deposited on Rh(111) and Pt(111) substrates: An experimental and first-principles investigation*, Physical Review B **82**, 094409 (2010).

[142] A. Fert, N. Reyren, and V. Cros, *Magnetic skyrmions: advances in physics and potential applications*, Nature Reviews Materials **2**, 17031 (2017).

[143] S. Rohart and A. Thiaville, *Skyrmion confinement in ultrathin film nanostructures in the presence of Dzyaloshinskii-Moriya interaction*, Physical Review B **88**, 184422 (2013).

[144] A. S. Varentcova, S. von Malottki, M. N. Potkina, G. Kwiatkowski, S. Heinze, and P. F. Bessarab, *Towards room temperature nanoscale skyrmions in ultrathin films* (2020), arXiv:2002.05285 [cond-mat.mes-hall] .

[145] S. Woo, K. Litzius, B. Krüger, M.-Y. Im, L. Caretta, K. Richter, M. Mann, A. Krone, R. M. Reeve, M. Weigand, P. Agrawal, I. Lemesh, M.-A. Mawass, P. Fischer, M. Kläui, and G. S. D. Beach, *Observation of room-temperature magnetic skyrmions and their current-driven dynamics in ultrathin metallic ferromagnets*, Nature Materials **15**, 501 (2016).

[146] W. Legrand, D. Maccariello, F. Ajejas, S. Collin, A. Vecchiola, K. Bouzehouane, N. Reyren, V. Cros, and A. Fert, *Room-temperature stabilization of antiferromagnetic skyrmions in synthetic antiferromagnets*, Nature Materials **19**, 34 (2020).

[147] C. Hanneken, F. Otte, A. Kubetzka, B. Dupé, N. Romming, K. von Bergmann, R. Wiesendanger, and S. Heinze, *Electrical detection of magnetic skyrmions by tunnelling non-collinear magnetoresistance*, Nature Nanotechnology **10**, 1039 (2015).

[148] A. Kubetzka, C. Hanneken, R. Wiesendanger, and K. von Bergmann, *Impact of the skyrmion spin texture on magnetoresistance*, Physical Review B **95**, 104433 (2017).

[149] J. H. Mentink, M. V. Tretyakov, A. Fasolino, M. I. Katsnelson, and T. Rasing, *Stable and fast semi-implicit integration of the stochastic Landau–Lifshitz equation*, Journal of Physics: Condensed Matter **22**, 176001 (2010).

[150] L. Rózsa, K. Palotás, A. Deák, E. Simon, R. Yanes, L. Udvardi, L. Szunyogh, and U. Nowak, *Formation and stability of metastable skyrmionic spin structures with various topologies in an ultrathin film*, Physical Review B **95**, 094423 (2017).

[151] U. Ritzmann, S. von Malottki, J.-V. Kim, S. Heinze, J. Sinova, and B. Dupé, *Trochoidal motion and pair generation in skyrmion and antiskyrmion dynamics under spinorbit torques*, Nature Electronics **1**, 451 (2018).

[152] B. Zimmermann, W. Legrand, D. Maccariello, N. Reyren, V. Cros, S. Blügel, and A. Fert, *Dzyaloshinskii-Moriya interaction at disordered interfaces from ab initio theory: Robustness against intermixing and tunability through dusting*, Applied Physics Letters **113**, 232403 (2018).

[153] L. Desplat, D. Suess, J.-V. Kim, and R. L. Stamps, *Thermal stability of metastable magnetic skyrmions: Entropic narrowing and significance of internal eigenmodes*, Physical Review B **98**, 134407 (2018).

[154] S. von Malottki, P. F. Bessarab, S. Haldar, A. Delin, and S. Heinze, *Skyrmion lifetime in ultrathin films*, Physical Review B **99**, 060409 (2019).

[155] M. Bode, S. Heinze, A. Kubetzka, O. Pietzsch, X. Nie, G. Bihlmayer, S. Blügel, and R. Wiesendanger, *Magnetization-Direction-Dependent Local Electronic Structure Probed by Scanning Tunneling Spectroscopy*, Physical Review Letters **89**, 237205 (2002).

[156] J. Tersoff and D. R. Hamann, *Theory of the scanning tunneling microscope*, Physical Review B **31**, 805 (1985).

[157] B. Dupé, G. Bihlmayer, M. Böttcher, S. Blügel, and S. Heinze, *Engineering skyrmions in transition-metal multilayers for spintronics*, Nature Communications **7**, 11779 (2016).

[158] F. Nickel, *Dichtefunktionaltheorie-basierte Untersuchung nicht-kollinearer Spinstrukturen in Übergangsmetall-Multilagen*, Master thesis, Christian-Albrechts-Universität zu Kiel (2020).

[159] N. Romming, A. Kubetzka, C. Hanneken, K. von Bergmann, and R. Wiesendanger, *Field-Dependent Size and Shape of Single Magnetic Skyrmions*, Physical Review Letters **114**, 177203 (2015).

[160] T. Jungwirth, J. Sinova, A. Manchon, X. Marti, J. Wunderlich, and C. Felser, *The multiple directions of antiferromagnetic spintronics*, Nature Physics **14**, 200 (2018).

[161] J. Barker and O. A. Tretiakov, *Static and Dynamical Properties of Antiferromagnetic Skyrmions in the Presence of Applied Current and Temperature*, Physical Review Letters **116**, 147203 (2016).

[162] X. Zhang, Y. Zhou, and M. Ezawa, *Antiferromagnetic Skyrmion: Stability, Creation and Manipulation*, Scientific Reports **6**, 24795 (2016).

[163] D. Hobbs, J. Hafner, and D. Spišák, *Understanding the complex metallic element Mn. I. Crystalline and noncollinear magnetic structure of α-Mn*, Physical Review B **68**, 014407 (2003).

[164] K. Schubert, *Ein Modell für die Kristallstrukturen der chemischen Elemente*, Acta Crystallographica Section B **30**, 193 (1974).

[165] D. A. Tulchinsky, J. Unguris, and R. J. Celotta, *Growth and magnetic oscillatory exchange coupling of Mn/Fe(001) and Fe/Mn/Fe(001)*, Journal of Magnetism and Magnetic Materials **212**, 91 (2000).

[166] M. Bode, S. Heinze, A. Kubetzka, O. Pietzsch, M. Hennefarth, M. Getzlaff, R. Wiesendanger, X. Nie, G. Bihlmayer, and S. Blügel, *Structural, electronic, and magnetic properties of a Mn monolayer on W(110)*, Physical Review B **66**, 014425 (2002).

[167] T. K. Yamada, M. M. J. Bischoff, T. Mizoguchi, and H. van Kempen, *STM and STS study of ultrathin Mn layers on Fe(001)*, Surface Science **516**, 179 (2002).

[168] J. Hafner and D. Spišák, *Ab initio investigation of the magnetism of tetragonal Mn: Bulk, surface, ultrathin films, and multilayers*, Physical Review B **72**, 144420 (2005).

[169] J. T. Kohlhepp and W. J. M. de Jonge, *Stabilization of Metastable Expanded Face-Centered-Tetragonal Manganese*, Physical Review Letters **96**, 237201 (2006).

[170] P.-J. Hsu, C.-I. Lu, Y.-H. Chu, B.-Y. Wang, C.-B. Wu, L.-J. Chen, S.-S. Wong, and M.-T. Lin, *Layered antiferromagnetic spin structures of expanded face-centered-tetragonal Mn(001) as an origin of exchange bias coupling to the magnetic Co layer*, Physical Review B **85**, 174434 (2012).

[171] S. Heinze, M. Bode, A. Kubetzka, O. Pietzsch, X. Nie, S. Blügel, and R. Wiesendanger, *Real-Space Imaging of Two-Dimensional Antiferromagnetism on the Atomic Scale*, Science **288**, 1805 (2000).

[172] S. Dennler and J. Hafner, *First-principles study of ultrathin magnetic Mn films on W surfaces.*, Physical Review B **72**, 214413 (2005).

[173] L. N. Liebermann, D. R. Fredkin, and H. B. Shore, *Two-Dimensional 'Ferromagnetism' In Iron*, Physical Review Letters **22**, 539 (1969).

[174] L. Liebermann, J. Clinton, D. M. Edwards, and J. Mathon, *'Dead' Layers in Ferromagnetic Transition Metals*, Physical Review Letters **25**, 232 (1970).

[175] C. Liu and S. D. Bader, *Magnetic properties of ultrathin fcc Fe(111)/Ru(0001) films*, Physical Review B **41**, 553 (1990).

[176] C. A. F. Vaz, J. A. C. Bland, and G. Lauhoff, *Magnetism in ultrathin film structures*, Reports on Progress in Physics **71**, 056501 (2008).

[177] R. Wu and A. J. Freeman, *Antiferromagnetic ordering of Fe/Ru(0001)*, Physical Review B **44**, 4449 (1991).

[178] U. Gradmann, *Ferromagnetism near surfaces and in thin films*, Applied Physics **3**, 161 (1974).

[179] A. Kubetzka, P. Ferriani, M. Bode, S. Heinze, G. Bihlmayer, K. von Bergmann, O. Pietzsch, S. Blügel, and R. Wiesendanger, *Revealing antiferromagnetic order of the Fe monolayer on W (001): Spin-polarized scanning tunneling microscopy and first-principles calculations*, Physical Review Letters **94**, 087204 (2005).

[180] S. Heinze, R. Abt, S. Blügel, G. Gilarowski, and H. Niehus, *Scanning Tunneling Microscopy Images of Transition-Metal Structures Buried Below Noble-Metal Surfaces*, Physical Review Letters **83**, 4808 (1999).

[181] A. Weismann, M. Wenderoth, S. Lounis, P. Zahn, N. Quaas, R. G. Ulbrich, P. H. Dederichs, and S. Blügel, *Seeing the Fermi Surface in Real Space by Nanoscale Electron Focusing*, Science **323**, 1190 (2009).

[182] P. Kurz, G. Bihlmayer, K. Hirai, and S. Blügel, *Three-Dimensional Spin Structure on a Two-Dimensional Lattice: Mn /Cu(111)*, Physical Review Letters **86**, 1106 (2001).

[183] M. Hoffmann, J. Weischenberg, B. Dupé, F. Freimuth, P. Ferriani, Y. Mokrousov, and S. Heinze, *Topological orbital magnetization and emergent Hall effect of an atomic-scale spin lattice at a surface*, Physical Review B **92**, 020401 (2015).

[184] M. dos Santos Dias, J. Bouaziz, M. Bouhassoune, S. Blügel, and S. Lounis, *Chirality-driven orbital magnetic moments as a new probe for topological magnetic structures*, Nature Communications **7**, 13613 (2016).

[185] J.-P. Hanke, F. Freimuth, A. K. Nandy, H. Zhang, S. Blügel, and Y. Mokrousov, *Role of Berry phase theory for describing orbital magnetism: From magnetic heterostructures to topological orbital ferromagnets*, Physical Review B **94**, 121114 (2016).

[186] S. Grytsiuk, J.-P. Hanke, M. Hoffmann, J. Bouaziz, O. Gomonay, G. Bihlmayer, S. Lounis, Y. Mokrousov, and S. Blügel, *Topologicalchiral magnetic interactions driven by emergent orbital magnetism*, Nature Communications **11**, 511 (2020).

[187] A. Belabbes, G. Bihlmayer, F. Bechstedt, S. Blügel, and A. Manchon, *Hund's Rule-Driven Dzyaloshinskii-Moriya Interaction at* $3d$–$5d$ *Interfaces*, Physical Review Letters **117**, 247202 (2016).

[188] D.-P. Ji, Q. Zhu, and S.-Q. Wang, *Detailed first-principles studies on surface energy and work function of hexagonal metals*, Surface Science **651**, 137 (2016).

[189] A. Al-Zubi, G. Bihlmayer, and S. Blügel, *Modeling magnetism of hexagonal Fe monolayers on 4d substrates*, physica status solidi (b) **248**, 2242 (2011).

[190] S. Paul, S. Haldar, S. von Malottki, and S. Heinze, *Role of higher-order exchange interactions for skyrmion stability* (2019), arXiv:1912.03474 [cond-mat.mes-hall] .

[191] F. Muckel, S. von Malottki, C. Holl, B. Pestka, M. Pratzer, P. F. Bessarab, S. Heinze, and M. Morgenstern, *Mechanisms of skyrmion collapse revealed by sub-nm maps of the transition rate* (2020), arXiv:2004.07178 [cond-mat.mes-hall] .

[192] L. Šmejkal, Y. Mokrousov, B. Yan, and A. H. MacDonald, *Topological antiferromagnetic spintronics*, Nature Physics **14**, 242 (2018).

List of Figures

1.1 Experimentally observed room temperature stable skyrmions in magnetic structures. . . . 2
1.2 Comparison between experimentally observed complex magnetic structures with their theoretical explanations in different ultrathin film systems. . . . 4

2.1 Schematic flow-chart of the self-consistency cycle in DFT. . . . 21

3.1 Schematic representation of the augmented planewave (APW) method. . . . 28
3.2 Sketch of an linearized augmented planewave (LAPW) basis function depending on the distance to an atomic core. . . . 29
3.3 Sketch of an local orbital basis function depending on the distance to an atomic core. . . . 31
3.4 Schematic representation of the unit cell in a film calculation using the full potential linearized augmented planewave (FLAPW) method. . . . 32
3.5 Schematic representation of spin spiral states with different opening angle θ. . 35

4.1 Illustration of the exchange interaction. . . . 43
4.2 Illustration of higher order exchange interactions (HOIs). . . . 45
4.3 Illustration of Dzyaloshinskii-Moriya interaction (DMI). . . . 46
4.4 Illustration of a spin interacting with an effective magnetic field. . . . 50
4.5 Illustration of the geodesic nudged elastic band (GNEB) method. . . . 51

5.1 Schematic structural setup for the DFT calculations for the exemplary system of Co/Ir(111) . . . 57
5.2 Determination of magnetocrystalline anisotropy energy in Co_{hcp}/Ir(111) from DFT calculations. . . . 58
5.3 Energy dispersions $E(\mathbf{q})$ of flat cycloidal spin spirals for Co/Ir(111) at $\mathbf{q} \to 0$. . 59
5.4 Calculated local density of states for Co/Ir(111) in the ferromagnetic state. . . . 61
5.5 Energy dispersions $E(\mathbf{q})$ of flat cycloidal spin spirals for Pt/Co/Ir(111) at $\mathbf{q} \to 0$. 63
5.6 Determination of the magnetocrystalline anisotropy energy for Pt/Co/Ir(111). . 64
5.7 Calculated local density of states for Pt/Co/Ir(111) in the ferromagnetic state. . 65
5.8 Spin-polarized scanning tunnelling microscopy measurements of Co/Ir(111) and Pt/Co/Ir(111). . . . 67
5.9 Calculated domain wall properties for Co/Ir111 and Pt/Co/Ir(111). . . . 69
5.10 Energy dispersions $E(\mathbf{q})$ of flat cycloidal spin spirals for Pt_{fcc}/Pt_{fcc}/Co/Ir(111) and Pt_{fcc}/Co_{fcc}/Co_{fcc}/Ir(111) at $\mathbf{q} \to 0$. . . . 70

6.1 Full energy dispersions $E(\mathbf{q})$ of flat cycloidal spin spirals for Co/Ir(111) and Pt/Co/Ir(111) comparing the atomistic spin model with the effective nearest neighbour approximation. . . . 76
6.2 Element resolved energy contribution due to spin-orbit coupling (SOC) to the energy dispersion of cycloidal spin spirals for Co/Ir(111) and Pt/Co/Ir(111). . 79

6.3 Layer resolved energy contribution due to spin-orbit coupling to the energy dispersion of cycloidal spin spirals for Co_{hcp}/Ir(111). 80
6.4 Electronic structure analysis of three spin spiral states during the sign change of Dzyaloshinskii-Moriya interaction for Co_{hcp}/Ir(111). 81
6.5 Spindynamics simulations for Co_{hcp}/Ir(111) applying different descriptions for magnetic interactions. 83
6.6 Energy dispersions $E(\mathbf{q})$ of different magnetic interaction parameter sets for the Dzyaloshinskii-Moriya interaction. 86
6.7 Spindynamics simulations and geodesic nudged elastic band calculations using different magnetic interaction parameter sets for the Dzyaloshinskii-Moriya interaction. 87
6.8 Full energy dispersion $E(\mathbf{q})$ of flat cycloidal spin spirals for Co/Ir(111) and Pt/Co/Ir(111) without spin-orbit coupling applying different thicknesses of the Ir(111) substrate. 91
6.9 Energy contribution due to spin-orbit coupling to the energy dispersion of cycloidal spin spirals for Co/Ir(111) and Pt/Co/Ir(111) applying different thicknesses of the Ir(111) substrate. 92
6.10 Full energy dispersions $E(\mathbf{q})$ comparing flat cycloidal spin spirals for Co/Ir(111) and Pt/Co/Ir(111) with conical spin spiral states. 94

7.1 Periodic table of elements used for 4d/Co bilayers on Ir(111) and Rh(111) . . . 98
7.2 Relaxed interlayer distance Δd (%) for 4d/Co/Ir(111) and 4d/Co/Rh(111) relative to the bulk distance of Ir(111) and Rh(111). 100
7.3 Calculated magnetic moments (μ_B) for 4d/Co/Ir(111) and 4d/Co/Rh(111) in the ferromagnetic state. 101
7.4 Calculated local density of states for 4d/Co/Ir(111) films in the ferromagnetic state. 102
7.5 Calculated local density of states for 4d/Co/Rh(111) films in the ferromagnetic state. 103
7.6 Full energy dispersions $E(\mathbf{q})$ of flat cycloidal spin spirals for 4d/Co/Ir(111) and 4d/Co/Rh(111) including spin-orbit coupling (SOC). 104
7.7 Obtained values of exchange interaction in 4d/Co/Ir(111) and 4d/Co/Rh(111) mapping the effective nearest neighbour approximation of the spin model to the DFT results. 106
7.8 Obtained values of exchange interaction J_i for the three nearest neighbours in 4d/Co/Ir(111) and 4d/Co/Rh(111) mapping the atomistic spin model to the DFT results. 107
7.9 Calculated strength of Dzyaloshinskii-Moriya interaction in effective nearest neighbour approximation D_{eff} for 4d/Co/Ir(111) and 4d/Co/Rh(111). 108
7.10 Element resolved energy contribution due to spin-orbit coupling to the energy dispersion of cycloidal spin spirals for 4d/Co/Ir(111) and 4d/Co/Rh(111). . . . 109
7.11 Calculated strength of uniaxial magnetocrystalline anisotropy energy K for 4d/Co/Ir(111) and 4d/Co/Rh(111). 110

8.1 Full energy dispersions $E(\mathbf{q})$ of flat cycloidal spin spirals for Rh/Co/Ir(111) . . 119

8.2 Energy dispersions $E(\mathbf{q})$ of flat cycloidal spin spirals for Rh/Co/Ir(111) comparing the atomistic spin model with the effective nearest neighbour approximation. . . . 120
8.3 Element resolved energy contribution due to spin-orbit coupling to the energy dispersion of cycloidal spin spirals for Rh/Co/Ir(111). . . . 122
8.4 Calculated magnetic moment (μ_B) for spin spirals in Rh/Co/Ir(111). . . . 123
8.5 Calculated local density of states for Rh/Co/Ir(111) in the ferromagnetic state. 123
8.6 Spindynamics simulations on skyrmions and antiskyrmions for Rh_{fcc}/Co/Ir(111). 125
8.7 Spin-polarized scanning tunnelling microscopy measurements of Rh_{hcp}/Co/Ir(111). . . . 126
8.8 Full energy dispersions $E(\mathbf{q})$ of flat cycloidal spin spirals for Co/Rh/Ir(111). . . . 128
8.9 Calculated properties of non-collinear skyrmions, antiskyrmions and domain walls for Rh_{hcp}/Co/Ir(111). . . . 130
8.10 Minimum energy paths for two mechanisms of skyrmion collapses into the ferromagnetic state for Rh_{hcp}/Co/Ir(111). . . . 132
8.11 Minimum energy paths for an antiskyrmion collapse into the ferromagnetic state for Rh_{hcp}/Co/Ir(111). . . . 134
8.12 Comparison of non-collinear magnetoresistance from experiments with calculations in Rh_{hcp}/Co/Ir(111). . . . 136
8.13 Calculated non-collinear magnetoresistance for Rh_{hcp}/Co/Ir(111) applying spin spirals in different directions of the two-dimensional Brillouin zone. . . . 137
8.14 Calculated tunnelling anisotropic magnetoresistance and non-collinear magnetoresistance for Rh_{hcp}/Co/Ir(111). . . . 138
8.15 Comparison between DFT calculated local density of states of majority d_{xy} and minority p_z spin states for the Rh surface and a simplified tight binding model for Rh_{hcp}/Co/Ir(111). . . . 139
8.16 Convergence of energy dispersion $E(\mathbf{q})$ for Rh_{fcc}/Co/Ir(111) at $\mathbf{q} \to 0$. . . . 143
8.17 Full energy dispersions $E(\mathbf{q})$ comparing flat cycloidal spin spirals for Rh_{fcc}/Co/Ir(111) with conical spin spiral states. . . . 144
8.18 Full energy dispersions $E(\mathbf{q})$ of flat cycloidal spin spirals for Rh_{hcp}/Co/Ir(111) applying two different structural relaxations. . . . 146

9.1 Spin-polarized scanning tunnelling microscopy measurements of Mn/Mn/W(001) compared to Fe/W(001) [179]. . . . 153
9.2 Full energy dispersions $E(\mathbf{q})$ of flat cycloidal spin spirals for Mn/Mn/W(001) applying two different structural relaxations. . . . 156
9.3 Calculated local density of states for Mn/Mn/W(001) . . . 158
9.4 Calculated vacuum local density of states for Mn/Mn/W(001). . . . 160
9.5 DFT calculated spin-polarized scanning tunnelling microscopy images at $U = +10\,\mathrm{mV}$ and charge density for Mn/Mn/W(001) in the $c(2\times2)$ antiferromagnetic (AFM) state. . . . 161
9.6 Comparison of spin-polarized scanning tunnelling microscopy measurements and simulations at $U = +10\,\mathrm{mV}$, $I = 3\,\mathrm{nA}$ for Mn/Mn/W(001) in the $c(2\times2)$ antiferromagnetic state. . . . 162

9.7 DFT Calculated results upon artificially increasing the distance of the Mn double layer from the W substrate for Mn/Mn/W(001) in the $c(2 \times 2)$ antiferromagnetic state. 163
9.8 DFT calculated spin-polarized scanning tunnelling microscopy (SP-STM) images at $U = +10\,\mathrm{mV}$ and charge density for Mn/Mn/W(001) in the $c(2 \times 2)$ antiferromagnetic (AFM) state including a magnetic moment in the Mn interface layer. 164

10.1 Spin-polarized scanning tunnelling microscopy measurements on Mn/Re(0001). 169
10.2 Different configurations of 3Q states. 169
10.3 Full energy dispersions $E(\mathbf{q})$ of flat cycloidal spin spirals for Mn/Re(0001). . . . 173
10.4 Calculated local density of states (LDOS) for Mn/Re(0001). 175
10.5 Comparison of experimental $\mathrm{d}I/\mathrm{d}U$ spectra with calculated vacuum local density of states (LDOS) for Mn/Re(0001). 176
10.6 Self-consistent calculations on in-plane rotation of spin-quantization axis for Mn/Re(0001). 178
10.7 Sketches of magnetic states upon converting a 3Q state into a 1Q state. 179
10.8 DFT results on the continuous transformation of multi-Q states in Mn unsupported monolayers. 180
10.9 DFT calculated total energy differences for the continuous transformation of multi-Q states in Mn/Re(0001). 181
10.10 DFT calculated change of magnetic spin moment and orbital moment for the continuous transformation of multi-Q states in $\mathrm{Mn_{hcp}}$/Re(0001). 183

11.1 Scanning tunnelling microscopy image of a skyrmion in $\mathrm{Rh_{hcp}}$/Co/Ir(111) without magnetic field. 186
11.2 Collapse mechanisms of a single skyrmion into the ferromagnetic state for $\mathrm{Rh_{hcp}}$/Co/Ir(111). 187
11.3 Combined measured and calculated spin-polarized scanning tunnelling microscopy image of the $c(2 \times 2)$ antiferromagnetic state for Mn/Mn/W(001). . 188
11.4 Magnetic states in Mn/Re(0001). 188

A.1 Element resolved energy contribution due to SOC to the energy dispersion of cycloidal spin spirals for $\mathrm{Co_{fcc}}$/Ir(111). 215
A.2 Element resolved energy contribution due to SOC to the energy dispersion of cycloidal spin spirals for $\mathrm{Pt_{fcc}/Co_{fcc}}$/Ir(111). 216
A.3 Element resolved energy contribution due to SOC to the energy dispersion of cycloidal spin spirals for $\mathrm{Pt_{fcc}/Co_{hcp}}$/Ir(111). 216
A.4 Element resolved energy contribution due to SOC to the energy dispersion of cycloidal spin spirals for $\mathrm{Pt_{hcp}/Co_{fcc}}$/Ir(111). 217
A.5 Element resolved energy contribution due to SOC to the energy dispersion of cycloidal spin spirals for $\mathrm{Pt_{hcp}/Co_{hcp}}$/Ir(111). 217

B.1 Radial symmetric skyrmion collapse mechanism for $\mathrm{Rh_{hcp}}$/Co/Ir(111). 219
B.2 Skyrmion collapse mechanism via chimera annihilation for $\mathrm{Rh_{hcp}}$/Co/Ir(111). . 220
B.3 Radial symmetric antiskyrmion collapse mechanism for $\mathrm{Rh_{hcp}}$/Co/Ir(111). . . . 221

C.1 Local density of states of majority d_{xz} and minority p_z states for the Co layer in Rh_{hcp}/Co/Ir(111). 223
C.2 Orbital resolved local density of states for the Rh surface layer in Rh_{hcp}/Co/Ir(111). 224
C.3 Orbital resolved local density of states for the Co layer in Rh_{hcp}/Co/Ir(111). . . 225

D.1 Unit cells of the 3Q state in the hexagonal lattice. 227
D.2 Unit cells of spin spiral states in high symmetry directions $\overline{\Gamma}$-$\overline{M}$ and $\overline{\Gamma}$-$\overline{K}$ of the hexagonal two-dimensional Brillouin zone. 229

List of Tables

5.1 Relaxed interlayer distances d_{ij} (a.u.) for Co/Ir(111) and Pt/Co/Ir(111). 57
5.2 Obtained values for magnetic interactions in Co/Ir(111) mapping the effective nearest neighbour approximation of the spin model to the DFT results. 60
5.3 Calculated magnetic moments (μ_B) in Co/Ir(111) in the ferromagnetic state. . . 61
5.4 Obtained values for magnetic interactions in Pt/Co/Ir(111) mapping the effective nearest neighbour approximation of the spin model to the DFT results. 64
5.5 Calculated magnetic moments (μ_B) for Pt/Co/Ir(111). 66
5.6 Obtained values for magnetic interactions in $Pt_{fcc}/Pt_{fcc}/Co_{fcc}/Ir(111)$ and $Pt_{fcc}/Co_{fcc}/Co_{fcc}/Ir(111)$ mapping the effective nearest neighbour approximation of the spin model to the DFT results. 71

6.1 Obtained values for magnetic interactions for Co/Ir(111) and Pt/Co/Ir(111) mapping the atomistic spin model to the results of DFT calculations. 77
6.2 Obtained values for magnetocrystalline anisotropy energy for Co/Ir(111) and Pt/Co/Ir(111) applying different thicknesses of the Ir(111) substrate. 93

7.1 Relaxed interlayer distances d_{ij} (a.u.) for the film systems $4d$/Co/Ir(111) and $4d$/Co/Rh(111). 99
7.2 Obtained values for magnetic interactions in ($4d$)/Co/Ir(111) mapping the atomistic spin model to the results of DFT calculations. 112
7.3 Obtained values for magnetic interactions in ($4d$)/Co/Rh(111) mapping the atomistic spin model to the results of DFT calculations. 113

8.1 Relaxed interlayer distances d_{ij} (a.u.) for Rh/Co/Ir(111) and Co/Rh/Ir(111). . 117
8.2 Obtained values for magnetic interactions in Rh/Co/Ir(111) mapping the atomistic spin model to the results of density functional theory calculations. . 121
8.3 Obtained values for magnetic interactions in Co/Rh/Ir(111) mapping the atomistic spin model to the results of DFT. 129
8.4 Obtained values for magnetic interactions in Rh/Co/Ir(111) mapping the atomistic spin model to the results of the DFT test calculations. 145
8.5 Calculated values for nearest neighbour exchange and Dzyaloshinskii-Moriya interaction from domain wall properties for Rh/Co/Ir(111). 147

9.1 Previous results obtained from DFT calculations on Mn/Mn/W(001) taken from [172]. 152
9.3 DFT calculated results for Mn/Mn/W(001) in three collinear states after structural relaxation. 155
9.4 Obtained values for magnetic interactions for Mn/Mn/W(001) mapping the atomistic spin model to the DFT calculations. 157

10.1 Computational results for Mn/Re(0001) in the row-wise antiferromagnetic state after structural relaxation. 170

10.2 Obtained values for magnetic interactions in Mn/Re(0001) mapping the atomistic spin model without higher order exchange interactions to the DFT calculations of single-Q states. 173
10.3 Calculated higher order exchange interactions for Mn/Re(0001). 174

D.1 Coordinates of magnetic moments of three 3Q states presented in Fig. D.1. . . 228

Appendices

Appendix A

Layer resolved DMI in Co/Ir(111) and Pt/Co/Ir(111)

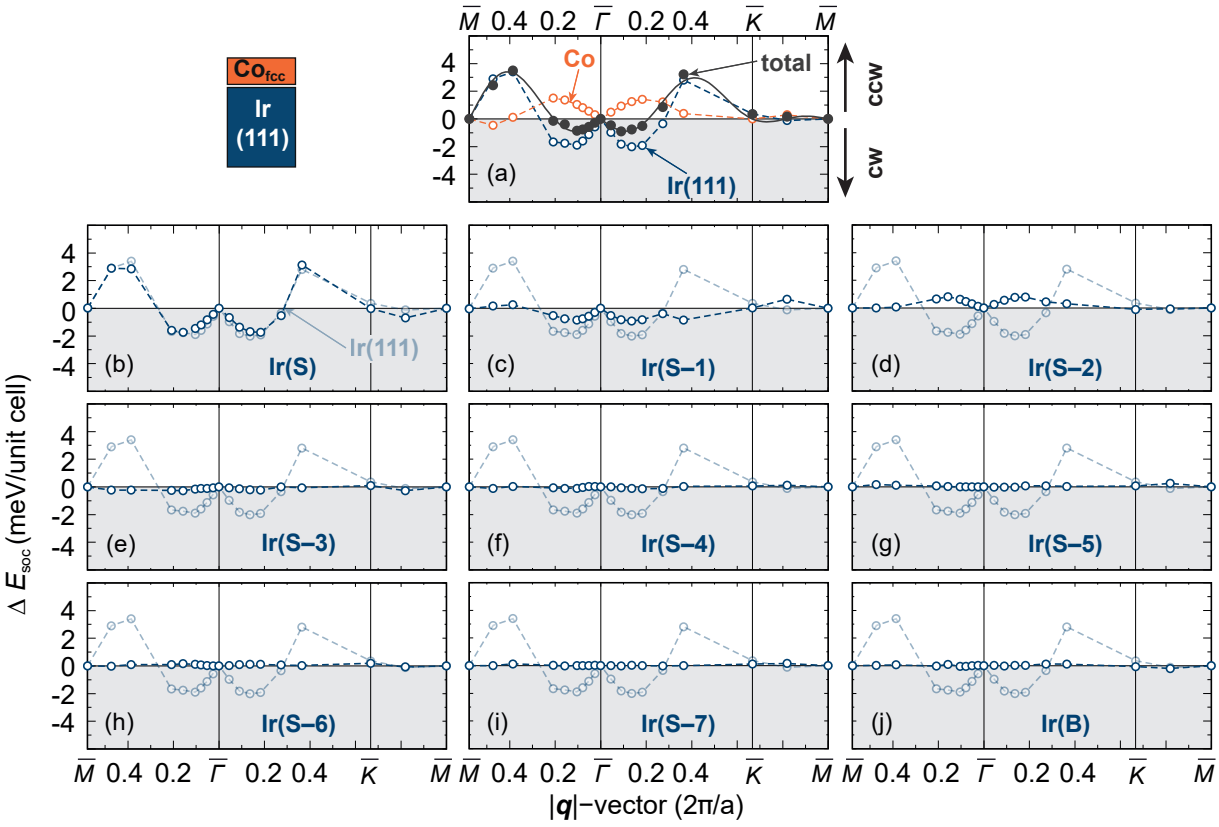

Figure A.1 | Element resolved energy contribution due to spin-orbit coupling (SOC) to the energy dispersion of cycloidal spin spirals for Co_{fcc}/Ir(111). (a) Element resolved contribution to SOC as shown in Fig. 6.2. (b-j) Contribution to SOC of each layer from the Ir(111) substrate presented in (a). (b) Contribution of the Ir(111) surface layer Ir(S). (c-i) Correspondent Ir layers below Ir(S). (j) Ir bottom layer Ir(B).

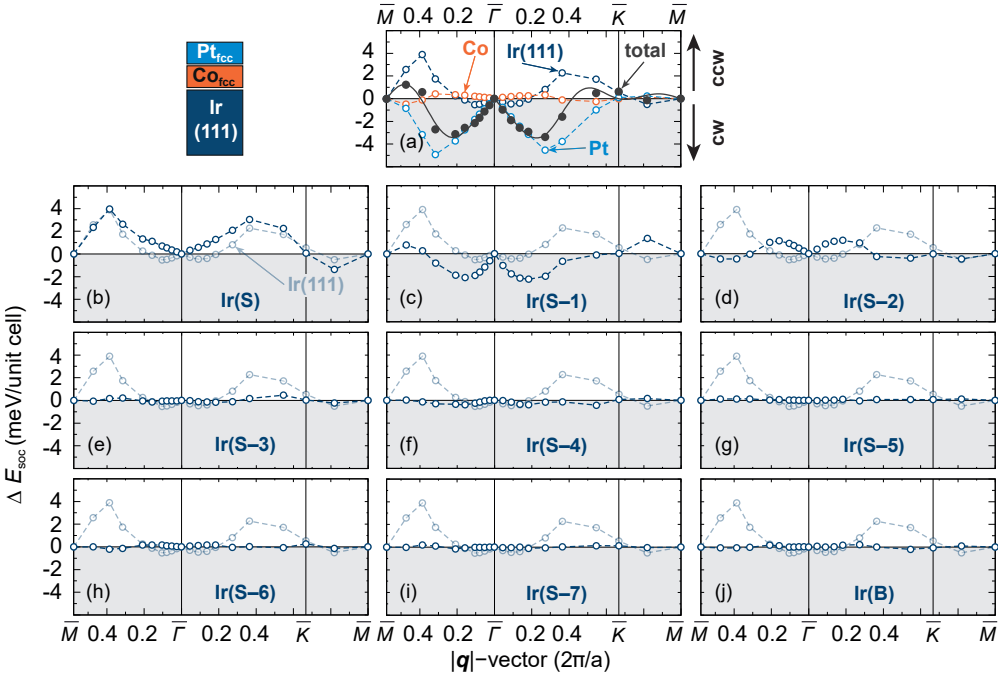

Figure A.2 | Element resolved energy contribution due to spin-orbit coupling (SOC) to the energy dispersion of cycloidal spin spirals for $Pt_{fcc}/Co_{fcc}/Ir(111)$. (a) Element resolved contribution to SOC as shown in Fig. 6.2. (b-j) Contribution to SOC of each layer from the Ir(111) substrate presented in (a). (b) Contribution of the Ir(111) surface layer Ir(S). (c-i) Correspondent Ir layers below Ir(S). (j) Ir bottom layer Ir(B).

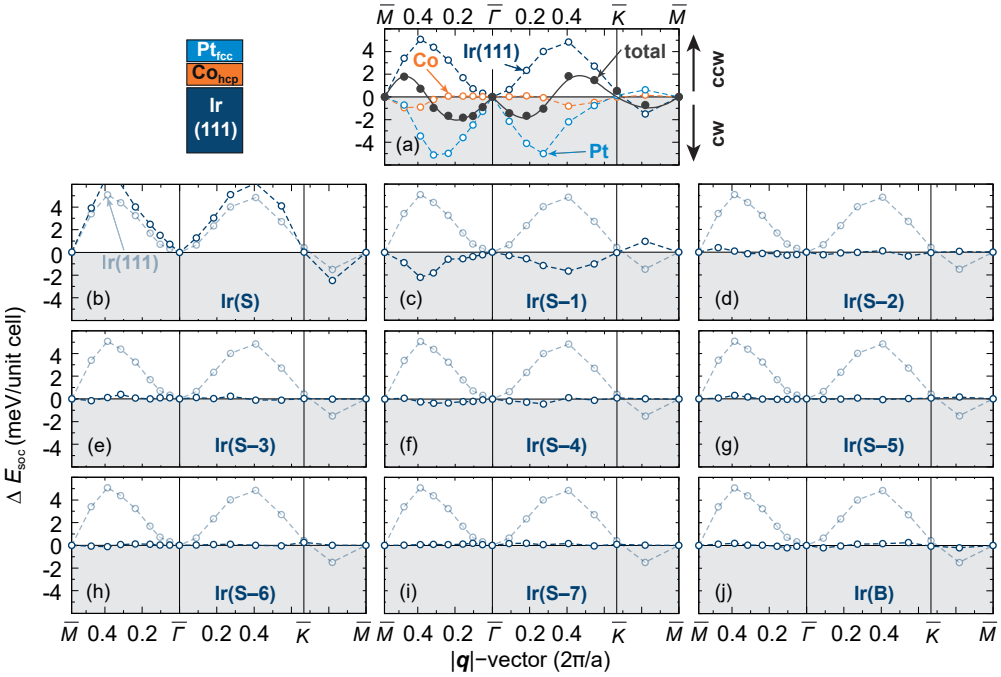

Figure A.3 | Element resolved energy contribution due to spin-orbit coupling (SOC) to the energy dispersion of cycloidal spin spirals for $Pt_{fcc}/Co_{hcp}/Ir(111)$. (a) Element resolved contribution to SOC as shown in Fig. 6.2. (b-j) Contribution to SOC of each layer from the Ir(111) substrate presented in (a). (b) Contribution of the Ir(111) surface layer Ir(S). (c-i) Correspondent Ir layers below Ir(S). (j) Ir bottom layer Ir(B).

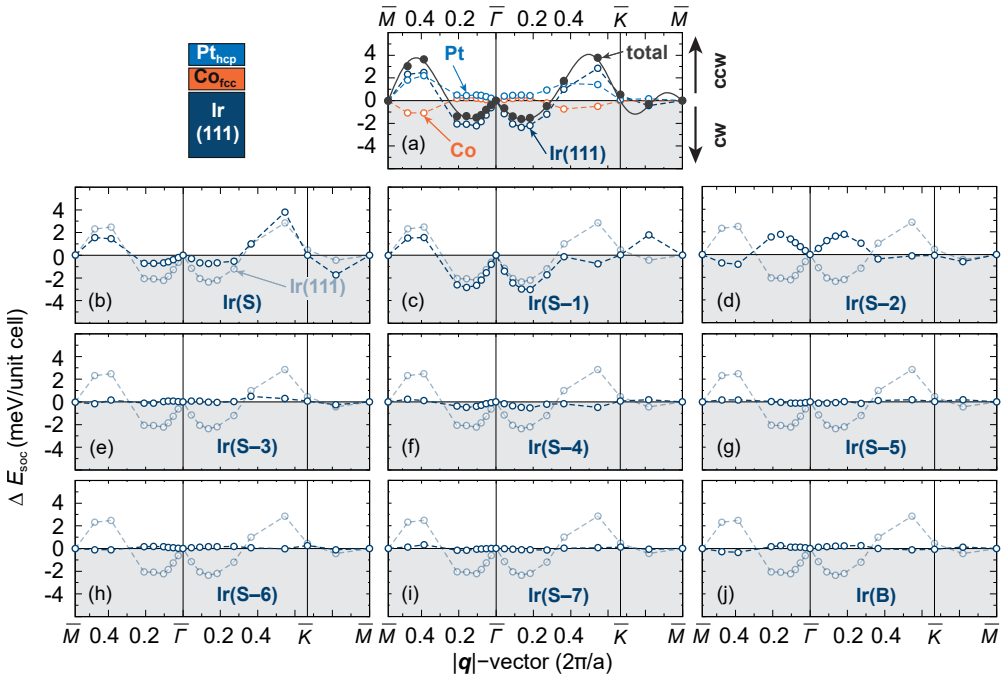

Figure A.4 | Element resolved energy contribution due to spin-orbit coupling (SOC) to the energy dispersion of cycloidal spin spirals for $Pt_{hcp}/Co_{fcc}/Ir(111)$. (a) Element resolved contribution to SOC as shown in Fig. 6.2. (b-j) Contribution to SOC of each layer from the Ir(111) substrate presented in (a). (b) Contribution of the Ir(111) surface layer Ir(S). (c-i) Correspondent Ir layers below Ir(S). (j) Ir bottom layer Ir(B).

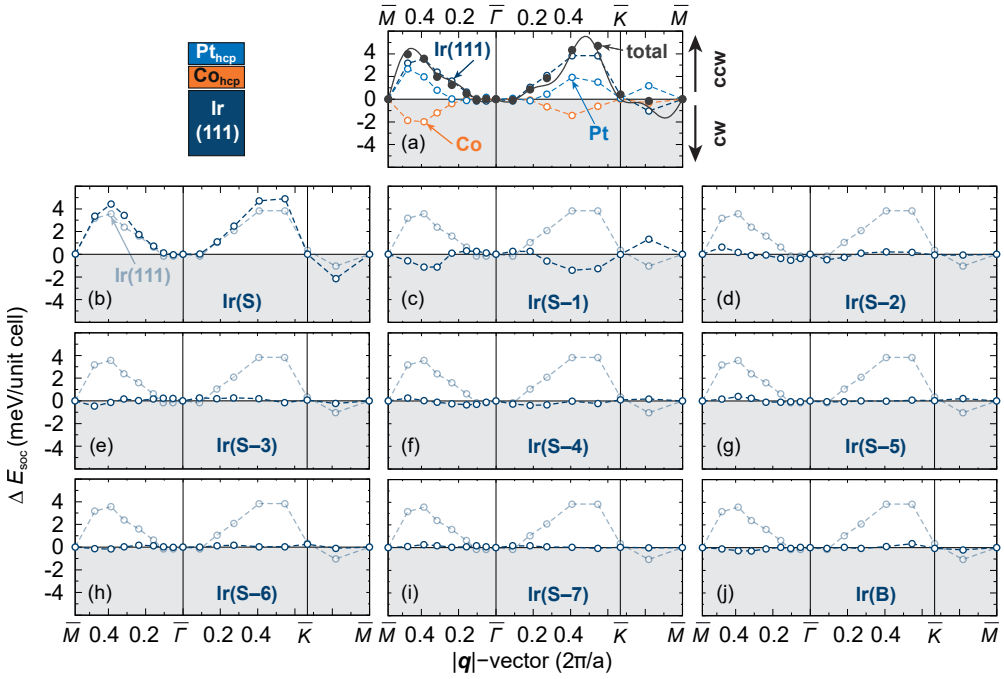

Figure A.5 | Element resolved energy contribution due to spin-orbit coupling (SOC) to the energy dispersion of cycloidal spin spirals for $Pt_{hcp}/Co_{hcp}/Ir(111)$. (a) Element resolved contribution to SOC as shown in Fig. 6.2. (b-j) Contribution to SOC of each layer from the Ir(111) substrate presented in (a). (b) Contribution of the Ir(111) surface layer Ir(S). (c-i) Correspondent Ir layers below Ir(S). (j) Ir bottom layer Ir(B).

Appendix B

Skyrmion collapse mechanisms in Rh/Co/Ir(111)

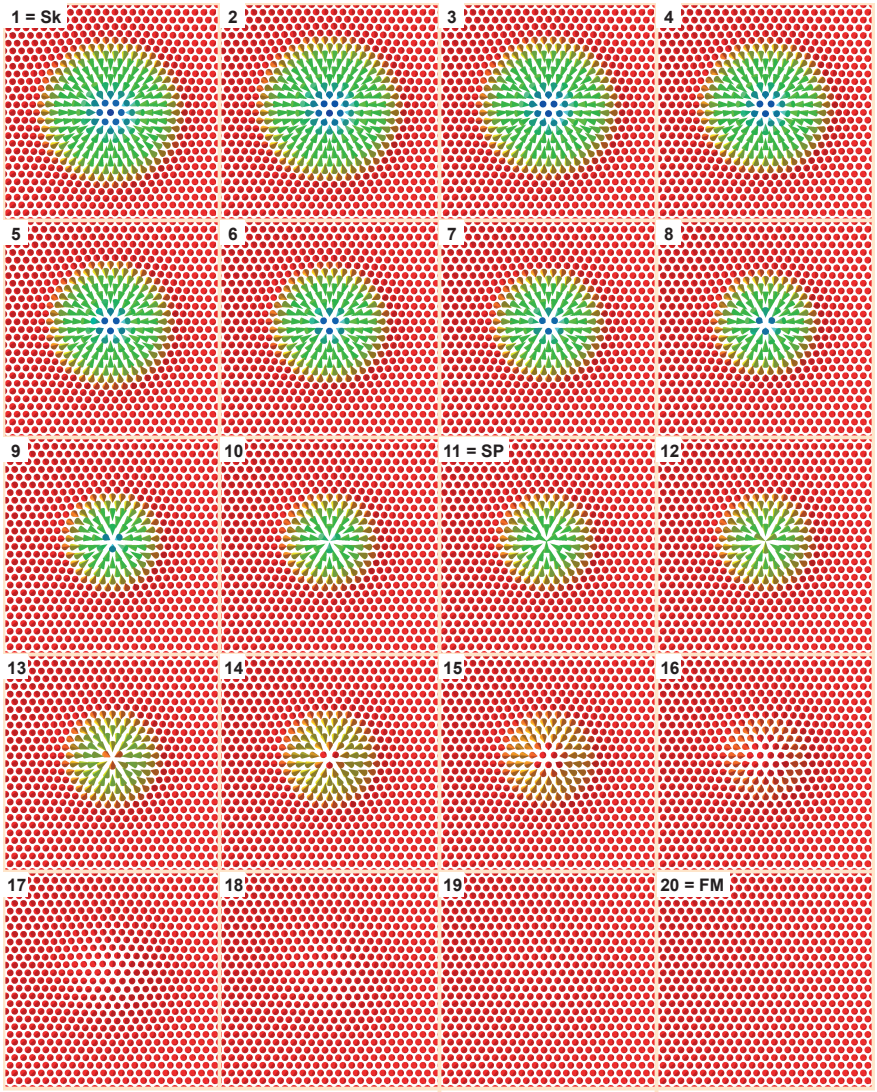

Figure B.1 | Radial symmetric skyrmion collapse mechanism for Rh_{hcp}/Co/Ir(111). Shown are the 20 images along the minimum energy path, where starting from an isolated skyrmion state (image 1), the skyrmion shrinks symmetrically reaching the saddle point (SP) in image 11 and further vanishes into the ferromagnetic (FM) state (image 20). Colours denote the out-of-plane magnetization direction (red upwards, blue downwards). Note that a small extract of the 70×70 spin lattice is shown and that the applied magnetic field is 1.2 T.

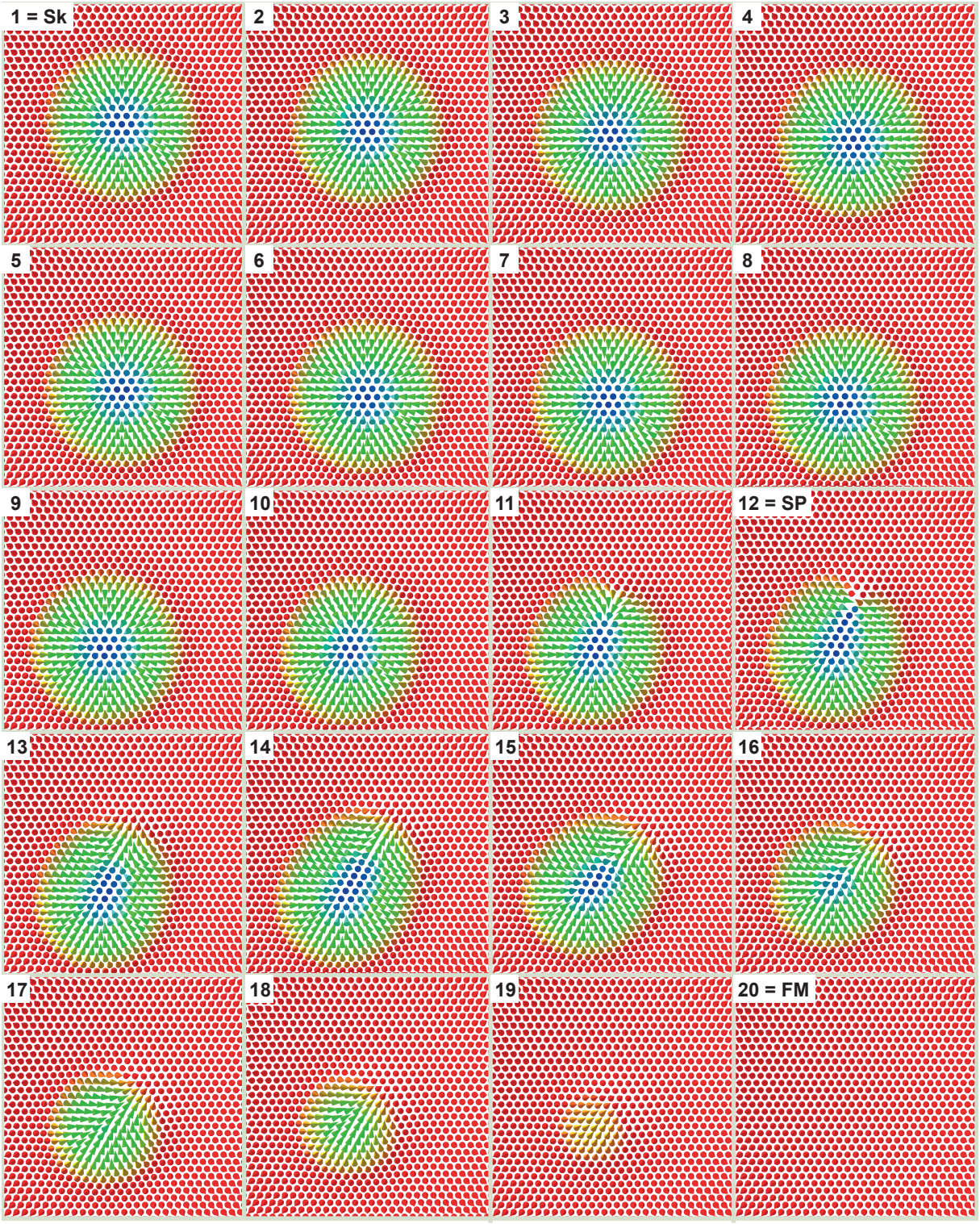

Figure B.2 | Skyrmion collapse mechanism via chimera annihilation for Rh_{hcp}/Co/Ir(111). Shown are the 20 images along the minimum energy path, where starting from an isolated skyrmion state (image 1), the skyrmion drifts and deforms reaching the saddle point (SP) in image 12 as a chimera skyrmion with vanishing topological charge. It further vanishes into the ferromagnetic (FM) state (image 20). Colours denote the out-of-plane magnetization direction (red upwards, blue downwards). Note that a small extract of the 70×70 spin lattice is shown and that the applied magnetic field is 0.0 T.

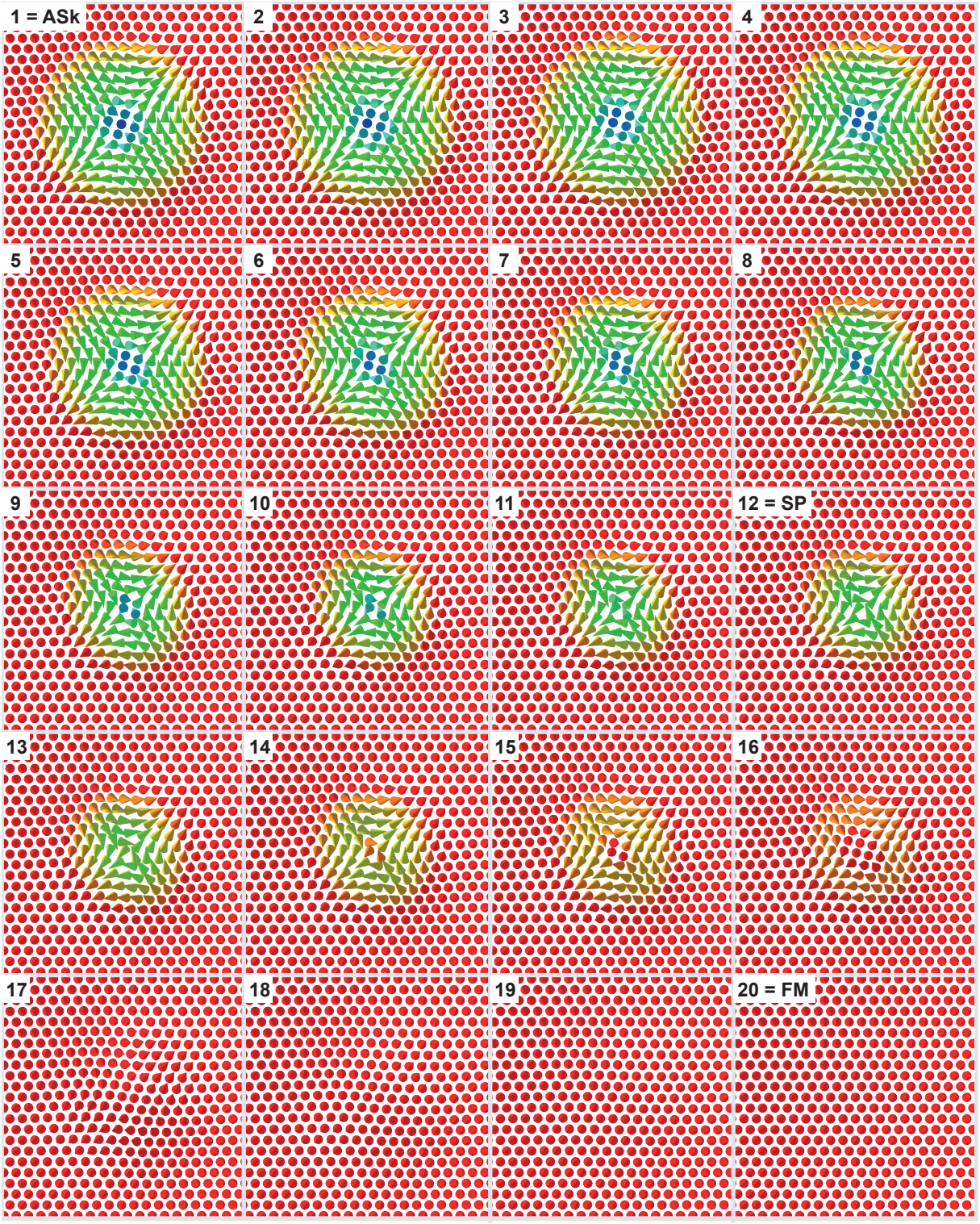

Figure B.3 | Radial symmetric antiskyrmion collapse mechanism for Rh_{hcp}/Co/Ir(111). Shown are the 20 images along the minimum energy path, where starting from an isolated antiskyrmion state (image 1), the antiskyrmion shrinks symmetrically reaching the saddle point (SP) in image 12 and further vanishes into the ferromagnetic (FM) state (image 20). Colours denote the out-of-plane magnetization direction (red upwards, blue downwards). Note that a small extract of the 70×70 spin lattice is shown and that the applied magnetic field is 0.0 T.

Appendix C

Orbital resolved LDOS for Rh_{hcp}/Co/Ir(111)

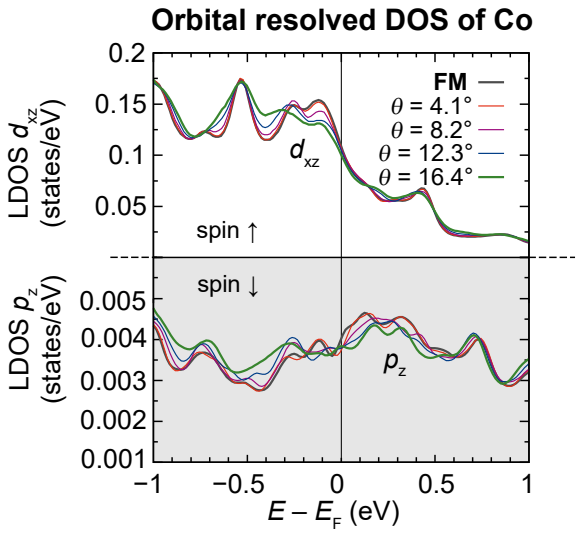

Figure C.1 | Local density of states (LDOS) of majority d_{xz} and minority p_z states for the Co layer in Rh_{hcp}/Co/Ir(111). Shown is the calculated LDOS from density functional theory for different spin spiral states along the $\overline{\Gamma}$-$\overline{K}$ direction of the hexagonal two-dimensional Brillouin zone. The angle θ between adjacent spins is given in the legend.

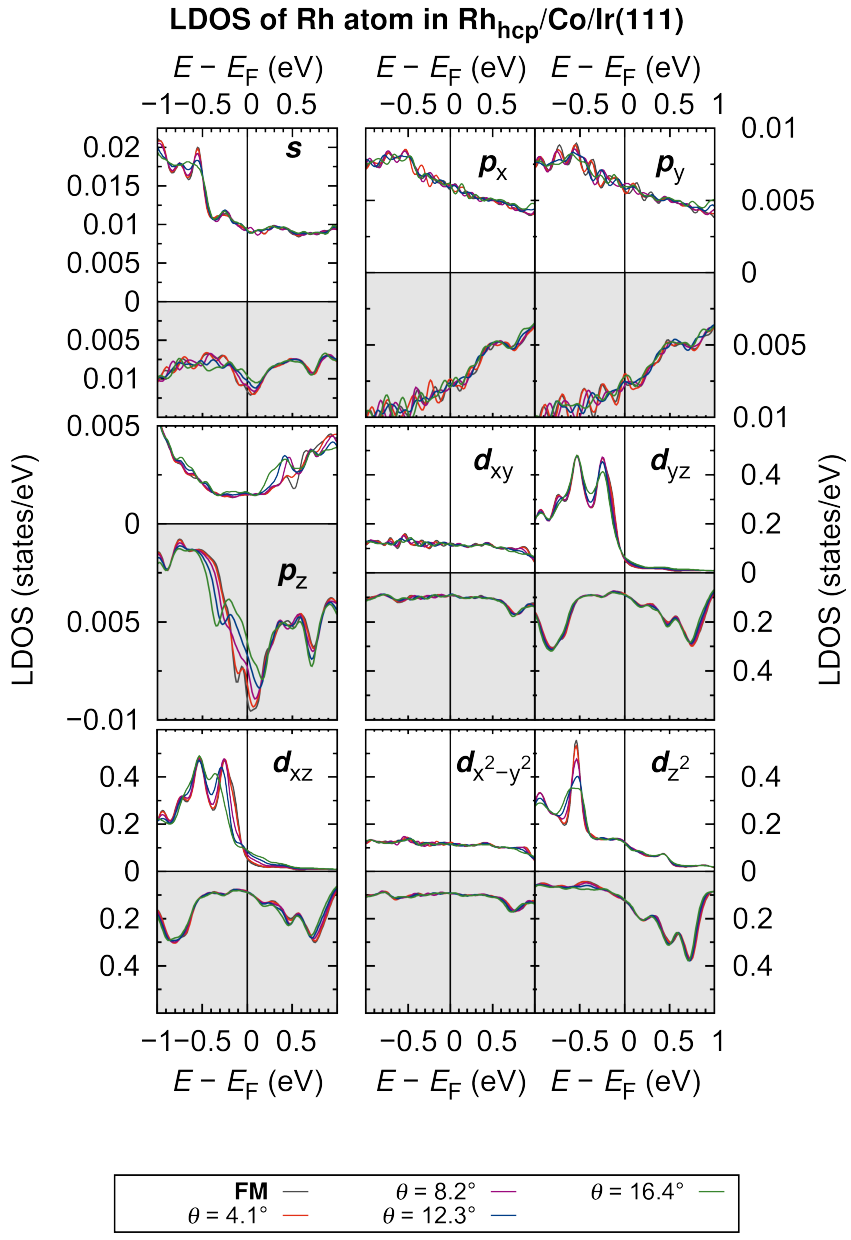

Figure C.2 | Orbital resolved local density of states (LDOS) for the Rh surface layer in Rh$_{hcp}$/Co/Ir(111). Shown are the calculated s, p, d orbital resolved LDOS from density functional theory for different spin spiral states along the $\overline{\Gamma}$-$\overline{K}$ direction of the hexagonal two-dimensional Brillouin zone. The angle θ between adjacent spins is given in the legend.

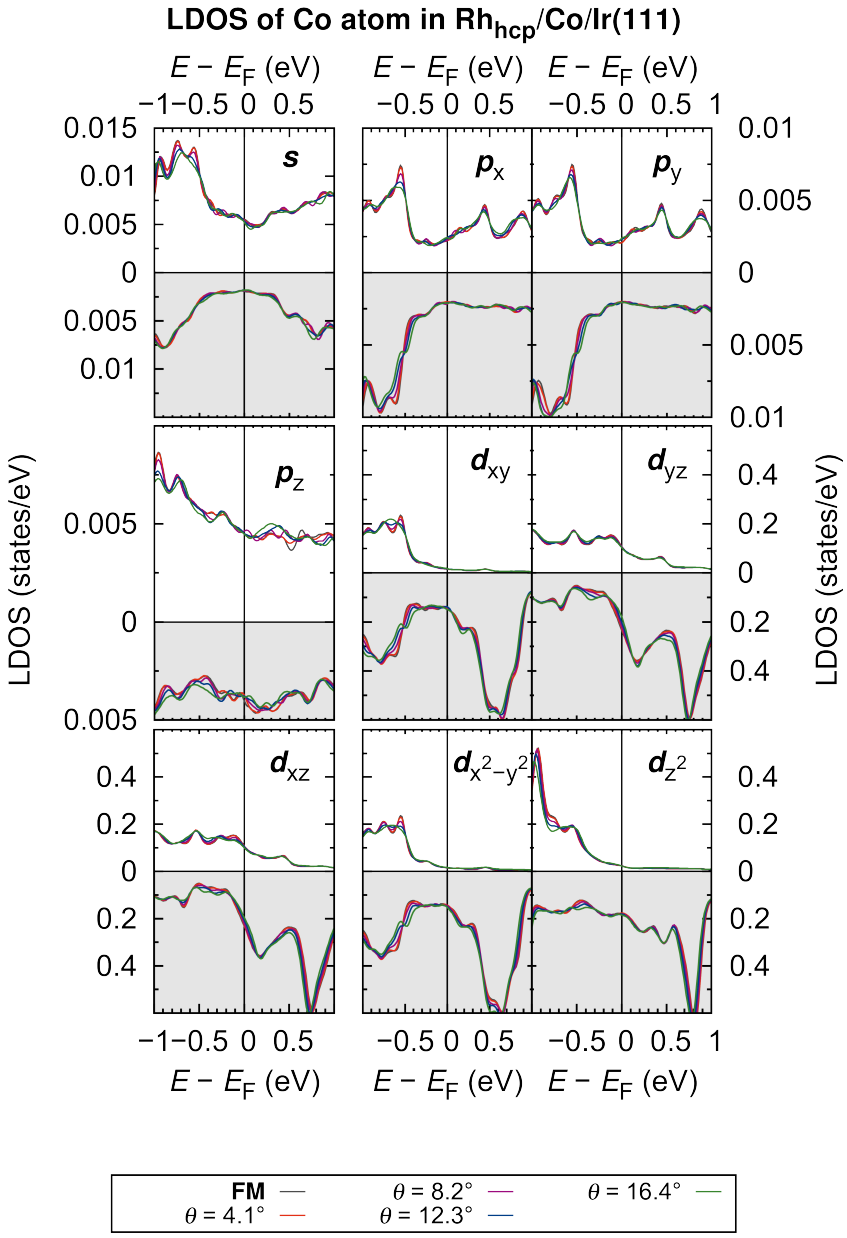

Figure C.3 | Orbital resolved local density of states (LDOS) for the Co layer in Rh$_{hcp}$/Co/Ir(111). Shown are the calculated s,p,d orbital resolved LDOS from density functional theory for different spin spiral states along the $\overline{\Gamma}$-$\overline{K}$ direction of the hexagonal two-dimensional Brillouin zone. The angle θ between adjacent spins is given in the legend.

Appendix D

Multi-Q states in DFT

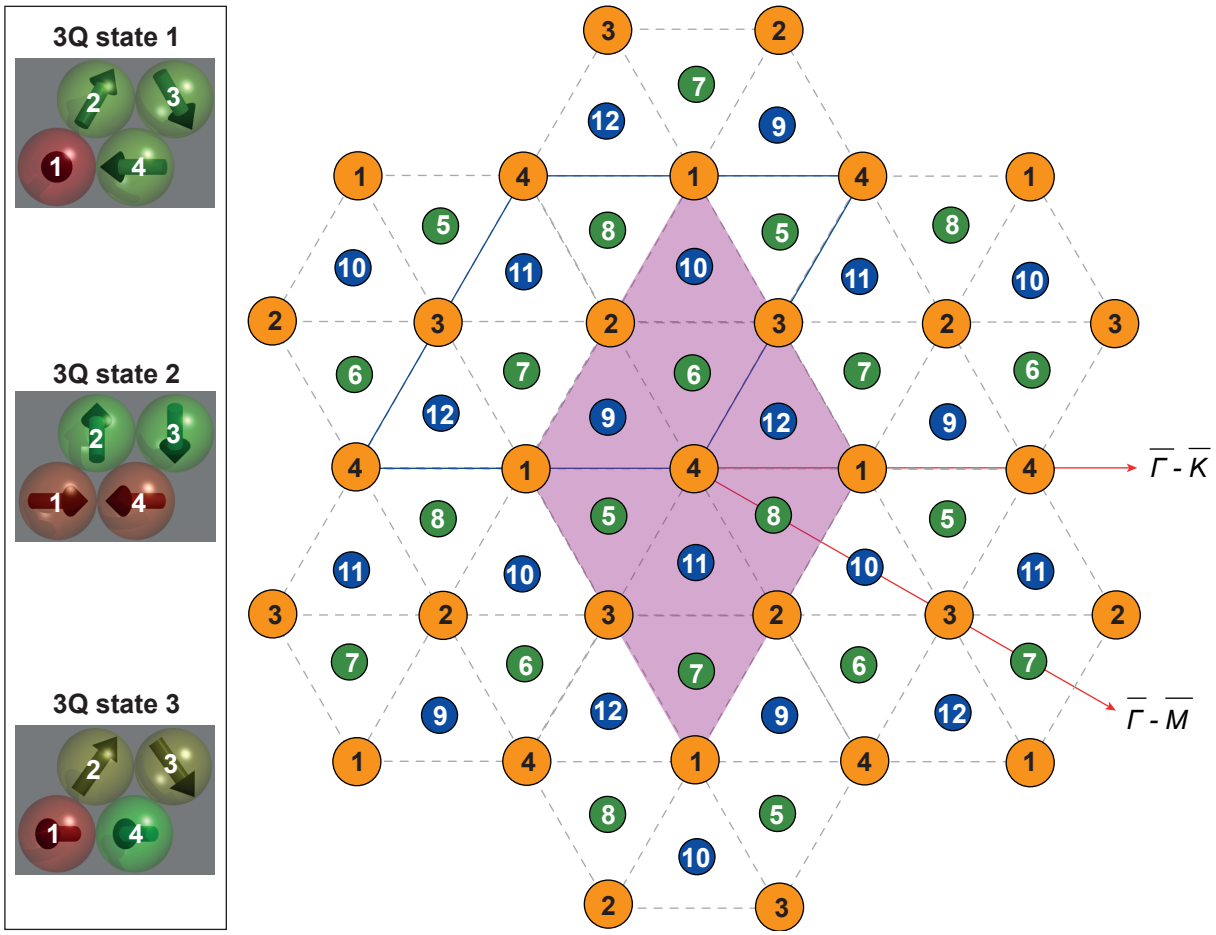

Figure D.1 | Unit cells of the 3Q state in the hexagonal lattice. In the left panel, three possible rotations of the 3Q states are presented: 3Q state 1 has one complete out-of-plane component, 3Q state 2 has neither a complete in-plane nor a complete out-of-plane component while in 3Q state 3 two spins are completely rotated in the plane. The numbers at the atoms denote the number in the unit cell drawn on the right. Shown is the hexagonal lattice of the magnetic atoms shown in the left panel (orange with numbers 1, ..., 4) including the in-plane positions of hcp (green with numbers 5, ..., 8) and fcc (blue with numbers 9, ..., 12) atoms. The unit cell surrounded with a blue line shows the unit cell with a 60° angle whereas the purple shaded area shows the cell with a 120° angle between $\mathbf{a}_1$ and $\mathbf{a}_2$. All angles of the stackings are presented in Tab. D.1. The pictures of the left panels are provided by André Kubetzka.

Table D.1 | Coordinates of magnetic moments of three 3Q states presented in Fig. D.1. The coordinates are given in Cartesian (x, y, z) and spherical (θ, ϕ) in ^{c}irc where $r = 1$. Note that the angles are rounded to 1 decimal digit and are not accurate enough to calculate energies of perfect 3Q states.

spin	3Q state 1					3Q state 2					3Q state 3				
	x	y	z	θ	ϕ	x	y	z	θ	ϕ	x	y	z	θ	ϕ
1	0	0	1	0	0	$\sqrt{6}/3$	0	$1/3$	54.7	0	$-1/\sqrt{3}$	0	$\sqrt{6}/3$	35.3	180
2	$\sqrt{2}/3$	$\sqrt{6}/3$	$-1/3$	109.5	60	0	$\sqrt{6}/3$	$-1/\sqrt{3}$	125.3	90	$1/\sqrt{3}$	$\sqrt{6}/3$	0	90	54.7
3	$\sqrt{2}/3$	$-\sqrt{6}/3$	$-1/3$	109.5	−60	0	$-\sqrt{6}/3$	$-1/\sqrt{3}$	125.3	−90	$1/\sqrt{3}$	$-\sqrt{6}/3$	0	90	−54.7
4	$-\sqrt{8}/3$	0	$-1/3$	109.5	180	$-\sqrt{6}/3$	0	$1/\sqrt{3}$	54.7	180	$-1/\sqrt{3}$	0	$-\sqrt{6}/3$	144.7	180
5	$-\sqrt{2}/3$	$-\sqrt{6}/3$	$1/3$	70.5	−120	0	$-\sqrt{6}/3$	$1/\sqrt{3}$	54.7	−90	$-1/\sqrt{3}$	$-\sqrt{6}/3$	0	90	−125.3
6	0	0	1	0	180	$-\sqrt{6}/3$	0	$-1/\sqrt{3}$	125.3	180	$1/\sqrt{3}$	0	$-\sqrt{6}/3$	144.7	0
7	$\sqrt{8}/3$	0	$1/3$	70.5	180	$\sqrt{6}/3$	0	$-1/\sqrt{3}$	125.3	0	$1/\sqrt{3}$	0	$\sqrt{6}/3$	35.3	0
8	$-\sqrt{2}/3$	$\sqrt{6}/3$	$1/3$	70.5	120	0	$\sqrt{6}/3$	$1/\sqrt{3}$	54.7	90	$-1/\sqrt{3}$	$\sqrt{6}/3$	0	90	54.7
9	$\sqrt{2}/3$	$-\sqrt{6}/3$	$-1/3$	109.5	−60	0	$-\sqrt{6}/3$	$-1/\sqrt{3}$	125.3	−90	$1/\sqrt{3}$	$-\sqrt{6}/3$	0	90	−54.7
10	$\sqrt{8}/3$	0	$-1/3$	109.5	180	$-\sqrt{6}/3$	0	$1/\sqrt{3}$	54.7	180	$-1/\sqrt{3}$	0	$-\sqrt{6}/3$	144.7	180
11	0	0	1	0	0	$\sqrt{6}/3$	0	$1/3$	54.7	0	$-1/\sqrt{3}$	0	$\sqrt{6}/3$	35.3	180
12	$\sqrt{2}/3$	$\sqrt{6}/3$	$-1/3$	109.5	60	0	$\sqrt{6}/3$	$-1/\sqrt{3}$	125.3	90	$1/\sqrt{3}$	$\sqrt{6}/3$	0	90	54.7

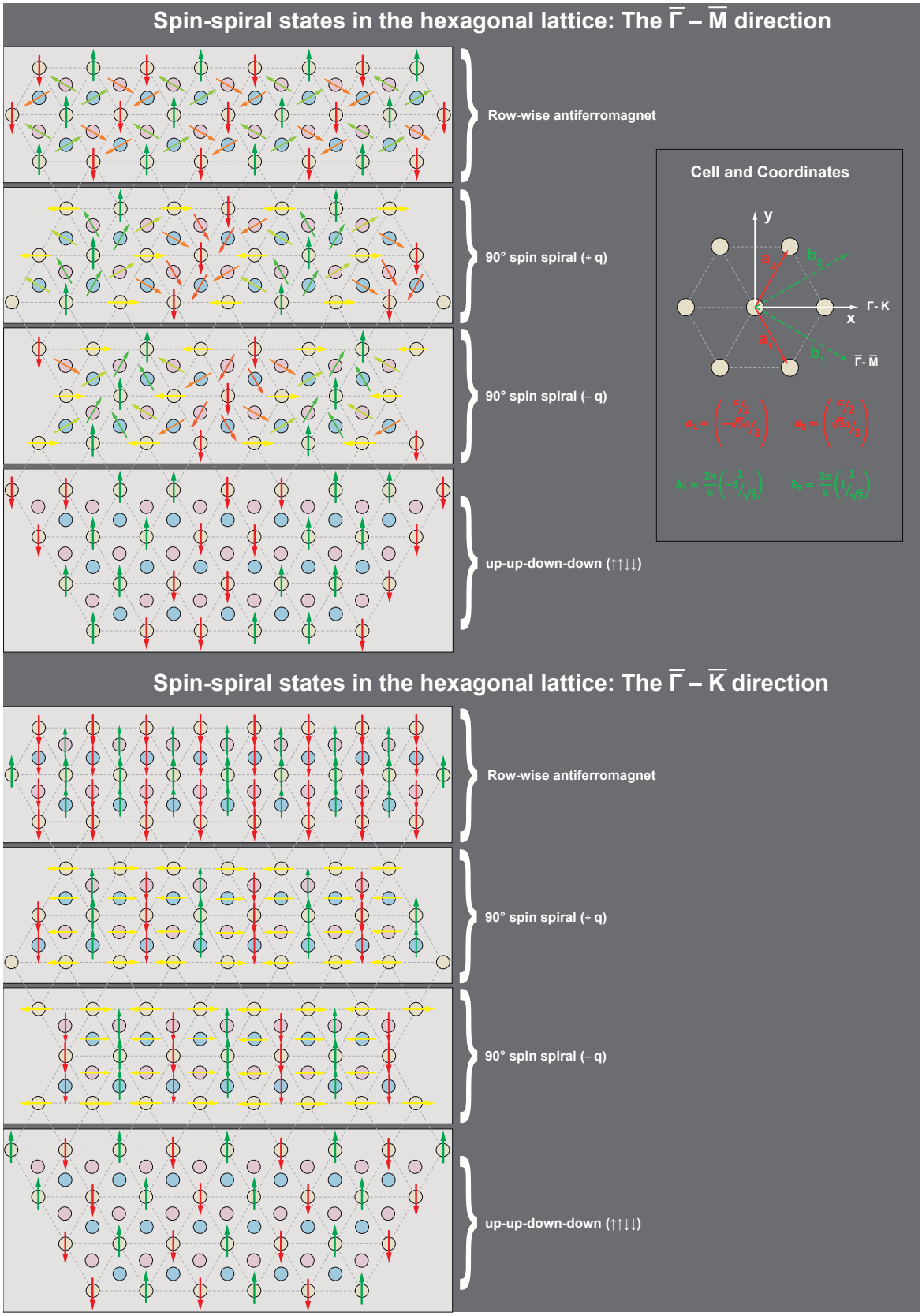

Figure D.2 | Unit cells of spin spiral states in high symmetry directions $\overline{\Gamma}$-$\overline{M}$ and $\overline{\Gamma}$-$\overline{K}$ of the hexagonal two-dimensional Brillouin zone. Shown are the RW-AFM states, right- and left rotating 90° spin spiral as well as the ↑↑↓↓. The bright circles, which are connected by grey dashed lines denote starting point atoms in the stacking whereas the blue and red circles show the atom position of hcp and fcc stacking, respectively.

Acknowledgements

This thesis would not have been possible without the support of supervisors, co-workers, friends and family. I deeply appreciate every relation I experienced on my way. In the following, I want to express my honest appreciation to several persons in particular.

Therefore, my first acknowledgement goes to Prof. Stefan Heinze for the opportunity of doing my PhD in his group. I joined the group five years ago and throughout, I especially experienced all positive sides of scientific work: great working surrounding, valuable discussions, support, encouragement and advice whenever it was needed. Besides I always was given the opportunity to follow my own ideas. Due to all these facts it was possible for me to continuously work on the projects even if it appeared to be tough and hindering.

As presented in this work, our DFT calculations are triggered by experiments and vice versa. Due to the excellent collaboration with experimental groups from Hamburg and Würzburg, it was possible to publish manuscripts where we could show how experiment and theory can intertwine on a high level. Namely, I want to thank Marco Perini, Jonas Spethmann, André Kubetzka, Kirsten von Bergmann and Prof. Roland Wiesendanger from the University of Hamburg for great collaboration, helpful discussions, patience and nice visits. Furthermore, Jonas, André and Kirsten gave me the opportunity to get insight in their experimental procedures within a three days STM crash course my voluntary report is still ongoing. From the University of Würzburg I want to thank Martin Schmitt, Matthias Vogt and especially Prof. Matthias Bode from whom I also received great support and nice discussions whenever I dropped by.

As part of the FET-Open project MAGicSky I enjoyed connecting with various scientists who worked on a similar topic. Especially with the research group of the PGI Jülich I had the opportunity to discuss results, problems and possibilities. I really appreciate the help of Gustav Bihlmayer, who always was ready to help with potential problems with the FLEUR code. Furthermore, I enjoyed discussing various topics with Bernd Zimmermann, Gideon Müller, Markus Hoffmann, Nikolai Kiselev and Prof. Stefan Blügel.

I want to mention my (also former) co-workers from the group in Kiel, Stephan von Malottki, Marie Böttcher, Soumyaioti Haldar, Hendrik Schrautzer, Felix Nickel, Henning Pralow, Nanning Petersen, Moritz Goerzen, Lydia Stühmer, Mara Gutzeit, Tim Drevelon, Souvik Paul, Pavel Bessarab, Anastasiia Varentcova, Grzegorz Kwiatkowski, Paolo Ferriani and Bertrand Dupé who all have and had a huge impact on my scientific improvement. Special thanks go to Stephan and Marie for awesome non-forgetable first conferences and discussions and Soum for supporting me with

his knowledge on computers and DFT.

Further, I want to thank Patrick Ludwig for taking care of the institutes coffee and the maintenance of computer and electronic parts. Without both, nothing is achievable in science. From the beginning of my Master's studies, our secretary Doris Schulz also took great care of me and helped me with all my questions. Sincere thanks to all my friends from volleyball, biking, gym and much more, who always gave me the opportunity to get rid of stress when something else is occurring. Unfortunately, the list of names is too long, but I would thank in specific the Trio Infernale of Lars and Arne for awesome races during our bachelors, masters and now PhDs studies. Mani for all the surfing, biking and constructions we did together and Volker, Hoang, Frank, Lars, Christian from my volleyball crew.

Last but not least, of course I want to thank my family for supporting me the whole life, the whole years and raising me to a grown up person that I (hopefully soon) will be.

Eidesstattliche Erklärung

Hiermit versichere ich an Eides statt, dass die vorliegende Dissertation – abgesehen von der Beratung durch meinen wissenschaftlichen Lehrer und der Verwendung der angegebenen Hilfsmittel – nach Inhalt und Form meine eigene ist. Sie hat weder ganz noch teilweise an einer Stelle im Rahmen eines Prüfungsverfahrens vorgelegen. Die hier vorgestellten Ergebnisse sind in Teilen bereits in wissenschaftlichen Fachzeitschriften veröffentlicht worden. Eine ausführliche Publikationsliste findet sich am Beginn dieser Arbeit. Diese Arbeit ist unter Einhaltung der Regeln guter wissenschaftlicher Praxis der Deutschen Forschungsgemeinschaft entstanden. Es wurde kein akademischer Grad entzogen.

Kiel, den

Peroration

Throughout my time as a PhD student I was very lucky with collaborators and supervisors having a high standard and understanding of scientific work: professionalism, profoundness, respect, kindness, the willingness to help and the ability to enjoy life's little pleasures. I believe that this is the right way in order to make good progress in science. For the future I hope to continue what I have learned and acquired. During the PhD work, I was drawing a periodic table which fitted my needs. It can serve as a quick review for people who deal with elements frequently.

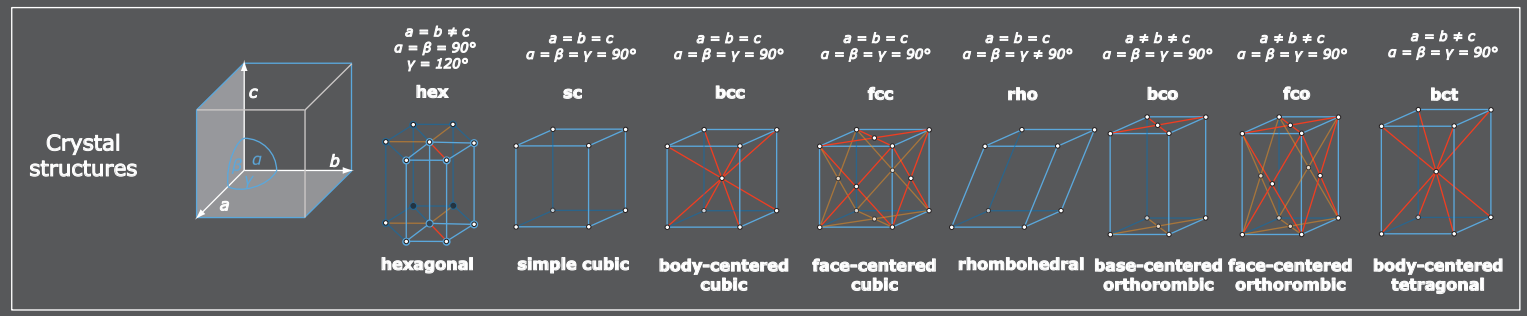

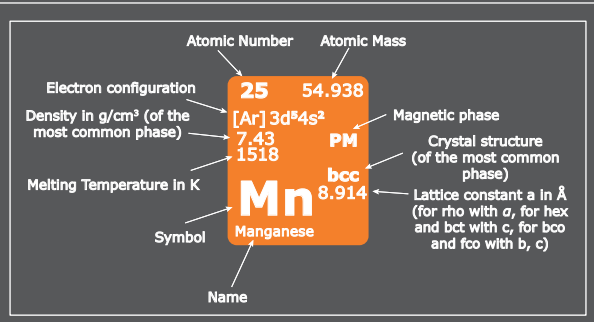

Magnetic phases:
DM: diamagnetic phase
PM: paramagnetic phase
FM: ferromagnetic phase
AFM: antiferromagnetic phase
Nonmagnetic elements are blank

	1	2	3	4	5	6	7	8	9	10	11	12	13	14	15	16	17	18
1	1 1.0080 1s¹ 0.089 14.0 DM **H** hex 3.776 6.162 Hydrogen																	2 4.0026 1s² 0.179 DM **He** hex 3.531 5.693 Helium
2	3 6.9400 [He] 2s¹ 0.53 453 PM **Li** bcc 3.510 Lithium	4 9.0122 [He] 2s² 1.85 1550 DM **Be** hex 2.286 3.583 Beryllium											5 10.810 [He] 2s²2p¹ 2.34 2600 DM **B** rho 5.067 58°4′ Boron	6 12.011 [He] 2s²2p² 2.26 4300 DM **C** hex 2.461 6.708 Carbon	7 14.007 [He] 2s²2p³ 1.03 63.3 DM **N** hex 4.042 6.601 Nitrogen	8 15.999 [He] 2s²2p⁴ 1.43 54.7 PM **O** sc 6.830 Oxygen	9 18.998 [He] 2s²2p⁵ 1.97 53.5 **F** sc 6.670 Fluorine	10 20.180 [He] 2s²2p⁶ 1.56 24.5 DM **Ne** fcc 4.455 Neon
3	11 22.990 [Ne] 3s¹ 0.97 371 PM **Na** bcc 4.291 Sodium	12 24.305 [Ne] 3s² 1.74 922 PM **Mg** hex 3.209 5.210 Magnesium											13 26.982 [Ne] 3s²3p¹ 2.70 933 PM **Al** fcc 4.050 Aluminium	14 28.085 [Ne] 3s²3p² 2.33 1683 DM **Si** fcc 5.431 Silicon	15 30.974 [Ne] 3s²3p³ 1.82 317.3 DM **P** sc 11.31 Phosphorus	16 32.060 [Ne] 3s²3p⁴ 2.07 386 DM **S** fco 10.46 12.87 24.49 Sulfur	17 35.450 [Ne] 3s²3p⁵ 2.09 172.2 DM **Cl** bco 6.240 4.480 8.260 Chlorine	18 39.948 [Ne] 3s²3p⁶ 1.78 83.9 DM **Ar** fcc 5.311 Argon
4	19 39.098 [Ar] 4s¹ 0.86 337 **K** bcc 5.334 Potassium	20 40.078 [Ar] 4s² 1.54 1111 PM **Ca** fcc 5.588 Calcium	21 44.956 [Ar] 3d¹4s² 2.99 1812 **Sc** hex 3.309 5.273 Scandium	22 47.867 [Ar] 3d²4s² 4.51 1933 PM **Ti** hex 2.951 4.684 Titanium	23 50.942 [Ar] 3d³4s² 6.1 2163 **V** bcc 3.024 Vanadium	24 51.996 [Ar] 3d⁵4s¹ 7.19 2130 AFM **Cr** bcc 2.885 Chromium	25 54.938 [Ar] 3d⁵4s² 7.43 1518 PM **Mn** bcc 8.914 Manganese	26 55.845 [Ar] 3d⁶4s² 7.86 1808 FM **Fe** bcc 2.866 Iron	27 58.933 [Ar] 3d⁷4s² 8.9 1768 FM **Co** fcc 3.544 Cobalt	28 58.693 [Ar] 3d⁸4s² 8.9 1726 FM **Ni** fcc 3.524 Nickel	29 63.546 [Ar] 3d¹⁰4s¹ 8.96 1356 DM **Cu** fcc 3.615 Copper	30 65.380 [Ar] 3d¹⁰4s² 7.14 693 DM **Zn** hex 2.665 4.947 Zinc	31 69.723 [Ar] 3d¹⁰4s²4p¹ 5.91 303 DM **Ga** bco 4.519 7.657 4.526 Gallium	32 72.630 [Ar] 3d¹⁰4s²4p² 5.32 1211 DM **Ge** fcc 5.658 Germanium	33 74.922 [Ar] 3d¹⁰4s²4p³ 5.72 1090 DM **As** rho 4.132 54°1′ Arsenic	34 78.971 [Ar] 3d¹⁰4s²4p⁴ 4.79 490 DM **Se** hex 4.366 4.959 Selenium	35 79.904 [Ar] 3d¹⁰4s²4p⁵ 4.10 266 DM **Br** bco 6.240 4.519 7.657 4.526 Bromine	36 83.798 [Ar] 3d¹⁰4s²4p⁶ 3.07 116.5 DM **Kr** fcc 5.658 Krypton
5	37 85.468 [Kr] 5s¹ 1.53 312 **Rb** bcc 5.620 Rubidium	38 87.620 [Kr] 5s² 2.60 1043 PM **Sr** fcc 6.085 Strontium	39 88.906 [Kr] 4d¹5s² 4.46 1796 **Y** hex 3.647 5.731 Yttrium	40 91.224 [Kr] 4d²5s² 6.49 2125 PM **Zr** hex 3.232 5.148 Zirconium	41 92.906 [Kr] 4d⁴5s¹ 8.4 2741 **Nb** bcc 3.299 Niobium	42 95.962 [Kr] 4d⁵5s¹ 10.2 2890 PM **Mo** bcc 3.147 Molybdenum	43 98.906 [Kr] 4d⁵5s² 11.5 2445 **Tc** hex 2.743 4.400 Technetium	44 101.07 [Kr] 4d⁷5s¹ 12.2 2583 PM **Ru** hex 2.706 4.281 Ruthenium	45 102.91 [Kr] 4d⁸5s¹ 12.4 2239 PM **Rh** fcc 3.804 Rhodium	46 106.42 [Kr] 4d¹⁰ 12.0 1825 PM **Pd** fcc 3.891 Palladium	47 107.87 [Kr] 4d¹⁰5s¹ 10.5 1234 DM **Ag** fcc 4.086 Silver	48 112.41 [Kr] 4d¹⁰5s² 8.65 594 DM **Cd** hex 2.979 5.619 Cadmium	49 114.82 [Kr] 4d¹⁰5s²5p¹ 7.31 429.8 DM **In** bct 3.253 4.956 Indium	50 118.71 [Kr] 4d¹⁰5s²5p² 7.30 505 PM **Sn** bct 3.253 4.956 Tin	51 121.76 [Kr] 4d¹⁰5s²5p³ 6.62 904 DM **Sb** rho 4.308 11.25 Antimony	52 127.60 [Kr] 4d¹⁰5s²5p⁴ 6.24 723 DM **Te** hex 4.457 5.927 Tellurium	53 126.90 [Kr] 4d¹⁰5s²5p⁵ 4.94 387 **I** bco 7.265 4.786 9.791 Iodine	54 131.29 [Kr] 4d¹⁰5s²5p⁶ 3.77 161.3 DM **Xe** fcc 6.197 Xenon
6	55 132.91 [Xe] 6s¹ 1.90 302 **Cs** bcc 6.140 Caesium	56 137.33 [Xe] 6s² 3.5 998 PM **Ba** bcc 5.025 Barium	57 / 71	72 178.49 [Xe] 4f¹⁴5d²6s² 13.1 2495 **Hf** hex 3.165 5.051 Hafnium	73 180.95 [Xe] 4f¹⁴5d³6s² 16.6 **Ta** bcc 3.303 Tantalum	74 183.84 [Xe] 4f¹⁴5d⁴6s² 19.3 3683 PM **W** bcc 3.165 Tungsten	75 186.21 [Xe] 4f¹⁴5d⁵6s² 21.0 3453 **Re** hex 2.761 4.458 Rhenium	76 190.23 [Xe] 4f¹⁴5d⁶6s² 22.6 3318 PM **Os** hex 2.734 4.320 Osmium	77 192.22 [Xe] 4f¹⁴5d⁷6s² 22.5 2683 PM **Ir** fcc 3.839 Iridium	78 195.08 [Xe] 4f¹⁴5d⁹6s¹ 21.4 2045 PM **Pt** fcc 3.924 Platinum	79 196.97 [Xe] 4f¹⁴5d¹⁰6s¹ 19.3 1337 DM **Au** fcc 4.078 Gold	80 200.59 [Xe] 4f¹⁴5d¹⁰6s² 13.6 234.3 DM **Hg** rho 2.993 70° Mercury	81 204.38 [Xe] 4f¹⁴5d¹⁰6s²6p¹ 11.85 577 DM **Tl** hex 3.456 5.526 Thallium	82 207.20 [Xe] 4f¹⁴5d¹⁰6s²6p² 11.4 601 DM **Pb** fcc 4.950 Lead	83 208.98 [Xe] 4f¹⁴5d¹⁰6s²6p³ 9.8 544.5 DM **Bi** rho 4.550 11.86 Bismuth	84 209.98 [Xe] 4f¹⁴5d¹⁰6s²6p⁴ 9.4 527 **Po** sc 3.352 Polonium	85 210.99 [Xe] 4f¹⁴5d¹⁰6s²6p⁵ 575 **At** Astatine	86 222.02 [Xe] 4f¹⁴5d¹⁰6s²6p⁶ 4.4 203 fcc **Rn** Radon
7	87 223.02 [Rn] 7s¹ 1.74 300 **Fr** Francium	88 228.03 [Rn] 7s² 5.0 **Ra** bcc 5.150 Radium	89 / 103	104 267.12 [Rn] 5f¹⁴6d²7s² **Rf** Rutherfordium	105 268.13 [Rn] 5f¹⁴6d³7s² **Db** Dubnium	106 271.13 [Rn] 5f¹⁴6d⁴7s² **Sg** Seaborgium	107 267.13 [Rn] 5f¹⁴6d⁵7s² **Bh** Bohrium	108 277.15 [Rn] 5f¹⁴6d⁶7s² **Hs** Hassium	109 276.15 [Rn] 5f¹⁴6d⁷7s² **Mt** Meitnerium	110 281.16 [Rn] 5f¹⁴6d⁸7s¹ **Ds** Darmstadtium	111 280.16 [Rn] 5f¹⁴6d¹⁰7s¹ **Rg** Roentgenium	112 285.17 [Rn] 5f¹⁴6d¹⁰7s² **Cn** Copernicium	113 284.18 [Rn] 5f¹⁴6d¹⁰7s²7p¹ 5.0 **Uut** Ununtrium	114 289.19 [Rn] 5f¹⁴6d¹⁰7s²7p² **Fl** Flerovium	115 288.19 [Rn] 5f¹⁴6d¹⁰7s²7p³ **Uup** Ununpentium	116 292.20 [Rn] 5f¹⁴6d¹⁰7s²7p⁴ **Lv** Livermorium	117 294.00 [Rn] 5f¹⁴6d¹⁰7s²7p⁵ **Uus** Ununseptium	118 294.00 [Rn] 5f¹⁴6d¹⁰7s²7p⁶ **Uuo** Ununoctium

Lanthanide Series	57 138.91 [Xe] 5d¹6s² 6.17 1193 **La** hex 3.770 1.216 Lanthanum	58 140.12 [Xe] 4f²6s² 6.77 PM 1071 **Ce** fcc 4.850 Cerium	59 140.91 [Xe] 4f³6s² 6.77 1204 **Pr** hex 3.673 11.84 Praseodymium	60 144.24 [Xe] 4f⁴6s² 7.00 PM 1283 **Nd** hex 3.658 11.80 Neodymium	61 146.92 [Xe] 4f⁵6s² 1350 **Pm** hex Promethium	62 150.36 [Xe] 4f⁶6s² 7.54 PM 1345 **Sm** rho 8.996 23° Samarium	63 151.96 [Xe] 4f⁷6s² 7.90 PM 1095 **Eu** bcc 4.582 Europium	64 157.25 [Xe] 4f⁷5d¹6s² 8.23 FM 1585 **Gd** hex 3.636 5.783 Gadolinium	65 158.93 [Xe] 4f⁹6s² 8.54 PM 1633 **Tb** hex 3.601 5.694 Terbium	66 162.50 [Xe] 4f¹⁰6s² 8.78 PM 1680 **Dy** hex 3.590 5.648 Dysprosium	67 164.93 [Xe] 4f¹¹6s² 9.05 PM 1743 **Ho** hex 3.577 5.616 Holmium	68 167.26 [Xe] 4f¹²6s² 9.37 PM 1759 **Er** hex 3.559 5.587 Erbium	69 168.93 [Xe] 4f¹³6s² 9.31 PM 1818 **Tm** hex 3.538 5.555 Thulium	70 173.05 [Xe] 4f¹⁴6s² 6.97 1097 **Yb** fcc 5.486 Ytterbium	71 174.97 [Xe] 4f¹⁴5d¹6s² 9.84 1929 **Lu** hex 3.503 5.551 Lutetium
Actinide Series	89 227.03 [Rn] 6d¹7s² 10.1 1323 **Ac** fcc 5.311 Actinium	90 232.04 [Rn] 6d²7s² 11.7 2020 **Th** fcc 5.084 Thorium	91 231.04 [Rn] 5f²6d¹7s² 15.4 1470 **Pa** bct 3.932 3.238 Protactinium	92 238.05 [Rn] 5f³6d¹7s² 19.07 1406 **U** bco 4.519 7.657 4.526 Uranium	93 237.05 [Rn] 5f⁴6d¹7s² 20.3 913 **Np** Neptunium	94 244.06 [Rn] 5f⁶7s² 19.8 914 **Pu** Plutonium	95 243.06 [Rn] 5f⁷7s² 11.8 1267 **Am** hex 3.468 11.24 Americium	96 248.07 [Rn] 5f⁷6d¹7s² 13.51 1600 **Cm** Curium	97 249.08 [Rn] 5f⁹7s² 14.78 1259 **Bk** Berkelium	98 252.08 [Rn] 5f¹⁰7s² 15.1 1173 **Cf** Californium	99 254.09 [Rn] 5f¹¹7s² 8.84 1133 **Es** Einsteinium	100 257.10 [Rn] 5f¹²7s² 1125 **Fm** Fermium	101 260.10 [Rn] 5f¹³7s² **Md** Mendelevium	102 259.10 [Rn] 5f¹⁴7s² **No** Nobelium	103 262.11 [Rn] 5f¹⁴6d¹7s² **Lr** Lawrencium

Information from: www.periodni.com; Ashcroft, N. and Mermin, N., Solid State Physics (1976); Design by Sebastian Meyer, basti-f2@gmx.de